Cross-Shelf Circulation and Momentum and Heat Balances over the Inner Continental Shelf Near Martha's Vineyard, Massachusetts

by

Melanie Rinn Fewings

B.S. Physics, Western Washington University, 1996
M.S. Applied Physics, Cornell University, 1999

Submitted in partial fulfillment of the requirements for the degree of

Doctor of Philosophy in Physical Oceanography

at the

MASSACHUSETTS INSTITUTE OF TECHNOLOGY

and the

WOODS HOLE OCEANOGRAPHIC INSTITUTION

September 2007

Signature of Author _____

Joint Program in Oceanography/Applied Ocean Science and Engineering
Massachusetts Institute of Technology
and Woods Hole Oceanographic Institution
August 16, 2007

Certified by _____

Steven J. Lentz
Senior Scientist, Department of Physical Oceanography
Woods Hole Oceanographic Institution
Thesis Supervisor

Accepted by _____

Raffaele Ferrari
Chairman, Joint Committee for Physical Oceanography
Massachusetts Institute of Technology
Woods Hole Oceanographic Institution

Cross-Shelf Circulation and Momentum and Heat Balances over the Inner Continental Shelf Near Martha's Vineyard, Massachusetts

by
Melanie Rinn Fewings

Submitted to the Department of Physical Oceanography
on August 16, 2007, in partial fulfillment of the
requirements for the degree of
Doctor of Philosophy in Physical Oceanography

Abstract

The water circulation and evolution of water temperature over the inner continental shelf are investigated using observations of water velocity, temperature, density, and bottom pressure; surface gravity waves; wind stress; and heat flux between the ocean and atmosphere during 2001–2007.

When waves are small, cross-shelf wind stress is the dominant mechanism driving cross-shelf circulation. The along-shelf wind stress does not drive a substantial cross-shelf circulation. The response to a given wind stress is stronger in summer than winter. The cross-shelf transport in the surface layer during winter agrees with a two-dimensional, unstratified model. During large waves and onshore winds the cross-shelf velocity is nearly vertically uniform, because the wind- and wave-driven shears cancel. During large waves and offshore winds the velocity is strongly vertically sheared because the wind- and wave-driven shears have the same sign.

The subtidal, depth-average cross-shelf momentum balance is a combination of geostrophic balance and a coastal set-up and set-down balance driven by the cross-shelf wind stress. The estimated wave radiation stress gradient is also large. The dominant along-shelf momentum balance is between the wind stress and pressure gradient, but the bottom stress, acceleration, Coriolis, Hasselmann wave stress, and nonlinear advection are not negligible. The fluctuating along-shelf pressure gradient is a local sea level response to wind forcing, not a remotely generated pressure gradient.

In summer, the water is persistently cooled due to a mean upwelling circulation. The cross-shelf heat flux nearly balances the strong surface heating throughout mid-summer, so the water temperature is almost constant. The along-shelf heat flux divergence is apparently small. In winter, the change in water temperature is closer to that expected due to the surface cooling. Heat transport due to surface gravity waves is substantial.

Thesis Supervisor: Steven J. Lentz
Title: Senior Scientist, Department of Physical Oceanography
Woods Hole Oceanographic Institution

Acknowledgments

My thesis advisor, Steve Lentz, gives me an admirable balance of advice and encouragement to be independent. I often feel that Steve treats me more as a colleague than as a student, and I really appreciate the humor and respect with which he carries out the process of advising. Steve's door is truly always open and he always has time for me. When I think I'm going to his office for fifteen minutes, and three hours later I am still there asking questions, his foot is never tapping. It is inspiring to work with a person of Steve's integrity and fairness (not to mention understanding of coastal oceanography).

I have a really wonderful Thesis Committee: Bob Beardsley, Heidi Sosik, John Trowbridge, and Glenn Flierl. With them to guide me, my thesis committee meetings and even the private session of my thesis defense turned out to be enjoyable discussions. Bob Beardsley is always supportive and excited about every result and full of ideas about other avenues to explore, and whenever we meet I feel buoyed up by his optimism. John Trowbridge was of crucial help in suggesting and planning, and generous in finding funding for, additional observations that became part of this thesis. It is amazing to watch John and Steve creating mooring arrays and making them into reality. Heidi was never upset that I didn't get to the stage of working with her data, and always enthusiastic about discussing the implications of the results in this thesis. Heidi has also really helped me improve my writing. Her pithy comments stick with me and echo in my head during later writing sessions, arresting my bad habits. Glenn Flierl was my advisor during my first year in the Joint Program. Although I later decided to work with Steve on a project quite far removed from Glenn's own work, Glenn remains patient and interested in what I'm doing. He often points out far-reaching theoretical connections to this mostly observational thesis work, connections that I would otherwise likely never have seen. Glen Gawarkiewicz went out of his way to invite me along on one of his research cruises and to help me learn more about being an observational oceanographer. He kindly agreed to be the Chairman of my Thesis Defense, and was very thoughtful in that role. My research experience

as a graduate student in physical oceanography was very challenging and as a whole extremely gratifying, and I thank every member of my Thesis Committee for being so generous with their time and advice.

Bob Weller led me to be hired at WHOI as a research associate when I wanted to try out physical oceanography. My first research cruise was with his group. Bob always encouraged me to enter the Joint Program, and as a result, here I am at the end of it. Thanks to Jim Price for support during the advisor-choosing process. Thanks to Joe Pedlosky for taking the time to notice that I might enjoy working with Steve Lentz, and the time to tell me so. I thank Nancy Rabalais of the Louisiana Universities Marine Consortium for inviting me, sight unseen, to join her summertime hypoxia-mapping cruise in the Gulf of Mexico. Thanks also to Jim Edson, Rocky Geyer, Parker MacCready, and the many other scientists at WHOI and elsewhere with whom I have had the privilege to interact during graduate school.

This thesis was greatly improved due to suggestions by, in addition to my thesis committee, Ken Brink, Tom Farrar, Carlos Moffat-Varas, and Kevin Brown, who all provided very helpful and detailed comments.

The Academic Programs Office at WHOI is always full of smiles and help and patience. Judy McDowell, John Farrington, Marcey Simon, and Stacey Drange watched over us students during my early years in the Joint Program, and now Julia Westwater, Marsha Gomes, Christine Charette, Laishona Vitelli, and Valerie Caron have the solutions to all my queries, and never an unsympathetic ear. Ronni Schwartz in the MIT Joint Program Office never forgets me although I see her maybe once a year. And who else will always call me "Dahling"? I also thank all the WHOI Physical Oceanography Department administrative staff, especially Annie Doucette, Hazel Salazar, and Maryanne Wray.

I was lucky to have Dave Chapman as a teacher for coastal oceanography class. He was always patient and thoughtful, and he displayed an example of grace under pressure that I have never seen surpassed.

The Joint Program students form a wonderful community. To all the physical oceanography students: it has been a thrilling and intimidating experience to have

such amazing fellow students. Thank you for your friendship and the lively scientific discussions.

Heather Furey has made me a warm welcome in her life since the day I arrived in Woods Hole. Albert Fischer, Deb Glickson, Jon Woodruff and Akiko Okusu, Tom Farrar, Clare Williams, Anne Thompson, Kristin Gribble, Elke Hodson, Dave Ralston and Malcolm Scully, Jess Thomson, Jessica Warren, Stephen Licht and Margaret Hayden, Seth John and Andrea Ryan, Gareth Lawson and Nicole Smith, how lonely these years of graduate school would have been without you in my life! With Greg Gerbi in the car there is never a shortage of conversation from Boston all the way to Woods Hole. Stephanie Waterman's company as a carpooling and running partner and roommate has made my late-night commutes to Woods Hole and time away from home much easier to bear in the last few years.

Andrew Mosedale, Jim Thomson, and Carlos Moffat-Varas are everything a person could imagine to hope for in classmates and officemates, and then some. They may be in Texas or Seattle or Chile, but they never leave my brain. I am rich with friends from the past six years.

My father, David, my mother, Irene, my sister, Natalie, and my grandmother Rose have given me their unswerving support for my whole life and never once asked me if I was ever going to stop going to school. I know their belief in me is always there, and that knowledge has helped me through the rough times.

For Kevin Brown I have thanks for thoughts and actions too many to count. They include never-ending support and patience, a commute that has ranged from 73 to 403 miles, music and laughter, gourmet cooking and home-brewed beer, and more than his share of housework during the final throes of this thesis.

We thank Robert Weller for providing mooring data from CBLAST 2003. We also thank Tom Farrar, Robert Weller, Jim Lerczak, and Jay Sisson for deployment of the CBLAST 2003 F ADCP, the Captain and crew of the *R/V Connecticut* for mooring recovery in fall 2003, Janet Fredericks and Craig Marquette for data downloading, and Craig Marquette, Jim Dunn, Jeff Lord, Scott Worrilow, John Lund, Rick Rupan, Carlos Moffat, Jessica Warren, Clare Williams, Greg Gerbi, and especially Captain

Ken Houtler and crew member Ian Hanley of *R/V Tioga* for deployment and recovery of the SWWIM I moorings. Peter Howd and Kent Hathaway generously let me do what I would with their beautiful data from North Carolina.

My last three years of thesis work were supported by National Aeronautics and Space Administration Headquarters under the Earth System Science Fellowship Grant NNG04GQ14H, and by WHOI Academic Programs Fellowship Funds. I also benefited from the freedom of a Clare Boothe Luce Fellowship during my first year in the Joint Program, which allowed me more time than is usual to explore different research topics before choosing an advisor.

This research was also funded by the National Aeronautics and Space Administration under grant NNG04GL03G and the Ocean Sciences Division of the National Science Foundation under grants OCE-0241292 and OCE-0548961. The Martha's Vineyard Coastal Observatory is partly funded by the Woods Hole Oceanographic Institution and the Jewett/EDUC/Harrison Foundation. The ADCP deployments at CBLAST site F were funded by National Science Foundation Small Grant for Exploratory Research OCE-0337892. Ship time for deployment and recovery of the F ADCP was provided by Robert Weller through Office of Naval Research contracts N00014-01-1-0029 and N00014-05-10090 for the Low-Wind Component of the Coupled Boundary Layers Air-Sea Transfer Experiment.

Contents

List of Figures

List of Tables

Chapter 1

Introduction

This thesis is an investigation of the dominant processes that cause cross-shelf circulation and heat transport on time scales of days to months over the inner continental shelf of the northern Middle Atlantic Bight in the northeastern United States. Wind, waves, tides, freshwater input from land, and heating and cooling from the overlying atmosphere can all be important forcing mechanisms for continental shelf circulation and heat transport. The circulation on the shelf is important for coastal ecosystems and the human populations that depend on coastal waters, because the circulation controls the transport of nutrients, larvae, harmful algal blooms, and pollutants. The import and export between the continental shelf and the open ocean of heat, salt, and organic carbon also impacts the global climate system and is affected by the circulation on the shelf.

The inner shelf, which is a transition region between the surfzone and the deeper continental shelf where the along-shelf flow tends to be geostrophic, is a region where the density stratification of the water is highly variable (*e.g.,* Chapter 4). The water can go from stratified to unstratified and back again within a few days. The physical dynamics of the inner-shelf circulation are intimately related to the stratification through the inhibiting effect of stratification on vertical mixing and through the influence of buoyancy forcing on the circulation. For this reason the circulation can be very different during summer and winter, since the stratification tends to be stronger in summer.

Ecological implications of the continental shelf circulation, though not the subject of this thesis, are one reason why understanding the physics of continental shelf circulation is important. The stratification and circulation are thought to be of primary importance in controlling the biological productivity of the continental shelf, particularly through the nutrients supplied to the euphotic zone by coastal upwelling (*e.g.*, Falkowski et al., 1998). These physical processes that affect phytoplankton biomass exert strong bottom-up controls on the productivity of the entire ecosystem. Through these controls, the influence of physical processes on phytoplankton is felt by higher trophic level organisms, such as fish, that are important food sources for humans. The highest levels of marine phytoplankton biomass (Figure 1-1) and primary productivity (Falkowski et al., 1998) are found over the continental shelves, and the shelves are therefore important to the cycling of carbon and other nutrients on both regional and global scales. Estimated annual mean export production is especially high over the continental shelves, as compared to the rest of Earth's oceans (Falkowski et al., 1998). The export production in the coastal regions supports most of the world's ocean fisheries. For these reasons, to understand processes that govern phytoplankton biomass in shelf waters is a long-standing goal of the oceanographic community. Understanding the physical mechanisms that drive the shelf circulation will be necessary for understanding the dynamics of phytoplankton biomass. In spite of this widespread interest and decades of study, the mechanisms, both physical and biological, that control biomass distributions are so complicated that a detailed understanding remains elusive.

Phytoplankton biomass in the Middle Atlantic Bight is high not only over the continental shelf, but over the inner shelf in particular (Figure 1-2). The seasonal cycle of phytoplankton biomass on the continental shelf of New England has been studied for over 75 years and is known to be complex. Researchers working near Woods Hole as early as 1926 noticed that the seasonal cycle of biomass in the inner shelf is different from that in the middle and outer regions of the shelf (Riley, 1947; Bigelow, 1926). In the middle and outer shelf, biomass is typically high during the "blooms" in late spring and in fall, and low at other times of year. In the inner

shelf, there is a fall bloom but biomass is often high during winter and low during spring (Figure 1-3). Temporary increases in stratification in the inner shelf due to the presence of fresh water are one hypothesized cause of these winter blooms (Gran and Braruud, 1935; Sverdrup, 1953).

The cross-shelf circulation is potentially crucial for maintaining the biological productivity of the inner shelf. Nevertheless, due to the number and complexity of processes influencing inner-shelf circulation, we have not understood very much about how variations in cross-shelf circulation take place. The inner shelf is the region where along-shelf advection of coastally-trapped buoyant inflows has the greatest effect on stratification and circulation; where the water is so shallow that the wind-driven surface layer often overlaps the bottom boundary layer so that turbulent vertical mixing dominates and the water column can become unstratified; and where vertical advection and the associated displacement of isopycnals takes place during wind-driven upwelling and downwelling. All of these processes are relevant not only to the character of the circulation but also to the transport of nutrients, larvae, pollutants, and other tracers, which makes the inner shelf an important subregion of the continental shelf to understand.

Along-shelf advection is relevant for heat and freshwater transport in the Middle Atlantic Bight due to the mean westward flow at mid-shelf (Shearman and Lentz, 2003) and the large freshwater inputs and strong wintertime cooling in the Gulf of Maine and other locations upstream (to the northeast) of the study site. Because the inner shelf is fairly shallow, surface heating and cooling have strong influences on the stratification throughout the water column, as does vertical mixing driven by winds and tides. Wind-driven coastal upwelling and downwelling can cause cross-shelf circulations in the inner shelf region. Most studies of wind-driven upwelling and downwelling have been in the middle and outer shelf regions. It is over the inner shelf, where the surface and boundary layers interact, that the cross-shelf divergence in cross-shelf transport that causes upwelling actually takes place.

The data used in this thesis were acquired in the vicinity of the Martha's Vineyard Coastal Observatory (MVCO). A diagram of the observatory is shown in Figure 1-4.

Some of the data were collected as part of the Low-Wind Component of the Coupled Boundary Layers/Air-Sea Transfer Defense Research Initiative (CBLAST-Low DRI) during 2001–2003. The mooring locations during CBLAST are shown in Figure 1-5. The CBLAST program and complementary wintertime measurements collected during the first Stratification, Wind, and Waves on the Inner Shelf at MVCO (SWWIM I) experiment in 2004–2005 provide an opportunity to study the mechanisms controlling coastal circulation and heat transport on the inner New England shelf. The key questions addressed in this thesis are

- What are the dominant processes that drive cross-shelf circulation on time scales of days to months over the inner continental shelf off New England?
- Which dynamical balances are dominant over this inner shelf?
- What are the mechanisms that control water temperature over the inner shelf?

Chapter 2 addresses these questions:

1. What are the dominant processes that drive cross-shelf circulation on time scales of days to months on the inner continental shelf off New England?
2. What is the relative importance of cross-shelf wind, along-shelf wind, and surface gravity waves in driving cross-shelf circulation over the inner shelf?

We examine the relation between the cross-shelf circulation profiles and the wind and wave forcing. We take advantage of the unusual length of the MVCO time series of wind stress, wave height and period, and water velocity to look separately at times when only one type of forcing was strong: along-shelf wind stress, cross-shelf wind stress, or surface gravity waves. This approach enables us to observe the separate responses of the cross-shelf circulation to those three forcings, in spite of the strong correlation in time of those forcings. The strong influence of cross-shelf wind stress and surface gravity waves, which have typically been neglected in inner- and mid-shelf studies, then becomes apparent. The response of the cross-shelf circulation to surface gravity waves alone is discussed in Appendix E. Chapter 2 examines the cases of wind

forcing alone and of combined wind and wave forcing, which is the most commonly observed case.

Chapter 3 addresses these questions:

1. Which dynamical balances are dominant over this inner shelf?

2. Are surfzone and mid-shelf dynamics both important?

We use the observations described above to calculate terms in the along-shelf and cross-shelf momentum budgets as a way to determine which dynamical balances are dominant over this inner shelf. Since the inner shelf is a transition region between the surfzone and the mid-shelf, we estimate momentum budget terms that are dominant in the surfzone (wave radiation stress gradients) as well as terms that are dominant at mid-shelf (*e.g.,* the Coriolis acceleration due to the along-shelf velocity). We also include the Hasselmann (1970) wave stress, which is due to the interaction of surface gravity waves with Earth's rotation and has not been included in any previous momentum budget estimated from observations.

Chapter 4 addresses these questions:

1. What are the mechanisms that control water temperature over the inner shelf?

2. Is surface heating and cooling or cross-shelf or along-shelf heat flux divergence the dominant influence on water temperature?

3. Is heat transport due to surface gravity waves important?

We use water temperature and velocity along with meteorological measurements to calculate terms in the heat budget for a cross-shelf section of water at MVCO. Using direct estimates of the surface heating and cross-shelf advective heat flux divergence, we determine whether surface heating and cooling or cross-shelf or along-shelf heat flux divergence is the dominant influence on the water temperature over this inner shelf. This is the first continental shelf study to include the heat transport due to the Stokes' drift generated by surface gravity waves. Chapter 5 summarizes the main results of this thesis.

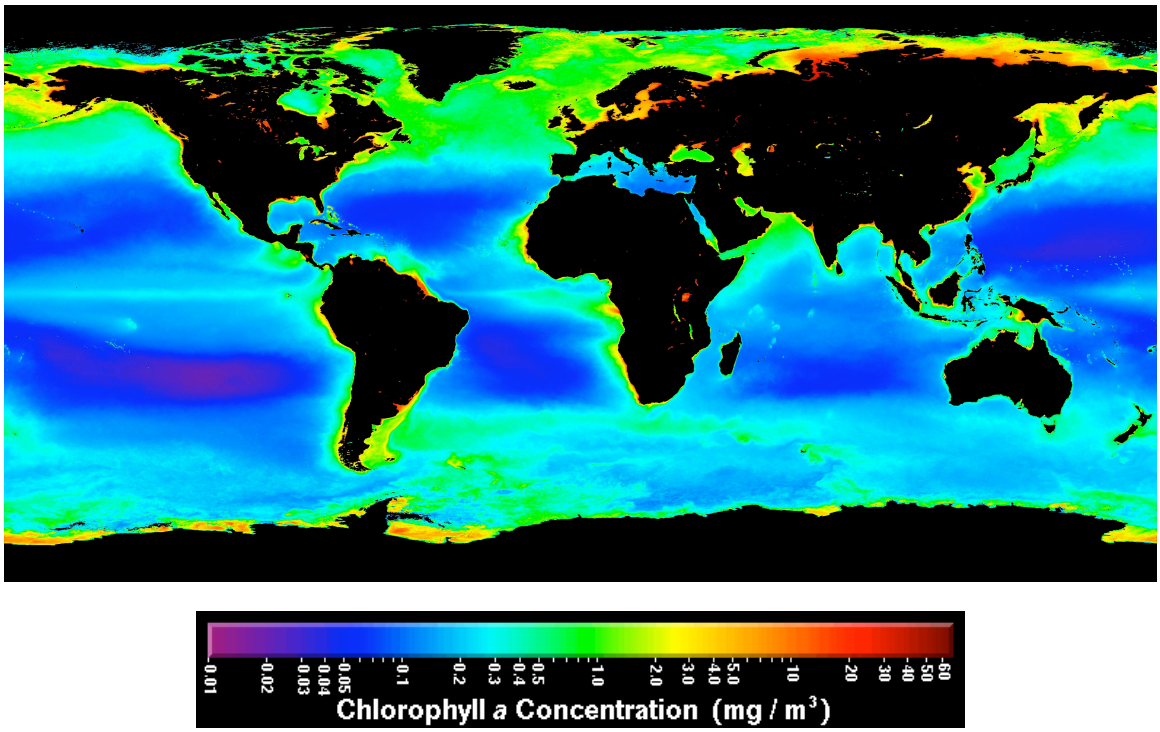

Figure 1-1: Global map of annual mean chlorophyll-a for the world oceans. Chlorophyll-a is a proxy for phytoplankton biomass. Coastal regions support a high standing stock of phytoplankton biomass. From the NASA Ocean Color Image Gallery, http://oceancolor.gsfc.nasa.gov.

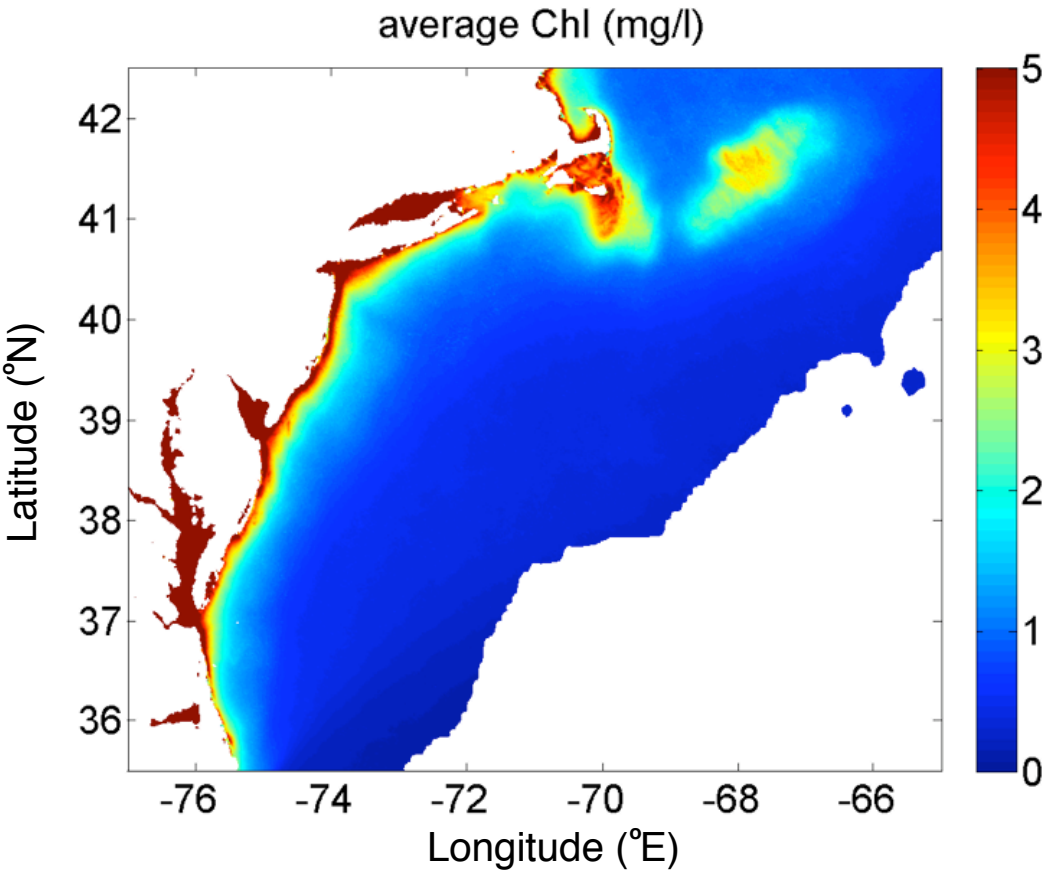

Figure 1-2: Annual mean chlorophyll-a distribution onshore of the 4000-m isobath off the northeastern United States, from NASA SeaWiFs data. The Middle Atlantic Bight extends from Cape Hatteras (lower left) to Cape Cod (upper middle). Chlorophyll-a concentration, a proxy for phyoplankton biomass, is highest in the waters closest to shore, over the inner shelf. Figure, data, and data processing courtesy Brittan Rabinovitch, Heidi Sosik, and Steve Lentz.

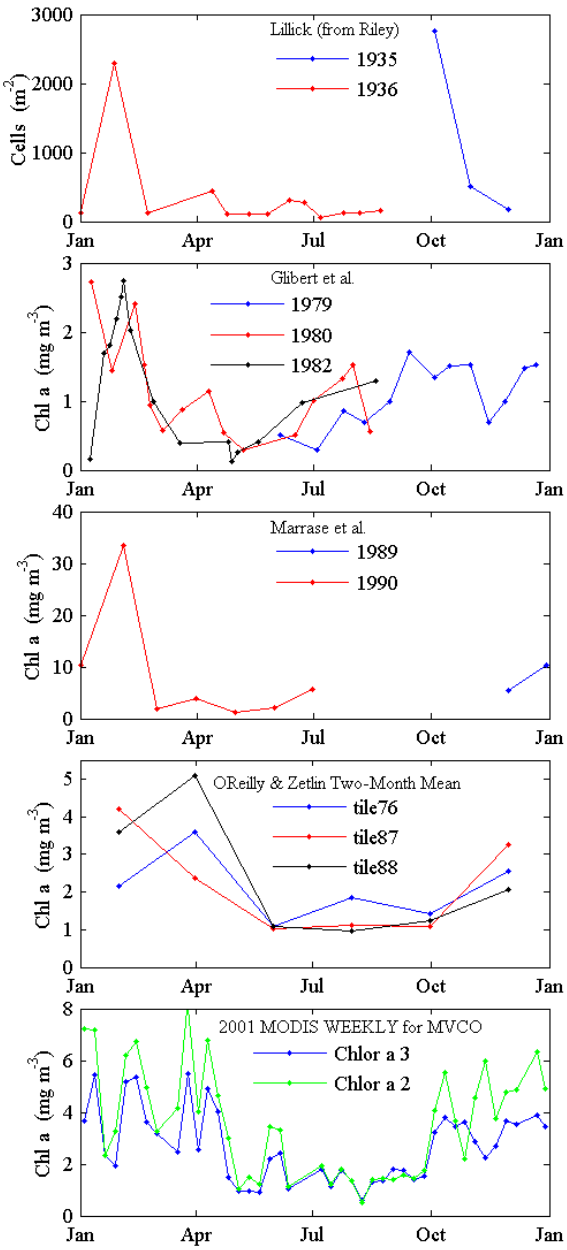

Figure 1-3: Seasonal variations in chlorophyll concentration for coastal waters near Woods Hole, MA as documented from in situ observations described in the literature (top 3 panels), and from weekly MODIS composites (bottom panel). In situ data are from Riley (1947), Lillick (1937), Glibert (1985), Marrase et al. (1992), and O'Reilly and Zetlin (1998), and MODIS/Terra data are Chlor_a_2 and Chlor_a_3 products from Level 3 4-km 8-day composites available through the Goddard DAAC. Note that for the top panel cell concentration data are presented (as opposed to chlorophyll concentration). In addition, data from O'Reilly and Zetlin (1998) are not from the same locations as the other studies; they represent the 3 MARMAP tiles closest to Woods Hole. Figure and caption courtesy Heidi Sosik.

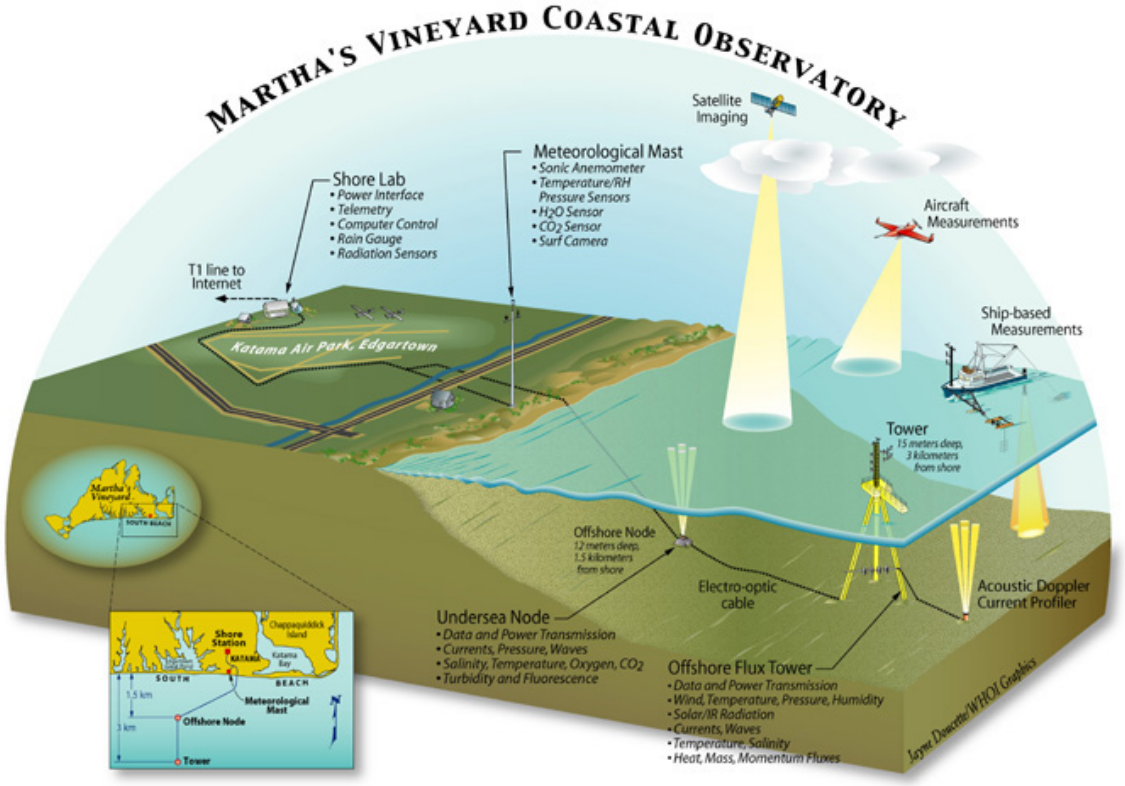

Figure 1-4: Cabled observatory off Martha's Vineyard, MA. Tower is referred to as Air-Sea Interaction Tower (ASIT) in later figures. Drawing by Jayne Doucette, WHOI.

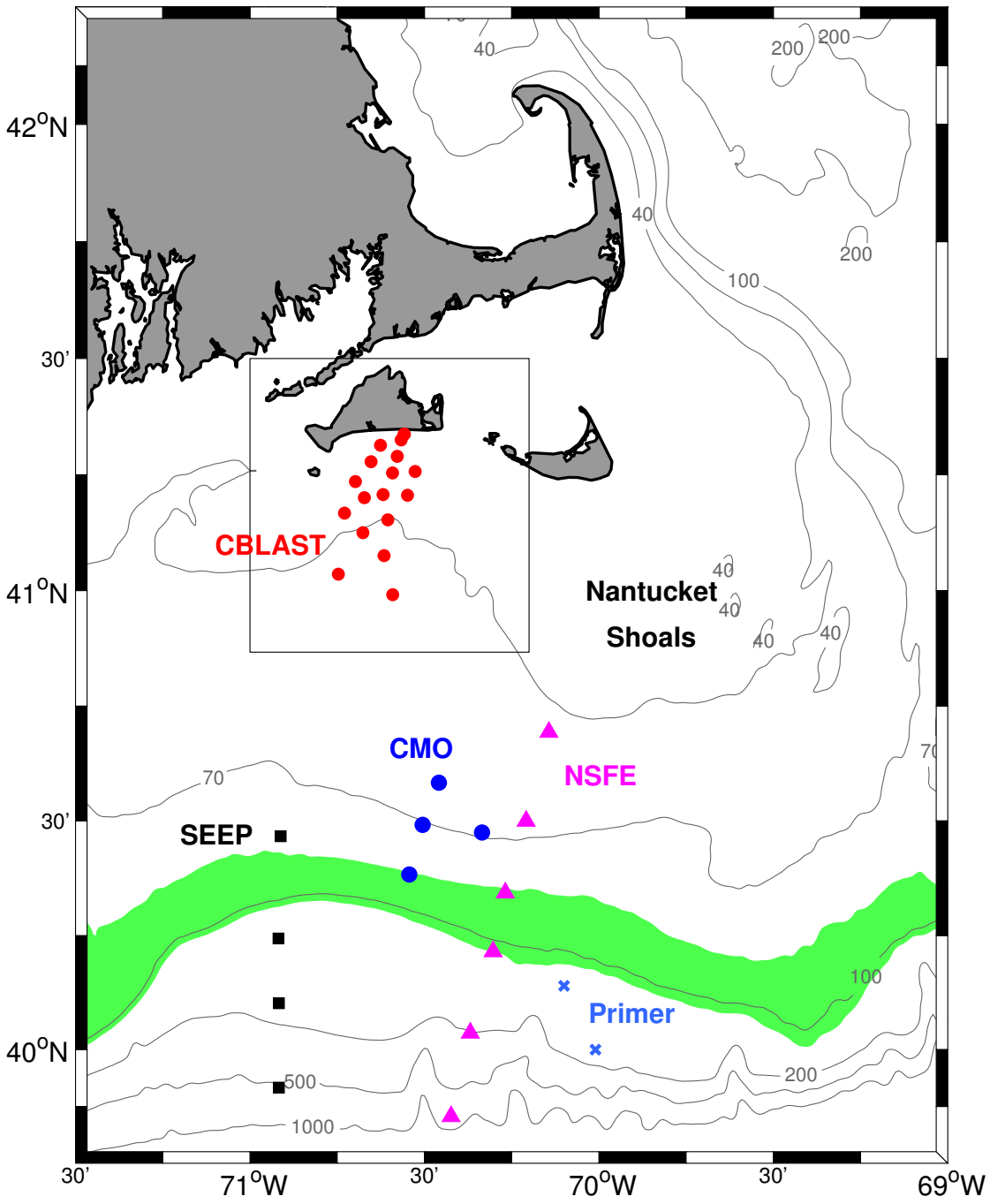

Figure 1-5: Locations of observational programs near Martha's Vineyard, MA. Isobaths are labeled in meters. The green area indicates the climatological location of the foot of the shelf-break front. Figure modified from Kipp Shearman.

Chapter 2

Cross-Shelf Circulation Driven By the Cross-Shelf Wind

This Chapter was submitted as a manuscript to *Journal of Physical Oceanography*. The authors are Melanie Fewings, Steven Lentz, and Janet Fredericks. The manuscript was reviewed and is currently under revision for resubmission. Appendix A is part of this manuscript.

2.1 Introduction

On continental shelves, cross-shelf circulations influence the water column density structure and the distributions of heat, salt, phytoplankton, nutrients, and pollutants. Cross-shelf exchange is an important mechanism for supplying nutrients to continental shelf ecosystems, which are some of the most productive on Earth (Falkowski et al., 1998). On the inner continental shelf in particular, cross-shelf exchange is thought to influence the ecosystem by transporting heat, nutrients, and larvae between the surfzone and mid-shelf (*e.g.*, Roughgarden et al., 1988; Austin, 1999).

The inner shelf is a complex region offshore of the surfzone, where the surface and bottom boundary layers interact (*e.g.*, Lentz, 1994, 1995). The location of the boundary between the inner shelf and the mid-shelf changes with time, depending on the thicknesses of the surface and bottom boundary layers, which determine the water

depth where the boundary layers overlap. As a result of the overlapping boundary layers, the inner shelf exhibits a divergence in the cross-shelf transport driven by along-shelf winds, which leads to coastal upwelling and downwelling (Ekman, 1905).

The mechanisms that drive cross-shelf flow over the inner shelf are not well-understood. In the middle and outer regions of the shelf, along-shelf winds drive coastal upwelling and downwelling circulations that transport material and heat in the cross-shelf direction (*e.g.* Ekman, 1905; Sverdrup, 1938; Smith, 1981). Observations on the North Carolina (Lentz, 2001), Oregon (Kirincich et al., 2005), and California (Cudaback et al., 2005) continental shelves and numerical model studies (*e.g.,* Austin and Lentz, 2002; Tilburg, 2003) show, however, that the along-shelf wind is not very effective at driving cross-shelf flow on the inner shelf. Along-shelf variations in topography and along-shelf currents are one proposed mechanism for cross-shelf exchange flows on the inner shelf (Austin and Lentz, 2002).

Here, we examine a different mechanism for driving cross-shelf exchange on the inner shelf: cross-shelf wind. Cross-shelf wind stresses have usually been assumed ineffective at driving shelf circulations (*e.g.*, Csanady, 1978; Allen, 1980; Brink, 1998). Over middle and outer continental shelves, the cross-shelf momentum balance is typically geostrophic on subtidal time scales: the cross-shelf pressure gradient force balances the Coriolis force due to the along-shelf flow (Brown et al., 1985; Thompson and Pugh, 1986; Brown et al., 1987; Noble and Butman, 1983; Lee et al., 1984, 1989; Lentz et al., 1999; Shearman and Lentz, 2003; Liu and Weisberg, 2005). Therefore, the cross-shelf wind stress is relatively unimportant in the steady depth-average momentum balance at mid-shelf. The mountain-gap winds in the Gulfs of Tehuantepec and Papagayo are exceptions, where the wind stress curl due to spatial variations in a strong cross-shelf wind forces a substantial cross-shelf circulation, even outside the inner shelf (McCreary et al., 1989). In contrast, our focus here is on spatially uniform wind stress.

The ratio R of the cross-shelf wind stress to the Coriolis force due to along-shelf flow, $R = \tau_s^x/(\rho_0 f h v_{da})$, where τ_s^x is cross-shelf wind stress, ρ_0 is water density, f is the Coriolis parameter, h is water depth, and v_{da} is depth-average along-shelf current,

suggests the cross-shelf wind stress is an important term in the momentum balance where h is small or v_{da} is weak. We estimate R for a number of sites along the Middle Atlantic Bight by comparing the standard deviations of τ_s^x and $\rho_0 f h v_{da}$ on subtidal time scales (Figure 2-1). (Note R goes roughly as h^{-1}, and R is plotted against h in Figure 2-1. We do not use Figure 2-1 to argue for a relation between h^{-1} and h, but to illustrate the water depths h at which $R \sim O(1)$). The estimates in Figure 2-1 suggest the cross-shelf wind stress is 30% or more of the Coriolis force in water depths less than 25 m, at mid-latitudes on the East Coast of the United States. At the Martha's Vineyard Coastal Observatory (MVCO), the ratio is 0.9, indicating that the cross-shelf wind stress is an important forcing mechanism at this site. The large spread in R values in shallow water is due to both smaller variations in cross-shelf wind stress τ_s^x and larger variations in along-shelf flow v_{da} at sites farther to the south in the Middle Atlantic Bight (open symbols in Figure 2-1; sites north of latitude 38° are indicated by solid symbols). Momentum balances calculated from observations in 10–16 m water depth in the South Atlantic Bight (Blanton, 1981; Lee et al., 1989), 8 m depth in the Middle Atlantic Bight (Lentz et al., 1999), and 15 m depth on the West Florida Shelf (Liu and Weisberg, 2005) have also indicated that the cross-shelf wind stress is an important term in shallow water.

The cross-shelf wind stress, in addition to being important in the momentum balance, may also drive a substantial cross-shelf circulation. Analytical theories (Ekman, 1905; Garvine, 1971) and a recent idealized numerical modeling study (Tilburg, 2003) have suggested that cross-shelf winds could drive significant cross-shelf circulations where the water is so shallow that the circulation through the entire water column takes place within the overlapping top and bottom boundary layers of the inner shelf. Numerical modeling studies (Li and Weisberg, 1999a,b) of the West Florida Shelf reveal that the cross-shelf wind stress plays an important role in driving along-shelf and cross-shelf currents over that inner shelf. In the Santa Barbara channel in California, strong offshore wind stresses south of Gaviota Pass in the Santa Ynez mountains are significantly correlated with a two-layer cross-shelf circulation over the inner shelf, with surface-intensified offshore flow in the upper water column and onshore flow in

the lower water column (Cudaback et al., 2005). Nevertheless, there has been to date no observational study that examines the dependence of the cross-shelf velocity profile in the inner shelf on the strength of the cross-shelf wind forcing.

It has previously been difficult to separate the influences of waves, cross-shelf wind, and along-shelf wind in observational studies because all three types of forcing are usually correlated. With a nearly 6-year-long time series of wind, wave, and velocity data, however, we are able for the first time to look at the structure of the cross-shelf flow during times when only one of the three types of forcing was strong. The dependence of the cross-shelf flow on wave forcing alone is discussed in Appendix E. Here, we examine the response of the cross-shelf flow to cross-shelf wind stress alone, along-shelf wind stress alone, and combined waves and cross-shelf wind stress. We present observations that demonstrate that cross-shelf winds are more effective than along-shelf winds at driving cross-shelf exchange flow at an inner shelf site. We also show that the response to combined wave and cross-shelf wind stress forcing is roughly the sum of the separate responses to wave forcing and cross-shelf wind stress forcing, at least in winter.

2.2 Data Analysis Methods

2.2.1 Martha's Vineyard Coastal Observatory

We use time series of water velocity profiles, wave, and meteorological data that extend over 6 years from the underwater-cabled Martha's Vineyard Coastal Observatory (MVCO). An underwater node for this observatory is located 1.5 km off the south shore of Martha's Vineyard, Massachusetts, on the northeastern United States continental shelf at 41°20.2'N, 70°33.39'W, in 12 m of water, well outside the surf zone (Figure 2-2). The long time series used here are from a bottom-mounted acoustic Doppler current profiler (ADCP) and temperature and pressure sensors, all located at the underwater node at 12-m depth and connected to a shore laboratory by underwater power and fiber-optic data transmission cables. Meteorological data

are from two masts on Martha's Vineyard (mast Met A at 41°21.0'N, 70°31.6'W, which is 2.5 km east and 1.5 km north of the underwater node, and mast Met B at 41°21.72'N, 70°31.35'W) and from the MVCO Air-Sea Interaction Tower (ASIT) on the 15-m isobath. Wind stress was calculated from the Smith (1988) bulk formula, using wind velocity measured 12.5 m above sea level on the MVCO shore masts and 18.4 m above sea level on the ASIT. The wind stresses at the shore masts have been adjusted as described in Appendix A to be representative of winds over the water at the ASIT.

The data cover the period from 19 June 2001 to 10 May 2007. More data are available during winter than summer. The instrument sampling frequencies are all between 2 Hz and 1 cycle min^{-1}. The data are archived by the Woods Hole Oceanographic Institution, and time series of 20-minute average water velocity, meteorological data, and spectrally resolved wave data are available online at http://www.whoi.edu/mvco. Detailed information about the instruments is available at that site.

There are four periods of at least one month with no available data: September through November 2001, June through July 2002, May through August 2004, and August 2005. In addition, we discarded the velocity and wave data during several periods when the signal correlation from the ADCP was low: 7 February 2002 to 17 April 2002, 22 February 2004 to 4 April 2004, 8–19 April 2005, 2 February 2006 to 7 March 2006, and 25 February 2007 to 24 April 2007. We also linearly interpolated across all gaps shorter than 12 hr.

2.2.2 Coordinate System

We define the along-shelf direction as the major principal axis direction of the depth-average subtidal flow (defined in Section 2.2.6) when waves are small (significant wave height $H_{sig} \lesssim 0.75$ m; see Section 2.4.2 for details). Periods of small waves were chosen because there is a significant wave-driven cross-shelf depth-average flow at this site (Appendix E). The major principal axis direction is oriented 5.5° clockwise from east, roughly parallel to the local isobaths (Figure 2-2).

We use a coordinate system with x positive offshore, y positive along-shelf east-

ward, and z positive upward, where $z = 0$ is the mean sea surface height over the deployment. The horizontal component of the water velocity in this coordinate system is $\boldsymbol{u} = (u, v)$. The wind stress is $\boldsymbol{\tau_s} = (\tau_s^x, \tau_s^y)$.

Wave and wind directions are reported as degrees counterclockwise from the positive x axis. We use "upwelling-favorable" wind stress to indicate a wind stress oriented eastward along-shelf. Wind direction is reported in the oceanographic convention: an onshore wind is blowing from the sea, toward land.

2.2.3 Water Velocity

The MVCO ADCP is a 1200 kHz RDI Workhorse Monitor, with 0.5-m bins, deployed in a bottom-mounted, upward-looking configuration. We used data from the bottom-most bin, at depth $z_{bot} = -9.5$ m, to the top good bin, $z_{top} = -2.0$ m. We determined the top good bin based on the bin-bin shear and the signal correlation returned by the ADCP.

To calculate depth-average velocities (below the wave troughs), we assumed the velocity is constant from the lowest ADCP bin to the bottom ($z = -12$ m), and from the top good ADCP bin to the mean water surface. The results presented here do not change significantly if we instead use linear extrapolation to the surface, or bottom, or both.

2.2.4 Waves

The significant wave height H_{sig}, dominant wave period T_w, wave direction θ_w, and wave phase speed c are calculated from the ADCP velocity measurements as described at http://www.whoi.edu/mvco.

The predicted onshore volume transport due to the dominant waves, Q_w, is (Longuet-Higgins, 1953):

$$Q_w = \frac{gH_{sig}^2}{16c} \cos\theta_w \tag{2.1}$$

where g is the acceleration due to gravity and θ_w is the direction the waves are going, measured counterclockwise from the positive x axis, so $\theta_w = 180^\circ$ indicates

waves propagating directly onshore. Note that Q_w depends on the wave period T_w through the phase speed $c(T_w)$. This volume transport Q_w takes place above the wave troughs in an Eulerian reference frame. We use $H_{sig}^2 \cos\theta_w$ as the measure of the strength of the wave forcing at a given time. For a typical wave propagating directly onshore at MVCO, with period $T_w = 5.5$ s and significant wave height $H_{sig} = 1$ m, $H_{sig}^2 \cos\theta_w = -1$ m^2 and $Q_w = -0.08$ m^2 s^{-1}.

If the circulation is along-shelf uniform, there is a predicted offshore return flow (undertow) with a volume transport equal to $-Q_w$ (Figure 2-3, left). See Appendix E for discussion of the depth distribution of the undertow at this site.

2.2.5 Removing Tides

The tidal velocities at MVCO are dominated by the M_2 tide (the lunar semidiurnal tide, with period 12.42 hr), and are relatively large (Shearman and Lentz, 2004). Near the surface on the 12-m isobath, the tidal velocity reaches 25 cm s^{-1} for the M_2 tide, and over 35 cm s^{-1} for the full tide; the depth-average tidal velocities reach 30 cm s^{-1}. These tidal velocities are elliptical (eccentricity $\epsilon = 0.1$) and oriented nearly along-shelf (the major axis orientation is 1.5° counterclockwise from due east for the M_2 tide). The tidal components other than M_2 with major axis amplitude at least 2 cm s^{-1} at any ADCP bin at the MVCO Node were the K_1, N_2, H_1, and S_2 tides. The tide [as determined by T_TIDE (Pawlowicz et al., 2002)] contributes 79% (74%) of the variance in the along- (cross-) shelf depth-average velocity 20-min time series.

Because we are interested here in the non-tidal component of the velocity, we subtract from the observed velocity time series (at each ADCP bin depth) a least-squares-fit tidal prediction generated by T_TIDE (Pawlowicz et al., 2002). Because some tidal components can be clearly distinguished in only part of the water column, to be consistent we remove from all depth bins the tidal components with signal-to-noise ratio greater than 2 for at least 8 of the 16 ADCP bins. To avoid removing seasonal variability, we limit the prediction to tidal frequencies greater than 1 cycle/month.

2.2.6 Low-Pass Filtering

For analysis of the relation between water velocity, waves, and wind, we filtered the de-tided 20-min water velocity, wave, and wind data with a low-pass filter of the same form as PL64 (Flagg et al., 1976; Limeburner et al., 1983), but with a half-amplitude point of $(24\ \mathrm{hr})^{-1}$. We use $(24\ \mathrm{hr})^{-1}$ rather than a lower frequency because the diurnal sea-breeze and diurnal tidal components are not strong at MVCO. To avoid edge effects from the filter, we de-tided the time series, linearly interpolated across the gaps in the time series, then applied the filter, put back the original gaps, and excluded data within 1/2 the filter window width of the gaps. We refer to the low-pass filtered water velocity as the subtidal flow.

2.2.7 Surface Layer Transport

To calculate the wind-driven cross-shelf transport in the surface layer, we separate the cross-shelf flow $u(z,t)$ into a depth-average part $u_{da}(t)$, and a depth-varying part $\tilde{u}(z,t)$:

$$\tilde{u}(z,t) = u(z,t) - u_{da}(t) \tag{2.2}$$

where

$$u_{da}(t) = \frac{1}{h}\int_{-h}^{0} u(z,t)\,dz \tag{2.3}$$

is the depth-average cross-shelf flow. We then define the cross-shelf surface layer transport U_s as

$$U_s(t) = \int_{z_{cross}}^{0} \tilde{u}(z,t)\,dz \tag{2.4}$$

where z_{cross} is the depth of the first zero crossing of $\tilde{u}(z,t)$. U_s is an Eulerian cross-shelf volume transport per unit along-shelf distance. The total cross-shelf velocity $u(z,t)$ is driven by a combination of cross-shelf and along-shelf winds, waves, and any other forcing that is present (for example, pressure gradients due to topographic variations). We are interested only in the wind-driven part of the depth-dependent cross-shelf transport. We subtract the depth-average flow from $u(z,t)$ to calculate U_s following the approach of previous observational studies (Lentz, 2001; Kirincich

et al., 2005).

2.2.8 Bin Averaging

We take advantage of the large number of synoptic wind and wave forcing events in the MVCO time series to separate those events into cases where only the cross-shelf wind or the along-shelf wind forcing is strong, and the other two forcings are weak (see Sections 2.4.1–2.4.2 for definitions of weak forcing). By examining those three cases separately, we are able to isolate the effect of each forcing mechanism on the cross-shelf flow. For example, to determine the dependence of the cross-shelf velocity profile on the cross-shelf wind stress, we calculated the time-mean cross-shelf velocity profile for cross-shelf wind stress bins covering the full range of observed low-frequency cross-shelf wind stresses (-0.49 Pa to 1.05 Pa). Each velocity profile is a mean over times when τ_s^x is in the wind stress range covered by that bin. It is also a conditional average velocity profile: the time average is taken only over times that satisfy the condition that the along-shelf wind stress and the waves are both small. We then use each average velocity profile to calculate the U_s that corresponds to that cross-shelf wind stress forcing.

2.2.9 Standard Error

Our standard error calculations for the low-pass filtered data assume one independent data point every 24 hours, based on the filter cutoff of $(24\text{ hr})^{-1}$ and the observed decorrelation time scales of the wind stress ($\sim$ 19–21 hr), wave forcing (~ 31 hr for $H_{sig}^2 \cos\theta_w$), along-shelf velocity (~ 17 hr), and cross-shelf velocity (~ 4 hr), where we estimate the decorrelation time as twice the time over which the autocorrelation function of the 20-min data drops from 1 (at zero lag) to 0.5.

2.3 Models of Wind- and Wave-Driven Flow

We compare the observed cross-shelf velocity profiles $u(z,t)$ to the profiles predicted by simple models of wind- and wave-forced flow. The comparison reveals whether or not the observations are consistent with our understanding of wind and wave forcing, and also whether the existing models are adequate to reproduce observed flows. Finally, we use the process models described below as tools to give a dynamical interpretation of the observations.

2.3.1 Model of Wind-Driven Flow

The cross-shelf velocity profile for cross-shelf wind stress forcing in water shallow compared to the boundary layer depth, with a no-slip bottom, a coastal wall, and a constant eddy viscosity, was found analytically by Ekman (1905). That velocity profile has a two-layer structure, with the strongest flow at the surface in the direction of the wind stress and a compensating return flow in the lower layer. To account for the dependence of eddy viscosity on wind stress forcing, we use a slightly more complicated model.

We compare the observed cross-shelf velocity profiles $u(z)$ to the cross-shelf velocity profile $u_\tau(z)$ predicted by a two-dimensional (along-shelf uniform) numerical model with constant density. We use only winter data to compare with the model, since the water column at MVCO is more likely to be unstratified in winter than summer. The model is described in detail in Lentz (1995). It numerically finds the steady solution to the linear momentum equations, with prescribed wind stress and along-shelf pressure gradient forcing, a coastal boundary condition of zero net cross-shelf flow, and a choice of eddy viscosity profiles. The eddy viscosity in the model depends on the surface and bottom stresses, and therefore on the velocity profile. Lentz (1995) considered the cases of forcing by an along-shelf wind stress and an along-shelf pressure gradient. Here, we consider forcing by a cross-shelf or along-shelf wind stress. We use model parameters identical to those given in Lentz (1995). The exact choice of eddy viscosity profile is not important here. We show results for bilinear cutoff, cubic,

and cubic divided by $\sqrt{2}$ (MYApprox) eddy viscosity profiles. Detailed descriptions of the bilinear cutoff and cubic profiles are given in Lentz (1995). The different eddy viscosities are only used here to show the range of the predicted cross-shelf velocity response for reasonable choices of the eddy viscosity profile.

We do not expect such a simple numerical model to reproduce exactly the observed cross-shelf flow. The vertical mixing of momentum in reality may depend on the waves, stratification, and surface buoyancy fluxes, none of which are included in the model. The dependence of the vertical mixing of momentum on the wind stress and bottom stress is also likely more complicated than what the model represents with its eddy viscosity profiles. Here, we examine the possibility that the observed cross-shelf flow is driven by a single physical process: forcing by the cross-shelf wind. We therefore use the simplest possible numerical model that can represent that physical process, with the mixing depending on the wind stress in a reasonable way.

To calculate the surface layer transport U_s predicted by the model, we sample the model velocity profile in the same way the ADCP samples the observed water column. We discard the model velocity profile $u_\tau(z,t)$ above the depth of the top good ADCP bin and below the depth of the bottom good ADCP bin, use a constant velocity profile from $z_{top} = -2.0$ m to $z = 0$ and from $z_{bot} = -9.5$ m to $z = -h$, and calculate U_s from the result.

2.3.2 Model of Wave-Driven Flow

The companion study in Appendix E demonstrates that the observed cross-shelf velocity profiles at MVCO during weak wind stresses in winter seem to match the prediction of Hasselmann (1970) for the Eulerian flow driven by surface gravity waves under the influence of Earth's rotation. In that model, the velocity profile u_H is predicted to be equal in magnitude and opposite in sign to the Lagrangian Stokes drift velocity profile u_{st} (Hasselmann, 1970), as in Figure 2-3:

$$u_H(z,t) = -u_{st}(z,t) \tag{2.5}$$

where the x-component of the Stokes drift due to a monochromatic wave is (Longuet-Higgins, 1953)

$$u_{st}(z,t) = \frac{gkH_{sig}^2}{8c} \frac{\cosh\left[2k\left(z+h\right)\right]}{\sinh\left(2kh\right)} \cos\theta_w \tag{2.6}$$

The derivation of (2.5) is reviewed in detail in, *e.g.*, Xu and Bowen (1994). We use (2.5) as the model for wave-driven offshore flow (undertow) to compare with the ADCP observations in winter. The depth-average of u_{st} calculated from Eq. (2.6) using the observed dominant wave characteristics, which we use here for simplicity, is about 15% larger than the depth-average of u_{st} calculated by integrating over the directionally-resolved wave spectrum (Appendix E).

2.4 Context

2.4.1 Wind Stress Forcing

The wind stress forcing at this site is dominated by synoptic variability (time scales of a few days, associated with the passage of weather systems), and does not have a large mean value. Monthly mean cross-shelf (along-shelf) wind stresses are no more than 0.03 (0.07) Pa in any season (Figure 2-4), and the standard deviations are at least twice as large as the means, during all seasons. Both the mean and the variability of the wind stress are larger in winter than summer. The winds at this site are not strongly polarized in any season, in contrast to the mean upwelling-favorable winds on the West Coast of the United States in summer (*e.g.*, Huyer, 1983). The standard deviations of the cross-shelf and along-shelf wind stress components at this site have similar magnitudes, about 0.08–0.09 Pa.

For the remaining analysis, $|\tau_s^x| < 0.035$ Pa is considered a small (low-pass filtered) cross-shelf wind, and $|\tau_s^y| < 0.035$ Pa a small along-shelf wind. If we choose a smaller cutoff value, too few data remain for statistically significant calculations in the small wind regime. We identify times when the total wind stress was small as having $|\boldsymbol{\tau_s}| < 0.035$ Pa. The total wind stress is small 30% of the time.

2.4.2 Wave Forcing

The monthly mean significant wave height, and the strength of the synoptic variability in wave forcing, are larger during winter than summer (Figure 2-4). The mean dominant wave period is about 5.5 s, with little seasonal variation.

The time-mean of the wave forcing $H_{sig}^2 \cos\theta_w$ is comparable in magnitude to the low-frequency variability of $H_{sig}^2 \cos\theta_w$. This is partly because $H_{sig}^2 \cos\theta_w$ is almost always negative, since the waves are propagating onshore ($\theta_w \sim 180°$). The mean wave forcing over all times is -1.2 m^2, and the standard deviation on subtidal time scales is 1.5 cm s^{-1}. Both the mean wave forcing and its variability are larger in winter than summer.

We use $H_{sig}^2 \cos\theta_w = 0.5$ m^2 as the cutoff below which the wave forcing is small. This corresponds to $H_{sig} \lesssim 0.75$ m. If we choose a smaller cutoff value, too few data remain for statistically significant calculations in the small wave regime. The waves are small 40% of the time. Waves and wind stress are both small 20% of the time.

2.4.3 Mean Flow

The time-mean depth-average flow observed by the ADCP (mean for all times and all wave conditions) is westward and offshore (Figure 2-2), and stronger (more westward) in summer than winter. The offshore component of the mean flow is almost entirely explained by wave-driven undertow (Appendix E), and is therefore consistent with a two-dimensional (along-shelf uniform) circulation. The monthly mean cross-shelf depth-average flow is approximately 1 cm s^{-1} during all seasons (Figure 2-4). The monthly mean along-shelf depth-average flow is 1 cm s^{-1} or less westward during November–February, but up to about 6 cm s^{-1} westward during April–September. Accordingly, we define summer as April 1–September 30 and winter as October 1–March 31 for this study. The time-mean depth-average flow during times when waves are small is nearly in the along-shelf westward direction, and has a strength of 3 cm s^{-1} consistent with (but slightly smaller than) the time-mean flows observed at mid-shelf in this area (Beardsley et al., 1985; Shearman and Lentz, 2003; Lentz, 2007a).

2.4.4 Wave and Wind Forcing are Correlated

The three forcing mechanisms considered here (waves, cross-shelf wind, and along-shelf wind) are all correlated (Figure 2-5). The correlation coefficient of τ_s^x with τ_s^y is only $r = -0.06$ at zero lag (95% significance level is $|r_s| = 0.01$), but the correlation of onshore wind stress with upwelling-favorable wind stress ($\tau_s^x < 0$ and $\tau_s^y > 0$) is $r = -0.43$ at zero lag ($|r_s| = 0.08$). At this location an upwelling-favorable wind stress is usually associated with an onshore wind stress (Figure 2-5c).

The correlation of wind stress magnitude $|\boldsymbol{\tau}_s|$ with $H_{sig}^2 \cos\theta_w$ has an extreme of $r = -0.52$ ($|r_s| = 0.05$) on subtidal time scales, when $H_{sig}^2 \cos\theta_w$ is lagged 3 hr with respect to the wind stress. Although offshore wind stresses are generally associated with small waves, onshore wind stresses are strongly correlated with wave height because the fetch is much larger for onshore than offshore winds (Figure 2-5a). Strong along-shelf winds of either direction are associated with large waves (Figure 2-5b). These correlations are one reason why it has previously been difficult to separate the influences of waves, cross-shelf wind, and along-shelf wind observationally.

2.5 Results

2.5.1 Correlation of Cross-Shelf Flow with Forcing

The cross-shelf flow $u(z,t)$ on the inner shelf at MVCO is significantly linearly correlated at zero lag at the 95% confidence level with the wave forcing $H_{sig}^2 \cos\theta_w$ and the cross-shelf wind stress τ_s^x, and also with the along-shelf wind stress τ_s^y at a few depths near the surface (Figure 2-6b). Although the relation between the wind and wave forcing and the resulting cross-shelf flow is not linear, as discussed below, the linear correlation coefficient still gives a crude measure of the strength of the relation. The correlation with along-shelf wind stress, which is the forcing mechanism usually thought to drive cross-shelf exchange via coastal upwelling and downwelling, is the weakest of the three.

The cross-shelf flow in the lower half of the water column is mainly associated with

cross-shelf wind stress (onshore flow for offshore winds; Figure 2-6b). Cross-shelf flow in the uppermost part of the water column is equally correlated with waves and with cross-shelf wind stress.

The results are different when we use all data (Figure 2-6a) or use only data from times when one forcing mechanism is strong (Figure 2-6b) because the different forcing types are correlated (Section 2.4.4). For example, the responses to wave and cross-shelf wind forcing can cancel each other. Flow is onshore in the top ADCP bins during shoreward winds, and offshore during wave forcing (Figure 2-6b). Because shoreward winds are correlated with large wave events (Figure 2-5), shoreward winds appear unimportant in driving cross-shelf flow in the upper water column until only times of small waves are considered (compare solid black dots in Figure 2-6a and b). Also, when we consider all times together, the along-shelf wind incorrectly appears to be an important forcing mechanism for cross-shelf flow (Figure 2-6a). That is why, in this study, we consider only the events when either wind or wave forcing is strong, but not both, in order to understand the response of the system to each forcing mechanism separately.

2.5.2 Cross-Shelf Flow Profiles During Wind Forcing Alone

There is a non-zero time-mean cross-shelf velocity present when both waves and winds are weak (Figure 2-7a, solid line). We refer to this as the background velocity profile. The background velocity has a two-layer structure: onshore in the lowest part of the water column, and offshore in the upper part of the water column. It reaches a maximum of about 1 cm s^{-1} in the uppermost ADCP bin. The background velocity is slightly stronger in summer than winter (Figure 2-7a, dashed and dash-dot lines). There are several possible explanations for this background velocity, including pressure gradients due to along-shelf variations in bathymetry. Since the background velocity profile is present when wave and wind forcing are both weak, we assume it is not directly driven by waves or winds. We subtract this background velocity profile in all of the following analyses, including the velocity profiles shown in Figure 2-7b–d.

During wave forcing (when the wind stress is small), the cross-shelf flow is offshore

through most of the water column below the wave troughs for waves propagating onshore. The flow is surface-intensified and stronger during larger waves (Figure 2-7b). Onshore-propagating waves generate an offshore flow (undertow) at this location, even though it is 1.5 km offshore, well outside the surfzone ($H_{sig}/h > 0.4$ never occurred, and $H_{sig}/h > 0.25$ occurred less than 1% of the time in the unfiltered data). The dependence of the cross-shelf flow on wave forcing at this site is described in (Appendix E) and will not be detailed here.

During cross-shelf wind stress forcing (when waves and along-shelf wind stress are both small), the cross-shelf flow has a two-layer structure (Figure 2-7c). For onshore winds, the flow is onshore in the upper water column and offshore in the lower water column. For offshore winds, the flow is nearly the reverse. The cross-shelf velocity profiles we observe during offshore wind stress forcing are similar to the spatial part of the first empirical orthogonal function (EOF) of the cross-shelf flow observed at 15 m depth on the southern California shelf south of the Gaviota mountain pass, where strong offshore winds occur (Cudaback et al., 2005). The temporal part of that EOF is correlated with the cross-shelf wind stress. The zero crossing of the cross-shelf velocity profile at MVCO is at a depth of 4.8–5.5 m (3.3–5.5 m) in winter (summer), approximately one-third to one-half the water depth, for the binned profiles for all cross-shelf wind stress values except when the wind stress magnitude is less than 0.3 Pa (not shown). This is consistent with the modeled u_τ (Section 2.3.1), which has its zero crossing at a depth of 4.6–4.7 m for wind stress values $0.05 < |\tau_s^x| < 0.25$ Pa. The model predictions of the cross-shelf velocity profiles u_τ compare reasonably well with the average observed profiles for both onshore and offshore wind stresses, considering that the model parameters have not been adjusted to maximize the fit to the data (Figure 2-7c). The model velocity profiles are shown for the cubic eddy viscosity profile, for $\tau_s^x = -0.06$ Pa and 0.07 Pa, which are the mean observed τ_s^x values for the wind stress ranges -0.1 Pa $< \tau_s^x < -0.05$ Pa and 0.05 Pa $< \tau_s^x < 0.1$ Pa, respectively.

During along-shelf wind stress forcing (when waves and cross-shelf wind stress are both small), the cross-shelf flow displays essentially no response (Figure 2-7d). This is

in contrast to typical mid-shelf sites, where the along-shelf wind stress is the dominant component of wind forcing, and drives a coastal upwelling or downwelling circulation. At MVCO, along-shelf winds do not generate as large a cross-shelf circulation as do cross-shelf winds (or waves). The observed profiles during along-shelf wind stress forcing are roughly consistent with the predicted u_τ when the model is driven with an along-shelf wind stress; the model profiles are shown in Figure 2-7d for $\tau_s^y = -0.07$ Pa and $\tau_s^y = 0.06$ Pa, which are the mean observed τ_s^y values for the wind stress ranges -0.1 Pa $< \tau_s^y < -0.05$ Pa and 0.05 Pa $< \tau_s^y <$ 0.1 Pa, respectively. The model predicts very little response of the cross-shelf circulation to along-shelf wind forcing at this water depth, in agreement with the observed (lack of) response.

2.5.3 Cross-Shelf Profiles During Combined Forcing

We also examined the cross-shelf velocity profiles during times when both cross-shelf wind and wave forcing were strong. Onshore winds rarely occur without substantial wave forcing, and offshore winds are sometimes accompanied by remotely generated waves propagating onshore, so it is important to understand the response to combined forcing.

We compare the observed profiles during combined forcing to a simple model of combined wind and wave forcing: we assume the velocity profile during combined forcing, $u_{\tau+H}$, is the sum of the model profiles during separate forcing (Sections 2.3.1–2.3.2):

$$u_{\tau+H} = u_\tau + u_H \tag{2.7}$$

where u_τ is the modeled velocity due to wind forcing only, and u_H is the modeled velocity due to wave forcing only, Eq. (2.5). Another approach is to incorporate the wave forcing into the numerical model of Lentz (1995), so that the wave-driven flow influences the surface and bottom stresses and therefore the eddy viscosity profile that determines the wind-driven response u_τ. We find that approach gives results very similar to (2.7) for all but the largest wave forcing, in which case the profile predicted by the combined model is less vertically sheared near the surface than

the linear superposition in (2.7). For simplicity, we use (2.7) to compare with the observations.

The comparison of $u_{\tau+H}$ with observed mean profiles is shown in Figure 2-8 for several representative forcing regimes, using winter data only because the models are unstratified. We subtracted from the observations both the background velocity profile (Figure 2-7c) and the part of the depth-average flow that differed from the depth average of u_H in each case (similarly to Section 2.2.7).

Although the mean observed wave height is constant within each row in Figure 2-8, the wave-driven circulation (dotted lines) decreases from left to right in each row, as the wind goes from onshore to offshore and the fetch decreases (*e.g.*, compare upper left and upper right panels in Figure 2-8). This is because, as the wind goes from onshore to offshore, the dominant wave period T_w increases, so the phase speed c increases, and both Q_w and u_H decrease (Sections 2.2.4 and 2.3.2). The increase in wave period for offshore winds is at first counterintuitive because the fetch is smaller for offshore winds. The explanation involves the presence of both wind waves (small T_w) and swell (large T_w). The wave height H_{sig} is calculated from the total energy in the water velocity spectrum. The amount of energy in the wind-wave part of that spectrum is smaller for smaller fetch (offshore winds). Therefore, for a given H_{sig} (along a row in Figure 2-8), more of the wave energy is due to remotely generated swell during offshore winds, so the dominant T_w is larger, and the predicted wave-driven circulation is smaller, for offshore winds.

The circulation driven by the cross-shelf wind stress during small waves (bottom row of Figure 2-8) is roughly symmetric in the wind direction, as discussed in Section 2.5.2. As the wave forcing increases (going from the bottom to the top row in Figure 2-8), however, the roughly symmetric wind-driven circulation evident in the bottom row is gradually overwhelmed by the wave-driven undertow, which is always directed offshore (as in the middle column). Therefore, during strong wave forcing (top row of Figure 2-8), the cross-shelf circulation is no longer symmetric in the wind direction: the cross-shelf velocity profile is nearly vertically uniform for large waves and onshore winds because the vertical shears are similar in magnitude but of op-

posite sign, while for large waves and offshore winds the velocity profile is strongly sheared because the wave- and wind-driven shears are large and of the same sign. The Eulerian velocity profiles during combined cross-shelf wind and strong wave forcing range from vertically uniform (upper left panel) to a profile with a depth-dependent part that looks like an upwelling circulation (upper right panel).

The response to combined wind and wave forcing is roughly a linear combination of the separate responses u_τ to wind forcing and u_H to wave forcing (Figure 2-8; Appendix E). The discrepancy between the modeled and observed profiles is larger in summer than winter (not shown); in summer, the observed profiles are more vertically sheared than in Figure 2-8 but the model profiles are the same because the models are unstratified. The linear correlation between the model $u_{\tau+H}(z,t)$ and the observations $u(z,t)$ at any one depth is $r_W = 0.75$ in winter and $r_S = 0.56$ in summer (average correlation coefficient for all depths, all correlations at zero lag), and the 95% confidence level is $r_s = 0.07 - 0.08$ in both cases. At mid-depth in winter, the correlation is $r = 0.82$. Therefore, the model $u_{\tau+H}(z,t)$ explains 56% of the subtidal variance in the cross-shelf velocity on average in winter ($r_W^2 = 0.56$), and as much as 67% of the variance at mid-depth.

2.5.4 Cross-Shelf Transport in the Upper Layer

Because the flow has a two-layer structure during cross-shelf wind forcing (Figures 2-7c and 2-8, bottom row), the dependence of the cross-shelf flow profile on wind forcing can be quantitatively characterized by the volume transport in the upper layer, U_s. The background velocity profile described in Section 2.5.2 (Figure 2-7a) is subtracted from the observed profile for each season separately before calculating U_s.

A substantial cross-shelf transport is associated with cross-shelf winds (Figure 2-9a). We observe an approximately linear relation between the strength of the cross-shelf transport and the cross-shelf wind stress over the range of wind stress values observed when waves are small, during both summer and winter. There were few times when the cross-shelf wind stress was strongly onshore but the waves were small (Figure 2-5a), so the observations do not extend to very large negative values of

τ_s^x. The upper-layer cross-shelf transport response is approximately twice as large in summer as in winter (Figure 2-9a) for a given strength of offshore wind stress.

We use the model prediction for wave-driven flow to extend the plot of U_s vs. τ_s^x in winter beyond the range of Figure 2-9 to larger values of wind stress, when waves are generally present. To do this, we consider all wave conditions, and subtract from the observed velocity profile the predicted wave-driven velocity profile u_H (Section 2.3.2). We then calculate an extended surface layer transport $U_s^{'}$ from the resultant $u(z,t) - u_H(z,t)$ in the same manner as in Section 2.2.7. $U_s^{'}$ compares well with the observed U_s during small waves in winter, where the two sets of data overlap (compare open and closed symbols, Figure 2-10). $U_s^{'}$ is approximately symmetric with respect to the cross-shelf wind direction (Figure 2-10, left). With the extended range of wind stress, we can see that the response is not actually linear for onshore wind stresses. For small cross-shelf wind stresses, $|\tau_s^x| < 0.025$ Pa, the response is approximately linear in τ_s^x. Above that wind stress magnitude, however, $|U_s^{'}|$ increases more slowly with increasing $|\tau_s^x|$.

The reduced slope of $U_s{'}$ vs. τ_s^x for large onshore wind stress forcing (Figure 2-10) can be thought of as due to overlap of the top and bottom Ekman layers for increasing wind stress, and a resulting shutdown of the wind-driven response. This is consistent with the idea that when the wind stress (cross-shelf or total) becomes large, the top and bottom boundary layers overlap to the extent that vertical transfer of momentum through the water column is extremely rapid. Then the cross-shelf velocity is reduced, and U_s (or $U_s^{'}$) cannot increase as rapidly with wind stress as it does for small wind forcing. The numerical model crudely represents this process, and the model predictions agree with the observed U_s. This model-data agreement suggests that the cross-shelf velocity response we observe at MVCO during cross-shelf wind stress forcing is indeed a response to the cross-shelf wind stress, and not to some other forcing that is simply correlated with cross-shelf wind stress.

The cross-shelf transport observed during cross-shelf wind forcing of either direction in winter is small compared to the transport expected at mid-shelf (dashed and dotted lines in Figure 2-9a), except during very weak cross-shelf wind stress

($0 < \tau_s^x < 0.025$ Pa). (The maximum predicted $U_s/\tau_s^x \rho_0 f$ for cross-shelf wind is larger than 0.2, and up to at least 0.45, for eddy viscosities that are not constant vertically, based on the numerical model of Lentz (1995)). The small cross-shelf transport at MVCO is consistent with the idea that this site at 12-m water depth is within the inner shelf for all but the smallest wind stresses in winter.

To compare the surface layer transport from the unstratified model with the observations, we used winter data only. In winter, however, the surface heat flux is often cooling the ocean and the water column may be actively convecting, rather than simply unstratified. In that case, with enhanced vertical mixing of momentum, we would expect a decreased cross-shelf transport response. Indeed, the surface transport U_s during offshore winds in winter is smaller when we consider only times when the ocean is strongly cooling (surface heat flux more negative than -50 W m^{-2}, not shown).

We observe almost no dependence of the cross-shelf transport U_s on the along-shelf wind stress during winter (Figures 2-9b and 2-10b). There seems to be a weak non-zero cross-shelf transport associated with upwelling-favorable wind forcing in summer, although there are very few events with upwelling-favorable wind stress but weak cross-shelf wind and small waves (Figure 2-9b). There is also some indication of onshore transport in the surface layer (*i.e.*, a downwelling circulation) during downwelling-favorable wind stress in summer during times when the surface heat flux is positive (> 50 W m^{-2}, not shown). It is unclear whether the data extended to all wave conditions (Figure 2-10b, open circles) actually represent the response to along-shelf wind forcing (it seems unlikely that upwelling-favorable wind causes a downwelling circulation in winter) or are artifacts of the small but finite cross-shelf wind forcing, or inaccuracy of the wave model (the surface heat flux was cooling the ocean during those events, and the strong vertical mixing that is probably associated with that surface cooling is neglected by the wave model). Nevertheless, both the observed and the predicted responses to along-shelf wind stress are small for this water depth. The observed and modeled U_s for along-shelf wind stress (Figure 2-9b, solid symbols and solid line) do agree reasonably well, considering that the signal of U_s vs. τ_s^y is so weak.

2.6 Discussion

2.6.1 Overestimation of the Importance of Along-Shelf Wind

The importance of cross-shelf wind forcing at MVCO leads us to re-examine the results of a previous inner-shelf study. Observational studies on the North Carolina and Oregon shelves have demonstrated a divergence across the inner shelf in the cross-shelf transport associated with along-shelf wind stress (Lentz, 2001; Kirincich et al., 2005). In both cases, the authors used the entire available time series to calculate a correlation between the surface layer transport U_s and the along-shelf wind stress at each water depth, because the time series were too short to separate into events where only one wind component was strong. The along-shelf and cross-shelf wind stress components can be correlated (Section 2.4.4). As a result, the importance of the along-shelf wind stress in driving a cross-shelf circulation may be overestimated in those studies (as in Figure 2-6a). We suggest that the cross-shelf Ekman transport U_s associated with the along-shelf wind on the North Carolina inner shelf may decrease even faster with decreasing water depth than demonstrated in Lentz (2001), because the subtidal cross-shelf and along-shelf wind stress components at that site are significantly positively correlated (Austin and Lentz, 1999). Therefore, a substantial fraction of the transport U_s attributed to along-shelf wind stress forcing at the North Carolina site may actually be due to cross-shelf wind stress. The cross-shelf wind stress probably does not contribute as much to U_s on the Oregon coast, where the wind stress is more polarized in the along-shelf direction.

2.6.2 Comparison to 2-D Model

A recent numerical model study showed that when the water depth is small enough for significant overlap of the surface and bottom boundary layers, the cross-shelf wind stress drives a stronger cross-shelf surface layer transport than does the along-shelf wind stress (Tilburg, 2003). Tilburg ran the model in a two-dimensional (along-shelf uniform) configuration, with initially linear stratification and a Mellor-Yamada level

2.5 turbulence closure scheme. For a constant wind stress magnitude, as a function of wind angle, the cross-shelf surface layer transport in that model was greatest for cross-shelf wind and zero for along-shelf wind in the very shallow inner shelf (5 m depth).

We observe a similar dependence of surface layer transport on wind stress angle, for a given range of wind stress magnitude, during small waves (Figure 2-11). We consider winter data only, to minimize the effects of stratification. The largest cross-shelf surface layer transport occurs for wind stress in the offshore or nearly onshore direction, and that surface layer transport is in the same direction as the wind stress. The weakest cross-shelf surface layer transport occurs when the wind stress is in the upwelling- or downwelling-favorable (along-shelf) direction. The U_s we observe is slightly larger than that predicted by Tilburg (2003) for onshore winds. His model run was for a water depth of 5 m, however, as opposed to the MVCO water depth of 12 m, and U_s is expected to increase with increasing water depth in the inner shelf, even in the region where the maximum upper-layer transport is downwind.

Tilburg (2003) also gives an estimate for the depth of the first zero crossing of the cross-shelf flow at mid-shelf, δ, as a function of wind stress and stratification (his Eq. 22). Tilburg uses the formula of Weatherly and Martin (1978), but with an adjusted coefficient to match his different definition of U_s based on the first zero crossing of the cross-shelf velocity (as in this study), rather than on the full boundary layer depth:

$$\delta = 2.3\sqrt{\frac{|\boldsymbol{\tau}_s|}{\rho_0}}\frac{1}{f(1+N^2/f^2)^{1/4}} \tag{2.8}$$

where $N = (-\frac{g}{\rho_0}\frac{\partial \rho}{\partial z})^{1/2}$ is the buoyancy frequency. If δ is larger than the water depth, Tilburg predicts a circulation governed by inner-shelf dynamics and not mid-shelf dynamics. For an unstratified water column ($N = 0$), (2.8) predicts $\delta > h$ at MVCO for $|\boldsymbol{\tau}_s| \geq 3 \times 10^{-4}$ Pa. For a typical summertime value of $N = 0.02$ s^{-1} in the Middle Atlantic Bight (Linder and Gawarkiewicz, 1998), (2.8) predicts $\delta > h$ at MVCO for $|\boldsymbol{\tau}_s| \geq 0.05$ Pa. This is consistent with the MVCO site being in the inner shelf nearly all the time, except during extremely weak winds when the water column is

strongly stratified. Indeed, it is only during summer that U_s approaches the predicted mid-shelf value for a given cross-shelf wind stress (compare dotted line and summer observations in Figure 2-9).

2.6.3 Comparison to Unstratified Model

There appears to be a slight asymmetry between the responses to onshore and offshore winds (Figure 2-10, left). With the available observations (which do not include density profiles for the entire time series) we cannot determine whether the slight asymmetry in Figure 2-10 is caused only by differences in surface heat flux or stratification between events, and not directly caused by the cross-shelf wind stress, or whether there is an inherent asymmetry in the response of the system to cross-shelf wind stresses of opposite directions.

Another possible explanation for the asymmetry in Figure 2-10 is uncertainty in the wind stress estimates. The bulk formula used here (Section 2.2.1) uses the same drag coefficient for all wind directions, even though the MVCO study location has land nearby to the north and water to the south, and the drag coefficient is larger over land than water. The atmospheric boundary layer may still be adjusting over the 12-m isobath at MVCO (1.5 km offshore) when the wind is blowing from land. Further, the adjusted wind stress times series from the MVCO shore masts (Appendix A) may still not accurately represent the wind stress at the 12-m isobath. Also, when the wind is in the same direction as the wave propagation the effective wind stress should be smaller than when the wind is against the waves, but we have not taken this into account here.

2.6.4 Seasonal Change in the Response to Wind

Stratification is expected to affect the cross-shelf circulation by suppressing vertical mixing, and therefore thinning the surface and bottom boundary layers and reducing their overlap. This would cause the boundary between the inner shelf and the mid-shelf to move closer to shore. As long as that boundary remains offshore of the

12-m isobath, we would expect a stronger cross-shelf circulation at MVCO (for either wind direction) during stronger stratification, as a result of decreased boundary layer overlap, based on Section 2.6.3.

Although the long MVCO velocity time series does not have associated stratification data, at MVCO the water is typically more stratified in summer than in winter. The cross-shelf wind does drive a larger cross-shelf transport U_s in summer than in winter (Figure 2-9, left). In summer, U_s does appear to approach the mid-shelf (deep-water) limit for offshore winds at least as large as 0.08 Pa (top dotted line at right in Figure 2-9a). This is consistent with the expected response to increased stratification, which may play an important role by reducing the overlap of the surface and bottom boundary layers.

The cross-shelf transport associated with along-shelf wind may be nonzero during upwelling-favorable wind stress forcing in summer, even though it is zero in winter (Figure 2-9, right). This is consistent with the expected response to increased stratification, if the MVCO site is within the inner shelf and therefore the transport associated with along-shelf wind is insignificant when stratification is weak (in winter or during downwelling-favorable winds, which could destroy the stratification in summer). Upwelling-favorable winds can bring colder, denser water onshore near the bottom of the water column, thereby maintaining the summer stratification and the reduced boundary layer overlap. The MVCO site seems to be closer to mid-shelf in summer during upwelling-favorable or offshore winds than in winter or during downwelling-favorable or onshore winds.

2.6.5 Implications for Lagrangian Particle Transport

The observed cross-shelf transport may seem weak ($U_s < 0.2$ m^2 s^{-1}), but it is enough to flush the entire volume of the inner shelf onshore of the 12-m isobath in about 1 day. Therefore, the cross-shelf wind-driven shear flows we observe are strong enough to change the density stratification of the inner shelf on biologically and physically relevant time scales, and to have significant effects on the inner shelf transport of heat, salt, larvae, nutrients, phytoplankton, pollutants, and carbon. Note, however,

that the Eulerian cross-shelf velocity profiles discussed up to this point are not the same as the Lagrangian water parcel velocities. It is the Lagrangian velocity, the velocity of a particle in the water column, that matters for tracer transport. The Lagrangian particle velocities may be very different from the Eulerian velocities as a result of surface gravity waves.

In particular, waves induce a net particle velocity, the Stokes drift $u_{st}(z,t)$ (2.6), in the direction of wave propagation (Stokes, 1847), as in Figure 2-3, right. We form an estimate of the total Lagrangian particle velocity $u_L(z,t)$ by adding the Stokes drift to the observed Eulerian velocity response to wind and waves:

$$u_L(z,t) \approx u(z,t) + u_{st}(z,t). \tag{2.9}$$

The Lagrangian cross-shelf transport in the surface layer, U_s^L, is estimated from u_L in the manner of Section 2.2.7. We again subtract the background velocity profile (Figure 2-7c) from $u(z,t)$.

Waves should cause a significant difference between the Eulerian circulation and the Lagrangian particle velocities at this site. The estimated Lagrangian cross-shelf transport is approximately the same magnitude as the Eulerian response to wind, even during strong wave forcing (Figure 2-12). The result is as if the incoming waves affected the Eulerian circulation but not the Lagrangian velocities. This is because the observed wave-driven Eulerian offshore flow is approximately equal to the Hasselmann (1970) prediction u_H, at least in winter (Appendix E), and $u_H(z,t) = -u_{st}(z,t)$ (Figure 2-3, right). Therefore, the wave-induced Stokes drift tends to cancel the wave-driven undertow throughout the water column in winter. As a result, the Lagrangian particle velocities are likely similar to the Eulerian cross-shelf velocities driven by cross-shelf wind stress alone. This is consistent with the non-acceleration theorem, in which a statistically steady eddy or wave field does not accelerate a mean flow in a generalized Lagrangian mean sense (Andrews and McIntyre, 1976).

2.7 Summary and Conclusions

We have shown that the forcing mechanisms for cross-shelf exchange on the inner shelf are fundamentally different from those at mid-shelf. A 6-year-long time series of wind, wave, and ADCP velocity data from the cabled MVCO observatory contains enough different wave and meteorological forcing events that we are able to observe, for the first time, the dependence of the cross-shelf flow profile on cross-shelf wind or along-shelf wind alone. The cross-shelf wind, not the along-shelf wind, is the main forcing mechanism for cross-shelf circulation at this site when waves are small, especially in winter (Figure 2-14, bottom). This is in contrast to coastal upwelling and downwelling in deeper water at mid-shelf driven by along-shelf winds (Figure 2-14, top).

There is a two-layer flow structure associated with cross-shelf wind forcing, with offshore flow in the surface layer for offshore winds and a compensating return flow in the lower layer. The zero crossing of the velocity is at approximately one-third the water depth, in agreement with simple models. The circulation is nearly symmetric in the wind stress direction when the wave forcing is small. In winter, the volume transport in the surface or bottom layer agrees with unstratified models of cross-shelf wind stress forcing. In summer, when stratification is stronger than in winter, a given cross-shelf wind stress is associated with a stronger (more vertically sheared) cross-shelf circulation than in winter.

The cross-shelf velocity profile during combined wave and wind forcing is approximately a linear superposition of the separate responses to cross-shelf wind and to waves. The combined wave and wind forcing yields an asymmetry in the response with respect to cross-shelf wind direction. During large waves, the circulation is vertically uniform for onshore winds, but strongly sheared for offshore winds. The relative importance of wind and wave forcing depends on water depth. Progressing from the outer edge of the surf zone through the inner shelf toward mid-shelf, as the water depth increases the circulation is dominated first by wave forcing (surfzone), then cross-shelf wind forcing (inner shelf), then along-shelf wind forcing (mid-shelf;

Figure 2-13).

The cross-shelf circulation driven by cross-shelf winds on the inner shelf, and its dependence on season and presumably on stratification, is substantial. These cross-shelf flows have important implications for the transport of nutrients, larvae, pollutants, heat, and salt on inner continental shelves. When considering transport of nutrients and other tracers, we must consider Lagrangian particle trajectories, on which waves have a strong effect at this site. By one crude estimate, the Lagrangian cross-shelf velocity profile in winter resembles just the wind-driven part of the Eulerian velocity profile. When the Stokes' drift profile is added to the Eulerian velocity profile to form the Lagrangian profile estimate, the Stokes' drift tends to cancel the wave-driven part of the Eulerian velocity profile, leaving only the wind-driven part.

The MVCO site is typical of many shallow coastal sites. The strength of the wind stress at MVCO is not unusual compared to other mid-latitude sites. The dependence that we describe for MVCO of the cross-shelf velocity profile on the cross-shelf wind should apply to many unsheltered inner shelf locations.

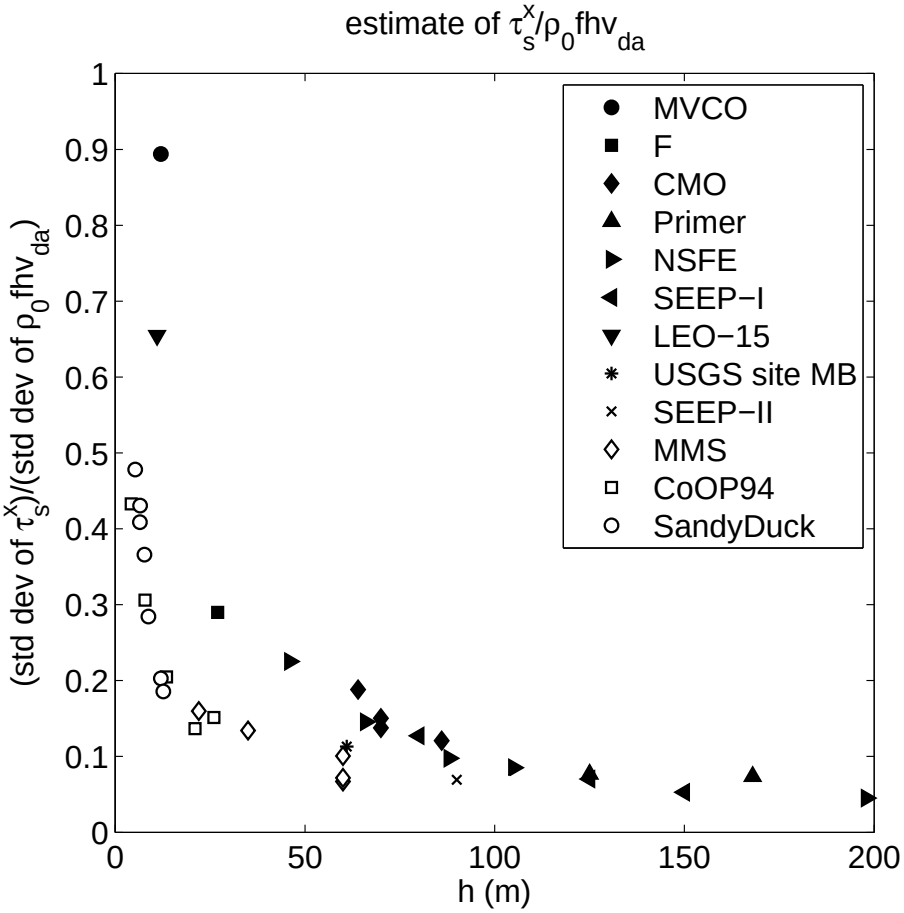

Figure 2-1: Size of cross-shelf wind stress, relative to Coriolis term in depth-integrated cross-shelf momentum balance, for several sites along the United States East Coast. The wind stress and depth-average flow for each site are calculated in the same way as for MVCO. The cross-shelf wind stress is an important forcing term (indicating the cross-shelf momentum balance is not geostrophic) in water shallower than about 25 m. The sites are MVCO; CBLAST F (Hutto et al., 2005); CMO (Shearman and Lentz, 2003); Shelfbreak Primer (Fratantoni and Pickart, 2003); NSFE (Beardsley et al., 1985); SEEP-I (Walsh et al., 1988); LEO-15 (Schofield et al., 2002); USGS site MB (http://stellwagen.er.usgs.gov/mab_sed.html); SEEP-II (Biscaye et al., 1994); MMS (Berger et al., 1994); SandyDuck (http://www.frf.usace.army.mil/SandyDuck/SandyDuck.stm); and CoOP94 (Lentz et al., 1999).

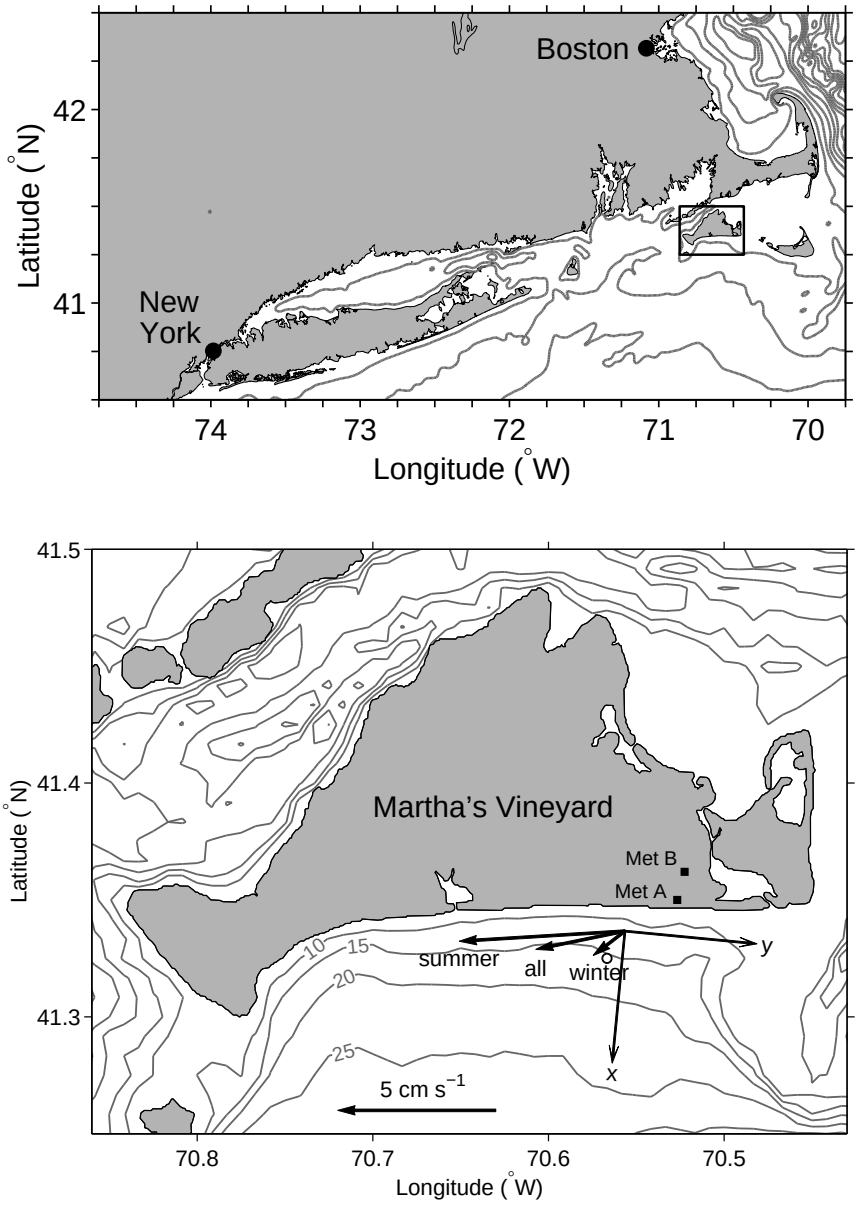

Figure 2-2: Top panel: location of study area (square outline). Bottom panel: detailed map of MVCO study area, with time-mean depth-average flow vectors for all times, winter, and summer (for all wave conditions). The along-shelf/cross-shelf coordinate system is based on the principal axis direction of the depth-average subtidal flow. The MVCO ADCP is located at the origin of the coordinate system. Open circle: ASIT. Mean flow during small waves is nearly along the $-y$ axis. Isobaths are labeled in meters.

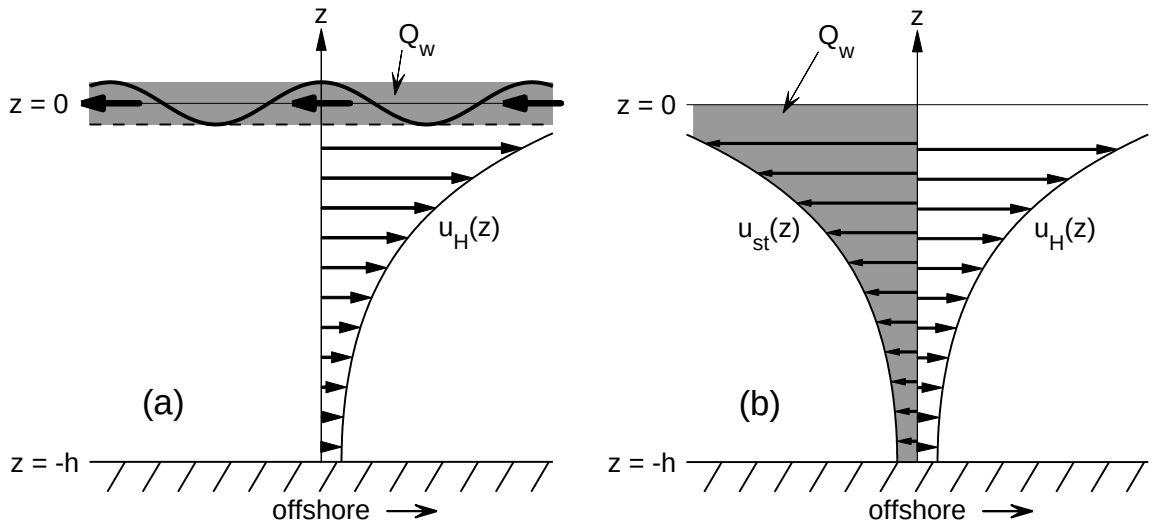

Figure 2-3: (a) Two-dimensional wave-driven circulation in an Eulerian reference frame (fixed in space). Above the wave troughs (above dashed line), there is a net wave-averaged onshore volume transport Q_w (indicated by the grey shaded area and thick arrows). This is because in an Eulerian frame above the wave troughs there is either no water, or water that has an onshore velocity. The wavy line indicates an instantaneous view of the sea surface. Because the circulation is two-dimensional, there must be a compensating Eulerian offshore volume transport $-Q_w$ below the wave troughs, which we refer to as undertow. Here, the undertow is shown with the vertical distribution u_H predicted by Hasselmann (1970). (b) Two-dimensional wave-driven circulation in a Lagrangian (particle-following) reference frame. There is an onshore particle velocity, the Stokes drift $u_{st}(z)$, at all depths. The onshore volume transport due to this water parcel motion is Q_w (indicated by the grey shaded area). There is also an offshore particle velocity at all depths due to the undertow. If the undertow is distributed as $u_H(z) = -u_{st}$, it exactly cancels the Stokes drift and the net particle motion and net volume transport are both zero. If the undertow is not distributed as u_H, the net particle motion will not be zero, but the net volume transport will still be zero as long as the vertical integral of the undertow is equal to $-Q_w$.

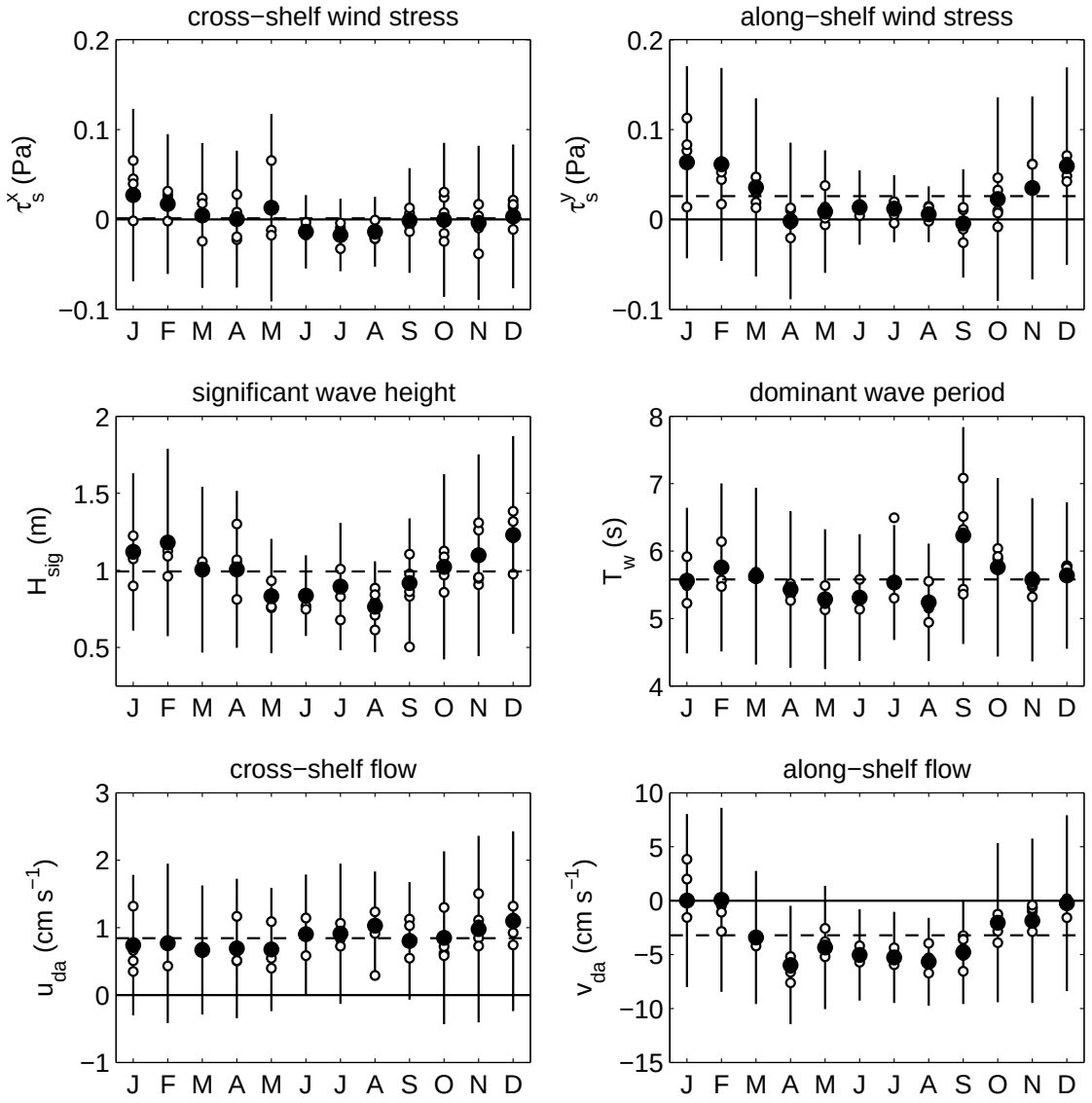

Figure 2-4: Monthly mean wind stress, wave characteristics, and depth-average flow at MVCO. Solid dots show the mean over all years. Open circles are individual monthly means, for each year separately. Vertical bars show ± one standard deviation of the low-pass filtered data for that month, over all years, indicating the strength of synoptic variability. Dashed horizontal line indicates the mean over the entire study period.

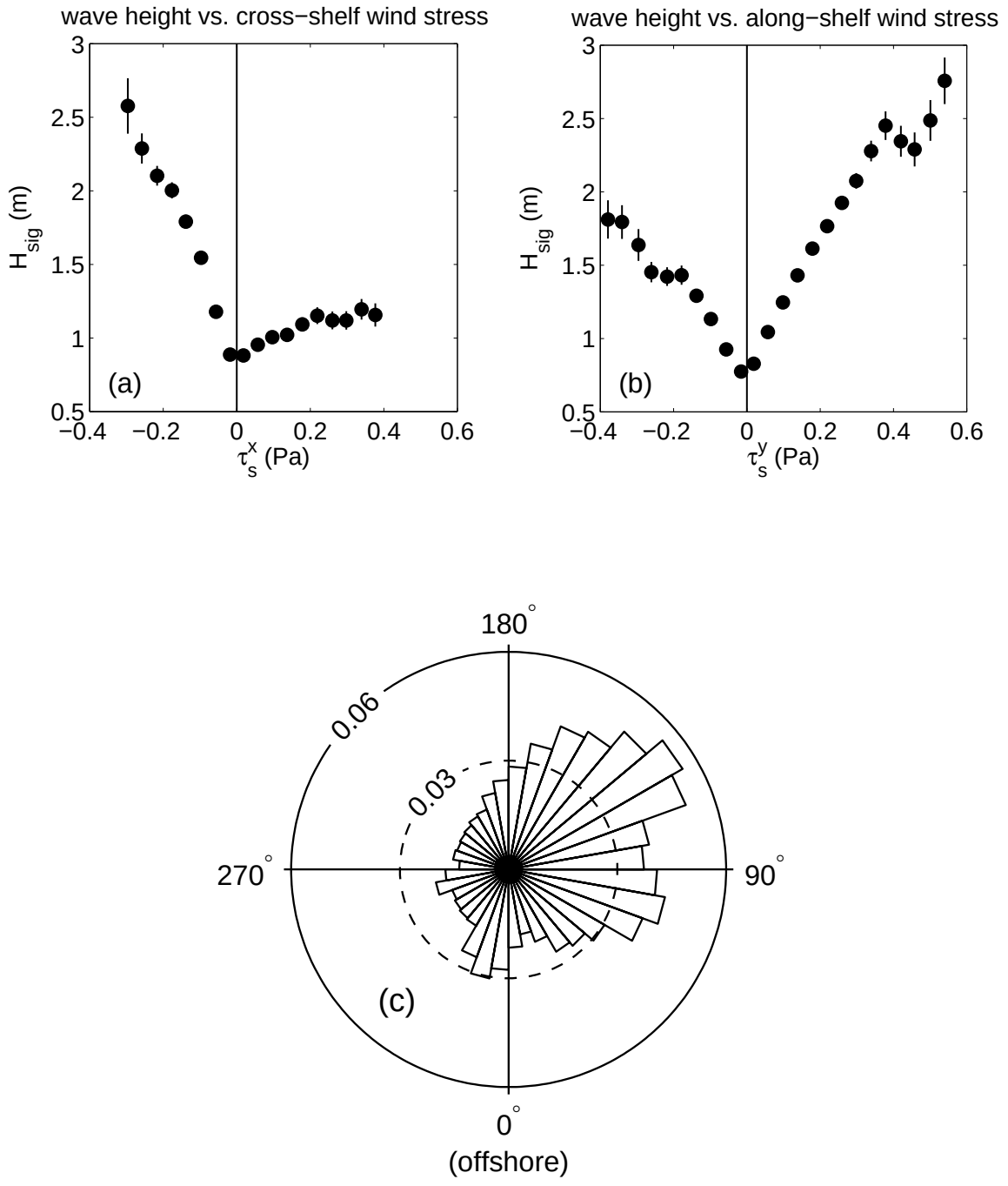

Figure 2-5: MVCO significant wave height H_{sig} as a function of (a) cross-shelf wind stress (positive offshore) and (b) along-shelf wind stress (positive = upwelling-favorable), and (c) normalized histogram of wind stress direction (measured counter-clockwise from offshore).

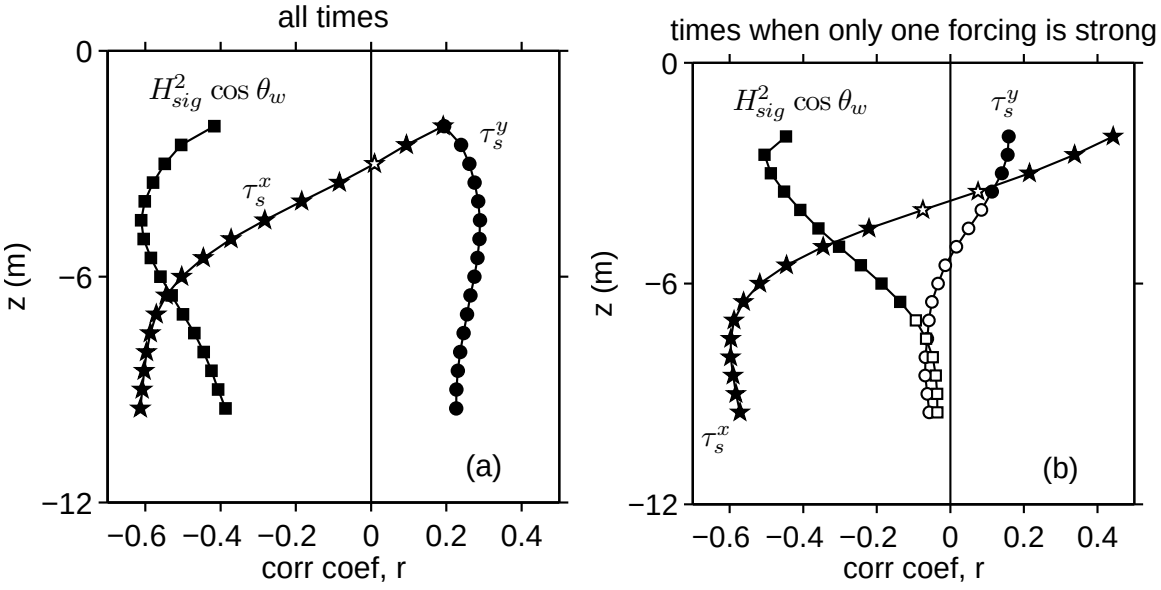

Figure 2-6: Correlation coefficient, as a function of ADCP bin depth, of cross-shelf velocity u in each ADCP bin with wave forcing $H_{sig}^2 \cos\theta_w$ (squares), cross-shelf wind stress τ_s^x (stars), and along-shelf wind stress τ_s^y (circles), at zero lag, assuming one independent point every 24 hrs, for (a) all times and (b) times when the other two forcing mechanisms are weak. Solid (open) symbols show correlations that are (are not) significant at the 95% confidence level.

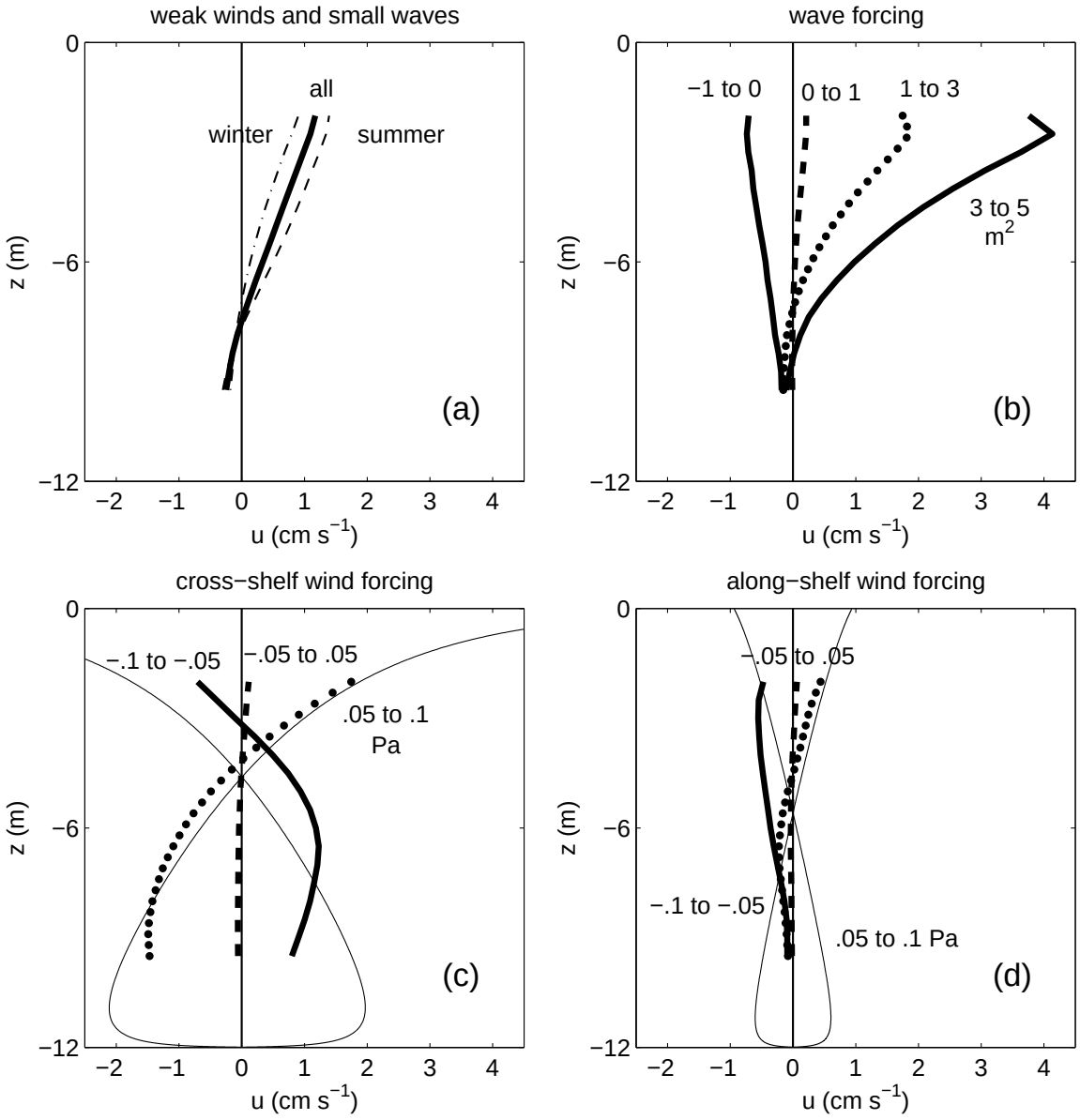

Figure 2-7: Vertical profiles of cross-shelf velocity. (a) The mean background velocity that exists during weak winds and small waves. (c)–(d) Relative to that background velocity, the velocity for times when (b) $-H_{sig}^2 \cos\theta_w$ is in the ranges shown, during weak winds; (c) τ_s^x is in the ranges shown, during small waves and weak along-shelf winds; and (d) τ_s^y is in the ranges shown, during small waves and weak cross-shelf winds. In (c) and (d), thin lines are model profiles (Section 2.3.1), with the model forced by the observed wind stress, with the cubic eddy viscosity profile.

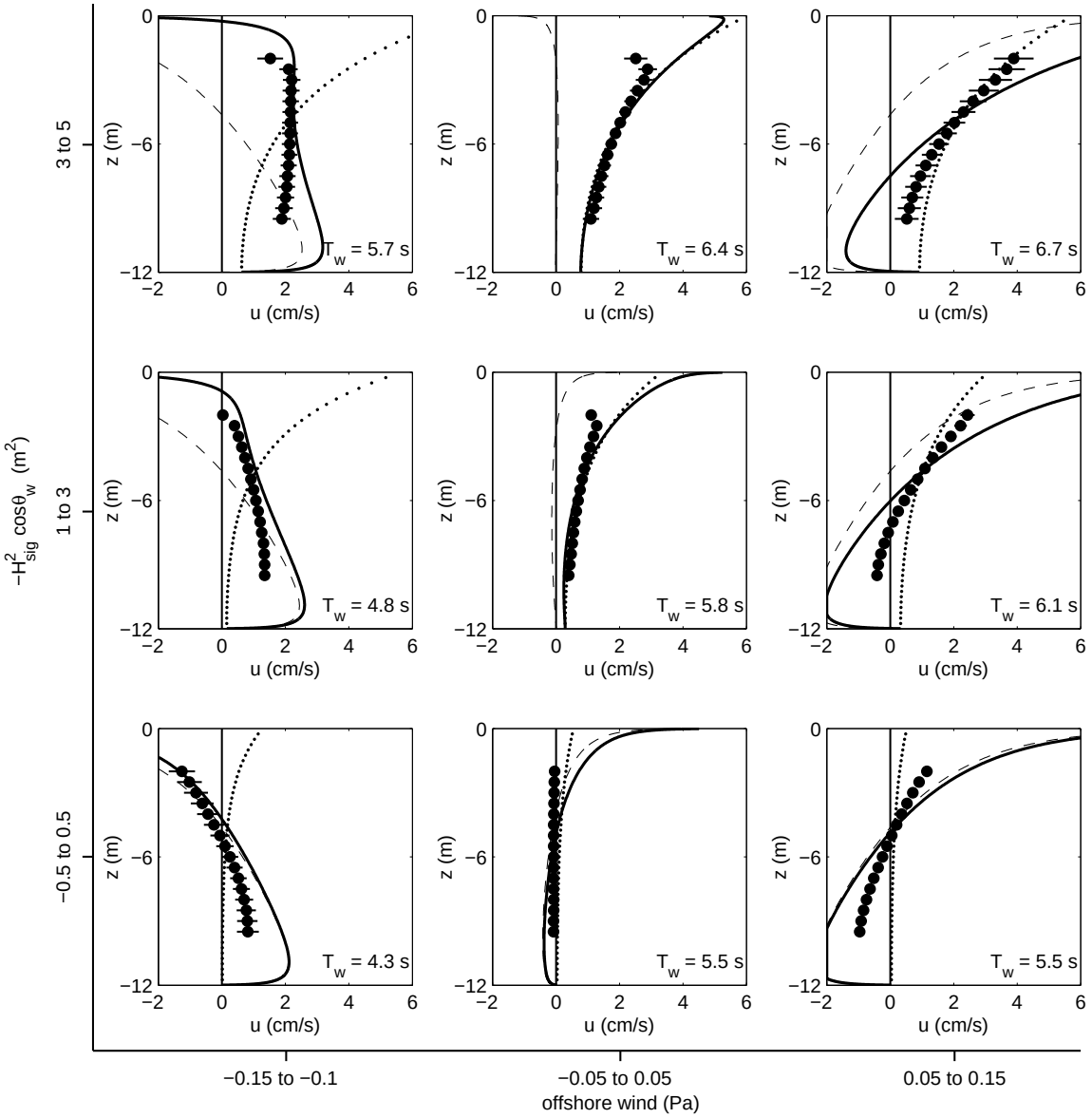

Figure 2-8: Vertical profiles of cross-shelf velocity during various forcing conditions in winter. Wave forcing increases from bottom to top. Wind stress is onshore, small, or offshore (at left, center, or right). Symbols: mean observed profiles; the part of u_{da} that differs from the predicted depth-average u_H has been subtracted. Dotted lines: predicted wave-driven flow, u_H (Section 2.3.2). Dashed: predicted wind-driven flow u_τ, using cubic eddy viscosity profile (Section 2.3.1). Solid lines: $u_{\tau+H}$. If the models are correct, the observations should fall on the solid lines. The mean observed wave period T_w is given in each case.

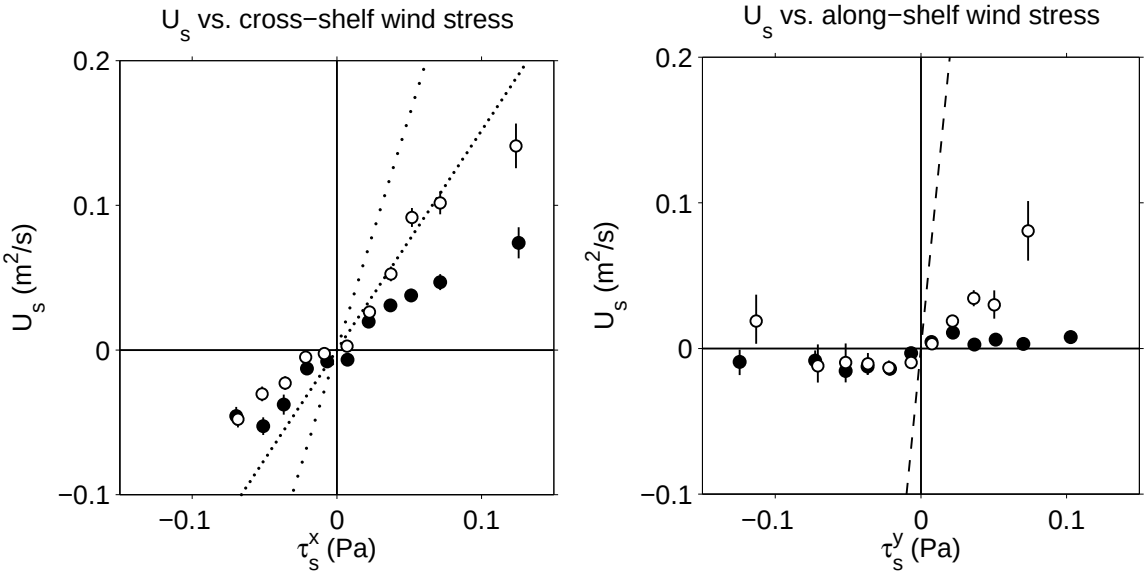

Figure 2-9: Cross-shelf transport in the upper water column during summer (open symbols) and winter (closed symbols), as a function of (left) cross-shelf and (right) along-shelf wind stress, during times when waves were small and the other wind component was weak in each case. Error bars are ± one standard error of the mean. Dashed and dotted lines indicate deep-water Ekman transport values: (at right) $U_s = \tau_s^y/\rho_0 f$ for along-shelf wind (Ekman, 1905), and (at left) $U_s = 0.2\tau_s^x/\rho_0 f$ or $0.32\tau_s^x/\rho_0 f$ for cross-shelf wind, from Weatherly and Martin (1978), with a modified coefficient of 0.32 for this definition of U_s from Tilburg (2003), or 0.2 based on Lentz (1995).

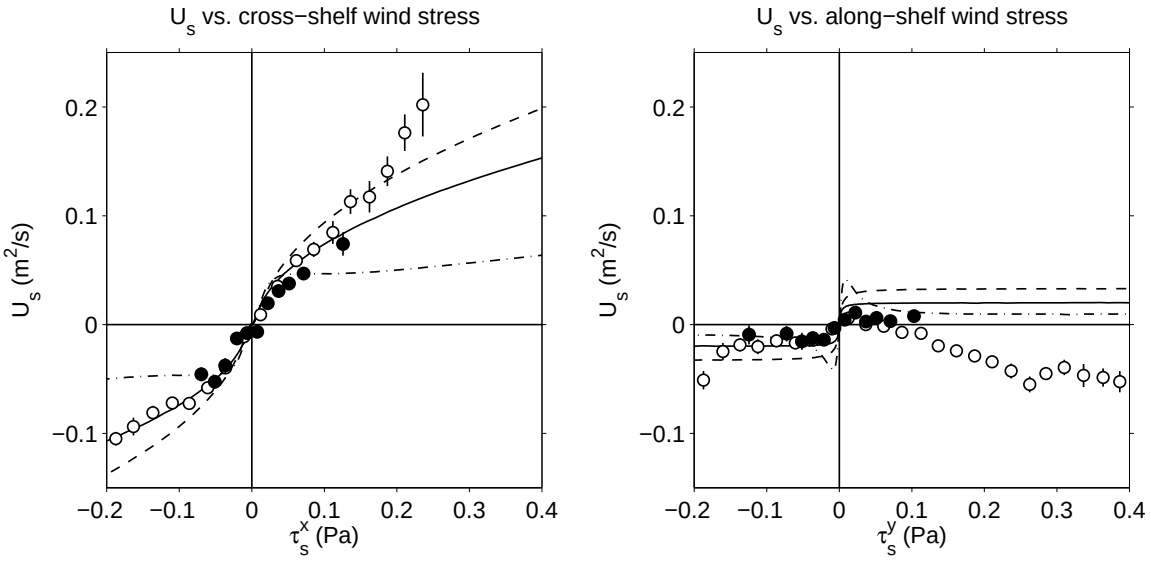

Figure 2-10: Cross-shelf transport in the upper water column, U_s (positive offshore), as a function of (left) cross-shelf or (right) along-shelf wind stress, during winter. Solid symbols: U_s during small waves and weak $|\tau_s^y|$ (left) or $|\tau_s^x|$ (right). Open symbols: U_s', which is U_s during any wave conditions and weak $|\tau_s^y|$ (left) or $|\tau_s^x|$ (right), but with the predicted wave-driven velocity profile $u_H(z,t) = -u_{st}(z,t)$ (Hasselmann, 1970) subtracted from $u(z,t)$ before calculating U_s. Error bars are $\pm$ one standard error of the mean. Lines indicate the U_s predicted by a simple numerical model with constant density and the MYApprox, cubic, or bilinear cutoff eddy viscosity profile (dashed, solid, or dash-dot line, respectively, forced by (left) cross-shelf or (right) along-shelf wind stress (Lentz, 1995).

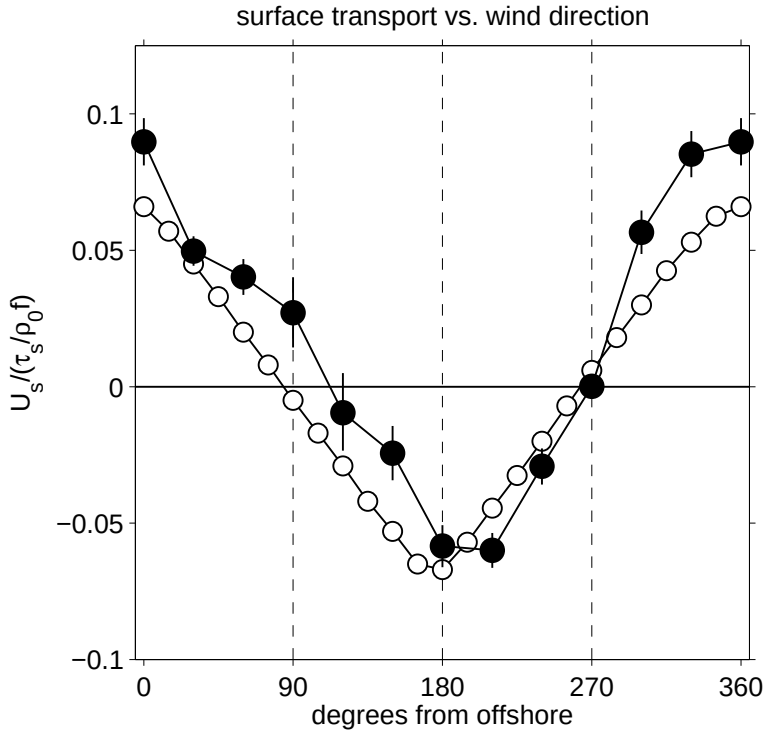

Figure 2-11: Normalized cross-shelf transport in the surface layer, $U_s/(|\boldsymbol{\tau}_s|/\rho_0 f)$ (positive offshore), as a function of wind direction. Open circles: numerical model results for $|\boldsymbol{\tau}_s| = 0.1$ Pa and $h = 5$ m (taken from Tilburg, 2003, Figure 16). Solid symbols: MVCO observations for $h = 12$ m and $0.075 < |\boldsymbol{\tau}_s| < 0.15$ Pa. The cross-shelf velocity profiles were bin averaged by wind direction, then U_s was calculated, then normalized by the bin-averaged $|\boldsymbol{\tau}_s|/\rho_0 f$. These data are restricted to times when waves are small, so there are fewer events for the onshore wind stress angles (near 180°) than for the offshore. In both the model and the observations, the largest surface layer transport is for cross-shelf, not along-shelf, winds.

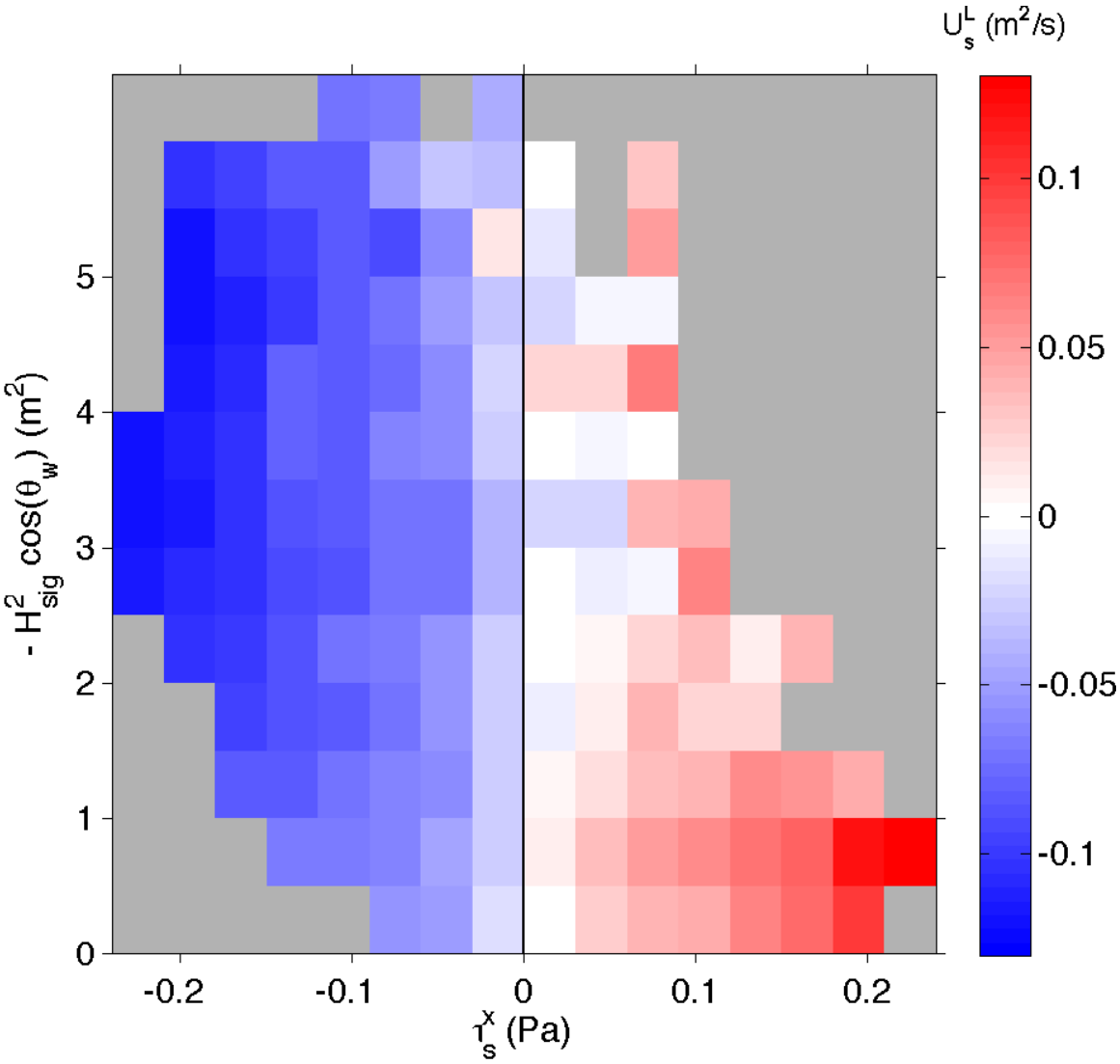

Figure 2-12: Estimated Lagrangian cross-shelf surface layer transport U_s^L in winter, as a function of cross-shelf wind stress τ_s^x and wave forcing $H_{sig}^2 \cos\theta_w$. U_s^L is calculated in the same way as U_s, but from the estimated Lagrangian velocity profile $u_L(z,t) = u(z,t) + u_{st}(z,t)$. Red (blue) indicates offshore (onshore) surface layer transport, which has the sense of upwelling (downwelling). Grey areas indicate forcing regimes that had fewer than 10 independent events. Most of the time, the system is in the lower central part of the diagram. As a result, although the downwelling region in the figure is larger than the upwelling region, the time-mean U_s^L is very small (-0.016 m^2 s^{-1}). The time-mean Lagrangian circulation by this crude estimate is essentially zero.

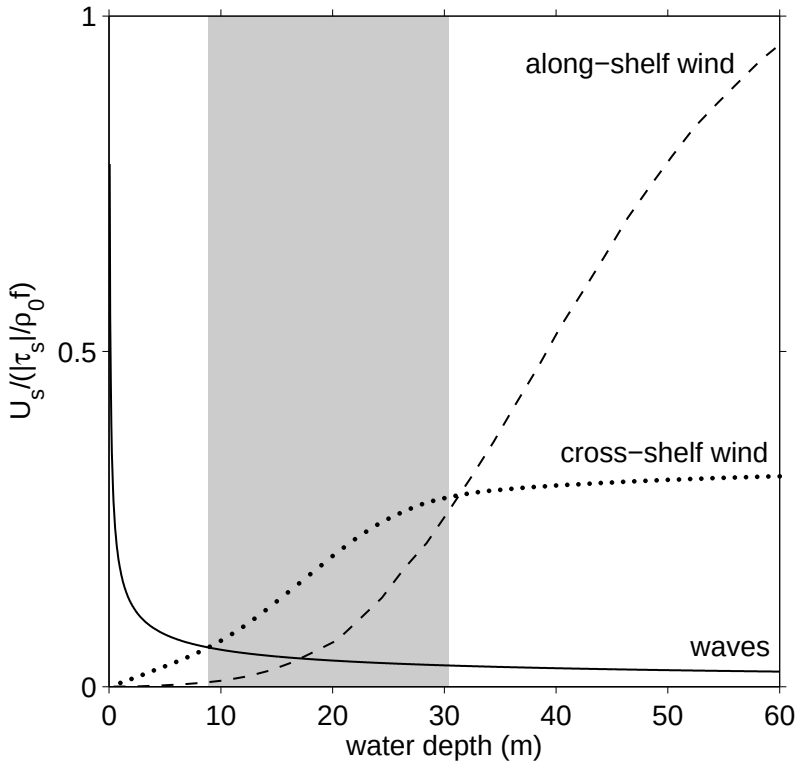

Figure 2-13: Relative importance of cross-shelf wind stress, along-shelf wind stress, and wave forcing: theoretical cross-shelf surface layer transport U_s normalized by deep-water Ekman transport $|\boldsymbol{\tau_s}|/\rho_0 f$, as a function of water depth. U_s is calculated numerically for cross-shelf wind or along-shelf wind based on a model with constant density, wind stress magnitude 0.1 Pa, and a bilinear cutoff eddy viscosity profile (Lentz, 1995). U_s is estimated for wave forcing via $U_s = gH_{sig}^2/16c$, using the shallow-water phase speed $c = \sqrt{gh}$ and the relation $H_{sig}^2 \sim (9\ \mathrm{m}^2\ \mathrm{Pa}^{-1})|\boldsymbol{\tau_s}|$ observed at MVCO. The region where cross-shelf wind stress is the dominant forcing mechanism is shaded grey. This is a conservative estimate; a cubic eddy viscosity profile predicts a wider region.

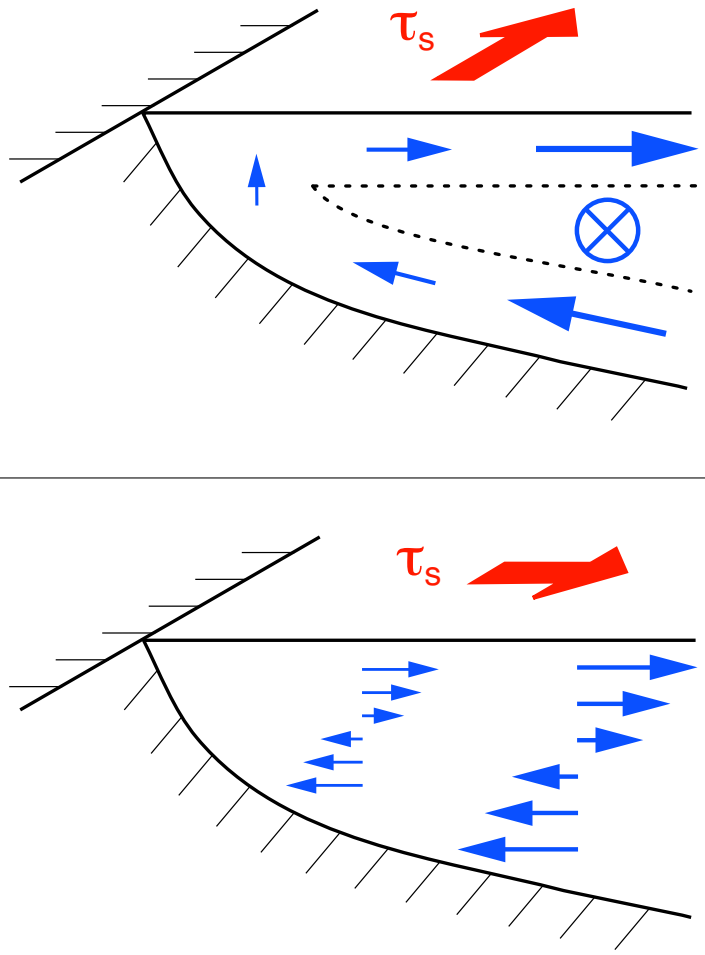

Figure 2-14: Cross-shelf circulation driven by a steady along-shelf or cross-shelf wind stress, assuming along-shelf uniform flow. Top panel: cross-shelf circulation (blue arrows) driven by an upwelling-favorable wind stress τ_s (red arrow). At mid-shelf (on the right-hand side of the diagram) the cross-shelf flow is offshore in the surface boundary layer, with a return flow in the bottom boundary layer (as shown) or in the interior; the along-shelf flow is in the direction of the wind stress (circle with "x"). Over the inner shelf where the surface and bottom boundary layers (dashed lines) overlap, the cross-shelf flow is weak compared to mid-shelf and upwelling occurs. Bottom panel: cross-shelf circulation (blue arrows) driven by an offshore wind stress τ_s (red arrow). The inner shelf extends over the entire region shown. Due to the overlapping surface and bottom boundary layers, the cross-shelf circulation near the surface is in the direction of the wind stress, with a return flow lower in the water column.

Chapter 3

A Momentum Budget for the Inner Continental Shelf

3.1 Introduction

The relatively shallow inner continental shelf, where the water is tens of meters deep, is a transition region between the surfzone where breaking waves dominate the dynamics and the mid-shelf where the frictional surface and bottom boundary layers are well separated and an interior geostrophic region exists. As a result, the inner shelf momentum balance may contain some elements of both the surfzone balance and the mid-shelf balance.

The cross-shelf momentum balance over the inner shelf can be a complex superposition of three balances. A geostrophic balance between the Coriolis acceleration and the cross-shelf pressure gradient tends to dominate the cross-shelf momentum balance farther offshore, at mid-shelf (Brown et al., 1985; Thompson and Pugh, 1986; Brown et al., 1987; Noble and Butman, 1983; Lee et al., 1984, 1989; Lentz et al., 1999; Shearman and Lentz, 2003; Liu and Weisberg, 2005). A wave set-down balance between the wave radiation stress divergence and the cross-shelf pressure gradient tends to dominate farther onshore, in the surfzone (Longuet-Higgins and Stewart, 1964; Bowen et al., 1968; Lentz and Raubenheimer, 1999). Both those balances can be important over the inner shelf. A coastal set-up or set-down balance between the cross-shelf

wind stress and the cross-shelf pressure gradient can also be important over the inner shelf due to the shallow water (Blanton, 1981; Lee et al., 1989; Lentz et al., 1999; Liu and Weisberg, 2005, and Chapter 2). Each balance is between the cross-shelf pressure gradient and a different term. The dynamics are complicated because the cross-shelf pressure gradient may be simultaneously balanced by one, two, or all of these three terms (*e.g.,* Lentz et al., 1999). In the surface and bottom Ekman boundary layers, vertical stress divergences due to wind and bottom stress are dominant terms in the momentum balance. In the inner shelf, the surface and bottom boundary layers often overlap, and then a geostrophic cross-shelf balance may not hold at any depth.

The along-shelf momentum balance over the inner shelf is simpler than at mid-shelf, where the Coriolis, wind stress, bottom stress, acceleration, and pressure gradient terms can all be important (Allen and Smith, 1981; Lentz and Winant, 1986; Lee et al., 1984, 1989). Over the inner shelf, the balance tends to be between three terms: along-shelf wind stress and bottom stress and pressure gradient (Scott and Csanady, 1976; Pettigrew, 1981; Lentz and Winant, 1986; Masse, 1988; Lee et al., 1989; Lentz, 1994). In the surfzone, the wave radiation stress gradient again becomes a dominant term and is balanced by bottom stress (Thornton and Guza, 1986; Svendsen and Putrevu, 1994; Feddersen et al., 1998; Lentz et al., 1999). Few previous studies have considered wave radiation stress over the inner shelf (Lentz et al., 1999).

In this chapter, terms in the cross-shelf and along-shelf depth-average momentum budgets are estimated to determine the dominant forces acting on the water column over the inner continental shelf near the Martha's Vineyard Coastal Observatory. We find that the cross-shelf momentum balance is dominated by the wind stress, Coriolis, and pressure gradient terms. The calculated wave radiation stress is also large but is not correlated with the cross-shelf pressure gradient; either the true wave radiation stress gradient is smaller than our estimate, possibly due to wave dissipation, or the wave radiation stress is balanced by a pressure gradient with a smaller cross-shelf scale than is resolved by these observations. The along-shelf momentum balance is between the wind stress and pressure gradient, with some contribution from bottom stress.

3.2 Data

The data used in this chapter are from four sources. The first data set is the long Martha's Vineyard Coastal Observatory (MVCO) time series of water velocity, wind velocity, air temperature, pressure, and relative humidity, and water column bottom pressure, which extend from 2001 to the present. The second data set is the Coupled Boundary Layers Air-Sea Transfer in Low Winds (CBLAST-Low) 2003 measurements in summer and fall 2003 of water temperature, velocity, bottom pressure, and water density. The third data set is the Stratification, Wind and Waves on the Inner Shelf at MVCO (SWWIM I) experiment, which included measurements of water velocity, temperature, density, and bottom pressure during winter and spring 2004–2005. Those three data sets are described in more detail in the earlier chapters of this thesis. The fourth data set used here is a time series of bottom pressure measurements near the 20-m isobath obtained during CBLAST 2001 in summer. The mooring locations for all four data sets are shown in Figure 3-1. Measurements of the along-shelf pressure gradient are only available in summer. For brevity we show the terms in the momentum budgets during times when pressure gradient estimates are available, although the other terms estimated from the MVCO time series are available from 2001-2007 and those data are included in the analysis when the pressure gradient is not needed. For this study, we define "summer" as May 1 through September 30, and "winter" as October 1 through April 30.

3.3 Methods

3.3.1 Subtidal Filtering

Here, "subtidal" indicates data that have been low-pass filtered to remove diurnal, semidiurnal, inertial, and higher-frequency motions. We use the PL64 filter (Flagg et al., 1976; Limeburner et al., 1983) with a $(33\ \mathrm{hr})^{-1}$ half-amplitude cutoff. To prevent edge effects from gaps in the data we de-tided the velocities and bottom pressures, linearly interpolated across gaps, filtered, and replaced the gaps, widening

each gap by 1/2 the filter window width to each side. To calculate the standard error of a mean, we require at least 10 independent data points and assume an independent data point every 33 hr. The decorrelation times of the wind and wave forcing and the cross- and along-shelf velocities are all less than 33 hr (Chapter 2).

3.3.2 Coordinate System

We use a separate (x, y) coordinate system for each mooring, with x positive offshore and y positive along-shelf eastward (Figure 3-1). The local along-shelf and cross-shelf coordinate directions are based on the principal axis directions of the subtidal depth-average velocity. z is measured positive upward, with $z = 0$ at the mean water level over each deployment. $z = -h(x)$ is the bottom.

3.3.3 Derivation of Momentum Balance

To derive a depth-averaged momentum balance equation, we start with the Reynolds-averaged cross-shelf momentum balance for an incompressible fluid. Using the Boussinesq approximation (*e.g.,* Kundu and Cohen, 2002) and including the momentum flux divergence (or wave radiation stress) due to surface gravity waves (Longuet-Higgins and Stewart, 1960), the cross-shelf momentum balance is

$$\frac{\partial u}{\partial t} + \nabla \cdot (\mathbf{u}u) - fv = -\frac{1}{\rho_0}\frac{\partial p}{\partial x} + \frac{\partial}{\partial z}\left(A_v \frac{\partial u}{\partial z}\right) - \frac{\partial \left(u'u'\right)}{\partial x} - \frac{\partial \left(v'u'\right)}{\partial y} - \frac{\partial \left(w'u'\right)}{\partial z} \quad (3.1)$$

where $\mathbf{u} = (u, v, w)$ is the velocity vector, $f = 2\Omega \sin\phi$ is the Coriolis parameter, $\Omega = 2\pi$ rad dy^{-1} is Earth's angular rotation frequency, ϕ is latitude, ρ_0 is the density of seawater, p is the dynamical pressure, A_v is the turbulent vertical eddy viscosity, and (u', v') are surface gravity wave orbital velocities. To write the momentum balance in the form of Eq. (3.1), the continuity equation $\nabla \cdot \mathbf{u} = 0$ has been used to add $u\nabla \cdot \mathbf{u} = 0$, and similarly for the wave velocity $\mathbf{u}'$. Integrating vertically over the water column from the surface $z = \eta$ to the bottom $z = -h(x)$, and averaging the wave momentum flux terms over many wave periods (with angle brackets representing

that time average) gives

$$\int_{-h}^{\eta} \frac{\partial u}{\partial t}\, dz + \int_{-h}^{\eta} \nabla \cdot (\mathbf{u}u)\, dz - \int_{-h}^{\eta} fv\, dz = \int_{-h}^{\eta} fv_{st}\, dz - \frac{1}{\rho_0}\int_{-h}^{\eta} \frac{\partial p}{\partial x}\, dz + \int_{-h}^{\eta} \frac{\partial}{\partial z}\left(A_v \frac{\partial u}{\partial z}\right) dz - \left\langle \int_{-h}^{\eta+\eta'} \frac{\partial\,(u'u')}{\partial x}\, dz \right\rangle - \left\langle \int_{-h}^{\eta+\eta'} \frac{\partial\,(v'u')}{\partial y}\, dz \right\rangle - \left\langle \int_{-h}^{\eta+\eta'} \frac{\partial\,(w'u')}{\partial z}\, dz \right\rangle \quad (3.2)$$

Applying the surface and bottom boundary conditions

$$A_v \frac{\partial u}{\partial z}\bigg|_{z=\eta} = \frac{\tau_s^x}{\rho_0} \quad (3.3)$$

and

$$A_v \frac{\partial u}{\partial z}\bigg|_{z=-h} = \frac{\tau_b^x}{\rho_0} \quad (3.4)$$

and using the definitions of wave radiation stress (*e.g.*, Longuet-Higgins and Stewart, 1964)

$$\frac{1}{\rho_0}\frac{\partial S^{xx}}{\partial x} \equiv \left\langle \int_{-h}^{\eta+\eta'} \frac{\partial\,(u'u')}{\partial x}\, dz \right\rangle, \qquad \frac{1}{\rho_0}\frac{\partial S^{yx}}{\partial y} \equiv \left\langle \int_{-h}^{\eta+\eta'} \frac{\partial\,(v'u')}{\partial y}\, dz \right\rangle \quad (3.5)$$

and depth-average velocity $\overline{\mathbf{u}} = (\overline{u}, \overline{v})$,

$$\overline{\mathbf{u}} \equiv \frac{1}{h}\int_{-h}^{\eta} \mathbf{u}\, dz \quad (3.6)$$

and the Hasselmann (1970) wave radiation stress (*e.g.*, Xu and Bowen, 1994) that is due to the Earth's rotation and involves the Stokes' drift velocity $\mathbf{u_{st}} = (u_{st}, v_{st})$ (Stokes, 1847),

$$f\overline{\mathbf{u}}_{\mathbf{st}} \equiv \frac{1}{h}\left\langle \int_{-h}^{\eta+\eta'} \frac{\partial\,(w'u')}{\partial z}\, dz \right\rangle \quad (3.7)$$

gives

$$\int_{-h}^{\eta} \frac{\partial u}{\partial t}\, dz + \int_{-h}^{\eta} \nabla\cdot(\mathbf{u}u)\, dz - hf\overline{v} = hf\overline{v}_{st} - \frac{1}{\rho_0}\int_{-h}^{\eta} \frac{\partial p}{\partial x}\, dz + \frac{\tau_s^x}{\rho_0} - \frac{\tau_b^x}{\rho_0} - \frac{1}{\rho_0}\frac{\partial S^{xx}}{\partial x} - \frac{1}{\rho_0}\frac{\partial S^{yx}}{\partial y} \tag{3.8}$$

If we apply Leibniz' rule,

$$\begin{aligned} \frac{\partial}{\partial t}\int_{-h}^{\eta} u\, dz - \frac{\partial \eta}{\partial t}\, u|_{z=\eta} + \nabla_H \cdot \int_{-h}^{\eta} \mathbf{u_H} u\, dz - (\nabla_H \eta)\cdot \mathbf{u_H} u|_{z=\eta} + (-\nabla_H h)\cdot \mathbf{u_H} u|_{z=-h} \\ + wu|_{z=\eta} - wu|_{z=-h} - hf\overline{v} \\ = hf\overline{v}_{st} - \frac{1}{\rho_0}\int_{-h}^{\eta} \frac{\partial p}{\partial x}\, dz + \frac{\tau_s^x}{\rho_0} - \frac{\tau_b^x}{\rho_0} - \frac{1}{\rho_0}\frac{\partial S^{xx}}{\partial x} - \frac{1}{\rho_0}\frac{\partial S^{yx}}{\partial y} \end{aligned} \tag{3.9}$$

and use the surface and bottom boundary conditions

$$\left.\frac{d\eta}{dt}\right|_{z=\eta} = \left.\frac{\partial \eta}{\partial t}\right|_{z=\eta} + \mathbf{u_H}|_{z=\eta}\cdot(\nabla_H \eta) = w|_{z=\eta} \tag{3.10}$$

$$\mathbf{u_H}|_{z=-h}\cdot(-\nabla_H h) = w|_{z=-h} \tag{3.11}$$

and divide by h, then the cross-shelf momentum equation is

$$\begin{aligned} \frac{\partial \overline{u}}{\partial t} = -\frac{1}{h}\frac{\partial}{\partial x}\int_{-h}^{\eta} u^2\, dz - \frac{1}{h}\frac{\partial}{\partial y}\int_{-h}^{\eta} vu\, dz + f\overline{v} + f\overline{v}_{st} - \frac{1}{\rho_0 h}\int_{-h}^{\eta}\frac{\partial p}{\partial x}\, dz \\ + \frac{\tau_s^x}{\rho_0 h} - \frac{\tau_b^x}{\rho_0 h} - \frac{1}{\rho_0 h}\frac{\partial S^{xx}}{\partial x} - \frac{1}{\rho_0 h}\frac{\partial S^{yx}}{\partial y} \end{aligned} \tag{3.12}$$

Similarly, the depth-averaged along-shelf momentum equation is

$$\begin{aligned} \frac{\partial \overline{v}}{\partial t} = -\frac{1}{h}\frac{\partial}{\partial x}\int_{-h}^{\eta} uv\, dz - \frac{1}{h}\frac{\partial}{\partial y}\int_{-h}^{\eta} v^2\, dz - f\overline{u} - f\overline{u}_{st} - \frac{1}{\rho_0 h}\int_{-h}^{\eta}\frac{\partial p}{\partial y}\, dz \\ + \frac{\tau_s^y}{\rho_0 h} - \frac{\tau_b^y}{\rho_0 h} - \frac{1}{\rho_0 h}\frac{\partial S^{xy}}{\partial x} - \frac{1}{\rho_0 h}\frac{\partial S^{yy}}{\partial y} \end{aligned} \tag{3.13}$$

3.3.4 Pressure Gradients

The pressure in Eqs. (3.12) and (3.13) can be decomposed into a contribution from near-bottom pressure and a contribution from the density structure of the overlying water column. We start with the hydrostatic equation,

$$\frac{\partial p}{\partial z} = -(\rho_0 + \widetilde{\rho})g \tag{3.14}$$

where the density has been separated into a reference density ρ_0 that is constant in space and time, and a part $\widetilde{\rho}$ that varies in space and time. This is equivalent to removing the static pressure gradient $\partial p_0/\partial z \equiv -\rho_0 g$ from Eq. (3.14), leaving

$$\frac{\partial \widetilde{p}}{\partial z} = -\widetilde{\rho}g \tag{3.15}$$

and we then drop the tildes. The mean bottom pressure is not accurately known from the observations. We remove the mean measured bottom pressure from each deployment and consider only time variations about the mean, following previous studies (*e.g.*, Brown et al., 1985; Lentz et al., 1999). A vertical integral from $-h$ to z gives

$$p = p^b - g\int_{-h}^{z} \rho\,(x, y, z, t)\; dz' \tag{3.16}$$

where $p^b = p|_{z=-h}$ is the bottom pressure.

The depth-average (time-varying part of the) pressure gradient can be written as the sum of the gradient of bottom pressure p^b and of a term due to density variations (Brown et al., 1985). For the depth-average cross-shelf pressure gradient,

$$\frac{1}{h}\int_{-h}^{\eta} \frac{\partial p}{\partial x}\, dz = \frac{\partial p^b}{\partial x} + \frac{1}{h}\frac{\partial}{\partial x}\int_{-h}^{\eta} g\rho z\, dz \tag{3.17}$$

where we assume $\eta << h$, and similarly for the along-shelf pressure gradient,

$$\frac{1}{h}\int_{-h}^{\eta} \frac{\partial p}{\partial y}\, dz = \frac{\partial p^b}{\partial y} + \frac{1}{h}\frac{\partial}{\partial y}\int_{-h}^{\eta} g\rho z\, dz \tag{3.18}$$

Alternatively, the pressure gradients can be written as the sum of a barotropic pressure gradient p^{bt} due to sea-level and atmospheric pressure variations, and a baroclinic pressure gradient p^{bc} due to density variations in the water column:

$$\frac{1}{h}\int_{-h}^{\eta}\frac{\partial p}{\partial x}\,dz = \frac{\partial p^{bt}}{\partial x} + \frac{\partial p^{bc}}{\partial x} \tag{3.19}$$

where

$$\frac{\partial p^{bt}}{\partial x} = \frac{\partial p^{b}}{\partial x} - \frac{\partial}{\partial x}\int_{-h}^{\eta} g\rho\,dz \tag{3.20}$$

and

$$\frac{\partial p^{bc}}{\partial x} = \frac{\partial}{\partial x}\int_{-h}^{\eta} g\rho\,dz + \frac{1}{h}\frac{\partial}{\partial x}\int_{-h}^{\eta} g\rho z\,dz \tag{3.21}$$

and similarly for the along-shelf pressure gradient.

3.3.5 Calculation of Momentum Budget Terms from Observations

We used centered differences to calculate derivatives with respect to time and space where possible. We used a constant value to extrapolate vertically to the surface ($\eta \approx 0$) and bottom of the water column; the results presented here do not change substantially if a linear extrapolation is used instead. We used the bathymetry described in Chapter 2 for $h(x)$ and linear wave theory to calculate the surface gravity wave phase speed and wavenumber for the observed dominant wave period, without assuming shallow-water waves.

Bottom Stress

To estimate bottom stress we used a quadratic drag formula

$$\tau_{\mathbf{b}} = -\rho_0 C_d\,|u_d|\,\mathbf{u_d} \tag{3.22}$$

where $C_d = 1.45\times10^{-3}$ is the drag coefficient estimated at $z = -9$ m at the Node from comparison with a near-bottom stress estimate based on turbulent covariance mea-

surements (*personal communication, J. Trowbridge*), and $\mathbf{u_d}$ is the observed velocity at $z = -9$ m.

Pressure Gradients

To estimate the along-shelf bottom pressure gradient and near-surface density gradient during CBLAST 2003, we used moorings T1 and T2, which were on the 15-m isobath. The mid-depth temperature and near-bottom conductivity sensors failed on T1 so only the near-surface density gradient is available.

To estimate along-shelf bottom pressure and density gradients during CBLAST 2001, we used the sensors labeled "bp" in Figure 3-1 when available, and a third sensor deployed about 15 km farther to the east on the same isobath (not shown) to fill in the bottom pressure gradient during some times when bottom pressure from the eastern "bp" sensor was not available. The along-shelf pressure gradient measured between the sensors farther apart was similar, but smaller in magnitude, to the gradient between the "bp" sensors shown in Figure 3-1.

To estimate the cross-shelf bottom pressure gradient and cross-shelf density gradient during CBLAST 2003 and SWWIM I, we used the Node and F moorings. Density information was available throughout the water column at the Node and F during CBLAST 2003, and at F and near-surface at the Node during SWWIM I. See Section 3.5.6 for discussion of uncertainties in the pressure gradient estimates.

Nonlinear Advection

The nonlinear advection terms were estimated as

$$-\frac{1}{h}\frac{\partial}{\partial x}\int_{-h}^{\eta} uu\,dz = -\frac{1}{h}\frac{1}{L}\int_{-h}^{0} uu\,dz\Big|_{x=L} \tag{3.23}$$

and

$$-\frac{1}{h}\frac{\partial}{\partial x}\int_{-h}^{\eta} vu\,dz = -\frac{1}{h}\frac{1}{L}\int_{-h}^{0} vu\,dz\Big|_{x=L} \tag{3.24}$$

where $x = L$ is the cross-shelf location of the Node mooring, thereby assuming the integral in each case goes linearly to zero at the coast ($x = 0$) as a function of x. The

nonlinear terms involving $\partial/\partial y$ cannot be estimated from the available observations.

Hasselmann Wave Stress

We estimated $f\mathbf{u_{st}}(z,t)$ from the Stokes' drift (Longuet-Higgins, 1953)

$$\mathbf{u_{st}}(z,t) = \frac{g\mathbf{k}H_{sig}^2}{8c}\frac{\cosh\left[2k\left(z+h\right)\right]}{\sinh\left(2kh\right)} \tag{3.25}$$

where $\mathbf{k}$ is the wave vector and c is the wave phase speed.

Wave Radiation Stress Gradients

We assumed no dissipation of surface gravity wave energy and then, following Lentz et al. (1999), estimated S^{xx} from Longuet-Higgins and Stewart (1964) as

$$S^{xx} = E\left[\frac{c_g}{c}\left(1+\cos^2\theta_w\right) - \frac{1}{2}\right] \tag{3.26}$$

where $E = g\rho_0 H_{sig}^2/16$ is the wave energy; c_g and c are the group velocity and phase speed, calculated from linear wave theory with the observed dominant wave period; and θ_w is the direction of wave propagation. We used conservation of wave energy flux $c_g E$ to estimate H_{sig} and θ_w on the 11- and 13-m isobaths from the H_{sig} and θ_w observed at the 12-m isobath. To calculate the cross-shelf gradient of S^{xx}, we estimated S^{xx} on the 11- and 13-m isobaths and used a finite difference approximation to $\partial S^{xx}/\partial x$. The result is the same if we instead calculate S^{xx} on the 11.9- and 12.1-m isobaths.

We assume $S_x^{yx} = 0$ since the MVCO Node site is always outside the surfzone (Appendix E) and we are assuming no wave dissipation. S_y^{xy} and S_y^{yy} cannot be estimated from the available observations.

Residuals

The residual R^x for the cross-shelf momentum budget is estimated as the difference between the observed acceleration and the acceleration predicted by the sum of all

the other estimated terms:

$$R^x = \frac{\partial \overline{u}}{\partial t} - \left(-\frac{1}{h}\frac{\partial}{\partial x}\int_{-h}^{\eta} u^2\, dz + f\overline{v} + f\overline{v}_{st} - \frac{1}{\rho_0 h}\int_{-h}^{\eta}\frac{\partial p}{\partial x}\, dz + \frac{\tau_s^x}{\rho_0 h} - \frac{\tau_b^x}{\rho_0 h} - \frac{1}{\rho_0 h}\frac{\partial S^{xx}}{\partial x} \right) \quad (3.27)$$

Similarly, the residual R^y for the along-shelf momentum budget is

$$R^y = \frac{\partial \overline{v}}{\partial t} - \left(-\frac{1}{h}\frac{\partial}{\partial x}\int_{-h}^{\eta} uv\, dz - f\overline{u} - f\overline{u}_{st} - \frac{1}{\rho_0 h}\int_{-h}^{\eta}\frac{\partial p}{\partial y}\, dz + \frac{\tau_s^y}{\rho_0 h} - \frac{\tau_b^y}{\rho_0 h} \right) \quad (3.28)$$

3.4 Results

3.4.1 Pressure and Bottom Pressure

During all times when estimates of the horizontal pressure gradients are available, the gradient of bottom pressure was large compared to the density contribution to the pressure gradient [see Eqs. (3.17) and (3.18)] (Figure 3-2) in both the along-shelf and cross-shelf directions. This is in contrast to mid-shelf (Lentz et al., 1999; Shearman and Lentz, 2003) and an inner shelf site influenced by a river outflow plume (Lentz et al., 1999) where the baroclinic pressure gradient can be the same size as the barotropic pressure gradient. Consequently, we use the bottom pressure gradient to represent the full pressure gradient when density measurements are not available.

3.4.2 Cross-Shelf Momentum Budget

In the time-mean depth-average cross-shelf momentum budget at the Node, the Coriolis term and wave radiation stress gradient are the dominant terms (Figures 3-3 and 3-4 and Table 3.1). The mean wind stress is small, especially in summer. Although we cannot estimate the mean cross-shelf pressure gradient, it should be comparable in magnitude to the Coriolis term if the cross-shelf balance at the Node is at least partly geostrophic, as in the fluctuating subtidal momentum budget below. At

mooring F, the Coriolis term is the largest estimated term in the time-mean budget and may be in geostrophic balance with the (unknown) mean cross-shelf pressure gradient (Figures 3-5 and 3-6 and Table 3.1). The wave radiation stress gradient and cross-shelf wind stress terms are negligible in the time-mean budget at F due to the larger water depth at F, and the inverse dependence of $S_x^{xx}/\rho_0 h$ and $\tau_s^x/\rho_0 h$ on water depth.

In the fluctuating subtidal budget at the Node, the sizes of the standard deviations of the terms indicate there are four dominant terms: the Coriolis acceleration, wave radiation stress gradient, pressure gradient, and cross-shelf wind stress (Table 3.1). This agrees with an observed momentum budget at 13-m depth on the North Carolina inner shelf (Lentz et al., 1999). The other estimated terms (acceleration of the cross-shelf flow, the nonlinear term involving u^2, the Hasselmann wave stress due to waves propagating in the along-shelf direction, and bottom stress) are one to two orders of magnitude smaller than the dominant terms (Table 3.1). At mooring F, the situation is similar except that wave radiation stress is negligible.

Linear regression and correlation analysis suggests that the cross-shelf momentum balance at the Node is not simply geostrophic, but instead is the superposition of at least two separate balances: coastal setup driven by the cross-shelf wind stress, and geostrophic balance. The Coriolis term and cross-shelf wind stress at the Node are both significantly correlated with the estimated cross-shelf pressure gradient, with regression slopes of order 1 (Tables 3.2 and 3.3; Figure 3-7, left panels; and Figure 3-8, upper left). At F, the along-shelf flow does not appear to be geostrophic; the correlation between the Coriolis and pressure gradient terms is barely significant in summer and low in winter, and the regression slope is $O(10^{-1})$, not O(1) (Tables 3.2 and 3.3 and Figure 3-7, right panels).

Geostrophy is more dominant than wind-driven setup at the Node in winter. The Coriolis term at the Node is more strongly correlated with the cross-shelf pressure gradient in winter than in summer (Figure 3-7, blue symbols in upper panel; and Table 3.2). The winter budget is improved by the addition of cross-shelf wind stress (Figure 3-8, lower left; and Table 3.2) but not further improved by the addition of

the wave radiation stress gradient (Figure 3-8, lower right).

Wind-driven setup is more important than geostrophy at the Node in summer. Even though the subtidal fluctuations in the Coriolis and pressure gradient terms are comparable in size (Table 3.1), those fluctuations are not highly correlated compared to other terms in the budget, and do not balance (Table 3.3). The summer budget closes no better (the correlation with pressure gradient is no higher, and the regression slope is no closer to 1) with cross-shelf wind stress plus the Coriolis term than with cross-shelf wind stress alone (Table 3.3, and compare Figure 3-7, upper left with Figure 3-8, left panels). The slope of the bin-averaged red dots in Figure 3-8, upper left is different from the slope in Table 3.3 because the bin-averaged data weight each pressure gradient bin equally, while the regression in Table 3.3 weights small pressure gradients more heavily because more of the observations occurred at small pressure gradient values. Similarly to winter, the summer budget is not improved by the addition of wave radiation stress gradient (Table 3.3 and Figure 3-8, lower right).

The large size of the wave radiation stress gradient at the Node (Table 3.1) compared to the measured cross-shelf pressure gradient suggests that the cross-shelf momentum balance is really a superposition of three separate balances: geostrophy (pressure gradient balancing Coriolis), wind-driven coastal setup (pressure gradient balancing cross-shelf wind stress), and wave-driven coastal set-down [pressure gradient balancing wave radiation stress due to shoaling waves, (Longuet-Higgins and Stewart, 1964)]. In spite of its large size, however, the wave radiation stress gradient is not significantly correlated with the estimated cross-shelf pressure gradient (Tables 3.2 and 3.3 and Figure 3-8, upper right). This may indicate that the wave radiation stress gradient is an overestimate. We assume no dissipation of wave energy to estimate the wave height at F from the measured wave height at the Node (Section 3.3.5), but substantial dissipation of swell energy (a factor of 4 reduction between shelf break and surfzone) has been observed over the broad North Carolina shelf during strong wave forcing (Herbers et al., 2000). It is possible that substantial dissipation of swell energy occurs between mooring F and the Node, and due to the one-sided finite difference estimate of the pressure gradient. Another possibility is that the cross-shelf

pressure gradient is an underestimate due to the large separation between the bottom pressure sensors at the Node and F compared to the distance from the Node to the surfzone and coast. The pressure gradient due to wave-driven set-down may exist over a smaller cross-shelf scale than is resolved by these observations (Section 3.5.1).

We compare the sizes of the cross-shelf wind stress, wave radiation stress gradient, and Coriolis terms in the budget to each other (Figure 3-9) in addition to the above comparison of those terms to the cross-shelf pressure gradient estimate, which is a much shorter time series. The cross-shelf wind stress term and the Coriolis term are not clearly related except when the along-shelf flow is eastward (Figure 3-9, upper left), but the size of the two terms is nearly the same (as measured by their standard deviations on subtidal time scales; Table 3.1). Therefore, the depth-average cross-shelf momentum budget is not expected to be geostrophic when cross-shelf wind stress forcing is present; instead, the cross-shelf wind stress and cross-shelf pressure gradient and Coriolis acceleration should form a balance (if wave forcing is unimportant), as shown in the preceding paragraphs. The wave radiation stress gradient is also comparable to the Coriolis term, at least when the along-shelf flow is westward (Figure 3-9, upper right). Therefore, according to this estimate of S_x^{xx}, the momentum budget should not be geostrophic when wave forcing is present, because S_x^{xx} is then an important term.

Wave forcing and wind forcing are strongly correlated at this site (Chapter 2 and Figure 3-9, lower left). Negative (onshore) cross-shelf wind stresses, and along-shelf wind stresses of either sign, are associated with substantial wave radiation stress gradients. Therefore, except for wind stress going from land to sea, the wind stress and wave radiation stress terms in the cross-shelf momentum budget tend to be important at the same time. The result is that the sum of those two terms is comparable to the Coriolis term and the cross-shelf momentum budget should generally not be geostrophic at this site (Figure 3-9, lower right).

3.4.3 Along-Shelf Momentum Budget

In contrast to the cross-shelf momentum budget in Section 3.4.2, we do not separate the plots of the along-shelf momentum budget terms into summer and winter times. Nearly all the along-shelf pressure gradient measurements were made in summer (there are 141 days of summer data, versus 12 days of winter data that are really in fall).

Dominant Balance: Wind Stress and Pressure Gradient

In the subtidal fluctuating along-shelf momentum budget (Figures 3-10 through 3-12), there is an approximate balance between the wind stress and pressure gradient. To most accurately compare the wind stress term $\tau_s^y/\rho_0 h$ with the pressure gradient term $(\partial p^b/\partial y)/\rho_0$ in the budget, we use for h the water depth at which the pressure gradient was measured: 19 m in 2001 and 15 m in 2003 (Table 3.4). The along-shelf pressure gradient was significantly correlated with the along-shelf wind stress during both CBLAST 2001 and CBLAST 2003, with a slope near 1 and an intercept near zero. The maximum correlation during 2001 (2003) is for the pressure gradient lagging the wind stress by -2 hr (20 min), but those maximum correlations are not significantly different from the correlations at zero lag in Table 3.4. The along-shelf wind stress and along-shelf pressure gradient are essentially in phase in time. This suggests the along-shelf pressure gradient is a response to local wind forcing, rather than being a remotely generated pressure gradient.

The direction of the component of wind stress most highly correlated with the along-shelf pressure gradient was 11° ($-1°$) clockwise from true east for 2001 (2003). The correlation coefficient and the slope and intercept of the regression of that wind stress component against the along-shelf pressure gradient were not significantly different than the results for the along-shelf component of the wind stress presented in Table 3.4.

Below, we compare the pressure gradient with terms in the along-shelf momentum budget other than the wind stress. Since we do not have measurements of the cross-

shelf variation in along-shelf pressure gradient, we assume that $\partial p^b/\partial y$ is constant in the cross-shelf direction.

Coriolis Acceleration in 27-m Water Depth

At mooring F, the Coriolis term $f\overline{u}$ due to the cross-shelf flow is the largest term in the depth-averaged budget after the pressure gradient; the subtidal fluctuations in $f\overline{u}$ are larger than in the wind stress (Table 3.5). Although $f\overline{u}$ is large compared to the other estimated terms at F, it is not correlated with the along-shelf pressure gradient (Table 3.6) or the acceleration term $\partial\overline{v}/\partial t$ (not shown). The lack of relationship of $f\overline{u}$ with other terms in the budget is not due to an inaccurate estimate of $f\overline{u}$ from uncertainty in the coordinate system; only the mean value of $f\overline{u}$, and not the standard deviation on subtidal time scales, is sensitive to rotating the coordinate system by $\pm 5°$. One possible explanation is that the cross-isobath flow $\overline{u}$ at F is mainly due to a locally three-dimensional flow caused by the nearby topographic variations (Figure 3-1) and is balanced by small-scale pressure gradients that are not resolved by the observations of bottom pressure used here, which are separated by over 10 km. $f\overline{u}$ is slightly correlated with the along-shelf wind stress ($r = 0.25$, $r_{95\%} = 0.14$), consistent with the idea of wind-forced cross-isobath flow due to the narrowing of the isobaths to the east of mooring F (*i.e.*, an eastward wind stress causes offshore flow at F throughout the water column).

Bottom Stress

The along-shelf wind stress and bottom stress are significantly correlated at both the Node and F, but do not balance (Table 3.7). The correlation is stronger in winter than summer, and stronger at the Node than at F. The bottom stress is 20% (10%) of the wind stress at the Node (F) on average (Table 3.7 and Figure 3-13). The bottom stress is less important at F, which is closer to mid-shelf, than at the Node partly due to the deeper water at F and the inverse dependence of $\tau_b^y/\rho_0 h$ on h. $\tau_b^y \sim 0.1 - 0.2\tau_s^y$ is similar to the bottom stress at the Coastal Mixing and Optics experiment site on the mid- to outer shelf south of MVCO, where the bottom stress is $\sim$7 times weaker

than the wind stress (Shearman and Lentz, 2003). It is the pressure gradient and not the bottom stress that primarily balances the wind stress near MVCO.

Balance of $\overline{u}$ and $\overline{u}_{st}$ in 12-m Water Depth

Although the Coriolis acceleration due to the depth-average cross-shelf flow $f\overline{u}$ and the Hasselmann wave stress $f\overline{u}_{st}$ are not dominant terms in the along-shelf momentum budget at the Node, they tend to balance (Appendix E). One explanation is that a balance between $f\overline{u}$ and $-f\overline{u}_{st}$ is consistent with an approximately along-shelf uniform circulation, in which the depth-average cross-shelf flow is constrained by continuity to be zero. The wave-averaged continuity equation is

$$\frac{1}{h}\int_{-h}^{\eta} u\,dz = -\frac{gH_{sig}^2}{16ch} \tag{3.29}$$

where η is the wave-averaged sea level elevation. The left-hand side of Eq. (3.29) is just the depth-average velocity $\overline{u}$, and $gH_{sig}^2/16ch = \overline{u}_{st}$. Therefore, $\overline{u} = -\overline{u}_{st}$ is required by continuity for along-shelf uniform flow with constant wave forcing. If the flow field is approximately uniform in the along-shelf direction, the terms $f\overline{u}$ and $f\overline{u}_{st}$ will tend to balance and will have the important role of completely determining the value of the depth-average cross-shelf flow $\overline{u}$, even though the terms themselves do not dominate the momentum budget. At the Node, the Coriolis term $f\overline{u}$ is determined by the wave forcing, consistent with approximately along-shelf uniform flow (Appendix E).

In contrast to the Node, at F the variability in $f\overline{u}$ is 6 times as large as in $f\overline{u}_{st}$ and the two terms are not significantly correlated. This imbalance suggests the flow near F is less uniform in the along-shelf direction than at the Node, consistent with the substantial synoptic variations in along-shelf advective heat flux divergence inferred from observations near F (Chapter 4). Another indication that the Node and mooring F are in dynamically different regions of the shelf is that the along-shelf depth-average flows $\overline{v}$ at the Node and F are barely significantly correlated during SWWIM I ($r = 0.27, r_{95\%} = 0.25$) and not highly correlated during CBLAST 2003 ($r = 0.58, r_{95\%} = 0.20$).

Other Terms

The remaining terms in the along-shelf momentum budget are not all negligible. At the Node, the acceleration and estimated nonlinear advection are about one-half to one-third the size of the pressure gradient and are comparable to the bottom stress (Table 3.5). At F, the acceleration term is comparable in size to the wind stress (Table 3.5), although the acceleration is not significantly correlated with the measured pressure gradient (Table 3.6). Including the bottom stress, acceleration, or all other estimated terms in addition to the wind stress does not make the along-shelf momentum budget close significantly better at the Node or at F than with wind stress and pressure gradient alone (Table 3.6 and Figures 3-14 and 3-15). The correlation with the pressure gradient becomes worse as more terms are added, the regression slope does not get closer to 1, and the intercept moves away from zero. One possible explanation is that the acceleration and nonlinear advection terms in the along-shelf momentum budget are associated with smaller-scale pressure gradients (*i.e.*, sea level variations with spatial scales of a few kilometers or less) than the pressure gradients resolved by these observations, which have scales of 10 km or more.

3.5 Discussion

3.5.1 Horizontal Scales of the Pressure Gradient

If the distances over which dynamically important sea level variations take place are small compared to the distance between the pressure sensors used here (10–15 km), our pressure gradient estimates may be too small. The cross-shelf pressure gradient and sea-level displacement has a varying cross-shelf scale, depending on whether the pressure gradient is due to geostrophic balance, coastal set-up/set-down driven by the cross-shelf wind, or coastal set-down driven by the wave radiation stress gradient (Figures 3-16 through 3-18). If the cross-shelf momentum balance is exactly geostrophic,

$$-f\overline{v} = -\frac{1}{\rho_0}\frac{\partial p^b}{\partial x} \tag{3.30}$$

then the pressure gradient is

$$\frac{\partial p^b}{\partial x} = \rho_0 f \overline{v} \tag{3.31}$$

If we use the hydrostatic relation to write the sea-level gradient $\partial\eta/\partial x$ in terms of the pressure gradient as

$$\frac{\partial \eta}{\partial x} = \frac{1}{\rho_0 g}\frac{\partial p^b}{\partial x} \tag{3.32}$$

then the sea-level gradient due to a geostrophic balance is

$$\frac{\partial \eta}{\partial x} = \frac{f}{g}\overline{v} \tag{3.33}$$

Integrating the above equation with respect to x gives the sea-level displacement relative to its value at (say) the 8-m isobath as

$$\eta(x) - \eta|_{h=8\text{ m}} = \frac{f}{g}\int_{x|_{h=8\text{ m}}}^{x} \overline{v}\, dx' \tag{3.34}$$

To estimate the cross-shelf pressure gradient and sea-level displacement for an exactly geostrophic balance over the MVCO bathymetry (Figure 3-16, top), we use for $\overline{v}$ the observed time-mean along-shelf flow in the Middle Atlantic Bight from Lentz (2007a): the flow increases linearly with water depth (Figure 3-16, middle) as

$$\overline{v} = \left(-0.065\text{ cm s}^{-1}\text{ m}^{-1}\right) h(x) - 2.1\text{ cm s}^{-1} \tag{3.35}$$

The cross-shelf pressure gradient due to geostrophic balance of the above velocity is negative (Figure 3-16, bottom) and the associated sea-level displacement, relative to the sea level at the 8-m isobath, is ~ -0.02 mm at the Node and ~ -0.4 mm at mooring F (Figure 3-19, top).

If the cross-shelf momentum budget is exactly a coastal set-up/set-down balance between the cross-shelf pressure gradient and cross-shelf wind stress,

$$\frac{\tau_s^x}{\rho_0 h} = \frac{1}{\rho_0}\frac{\partial p^b}{\partial x} \tag{3.36}$$

then the pressure gradient is

$$\frac{\partial p^b}{\partial x} = \frac{\tau_s^x}{h} \tag{3.37}$$

Again using the hydrostatic relation, the sea-level gradient is

$$\frac{\partial \eta}{\partial x} = \frac{\tau_s^x}{\rho_0 g h} \tag{3.38}$$

and the sea-level displacement relative to its value at the 8-m isobath is

$$\eta(x) - \eta|_{h=8\text{ m}} = \frac{\tau_s^x}{\rho_0 g} \int_{x|_{h=8\text{ m}}}^{x} \frac{1}{h}\, dx' \tag{3.39}$$

To estimate $\partial p^b/\partial x$ and $\partial \eta/\partial x$ for this balance, we use $\tau_s^x = 0.05$ N m^{-2} and the MVCO bathymetry $h(x)$. The cross-shelf pressure gradient due to this moderate offshore wind forcing is positive and larger near the coast due to the dependence of the pressure gradient on $1/h$ (Figure 3-17). The sea-level displacement, relative to sea level at the 8-m isobath, is ~ 0.03 mm at the Node and ~ 0.3 mm at mooring F (Figure 3-19, middle).

If the cross-shelf momentum budget is exactly a coastal set-down balance due to the cross-shelf wave radiation stress gradient from shoaling waves,

$$\frac{1}{\rho_0 h}\frac{\partial S^{xx}}{\partial x} = -\frac{1}{\rho_0}\frac{\partial p^b}{\partial x} \tag{3.40}$$

then the pressure gradient is

$$\frac{\partial p^b}{\partial x} = -\frac{1}{h}\frac{\partial S^{xx}}{\partial x} \tag{3.41}$$

The sea-level gradient is

$$\frac{\partial \eta}{\partial x} = -\frac{1}{\rho_0 g h}\frac{\partial S^{xx}}{\partial x} \tag{3.42}$$

and the sea-level displacement relative to its value at the 8-m isobath is

$$\eta(x) - \eta|_{h=8\text{ m}} = -\frac{1}{\rho_0 g} \int_{x|_{h=8\text{ m}}}^{x} \frac{1}{h}\frac{\partial S^{xx}}{\partial x}\, dx' \tag{3.43}$$

To estimate $\partial p^b/\partial x$ and $\partial \eta/\partial x$ for this balance, we use linear wave theory for a wave

propagating directly onshore over the MVCO bathymetry (Figure 3-17, top) with $H_{sig} = 2$ m at the 12-m isobath and a wave period of 6 s, assuming no dissipation of wave energy. The significant wave height decreases as the waves propagate from mooring F to the Node due to the shoaling bottom; the wave height only begins to increase again very close to the surfzone, onshore of the Node (Figure 3-18, top). We do not estimate H_{sig} or S^{xx} onshore of the outer edge of the surfzone, defined here as $H_{sig}/h = 1/3$ from Thornton and Guza (1983), following Lentz et al. (1999). The wave radiation stress is nearly constant in the cross-shelf direction near mooring F; the cross-shelf gradient of wave radiation stress for the MVCO bathymetry is negligible at mooring F compared to near the Node, and the stress divergence increases rapidly toward the coast onshore of the Node (Figure 3-18, middle). The cross-shelf pressure gradient due to this wave forcing is positive and much larger near the coast than at mooring F (Figure 3-18, bottom), similarly to the pressure gradient from cross-shelf wind forcing, due to the inverse dependence of both the pressure gradient and the wave radiation stress gradient on h. The associated sea-level displacement, relative to sea level at the 8-m isobath, is ~ 0.4 mm at the Node and ~ 0.7 mm at mooring F (Figure 3-19, bottom).

The sea-level displacement due to geostrophic balance or cross-shelf wind forcing increases (in magnitude) approximately linearly with distance from the coast, assuming $\overline{v}$ has the form in Eq. (3.35) (Figure 3-19, top and middle). In contrast, the sea-level displacement due to wave forcing increases rapidly near the Node but is nearly constant near mooring F (Figure 3-19, bottom). As a result, the sea-level gradient (or pressure gradient) estimated from the sea-level difference (or bottom pressure difference) between the Node and mooring F may be a good proxy for the sea-level gradient at the Node and at F when the Coriolis term due to along-shelf flow or the cross-shelf wind stress is the dominant forcing, but not when wave forcing is dominant. The sea-level gradient that would be estimated from the sea-level difference between the Node and F is the slope of the thin line in each panel of Figure 3-19, and the true sea-level gradient near the Node is the slope of the dashed line. The ratio of the true gradient to the estimated gradient is 0.8, 1.7, and 6.2 for the

geostrophic, wind, and wave balances, respectively. The pressure gradients discussed in Section 3.4 could therefore be underestimated by a factor of $\sim 5-10$ during wave forcing. This may be the reason for the lack of correlation of the estimated cross-shelf pressure gradient and wave radiation stress gradient, in spite of the apparently large wave radiation stress gradient.

3.5.2 Cross-Shelf Flow, Wind Stress, and Bottom Stress

The cross-shelf wind stress and bottom stress are strongly negatively correlated, but far from the same magnitude (Figure 3-20). The inverse relation between surface and bottom stress is consistent with the two-layer cross-shelf flow structure driven by cross-shelf wind forcing that has been observed at the Node (Chapter 2). When the wind is directed offshore, the near-surface flow is offshore and there is an onshore return flow near the bottom, leading to a (small bottom stress directed onshore, opposite to the wind stress. That bottom stress is only 4% of the wind stress on average.

3.5.3 Along-Shelf Flow and Wind Stress

The along-shelf depth-average flow is strongly correlated with the along-shelf wind stress on subtidal time scales (Figure 3-21), similarly to mid-shelf locations in the Middle Atlantic Bight (*e.g.*, Shearman and Lentz, 2003). The influence of the high correlation between $\overline{v}$ and τ_s^y provides an explanation for the relation between $S_x^{xx}/\rho_0 h$ and $f\overline{v}$ (Figure 3-9 and Section 3.4.2). Because $\overline{v} \sim \tau_s^y$ (Figure 3-21), the relation between S_x^{xx} and $\overline{v}$ (Figure 3-9, upper right) has the same shape as the relation between S_x^{xx} and τ_s^y (Figure 3-9, lower left).

The main along-shelf balance at the Node is between the along-shelf wind stress and along-shelf pressure gradient, with some contribution from bottom stress (Section 3.4.3). The wind stress and pressure gradient are not exactly in balance at all times, and the difference between those terms could act as forcing for the along-shelf flow, which might accelerate until the bottom stress became large enough to balance

the wind stress and pressure gradient. To test whether the time-varying imbalance between the wind stress and pressure gradient can explain the strong relation between $\overline{v}$ and τ_s^x, we use the approach of Lentz et al. (1999). If the bottom stress is related to the along-shelf velocity by a linear drag law of the form $\tau_b^y = \rho_0 r_b \overline{v}$, where r_b is the bottom drag coefficient, the along-shelf momentum equation can be written

$$\frac{\partial \overline{v}}{\partial t} + \frac{r_b \overline{v}}{h} = -\frac{1}{\rho_0}\frac{\partial p^b}{\partial y} + \frac{\tau_s^y}{\rho_0 h} \tag{3.44}$$

using only the acceleration term and the terms that are dominant near the MVCO Node. The left-hand terms in Eq. (3.44) are the "response" to the right-hand "forcing" terms. A linear drag law fits the MVCO subtidal data reasonably well (Figure 3-22), with a best-fit drag coefficient $r_b = (3.16 \pm 0.06) \times 10^{-4}$ m s^{-1}, close to the value of 2.5×10^{-4} m s^{-1} found by Lentz (2007a) for the Middle Atlantic Bight as a whole. The predicted along-shelf velocity $\overline{v}_p$ can be calculated as a function of the time-varying wind stress and pressure gradient forcing by integrating Eq. (3.44) in time to give (Lentz and Winant, 1986)

$$\overline{v}_p = \int_{t_0}^{t} \left(-\frac{1}{\rho_0}\frac{\partial p^b}{\partial y} + \frac{\tau_s^y}{\rho_0 h} \right) e^{-(t-t')/T_f}\, dt' + \overline{v}|_{t=t_0}\, e^{-(t-t_0)/T_f} \tag{3.45}$$

where $T_f \equiv (h/r_b)$ is the time scale over which bottom friction becomes important. At the Node ($h = 12$ m), $T_f = 10.5$ hr. The response on longer time scales, such as the subtidal time scales considered here (time scales > 33 hr), should be strongly affected by bottom friction (Lentz et al., 1999).

The along-shelf velocity predicted by Eq. 3.45 (Figure 3-23) is significantly correlated with the observed $\overline{v}$ during CBLAST 2003 at the 95% confidence level only if v_p is high-pass filtered with a 5–10 day cutoff. Low-frequency drifts due to settling of the pressure sensors into the bottom that were not perfectly removed from the pressure measurements may be adding low-frequency "noise" to v_p, or the model in Eqs. (3.44) and (3.45) may not be correct for the Node. During CBLAST 2001, v_p and v are not significantly correlated at the 95% confidence level and the time series is too short to remove a 10-day low-frequency signal from v_p.

Although v is not well-represented by v_p, v_p is strongly related to the along-shelf wind stress (Figure 3-24). A momentum balance of the form Eq. (3.44) does produce an along-shelf flow that is highly correlated with the along-shelf wind, for the forcing magnitudes and frictional time scale observed at the Node. If the difference between v_p and v on long (>5 days) time scales is only due to inaccurate pressure gradient estimates, then a balance between acceleration, bottom stress, wind stress, and pressure gradient is a plausible explanation for the strong relation between v and τ_s^x observed at the Node.

3.5.4 Thermal Wind Shear in Along-Shelf Flow

During summer and fall 2003, the vertical shear in the along-shelf subtidal flow at both the Node and mooring F was of the right magnitude and sign to be in thermal wind balance with the cross-shelf density gradient (Figure 3-25). The regression slope of $\partial v/\partial z$ against $-g(\partial\rho/\partial x)/\rho_0 f$ is order 1 at all depths for which the slope can be calculated, and the intercept is less than 1 cm s^{-1} m^{-1} in magnitude, although the correlation is only significant at the 95% confidence level at some depths, and barely significant at any depth at the Node. The density observations during CBLAST 2003 were 0.7, 2.4, 4.8, 7.2, and 9.6 m below the water surface at the Node, and 1, 6, 8, 9, 11.5, 12.5, 16, 19, and 22 m below the water surface at F, so the cross-shelf density gradient can be calculated in the upper 9.6 m of the water column. The regression slope tends to be larger than 1 ($\sim$1.5–3) in the upper 6–8 m of the water column, indicating that processes other than thermal wind balance (for instance, wind forcing) may be important for producing vertical shear in the along-shelf flow (or that the cross-shelf density gradient is an underestimate, which is possible due to the relatively large separation between the Node and F compared with the distance between the Node and the coast).

3.5.5 Vertical Shear in Cross-Shelf Flow

Surface gravity wave forcing is associated with vertical shear in the cross-shelf flow at the Node, because the Stokes' drift velocity u_{st} is vertically sheared and there is a tendency for $u = -u_{st}$ to hold at each depth in winter (Appendix E). Cross-shelf wind forcing also produces a vertically-sheared cross-shelf flow at this site (Chapter 2). During times when the wind stress is weak in both summer and winter, however, $u(z)$ is more sheared than $-u_{st}$ (Figure 3-26). This "extra" shear increases with wave forcing more strongly in summer than winter, suggesting that thermal stratification, which is stronger in summer than winter, may play a role (Figure 3-26, lower right panel).

Thermal wind shear is a possible explanation for the "extra" near-surface shear in the cross-shelf velocity at the Node in summer. The near-surface along-shelf density gradient is of the right sign (density increasing toward the east) and order of magnitude [$\Delta\rho \sim$ O(0.1 kg m^{-3}) over 10 km] to produce a thermal wind shear similar to the observed "extra" vertical shear in the cross-shelf flow, but the correlation between $\partial(u+u_{st})/\partial z$ and the near-surface estimate of $g(\partial\rho/\partial y)/\rho_0 f$ during weak wind stress forcing is not significant at the 95% confidence level at any depth. Measurements of the along-shelf density gradient during summer 2003 are only available near the surface, however, and may not accurately represent the near-bottom density gradient. There is a close relation between the near-surface along-shelf temperature and density gradients during summer 2003, and the near-bottom along-shelf temperature and density gradients during summer 2001 (Figure 3-27). With the near-bottom along-shelf temperature gradient as a proxy for the near-bottom along-shelf density gradient, we can test for thermal wind balance between $\partial(u + u_{st})/\partial z$ and the near-bottom estimate of $g(\partial\rho/\partial y)/\rho_0 f$ during summer 2003. The correlation is again not significant at any depth, although the regression slopes are order 1 (but not significantly different from zero at the 95% confidence level). Nevertheless, the two terms are of the same order. The available data do not rule out thermal wind shear as the source of the "extra" near-surface shear, but do not clearly support thermal wind shear either. It

is not clear whether this is only due to the short time series and the need to consider only times of weak wind stress forcing, or whether thermal wind shear is actually not the source of the extra shear. In addition, the along-shelf density gradient is significantly correlated with along-shelf wind stress, but not cross-shelf wind stress or surface gravity wave forcing (Figure 3-29).

3.5.6 Estimates of Uncertainties

In the regression analyses reported in Sections 3.4 and 3.5, the independent and dependent variables both have associated errors. We use a nonlinear least-squares regression technique that incorporates the error estimates described below (Reed, 1992).

Temperature, Conductivity, and Density

A constant offset of 1.13 S m^{-1} was removed from the conductivity time series from the western sensor in CBLAST 2001. For CBLAST 2003, conductivity offsets of -0.239 and -0.067 S m^{-1} were removed from the time series at 7.5-m depth on T2 and 1-m depth on T1, respectively; a linear correction $[3.28(yd - 226.3776) - 6] \times 10^{-4}$ S m^{-1} was added to the conductivity at 9.6-m depth at the Node, where yd (yearday) is time in days since the beginning of January 1, 2003; and an offset of 0.09 °C was added to the TidBiT temperature at 3-m depth on the second deployment of mooring F. No substantial temperature or conductivity offsets or drifts were evident in the SWWIM I MicroCAT data or Seagauge temperature data; TidBiT temperature and drift corrections during SWWIM I are described in Appendix B. Following Lentz et al. (1999), we estimate the uncertainty in the density measurements to be $\delta\rho = 0.1$ kg m^{-3}. The uncertainties in the cross-shelf density gradient term $-(g/\rho_0 f)(\partial\rho/\partial x)$ at a particular depth is $2(g/\rho_0 f)(\delta\rho/\Delta x)$, where Δx is the cross-shelf distance used in the finite difference approximation to the gradient, $\partial\rho/\partial x \approx \Delta\rho/\Delta x$, and similarly for the along-shelf gradient over a distance Δy.

Pressure Gradients

The relative amplitudes of the best-fit M_2 tidal variations in bottom pressure at the Node, T1, T2, and F indicate that the gain of the pressure sensor at the Node was likely off by 2%. Therefore, we multiplied the observed bottom pressure at the Node by 0.98 for this study. Using a factor of 0.98 or 1.00 does not qualitatively change the results presented here.

The estimates that are possible with these observations do not resolve pressure gradients with scales smaller than the separation of the pressure sensors (10–15 km). Only a single finite difference estimate of the pressure gradient is available in each case (the cross-shelf pressure gradient between T2 and F during CBLAST 2003 or between the Node and F during SWWIM I, and the along-shelf pressure gradient between T1 and T2 during CBLAST 2003 or between a pair of sensors on the 19-m isobath during CBLAST 2001); we do not have information about how the pressure gradients vary in the cross- or along-shelf direction. The pressure gradient estimates used here represent the spatially-averaged pressure gradient between the two sensors in each case, which is only an accurate estimate of the pressure gradient at each sensor if the true pressure gradient is constant in space on 10–15 km scales. It is also possible that, due to along-shelf variations in topography, the estimated "along-shelf" or "cross-shelf" pressure gradient in reality contains a part of the other component of the pressure gradient. The wind direction most highly correlated with the along-shelf pressure gradient is within 10° of the direction between the pressure gradient sensors in both 2001 and 2003 (Section 3.4.3 and Figure 3-1), however, suggesting that it is unlikely this effect dominates the pressure gradient estimates. Following Lentz et al. (1999), we estimate the uncertainty in the bottom pressure gradient terms estimated from Seagauge pairs as $(\delta p^b/\Delta x)/\rho_0$ with $\delta p^b = 20$ N m^{-2}, where Δx is the distance between the Seagauges (really Δy for the along-shelf gradients). This does not include pressure gradient uncertainty due to the difficulty of correctly removing drifts in the pressure time series due to settling of the sensors into the seafloor; improperly removed trends may be contributing some of the lower-frequency variations in the pressure

gradients and the momentum budget residuals in the bottom panels of Figures 3-3, 3-4, and 3-10 through 3-12.

Wind Stress

Following Lentz et al. (1999), we estimate the uncertainty in the wind stress magnitude as the root-mean-square difference between the wind stress magnitude in the adjusted MVCO shore mast time series and in the ASIT time series (Appendix A). The result is $\delta\tau_s = 0.03$ N m^{-2}, the same as Lentz et al. (1999) found between wind stress time series at locations 5 km apart off North Carolina. The uncertainty in the wind stress term in each momentum budget equation is $\delta\tau_s/(\rho_0 h)$. This uncertainty does not include possible errors in the bulk formula used to calculate the wind stress, although the Fairall et al. (2003) formula gives similar results (not shown). Spatial variations in the wind stress are substantial in the MVCO region (Appendix A), and have been at least partly compensated in the adjusted wind stress time series used here.

Velocity, Vertical Shear, Acceleration, Bottom Stress, Coriolis, and Nonlinear Terms

We estimate the uncertainty in the ADCP velocities as $\delta u = 0.01$ m s^{-1}, which does not include errors in the velocity components due to uncertainty in the coordinate system. The uncertainty in finite difference estimates of vertical shear is $2\delta u/\Delta z$, where Δz is the vertical distance between the two ADCP bins used in the finite difference. Following Lentz et al. (1999), the uncertainty in the subtidal-filtered acceleration terms is $\delta u/\Delta t$, where Δt is estimated as 1/4 the cutoff period of the filter, or ($33/4 \approx 8.25$) hr. The uncertainty in the bottom stress term in each momentum equation is $2C_d u\delta u/h$, in each Coriolis acceleration is $f\delta u$, and in the nonlinear terms is $2u\delta u/L$ and $(u+v)\delta u/L$ for the cross- and along-shelf momentum equations, respectively, where L is the distance from that mooring to shore.

Wave Radiation Stress Gradient

The estimated wave radiation stress gradient is very uncertain because the wave properties were measured at only one location (on the 12-m isobath). There is no observational information about the amount of wave energy that is dissipated as waves propagate through this study area. Lentz et al. (1999) suggest that a 50% uncertainty in wave radiation stress gradient is probably reasonable for their estimate during non-breaking waves off North Carolina. Assuming that is a reasonable estimate to use at MVCO, we calculate the uncertainty in the wave radiation stress term as $\delta(\partial S^{xx}/\partial x)/(\rho_0 h) = 0.5\sigma_{S_x^{xx}}/(\rho_0 h)$, where $\sigma_{S_x^{xx}}$ is the standard deviation of the wave radiation stress gradient S_x^{xx}.

3.6 Summary and Conclusions

The subtidal, depth-average cross-shelf momentum budget at MVCO is not geostrophic, as would be expected at mid-shelf. Instead, the inner shelf is a region where multiple dynamical balances are (sometimes simultaneously) important. In winter, the Coriolis term and cross-shelf pressure gradient at the 12-m isobath are substantial, significantly correlated, and tend to balance, as in a pure geostrophic balance at mid-shelf. At other times, particularly in summer, the cross-shelf wind stress and cross-shelf pressure gradient are positively correlated, consistent with coastal set-up and set-down driven by the cross-shelf wind stress. The estimated momentum flux divergence due to shoaling surface gravity waves (the wave radiation stress gradient) is also a leading-order term in the budget, but is not correlated with the cross-shelf pressure gradient, in contrast to what is expected for set-down due to shoaling waves outside the surf zone. It is likely that the pressure gradient due to wave-driven set-down occurs over a spatial scale too small to resolve with these observations. The wave radiation stress gradient and cross-shelf wind stress are important at the same time for onshore winds, and both will contribute to making the cross-shelf momentum balance ageostrophic. The other estimated terms in the cross-shelf momentum budget are at least an order of magnitude weaker than the dominant terms. For example,

the bottom stress in the cross-shelf direction, although highly negatively correlated with the wind stress due to the two-layer nature of the cross-shelf flow (Chapter 2), is only 4% of the wind stress.

The along-shelf momentum budget is more complex than the cross-shelf. No estimated term is negligible. The dominant terms are wind stress and pressure gradient. The bottom stress, acceleration, Coriolis, Hasselmann wave stress, and nonlinear advection terms, although of secondary importance, are about half as large as the pressure gradient. This is in contrast to the cross-shelf budget, in which the secondary terms are an order of magnitude smaller than the three or four dominant terms. The along-shelf wind stress and along-shelf bottom stress are strongly correlated at the 12-m isobath, but the bottom stress is 20% of the wind stress so they do not balance. Instead, the main balance is between the along-shelf wind stress and along-shelf pressure gradient. The along-shelf pressure gradient is consistent with a local sea level response to wind forcing, rather than being dominated by a remotely generated pressure gradient. Adding the bottom stress, acceleration, or all other estimated terms to the wind stress does not substantially improve the comparison with the pressure gradient, which may indicate that some of the secondary terms are poorly resolved. The along-shelf pressure gradient at the 27-m site seems to be composed of the large-scale (>10 km) pressure gradient associated with along-shelf wind stress and resolved by these observations, and a smaller-scale pressure gradient balanced by the Coriolis term due to the cross-shelf depth-average flow, and likely due to the narrowing of the isobaths to the east.

There is a strong relation between the along-shelf depth-average flow and the along-shelf wind stress. This may be due to along-shelf accelerations caused by the time-varying imbalance between wind stress and along-shelf pressure gradient, combined with a bottom stress that is approximately linearly related to the along-shelf subtidal flow.

In the upper water column, the vertical shear in the along-shelf flow is suggestive of thermal wind shear due to the cross-shelf density gradient. Nevertheless, the uncertainty in the cross-shelf density gradient is large, the time series of density

gradient is short, and it is possible that other influences on the vertical shear (*e.g.*, surface stress and bottom stress) are also important. Thermal wind shear due to the along-shelf density gradient is not ruled out as a source of vertical shear in the cross-shelf flow, which is greater than the shear expected due to the Hasselmann wave stress forcing, but the data are not conclusive.

The measurements of along-shelf density gradient available for this study were mainly collected during summer, when the wind forcing and wave forcing are relatively weak. Measurements of the along-shelf density gradient during strong winter forcing would likely help to determine which secondary terms in the along-shelf momentum budget are the most important. Sea-level displacements over horizontal scales too small to resolve with these observations seem to be leading to dynamically important pressure gradients in both the along-shelf and cross-shelf directions. The wave radiation stress gradient and the amount of wave dissipation over the inner shelf are also very uncertain, and could be estimated more accurately by recording the directional wave spectrum at several sites in a cross-shelf transect. It will be important in future studies to measure pressure gradients and spatial variations in wave characteristics on smaller scales than in this study.

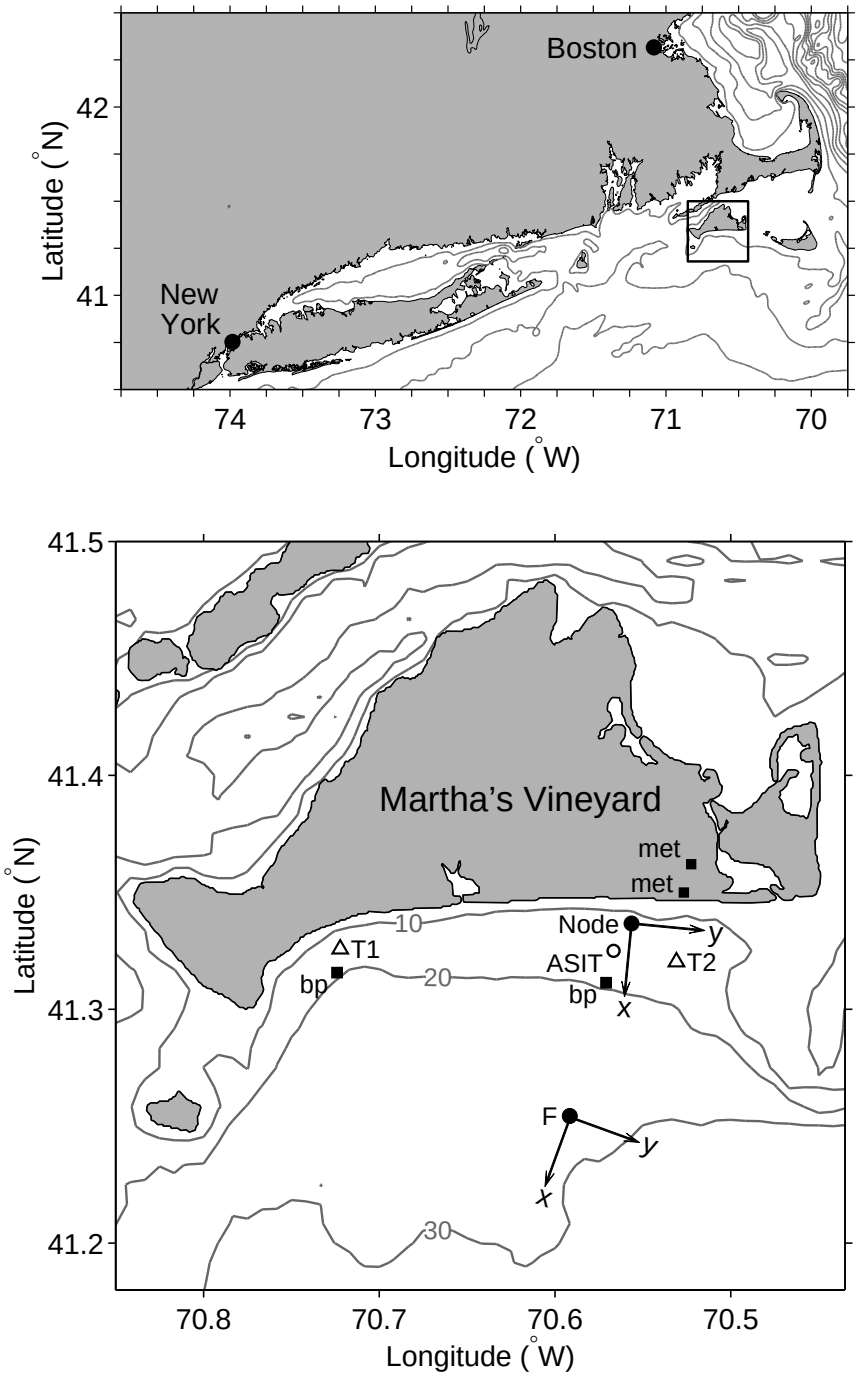

Figure 3-1: Top: location of detailed map (square outline), with isobaths in increments of 20 m (*i.e.*, the 20-m, 40-m, 60-m... isobaths). Bottom: detailed map of study area. Isobaths are labeled in meters. Solid circles: moorings Node and F, from CBLAST 2003 and SWWIM I. Triangles: moorings T1 and T2, deployed during CBLAST 2003 only. Open circle: MVCO air-sea interaction tower (ASIT). Squares on land: MVCO meteorological masts. Squares near 20-m isobath: bottom pressure measurements in 2001.

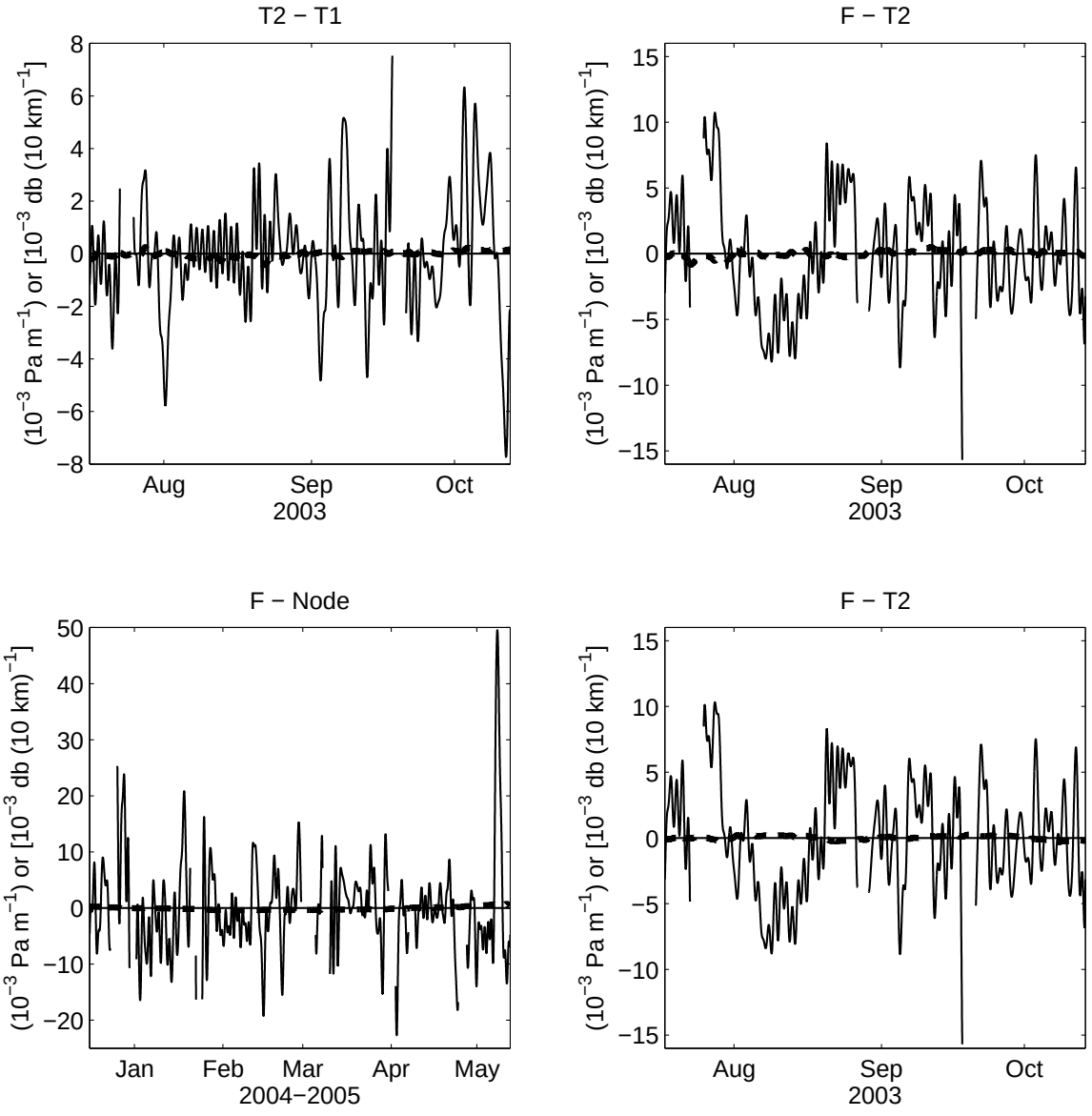

Figure 3-2: Upper panels, and lower left: comparison of the bottom pressure gradient $\partial p^b/\partial x$ (thin line) to the density gradient term $(1/h)\,\partial/\partial x\left(\int_{-h}^{0} g\rho z\,dz\right)$ (thick dashed) in the horizontal pressure gradients between moorings T1 and T2 and between moorings T2 and F during CBLAST 2003, and between Node and F during SWWIM I. Lower right: comparison of barotropic (thin) and baroclinic (thick dashed) cross-shelf pressure gradients during CBLAST 2003. Note different vertical axis scales.

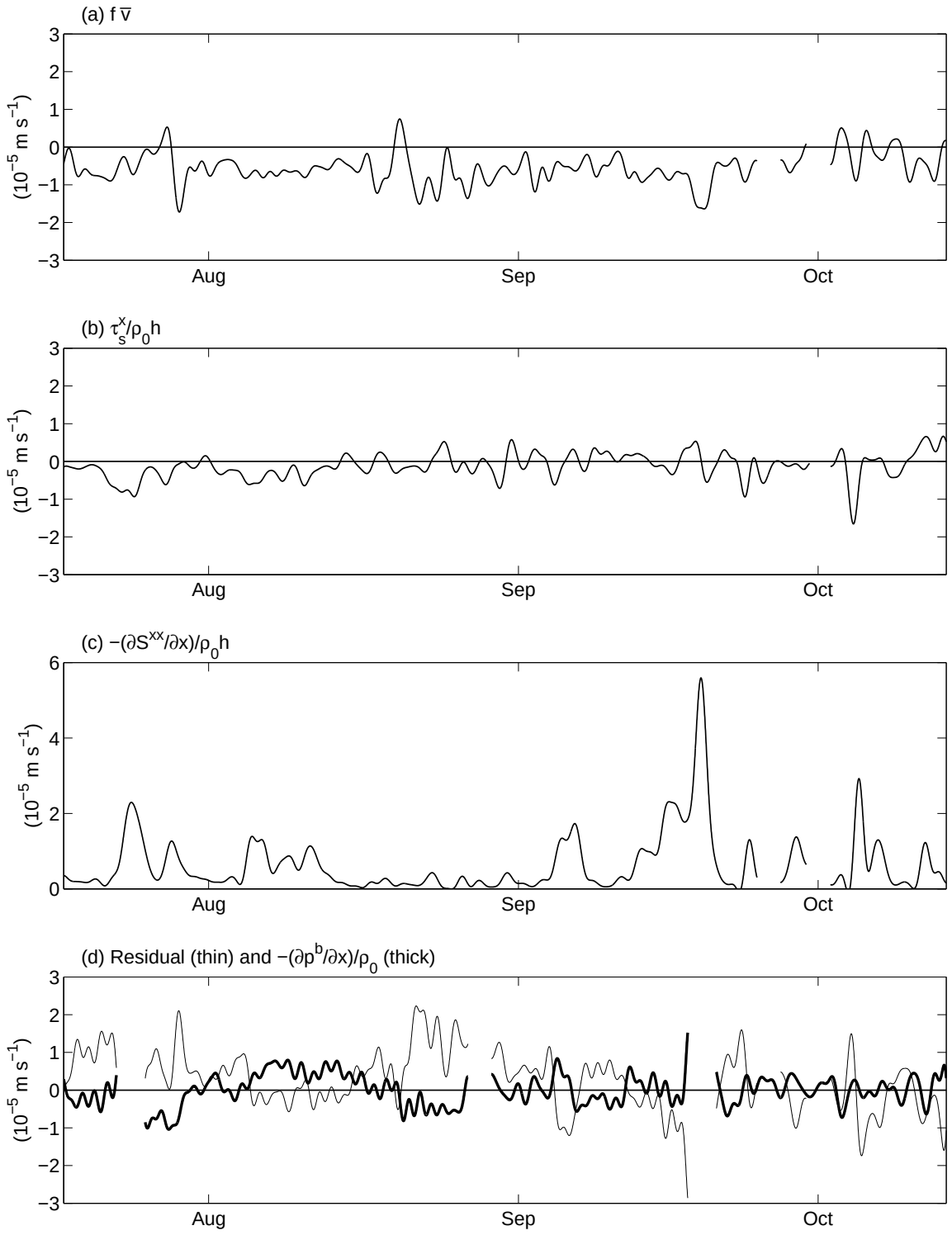

Figure 3-3: Dominant terms in subtidal cross-shelf momentum budget at the MVCO Node in 12-m water depth, summer 2003.

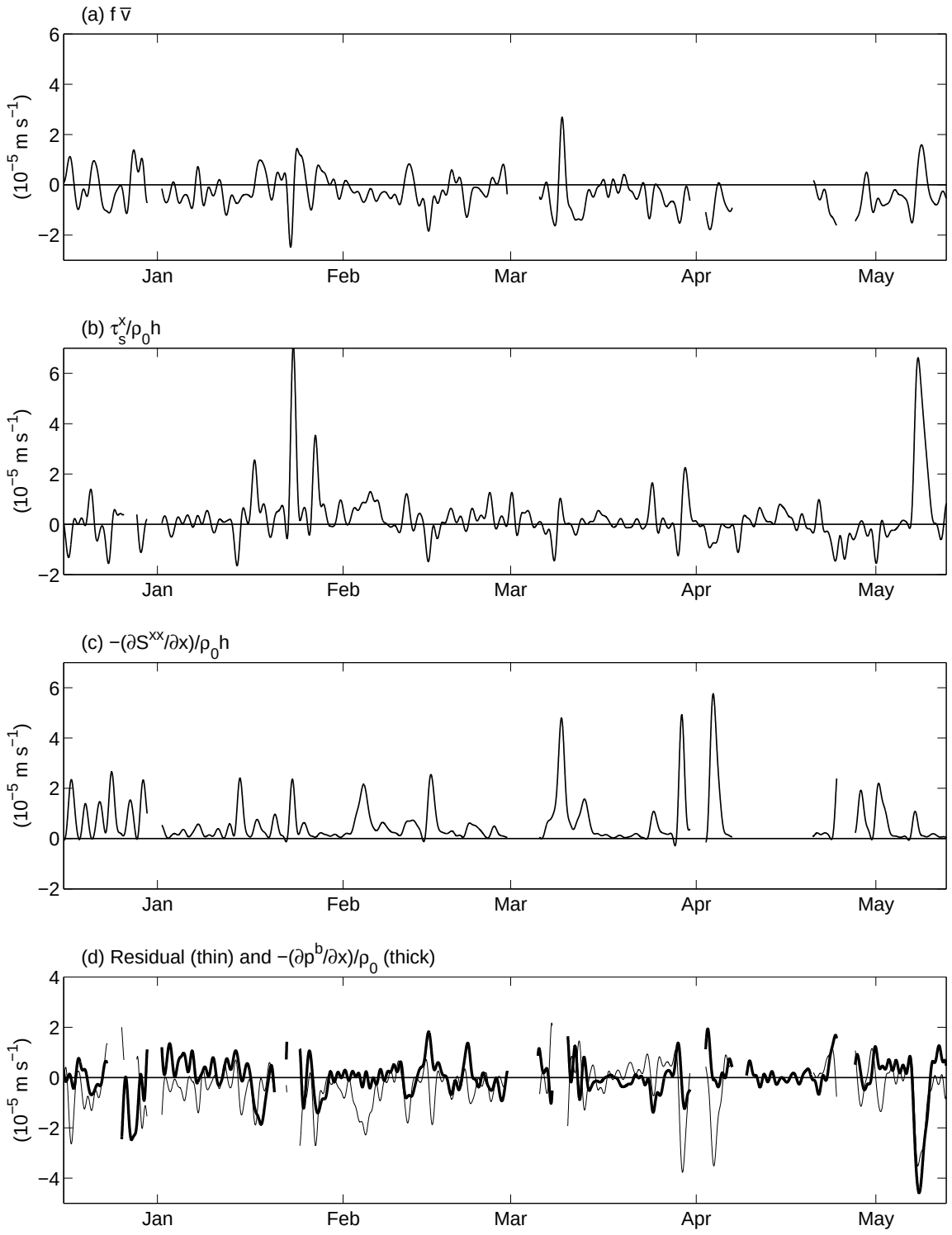

Figure 3-4: Dominant terms in subtidal cross-shelf momentum budget at the MVCO Node in 12-m water depth, winter and spring 2004–2005.

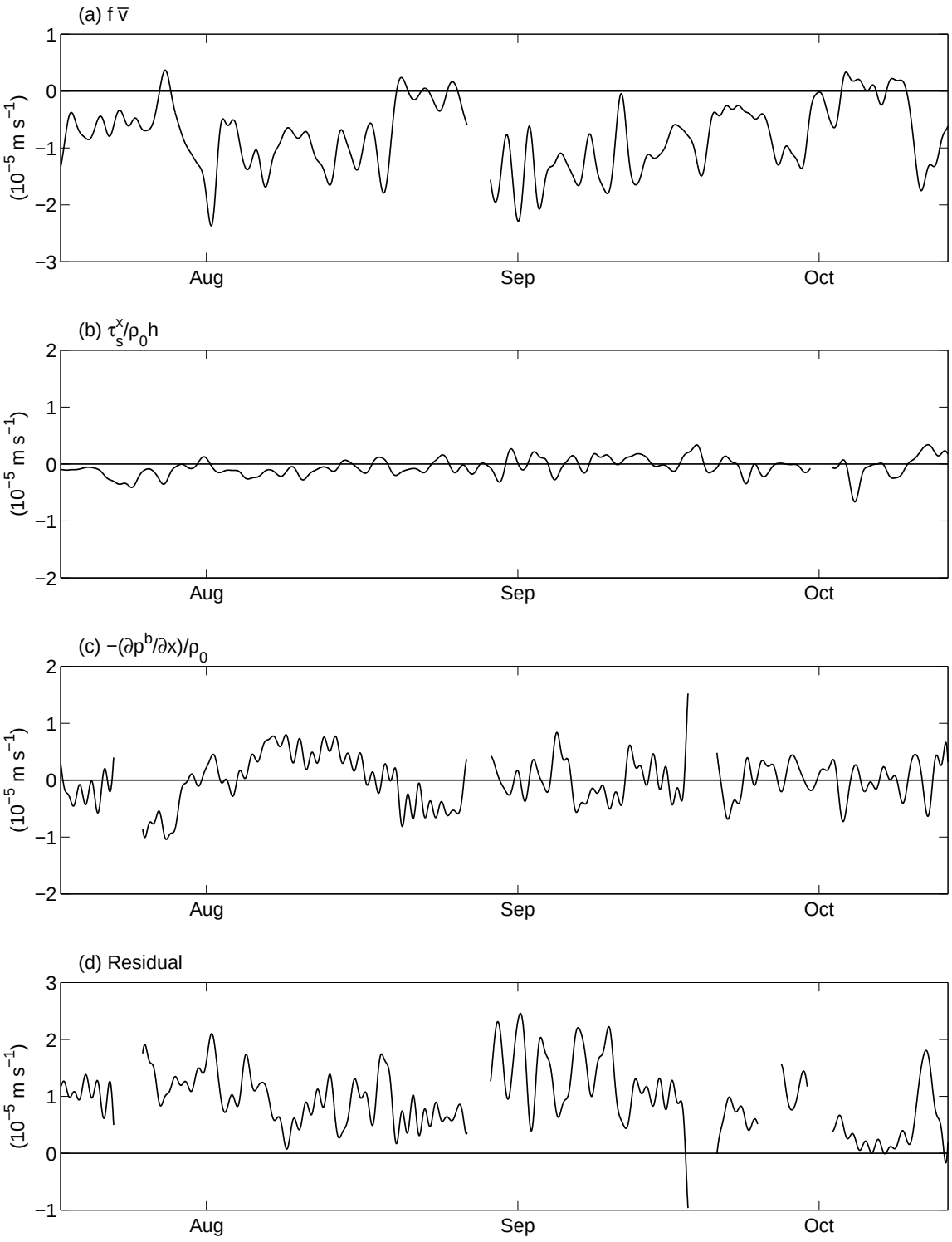

Figure 3-5: Dominant terms in subtidal cross-shelf momentum budget at mooring F in 27-m water depth, summer 2003.

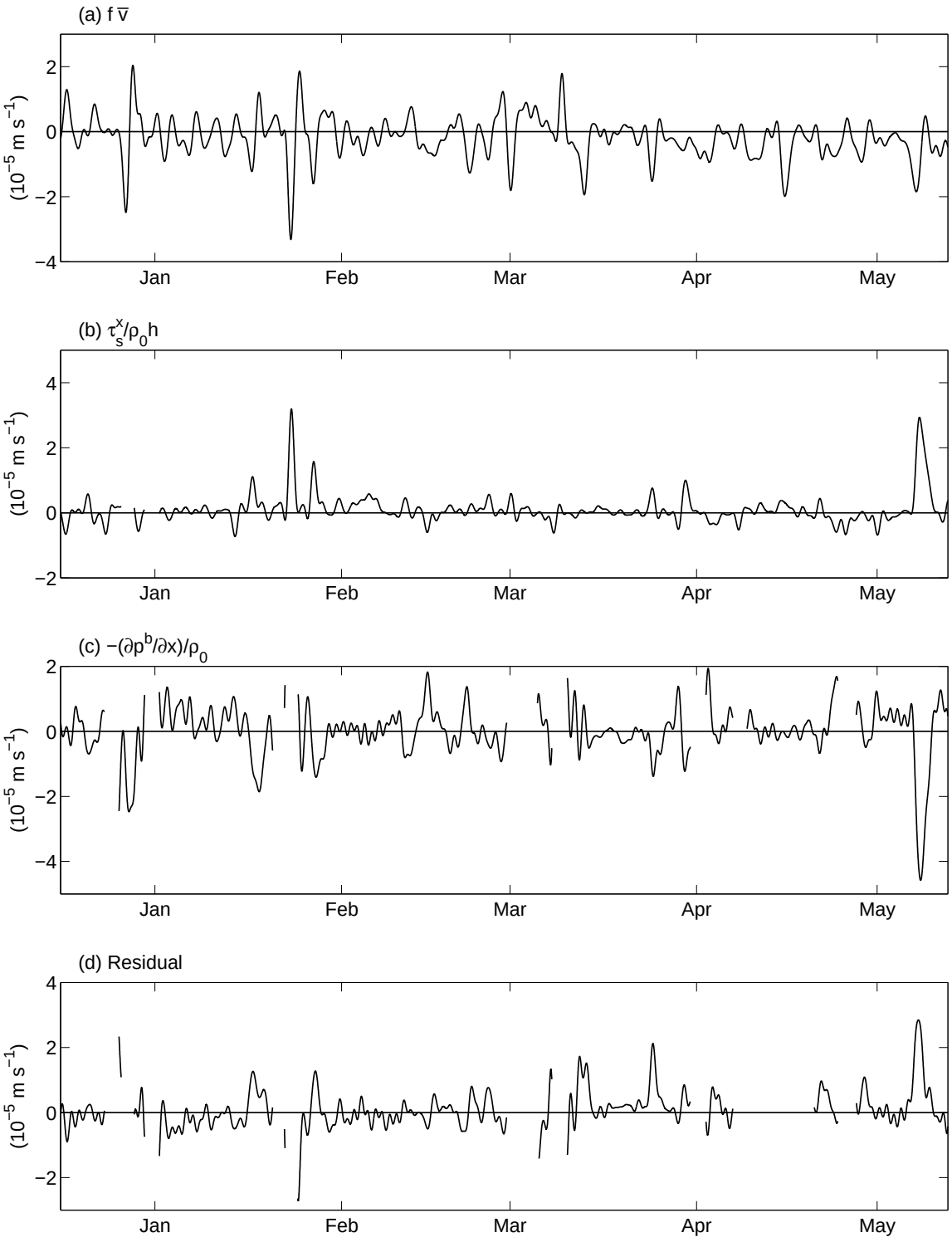

Figure 3-6: Dominant terms in subtidal cross-shelf momentum budget at mooring F in 27-m water depth, winter and spring 2004–2005.

Table 3.1: Statistics of terms in the cross-shelf momentum budget at the Node and F, during times when estimates of all terms are available. Units are 10^{-5} m s^{-1}. The mean pressure gradient cannot be estimated from these observations.

Node

	$\frac{\partial \overline{u}}{\partial t}$	$-\frac{1}{h}\frac{\partial}{\partial x}\int_{-h}^{0} u^2\,dz$	$f\overline{v}$	$f\overline{v}_{st}$	$-\frac{1}{\rho_0}\frac{\partial p^b}{\partial x}$	$\frac{\tau_s^x}{\rho_0 h}$	$-\frac{\tau_b^x}{\rho_0 h}$	$-\frac{1}{\rho_0 h}\frac{\partial S^{xx}}{\partial x}$
all times, mean	0.0	-0.1	-0.4	0.0	–	0.1	0.0	0.5
summer, mean	-0.0	-0.1	-0.6	-0.0	–	0.0	-0.0	0.5
winter, mean	0.0	-0.1	-0.3	0.0	–	0.1	0.0	0.6
all times, std dev	0.0	0.1	0.5	0.0	0.7	0.8	0.0	0.7
summer, std dev	0.0	0.1	0.4	0.0	0.7	0.9	0.0	0.5
winter, std dev	0.0	0.1	0.6	0.0	0.6	0.6	0.0	0.8

Mooring F

	$\frac{\partial \overline{u}}{\partial t}$	$-\frac{1}{h}\frac{\partial}{\partial x}\int_{-h}^{0} u^2\,dz$	$f\overline{v}$	$f\overline{v}_{st}$	$-\frac{1}{\rho_0}\frac{\partial p^b}{\partial x}$	$\frac{\tau_s^x}{\rho_0 h}$	$-\frac{\tau_b^x}{\rho_0 h}$	$-\frac{1}{\rho_0 h}\frac{\partial S^{xx}}{\partial x}$
all times, mean	0.0	-0.1	-0.4	-0.0	–	0.0	-0.0	0.0
summer, mean	-0.0	-0.1	-0.8	-0.0	–	0.0	-0.0	0.0
winter, mean	0.0	-0.0	-0.1	-0.0	–	0.0	0.0	0.0
all times, std dev	0.0	0.0	0.7	0.0	0.7	0.3	0.0	0.0
summer, std dev	0.0	0.0	0.6	0.0	0.7	0.4	0.0	0.0
winter, std dev	0.0	0.0	0.6	0.0	0.6	0.3	0.0	0.0

Table 3.2: Regression slope and intercept and correlation coefficient r of various terms in the MVCO Node and F cross-shelf momentum budgets against the cross-shelf pressure gradient term with zero lag in winter.

Node

	slope	intercept (10^{-5} m s^{-2})	r ($r_{95\%}$)
$f\overline{v}$	1.1 ± 0.3	-0.3 ± 0.1	0.69 (0.22)
$\frac{\tau_s^x}{\rho_0 h}$	1.1 ± 0.4	0.2 ± 0.1	0.53 (0.21)
$f\overline{v} + \frac{\tau_s^x}{\rho_0 h}$	1.6 ± 0.4	-0.2 ± 0.1	0.74 (0.22)
$-\frac{1}{\rho_0 h}\frac{\partial S^{xx}}{\partial x}$	0.2 ± 0.4	0.6 ± 0.1	0.10 (0.22)
$f\overline{v} + \frac{\tau_s^x}{\rho_0 h} - \frac{1}{\rho_0 h}\frac{\partial S^{xx}}{\partial x}$	1.5 ± 0.4	0.4 ± 0.2	0.67 (0.22)
$f\overline{v} + \frac{\tau_s^x - \tau_b^x}{\rho_0 h} - \frac{1}{\rho_0 h}\frac{\partial S^{xx}}{\partial x} - \frac{\partial \overline{u}}{\partial t} - \frac{1}{h}\frac{\partial}{\partial x}\int_{-h}^{0} u^2\, dz - f\overline{v}_{st}$	1.3 ± 0.3	0.3 ± 0.5	0.69 (0.22)

F

	slope	intercept (10^{-5} m s^{-2})	r ($r_{95\%}$)
$f\overline{v}$	-0.1 ± 0.1	-0.2 ± 0.0	0.32 (0.20)
$\frac{\tau_s^x}{\rho_0 h}$	0.5 ± 0.2	0.1 ± 0.0	0.48 (0.21)
$f\overline{v} + \frac{\tau_s^x}{\rho_0 h}$	0.9 ± 0.3	-0.1 ± 0.1	0.63 (0.21)
$-\frac{1}{\rho_0 h}\frac{\partial S^{xx}}{\partial x}$	0.0 ± 0.0	0.0 ± 0.0	0.22 (0.22)
$f\overline{v} + \frac{\tau_s^x}{\rho_0 h} - \frac{1}{\rho_0 h}\frac{\partial S^{xx}}{\partial x}$	0.8 ± 0.2	-0.1 ± 0.1	0.66 (0.22)
$f\overline{v} + \frac{\tau_s^x - \tau_b^x}{\rho_0 h} - \frac{1}{\rho_0 h}\frac{\partial S^{xx}}{\partial x} - \frac{\partial \overline{u}}{\partial t} - \frac{1}{h}\frac{\partial}{\partial x}\int_{-h}^{0} u^2\, dz - f\overline{v}_{st}$	0.6 ± 0.2	-0.1 ± 0.1	0.67 (0.22)

Table 3.3: Regression slope and intercept and correlation coefficient r of various terms in the MVCO Node and F cross-shelf momentum budgets against the cross-shelf pressure gradient term with zero lag in summer.

Node

	slope	intercept (10^{-5} m s^{-2})	r ($r_{95\%}$)
$f\overline{v}$	0.8 ± 0.4	-0.6 ± 0.1	0.49 (0.27)
$\frac{\tau_s^x}{\rho_0 h}$	1.2 ± 0.3	0.0 ± 0.1	0.80 (0.27)
$f\overline{v} + \frac{\tau_s^x}{\rho_0 h}$	1.5 ± 0.3	-0.5 ± 0.1	0.80 (0.27)
$-\frac{1}{\rho_0 h}\frac{\partial S^{xx}}{\partial x}$	-0.1 ± 0.3	0.5 ± 0.1	-0.11 (0.27)
$f\overline{v} + \frac{\tau_s^x}{\rho_0 h} - \frac{1}{\rho_0 h}\frac{\partial S^{xx}}{\partial x}$	1.3 ± 0.4	-0.0 ± 0.2	0.70 (0.27)
$f\overline{v} + \frac{\tau_s^x - \tau_b^x}{\rho_0 h} - \frac{1}{\rho_0 h}\frac{\partial S^{xx}}{\partial x} - \frac{\partial \overline{u}}{\partial t} - \frac{1}{h}\frac{\partial}{\partial x}\int_{-h}^{0} u^2\, dz - f\overline{v}_{st}$	1.2 ± 0.3	-0.2 ± 0.7	0.70 (0.27)

F

	slope	intercept (10^{-5} m s^{-2})	r ($r_{95\%}$)
$f\overline{v}$	-0.1 ± 0.2	-0.8 ± 0.0	0.30 (0.27)
$\frac{\tau_s^x}{\rho_0 h}$	0.5 ± 0.1	0.0 ± 0.0	0.78 (0.27)
$f\overline{v} + \frac{\tau_s^x}{\rho_0 h}$	1.0 ± 0.4	-0.9 ± 0.1	0.66 (0.27)
$-\frac{1}{\rho_0 h}\frac{\partial S^{xx}}{\partial x}$	-0.0 ± 0.0	0.0 ± 0.0	-0.07 (0.27)
$f\overline{v} + \frac{\tau_s^x}{\rho_0 h} - \frac{1}{\rho_0 h}\frac{\partial S^{xx}}{\partial x}$	1.0 ± 0.3	-0.8 ± 0.1	0.66 (0.27)
$f\overline{v} + \frac{\tau_s^x - \tau_b^x}{\rho_0 h} - \frac{1}{\rho_0 h}\frac{\partial S^{xx}}{\partial x} - \frac{\partial \overline{u}}{\partial t} - \frac{1}{h}\frac{\partial}{\partial x}\int_{-h}^{0} u^2\, dz - f\overline{v}_{st}$	0.7 ± 0.2	-0.9 ± 0.2	0.66 (0.27)

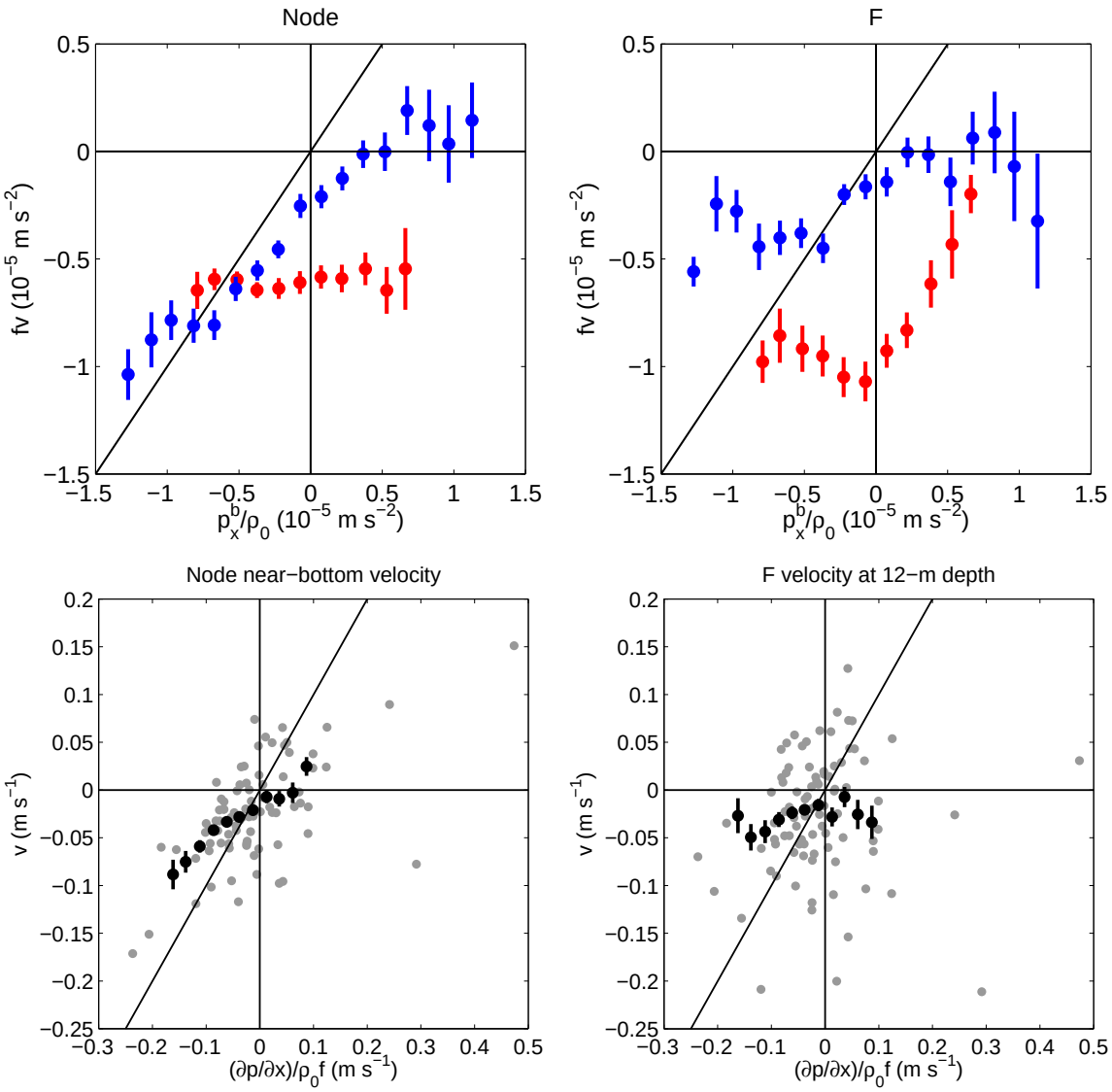

Figure 3-7: Top panels: test of geostrophic balance of depth-average along-shelf flow at (left) Node and (right) mooring F, during all times when estimates of the cross-shelf pressure gradient are available, for summer (red) and winter (blue). Bottom panels: test of geostrophic balance of along-shelf flow at 12-m depth at (left) Node and (right) mooring F during SWWIM I, when the density contribution to the pressure gradient can be estimated. Grey dots are subtidal data plotted every 33 hr, which are a subset of the points that go into the bin averages. Black symbols are bin-averaged data ± one standard error of the mean. Diagonal lines have slope 1.

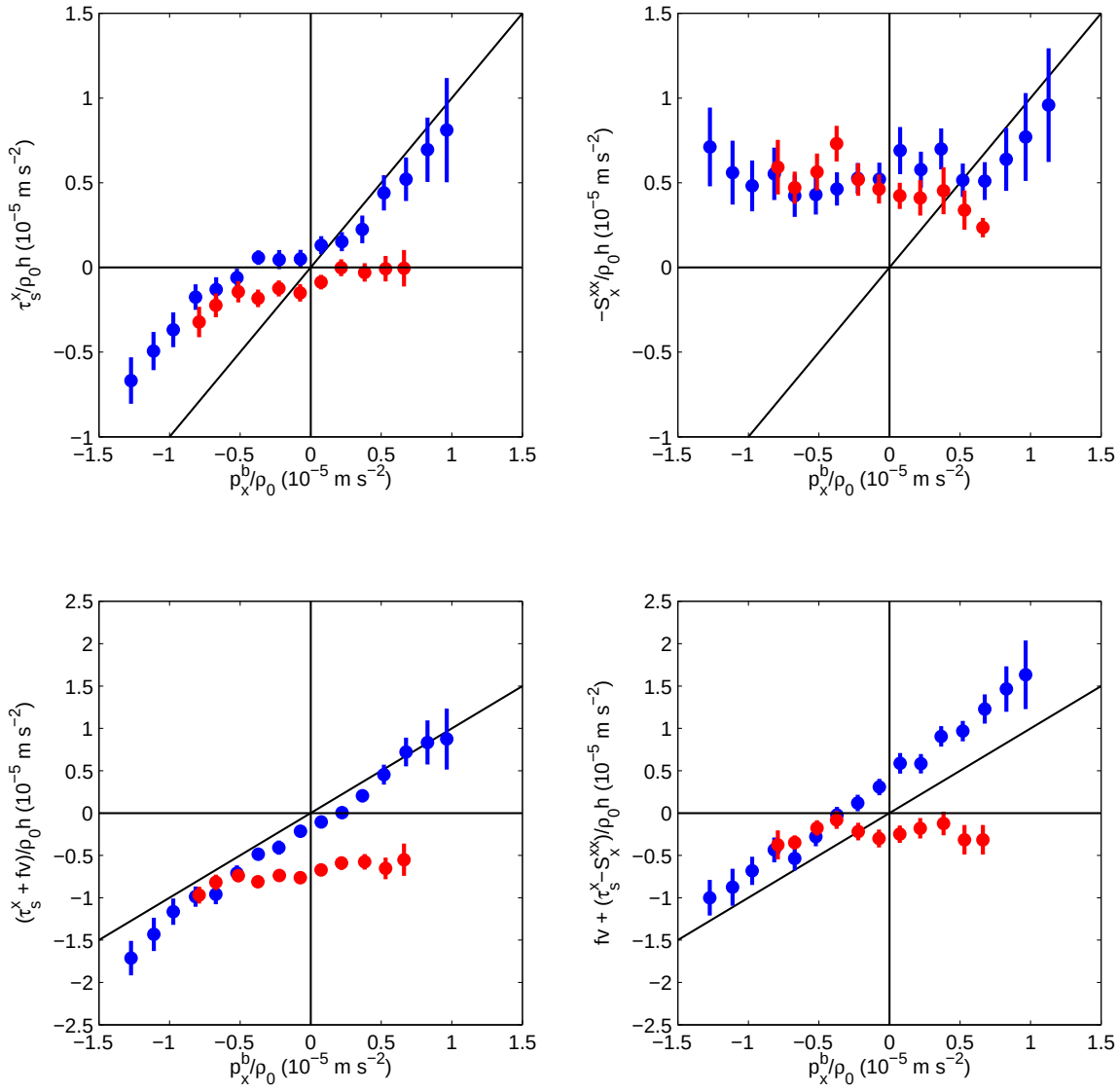

Figure 3-8: (Top left) cross-shelf wind stress, (top right) wave radiation stress gradient S_x^{xx}, (bottom left) wind stress plus $f\overline{v}$, and (bottom right) wind stress plus S_x^{xx} plus $f\overline{v}$, all versus cross-shelf pressure gradient in summer (red) and winter (blue). Note different vertical axis scales on top and bottom plots. Diagonal lines have slope 1. If the cross-shelf momentum budget closed exactly with the terms plotted, the symbols would lie on the diagonal line.

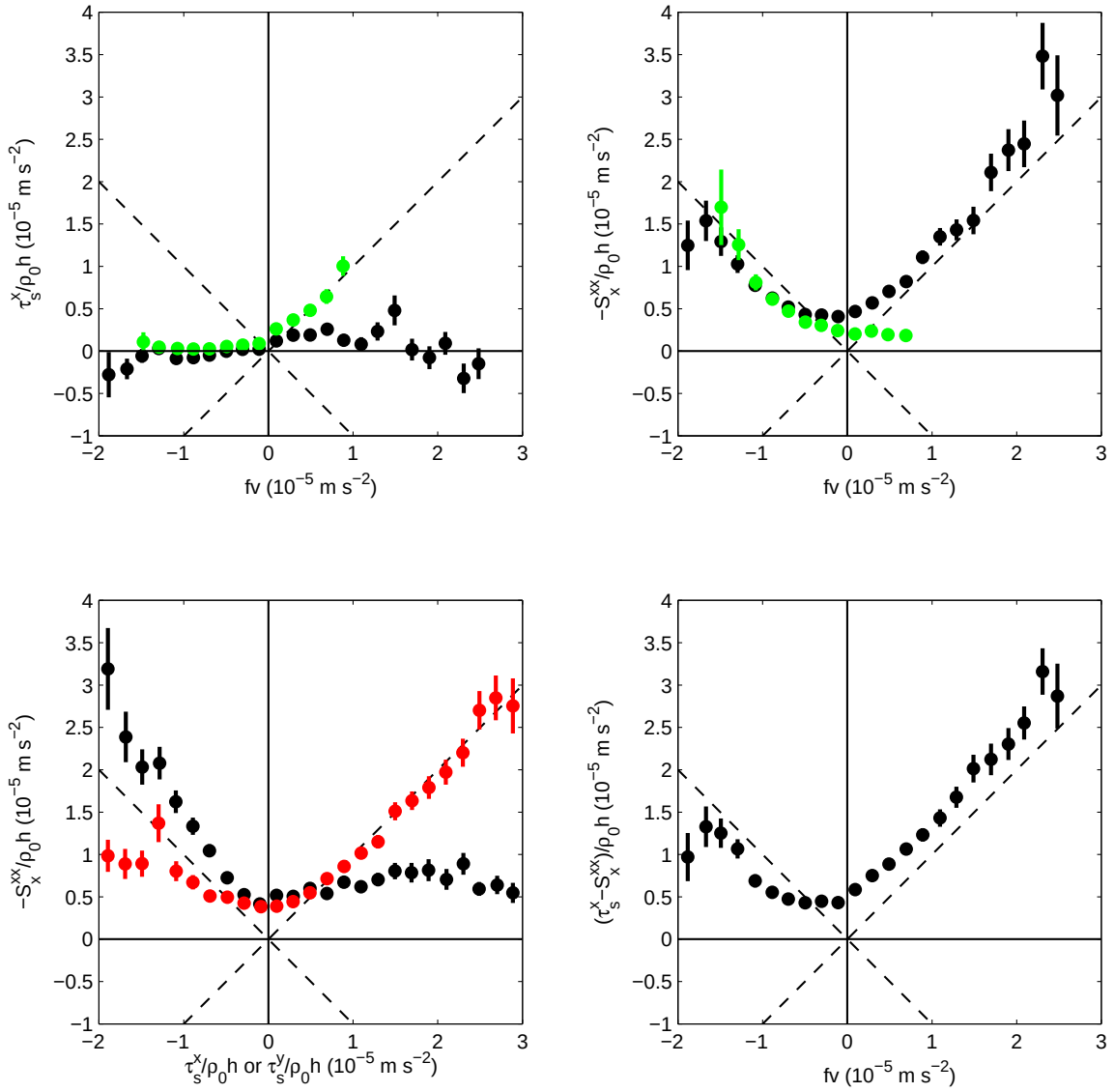

Figure 3-9: Comparison of (top left) cross-shelf wind stress, (top right) wave radiation stress gradient S_x^{xx}, and (bottom right) their sum to the Coriolis term due to the subtidal depth-average along-shelf flow at the 12-m isobath. Dashed lines have slope ± 1. In upper left, black symbols are during any wave forcing and green are during weak wave forcing. Restricting to weak along-shelf wind stress does not change the result. In upper right, black symbols are during any wind forcing and green are during weak along-shelf wind stress ($|\tau_s^x| < 0.035$N m^{-2}). Result during weak cross-shelf (total) wind stress is similar to black (green) symbols in upper right. Bottom left: wave radiation stress gradient versus cross-shelf (black) or along-shelf (red) wind stress term. Red curve continues similarly outside the range shown, to -3 and 4 N m^{-2}.

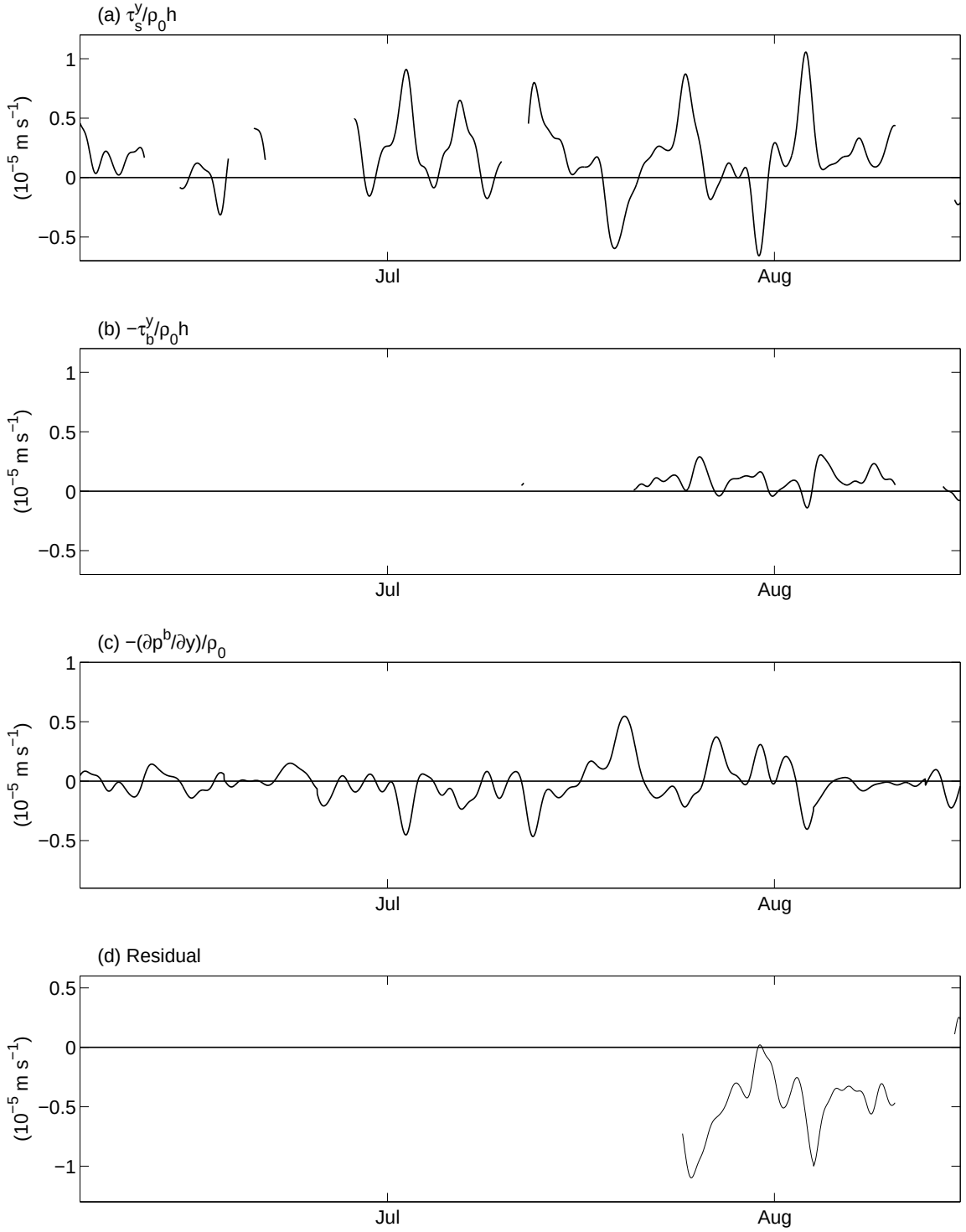

Figure 3-10: Dominant terms in subtidal along-shelf momentum budget at the MVCO Node in 12-m water depth, summer 2001.

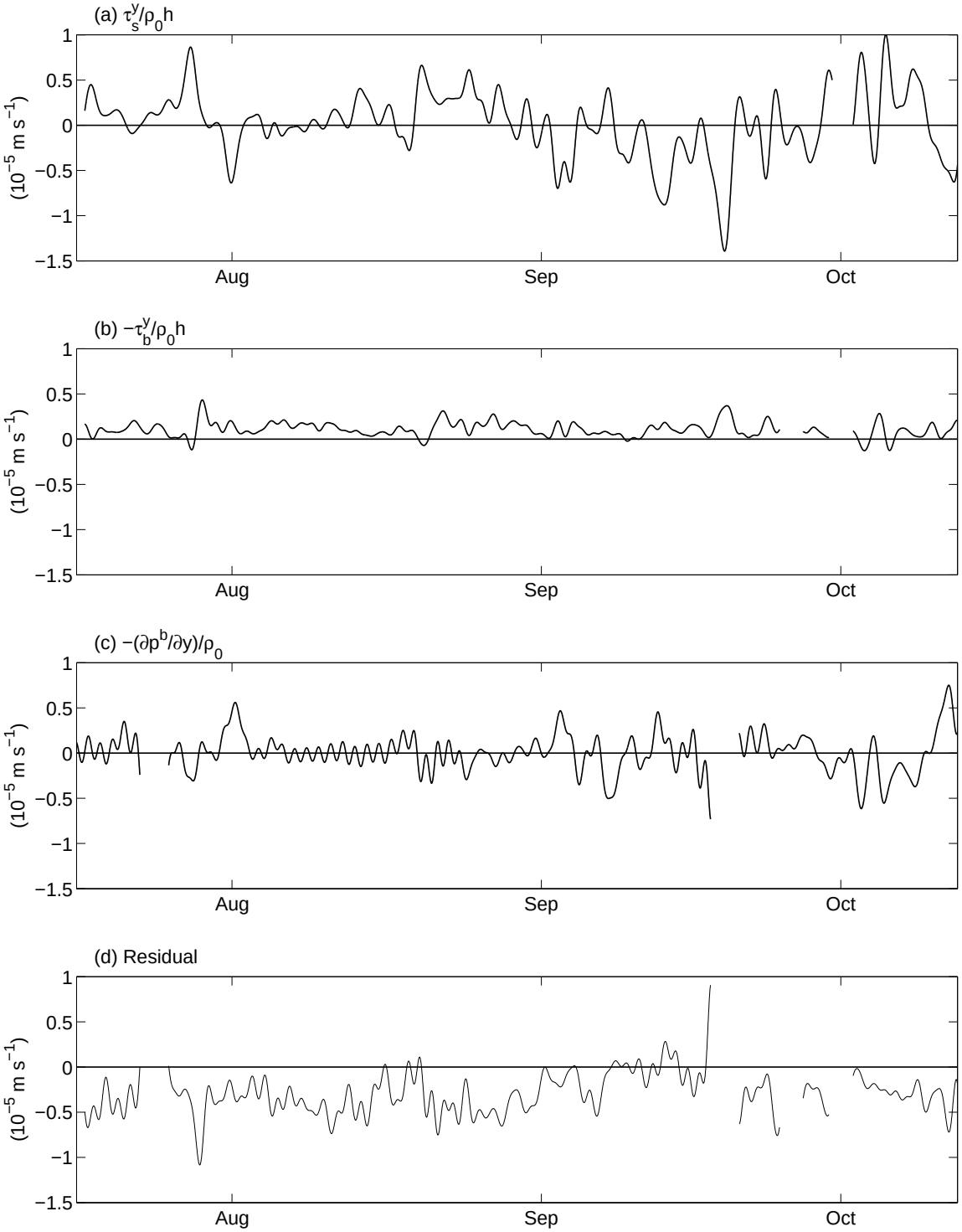

Figure 3-11: Dominant terms in subtidal along-shelf momentum budget at the MVCO Node in 12-m water depth, summer 2003.

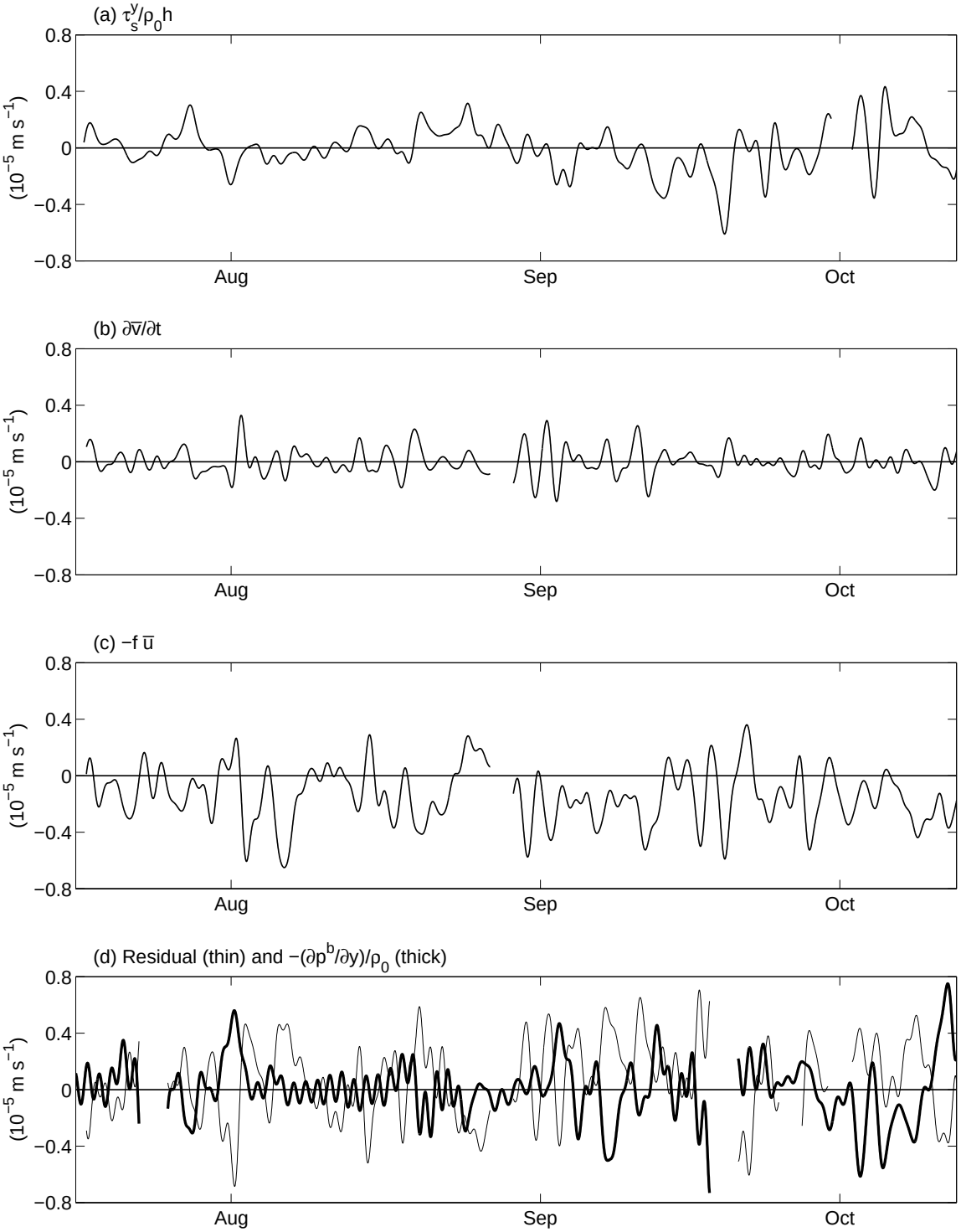

Figure 3-12: Dominant terms in subtidal along-shelf momentum budget at mooring F in 27-m water depth, summer 2003.

Table 3.4: Regression and correlation of along-shelf wind stress term $\tau_s^y/\rho_0 h$ versus along-shelf pressure gradient term p_y^b/ρ_0, using the wind stress in the Node coordinate system, at zero lag. For h in the wind stress term, we use the isobath on which the pressure sensors were deployed in each case.

Year	Isobath (m)	slope	intercept (10^{-5} m s^{-1})	corr coef r ($r_{95\%}$)
2001	19 m	0.8 ± 0.2	-0.1 ± 0.1	0.84 (0.35)
2003	15 m	0.6 ± 0.2	-0.0 ± 0.1	0.71 (0.26)

Table 3.5: Statistics of terms in the along-shelf momentum budget at the Node and F, during times when estimates of all terms are available. Units are 10^{-5} m s^{-1}. The mean pressure gradient cannot be estimated from these observations.

Node

	$\frac{\partial \overline{v}}{\partial t}$	$-\frac{1}{h}\frac{\partial}{\partial x}\int_{-h}^{0} uv\,dz$	$-f\overline{u}$	$-f\overline{u}_{st}$	$-\frac{1}{\rho_0}\frac{\partial p^b}{\partial y}$	$\frac{\tau_s^y}{\rho_0 h}$	$-\frac{\tau_b^y}{\rho_0 h}$
all times, mean	-0.0	0.2	-0.1	0.1	–	0.1	0.1
summer, mean	-0.0	0.2	-0.1	0.1	–	0.0	0.1
winter, mean	-0.0	0.2	-0.1	0.1	–	0.2	0.1
all times, std dev	0.1	0.1	0.1	0.0	0.2	0.3	0.1
summer, std dev	0.1	0.1	0.1	0.0	0.2	0.3	0.1
winter, std dev	0.1	0.1	0.1	0.1	0.3	0.5	0.1

Mooring F

	$\frac{\partial \overline{v}}{\partial t}$	$-\frac{1}{h}\frac{\partial}{\partial x}\int_{-h}^{0} uv\,dz$	$-f\overline{u}$	$-f\overline{u}_{st}$	$-\frac{1}{\rho_0}\frac{\partial p^b}{\partial y}$	$\frac{\tau_s^y}{\rho_0 h}$	$-\frac{\tau_b^y}{\rho_0 h}$
all times, mean	0.0	0.0	-0.1	0.0	–	-0.0	0.0
summer, mean	0.0	0.0	-0.1	0.0	–	-0.0	0.0
winter, mean	-0.0	0.0	-0.2	0.0	–	0.1	0.0
all times, std dev	0.1	0.0	0.2	0.0	0.2	0.1	0.0
summer, std dev	0.1	0.0	0.2	0.0	0.2	0.1	0.0
winter, std dev	0.1	0.0	0.1	0.0	0.3	0.2	0.0

Table 3.6: Regression slope and intercept, and correlation coefficient r, of various terms in the along-shelf momentum budget at the Node and F against the along-shelf pressure gradient term with zero lag.

Node

	slope	intercept (10^{-5} m s^{-2})	r ($r_{95\%}$)
$\frac{\tau_s^y}{\rho_0 h}$	1.5 ± 0.3	0.1 ± 0.1	0.71 (0.20)
$\frac{\tau_s^y - \tau_b^y}{\rho_0 h}$	1.2 ± 0.3	0.2 ± 0.1	0.68 (0.23)
$-\frac{\partial \overline{v}}{\partial t} + \frac{\tau_s^y - \tau_b^y}{\rho_0 h}$	1.3 ± 0.4	0.2 ± 0.1	0.67 (0.23)
$-\frac{\partial \overline{v}}{\partial t} + \frac{\tau_s^y - \tau_b^y}{\rho_0 h} - \frac{1}{h}\frac{\partial}{\partial x}\int_{-h}^{0} uv\, dz - f\overline{u} - f\overline{u}_{st}$	1.0 ± 0.3	0.3 ± 0.5	0.63 (0.24)

F

	slope	intercept (10^{-5} m s^{-2})	r ($r_{95\%}$)
$\frac{\tau_s^y}{\rho_0 h}$	0.5 ± 0.2	0.0 ± 0.0	0.63 (0.26)
$-f\overline{u}$	0.0 ± 0.3	-0.2 ± 0.0	-0.01 (0.26)
$-\frac{\partial \overline{v}}{\partial t}$	0.0 ± 0.1	-0.0 ± 0.0	-0.09 (0.26)
$-\frac{\partial \overline{v}}{\partial t} + \frac{\tau_s^y}{\rho_0 h}$	0.5 ± 0.3	0.0 ± 0.0	0.48 (0.27)
$-\frac{\partial \overline{v}}{\partial t} + \frac{\tau_s^y - \tau_b^y}{\rho_0 h} - \frac{1}{h}\frac{\partial}{\partial x}\int_{-h}^{0} uv\, dz - f\overline{u}_{st}$	0.4 ± 0.2	0.1 ± 0.1	0.53 (0.27)
$-\frac{\partial \overline{v}}{\partial t} + \frac{\tau_s^y - \tau_b^y}{\rho_0 h} - \frac{1}{h}\frac{\partial}{\partial x}\int_{-h}^{0} uv\, dz - f\overline{u} - f\overline{u}_{st}$	0.4 ± 0.4	-0.1 ± 0.1	0.31 (0.27)

Table 3.7: Regression and correlation of along-shelf bottom stress term $\tau_b^y/\rho_0 h$ versus along-shelf wind stress term $\tau_s^y/\rho_0 h$ at zero lag.

Node

	slope	intercept (10^{-5} m s^{-1})	corr coef r ($r_{95\%}$)
summer	0.16 ± 0.03	-0.10 ± 0.03	0.53 (0.10)
winter	0.22 ± 0.01	-0.12 ± 0.02	0.85 (0.08)

F

	slope	intercept (10^{-5} m s^{-1})	corr coef r ($r_{95\%}$)
summer	0.10 ± 0.05	-0.03 ± 0.03	0.45 (0.24)
winter	0.07 ± 0.02	-0.02 ± 0.02	0.48 (0.19)

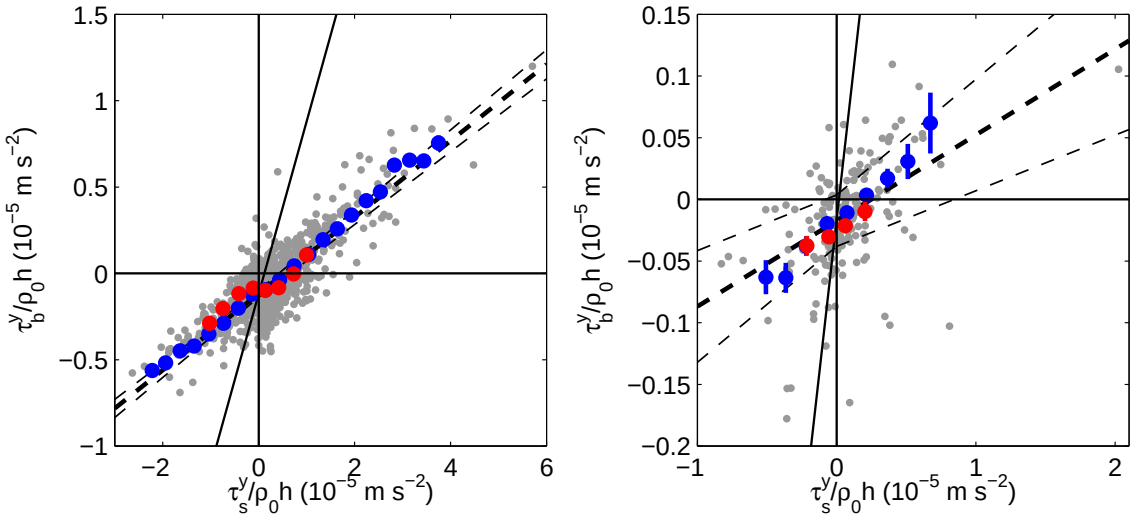

Figure 3-13: Bottom stress versus wind stress term in the along-shelf momentum budget at (left) Node and (right) F. Blue (red) circles are bin-averaged winter (summer) values. Grey dots are subtidal data plotted every 33 hr, which are the points used to estimate the regression slope and intercept and correlation coefficient, but are a subset of the points that go into the bin averages. Solid line has slope 1. Thick dashed line is a best-fit line for winter with 95% confidence limits shown by the thin dashed lines; see Table 3.7 for slopes, intercepts, and correlation coefficients. The wind and bottom stress are significantly correlated at the 95% confidence level in each case.

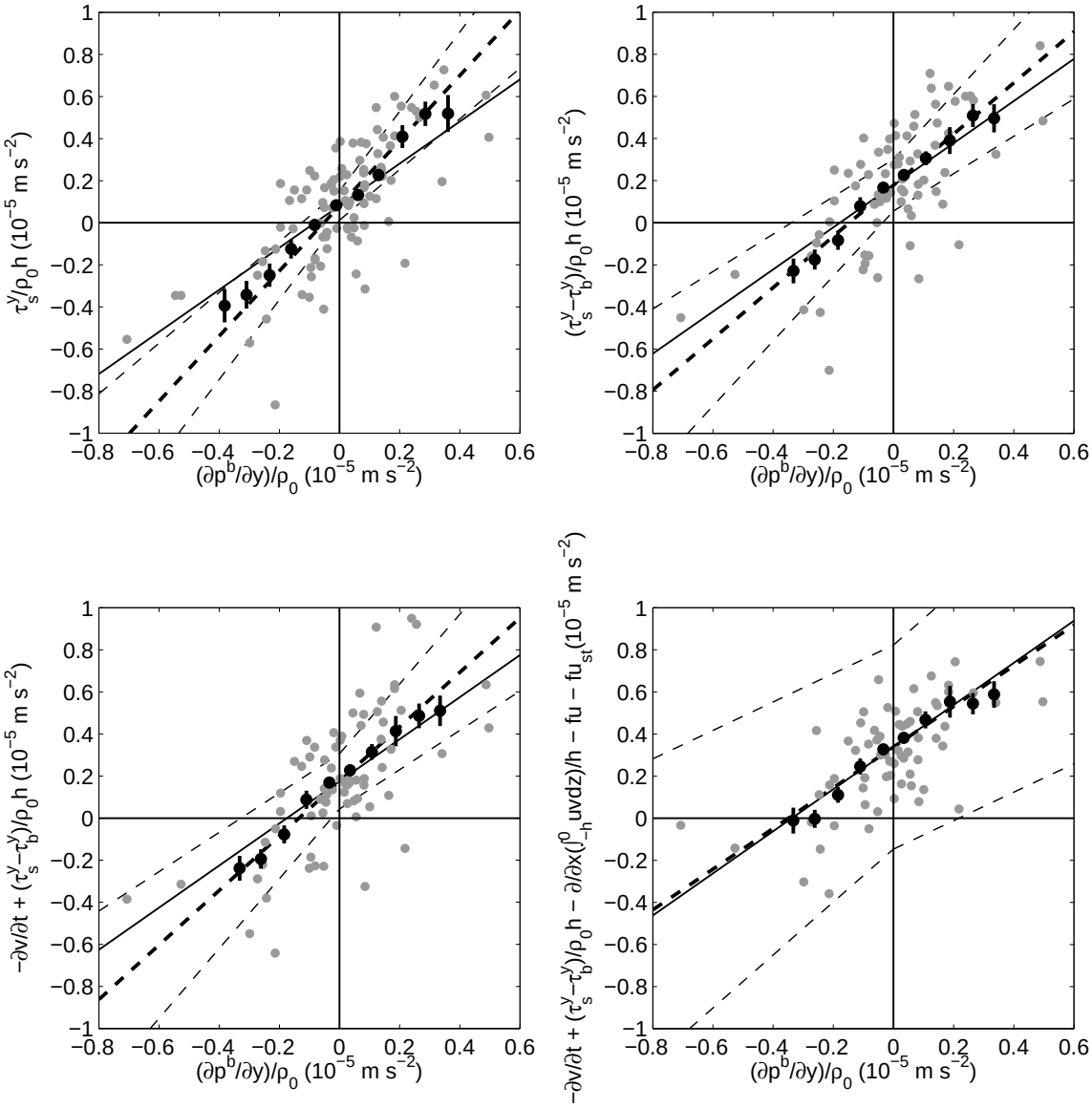

Figure 3-14: Comparison of terms in the along-shelf momentum budget at the Node. (Top left) along-shelf wind stress, (top right) wind stress plus bottom stress, (bottom left) wind stress plus bottom stress minus acceleration term, and (bottom right) the sum of all estimated terms in the momentum budget except pressure gradient, all versus the along-shelf pressure gradient. Black circles are bin-averaged values. Grey dots are subtidal data plotted every 33 hr, which are the points used to estimate the regression slope and intercept and correlation coefficient, but are a subset of the points that go into the bin averages. Solid line has slope 1. Thick dashed line is a best-fit line with 95% confidence limits shown by thin dashed lines in each case. The correlation in each plot is significant at the 95% confidence level (see Table 3.6 for slopes, intercepts, and correlation coefficients).

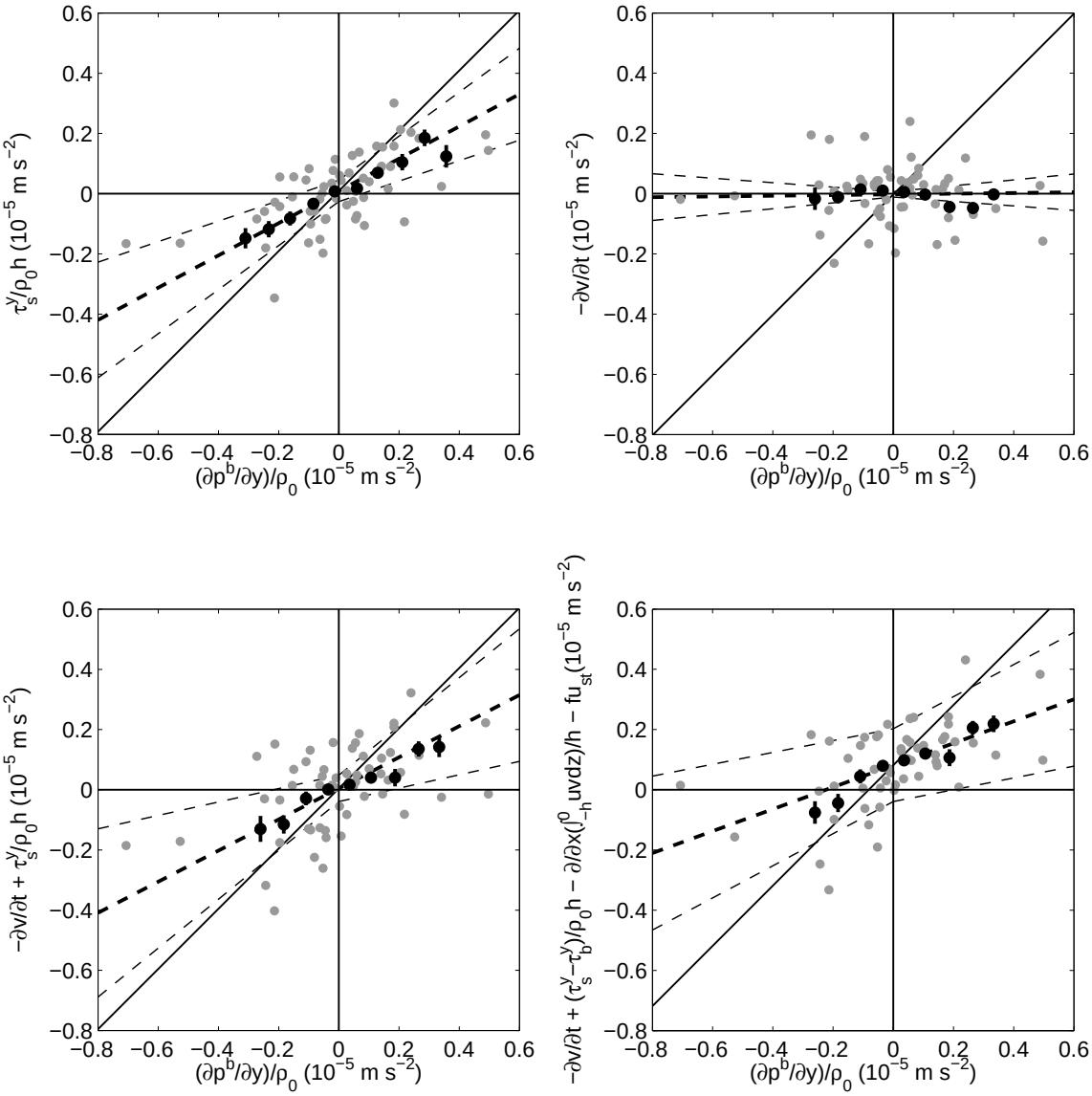

Figure 3-15: Comparison of terms in the along-shelf momentum budget at F. (Top left) along-shelf wind stress, (top right) acceleration, (bottom left) wind stress plus acceleration, and (bottom right) the sum of all estimated terms in the momentum budget except pressure gradient and Coriolis, all versus the along-shelf pressure gradient. Black circles are bin-averaged values. Grey dots are subtidal data plotted every 33 hr, which are the points used to estimate the regression slope and intercept and correlation coefficient, but are a subset of the points that go into the bin averages. Solid line has slope 1. Thick dashed line is a best-fit line with 95% confidence limits shown by thin dashed lines in each case. The correlation in each plot is significant at the 95% confidence level (see Table 3.6 for slopes, intercepts, and correlation coefficients).

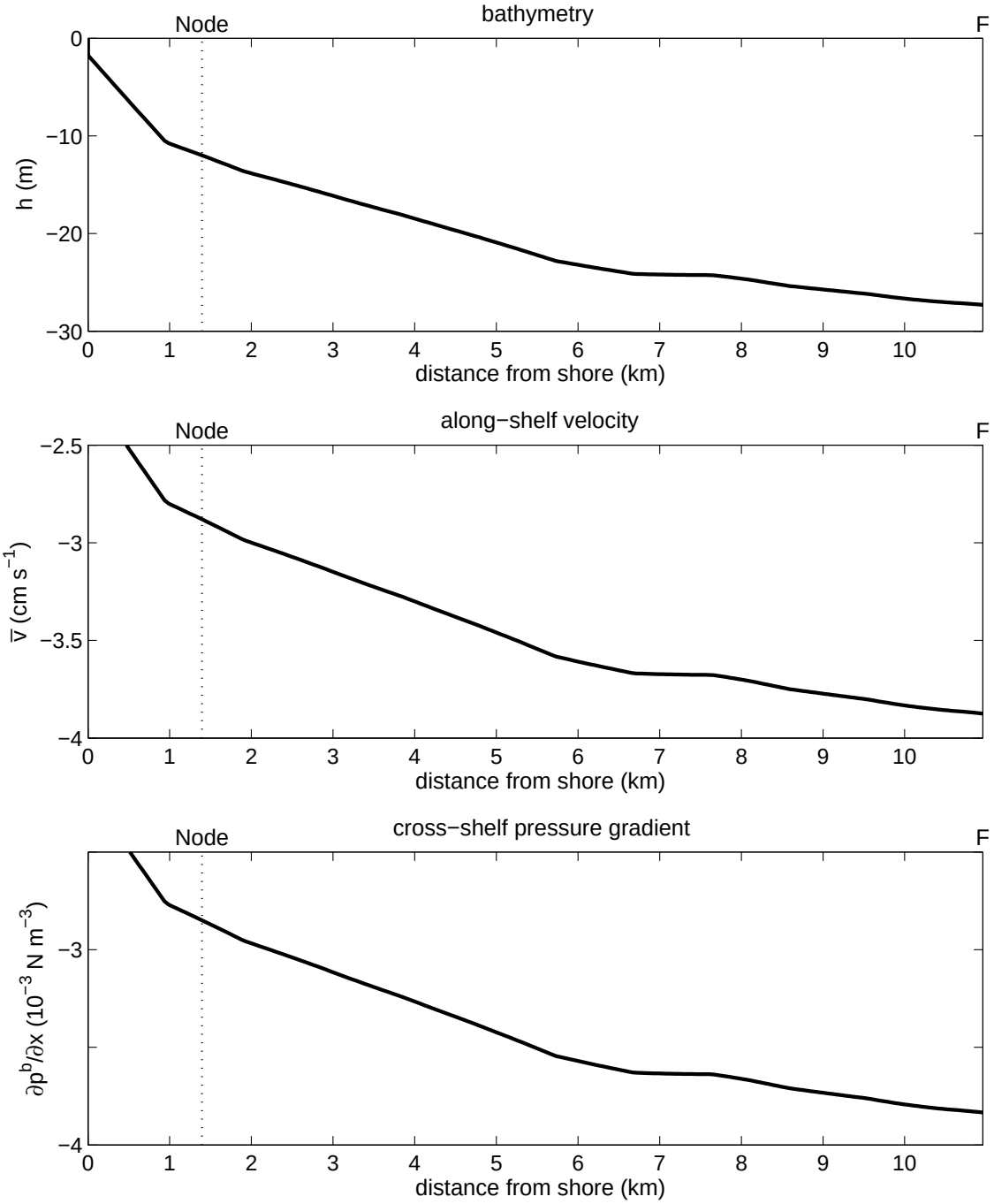

Figure 3-16: Cross-shelf structure of a cross-shelf pressure gradient due to geostrophy alone. Top panel: the bathymetry $h(x)$ at MVCO along a cross-shelf section from shore to mooring F, in the F coordinate system $\hat{y}$ direction from CBLAST 2003. Middle panel: the mean depth-average along-shelf velocity $\overline{v}$ from Lentz (2007a). Bottom panel: the cross-shelf pressure gradient if the cross-shelf momentum balance is exactly geostrophic, with $\partial p^b/\partial x = \rho_0 f \overline{v}$ and $\overline{v}$ as in the middle panel.

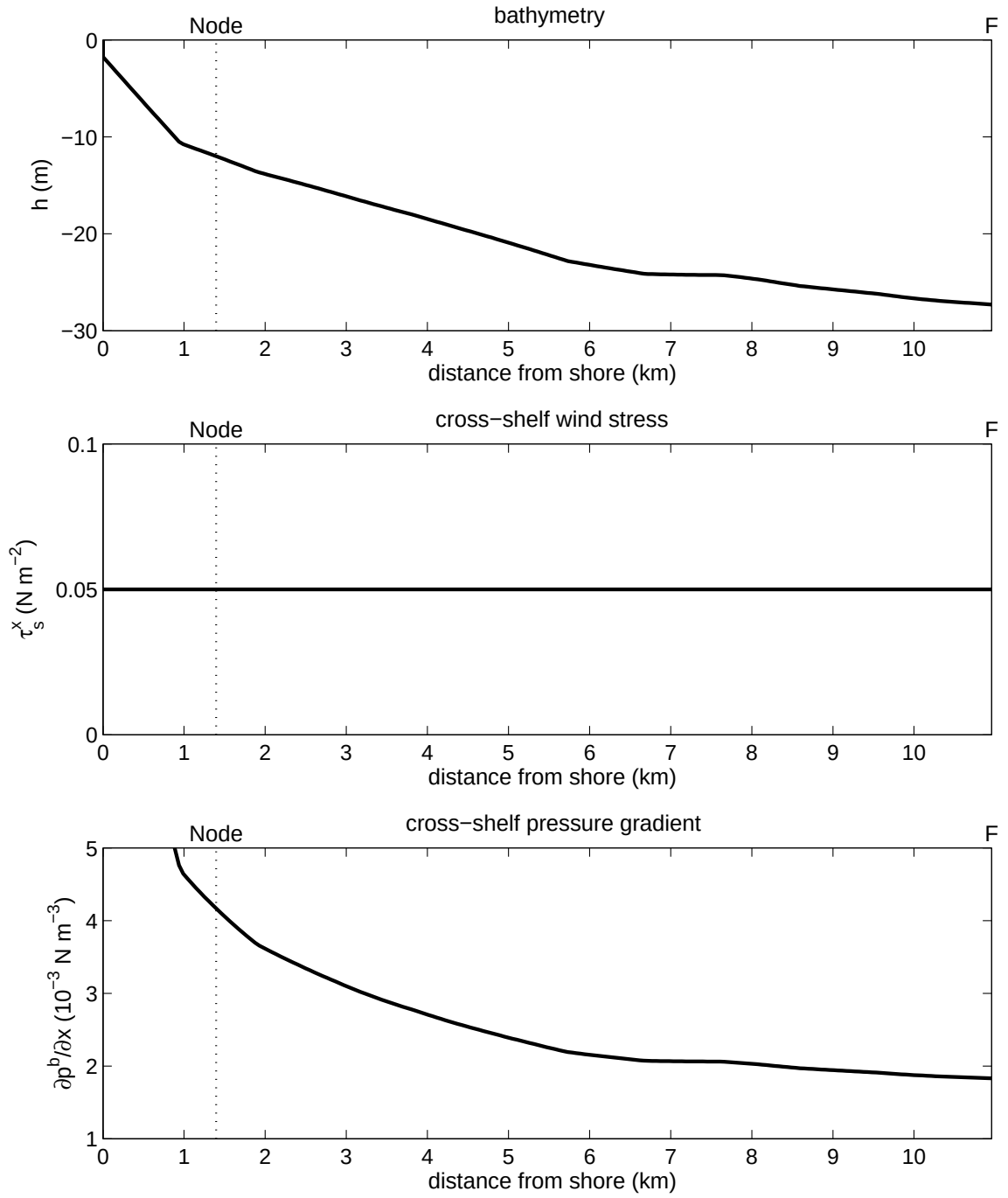

Figure 3-17: Cross-shelf structure of a cross-shelf pressure gradient due to cross-shelf wind stress alone. Top panel: the bathymetry $h(x)$ at MVCO along a cross-shelf section from shore to mooring F, in the F coordinate system $\hat{y}$ direction from CBLAST 2003. Middle panel: the cross-shelf wind stress (assumed constant and offshore, with $\tau_s^x = 0.05$ N m^{-3}. Bottom panel: the cross-shelf pressure gradient if the cross-shelf momentum balance is exactly a wind-driven coastal set-down balance, with $\partial p^b/\partial x = \tau_s^x/h$ and τ_s^x as in the middle panel.

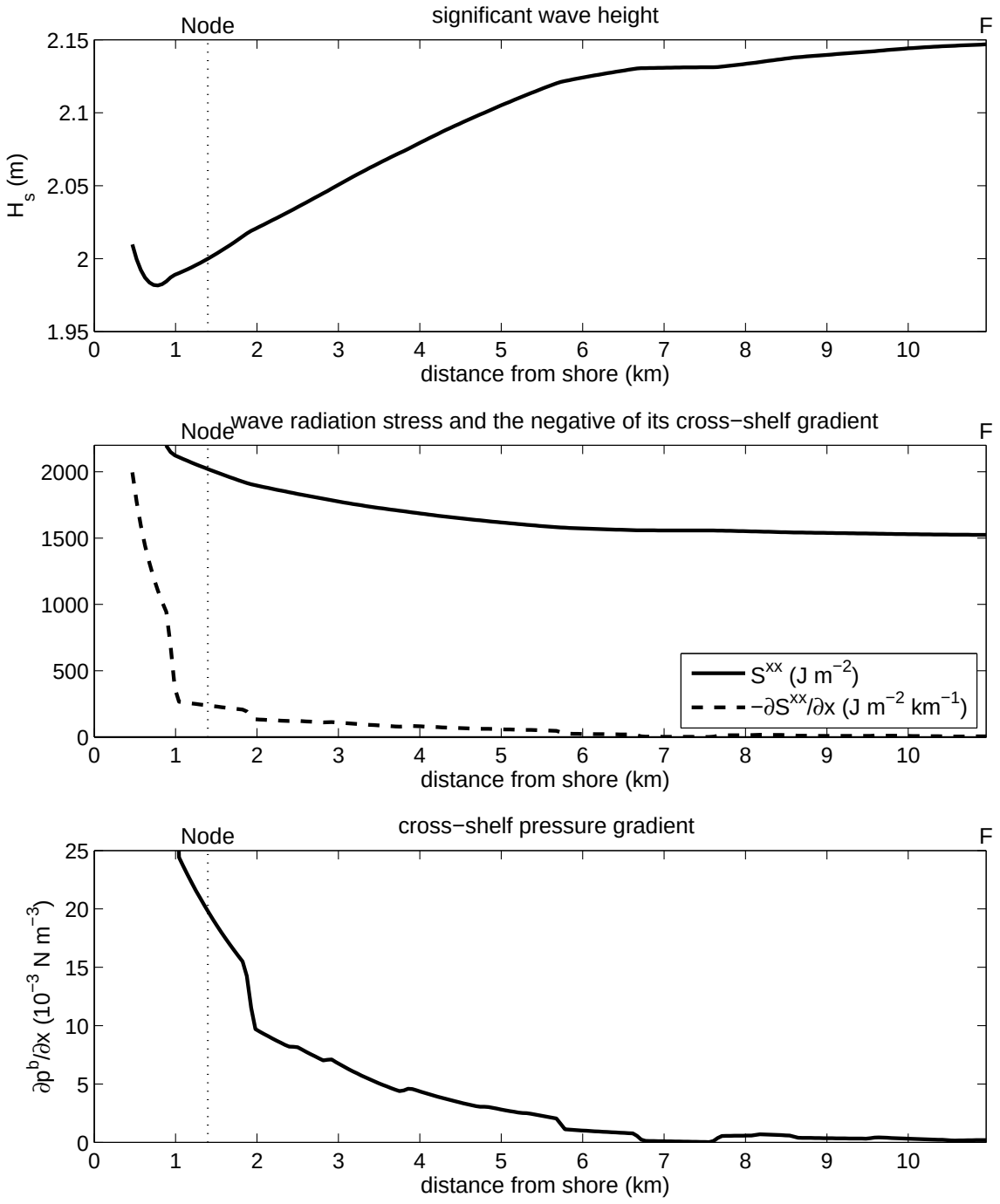

Figure 3-18: Cross-shelf structure of cross-shelf pressure gradient due to wave radiation stress gradient alone. Top panel: significant wave height as a function of distance from shore, for a wave propagating directly onshore with $H_{sig} = 2$ m at the 12-m isobath and period 6 s. Middle panel: the cross-shelf structure of the estimated wave radiation stress S^{xx} and the negative of its cross-shelf gradient for the same wave. Bottom panel: the cross-shelf pressure gradient if the cross-shelf momentum balance is exactly a wave-driven coastal set-down balance, with $\partial p^b/\partial x = -(\partial S^{xx}/\partial x)/h$ and S^{xx} as in the middle panel.

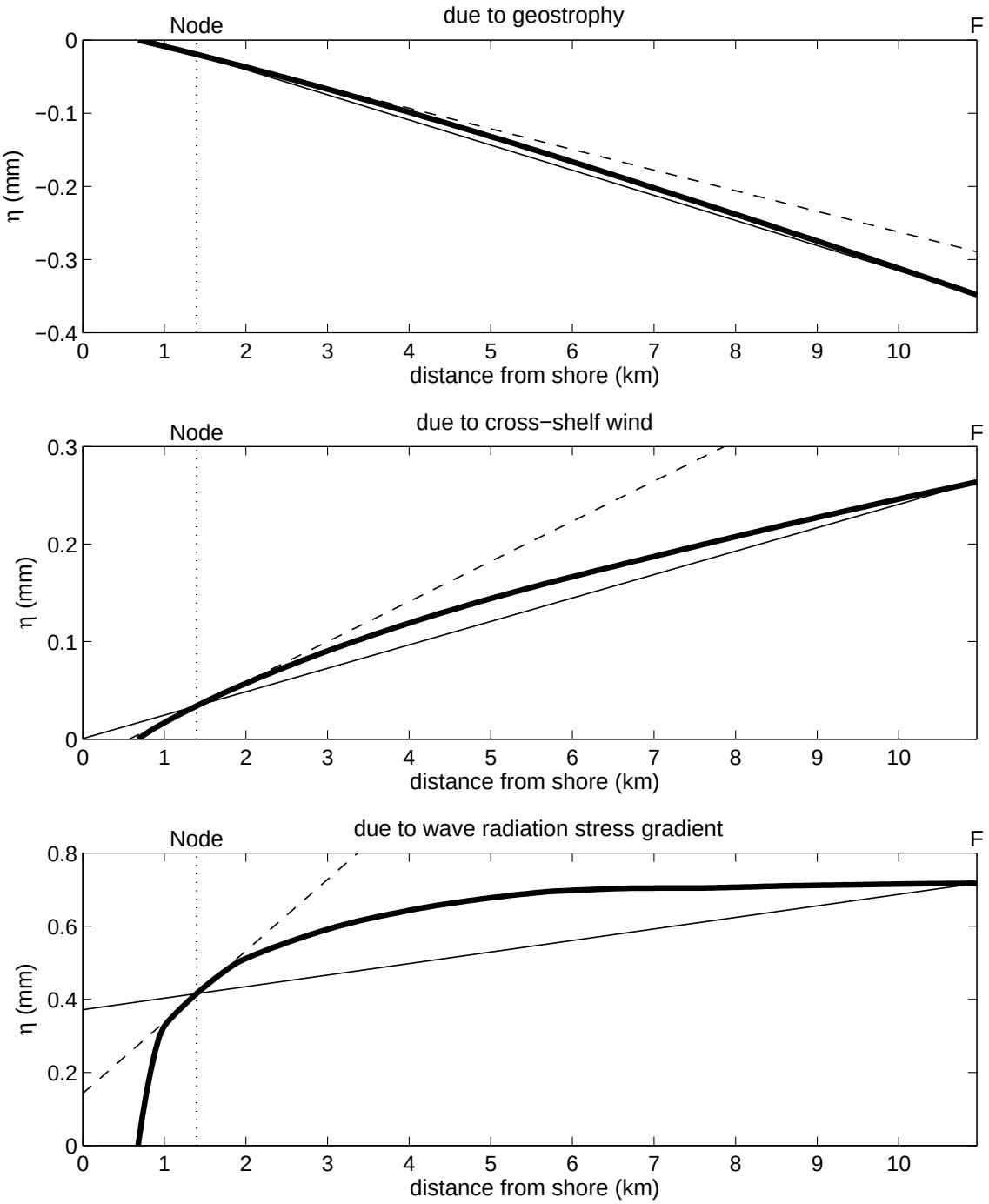

Figure 3-19: Cross-shelf structure of sea-level displacement η due to (top) geostrophy, (middle) cross-shelf wind, or (bottom) wave forcing. Thick line in each panel: η relative to its value at the 8-m isobath, using the cross-shelf pressure gradients from the bottom panels of Figures 3-16 through 3-18 and $\partial\eta/\partial x = (\partial p^b/\partial x)/\rho_0 h$ from the hydrostatic relation. Thin line: the effective η profile for a pressure gradient estimate when ∂p^b (or η) is measured at the Node and mooring F only. Dashed line: a least-squares fit to η near the Node (between 1.2 and 1.6 km from shore).

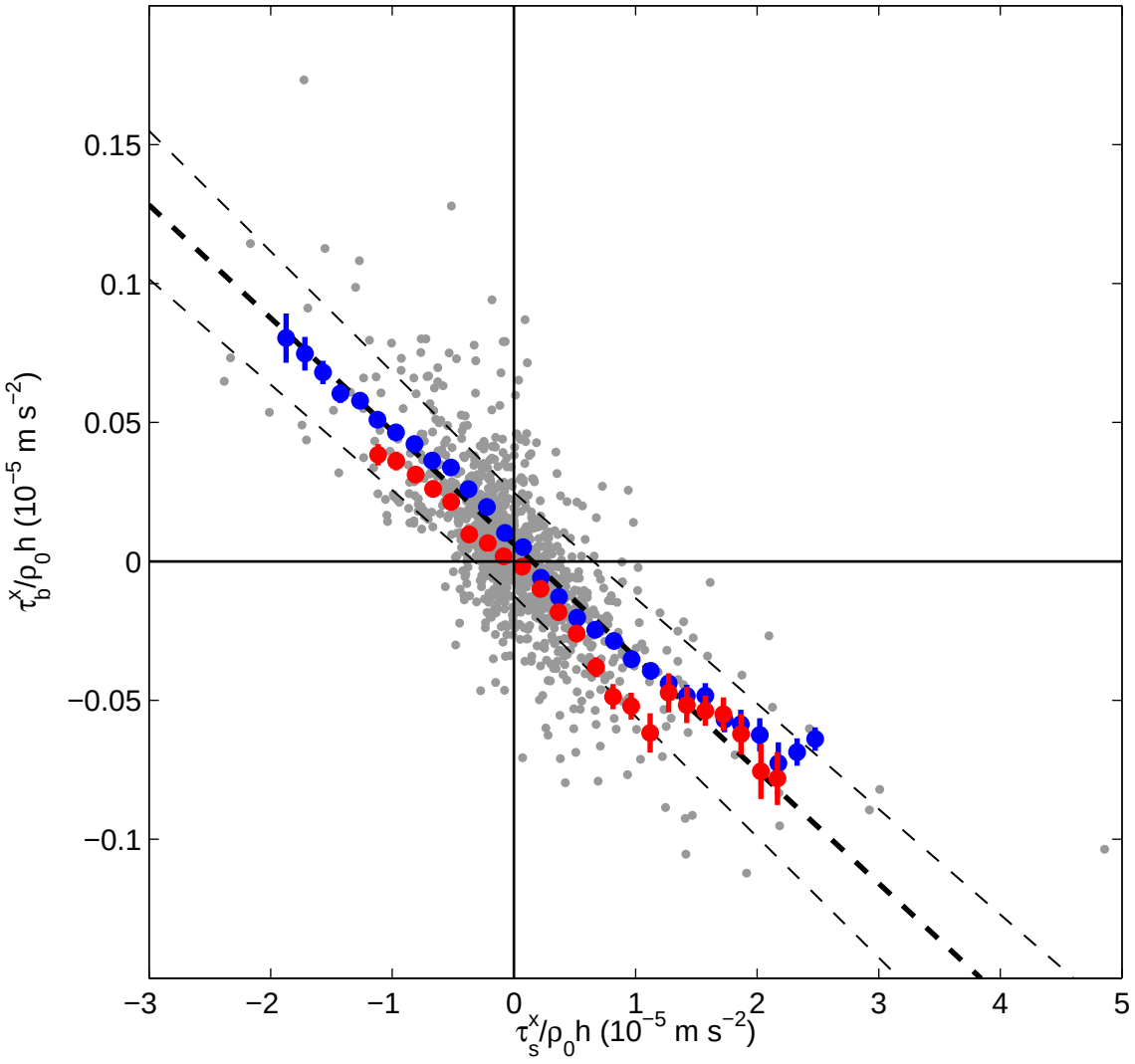

Figure 3-20: Bottom stress versus wind stress term in the cross-shelf momentum budget. Blue (red) circles are bin-averaged winter (summer) values. Grey dots are subtidal data plotted every 33 hr, which are the points used to estimate the regression slope and intercept and correlation coefficient, but are a subset of the points that go into the bin averages. Thick dashed line is a best-fit line for winter with 95% confidence limits shown by the thin dashed lines, and has slope -0.04 ± 0.02 and intercept $(-0.006 \pm 0.003) \times 10^{-5}$ m s^{-2}. The two terms are significantly correlated at the 95% confidence level in both seasons, with $r = -0.75$ ($|r_{95\%}| = 0.08$) in winter and $r = -0.70$ ($|r_{95\%}| = 0.09$) in summer.

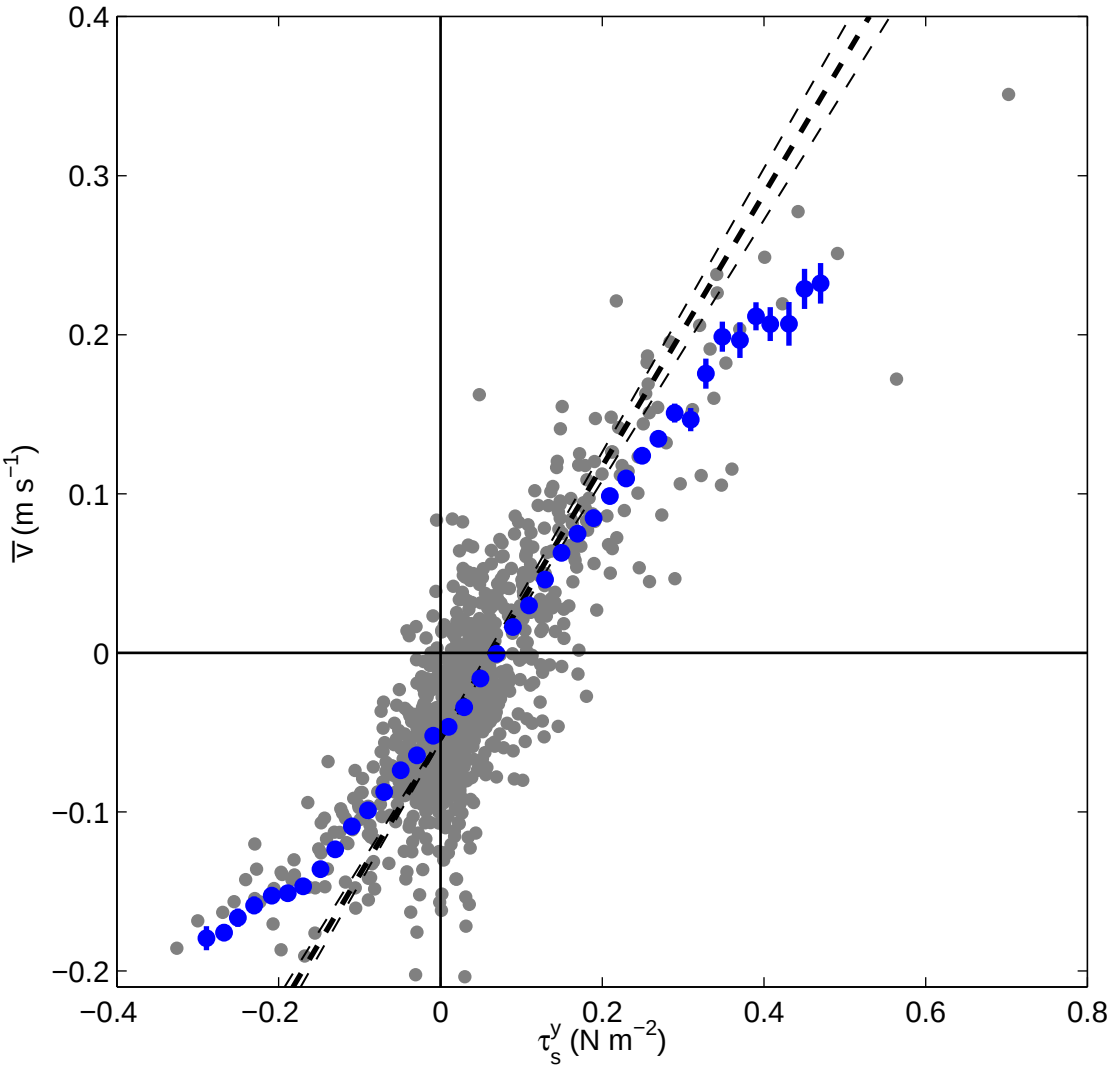

Figure 3-21: Depth-average along-shelf flow $\overline{v}$ versus along-shelf wind stress. Blue circles are bin-averaged values. Grey dots are subtidal data plotted every 33 hr, which are the points used to estimate the regression slope and intercept and correlation coefficient, but are a subset of the points that go into the bin averages. Thick dashed line is a best-fit line with 95% confidence limits shown by the thin dashed lines, and has slope 0.86 ± 0.04 m s^{-1} (N m^{-2})$^{-1}$ and intercept (-0.054 ± 0.002) m s^{-1}. The two terms are significantly correlated at the 95% confidence level, with $r = 0.83$ ($|r_{95\%}| = 0.06$).

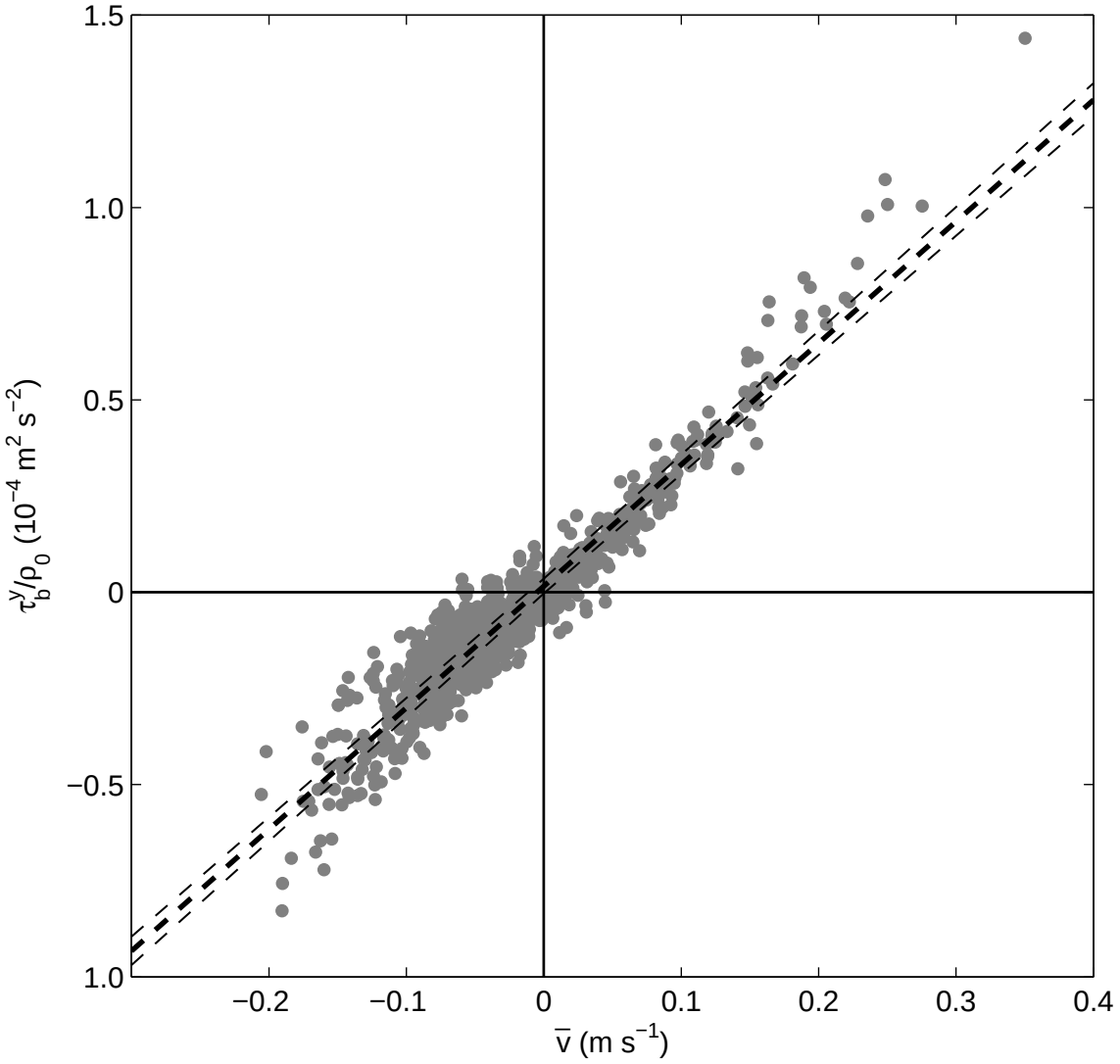

Figure 3-22: Determination of best-fit linear bottom drag coefficient r_b for subtidal along-shelf flow, for a drag law of the form $\tau_b^y = \rho_0 r_b \overline{v}$. Bottom stress divided by reference density, τ_b^y/ρ_0, is plotted versus depth-average along-shelf flow $\overline{v}$. Grey dots are subtidal data plotted every 33 hr, which are the points used to estimate the regression slope and intercept and correlation coefficient. Thick dashed line is a best-fit line with 95% confidence limits shown by the thin dashed lines, and has slope r_b equal to $(3.16 \pm 0.06) \times 10^{-4}$ m s^{-1} and intercept $(0.02 \pm 0.02) \times 10^{-4}$ m^2 s^{-2}. The two quantities plotted are significantly correlated at the 95% confidence level, with $r = 0.95$ ($|r_{95\%}| = 0.06$).

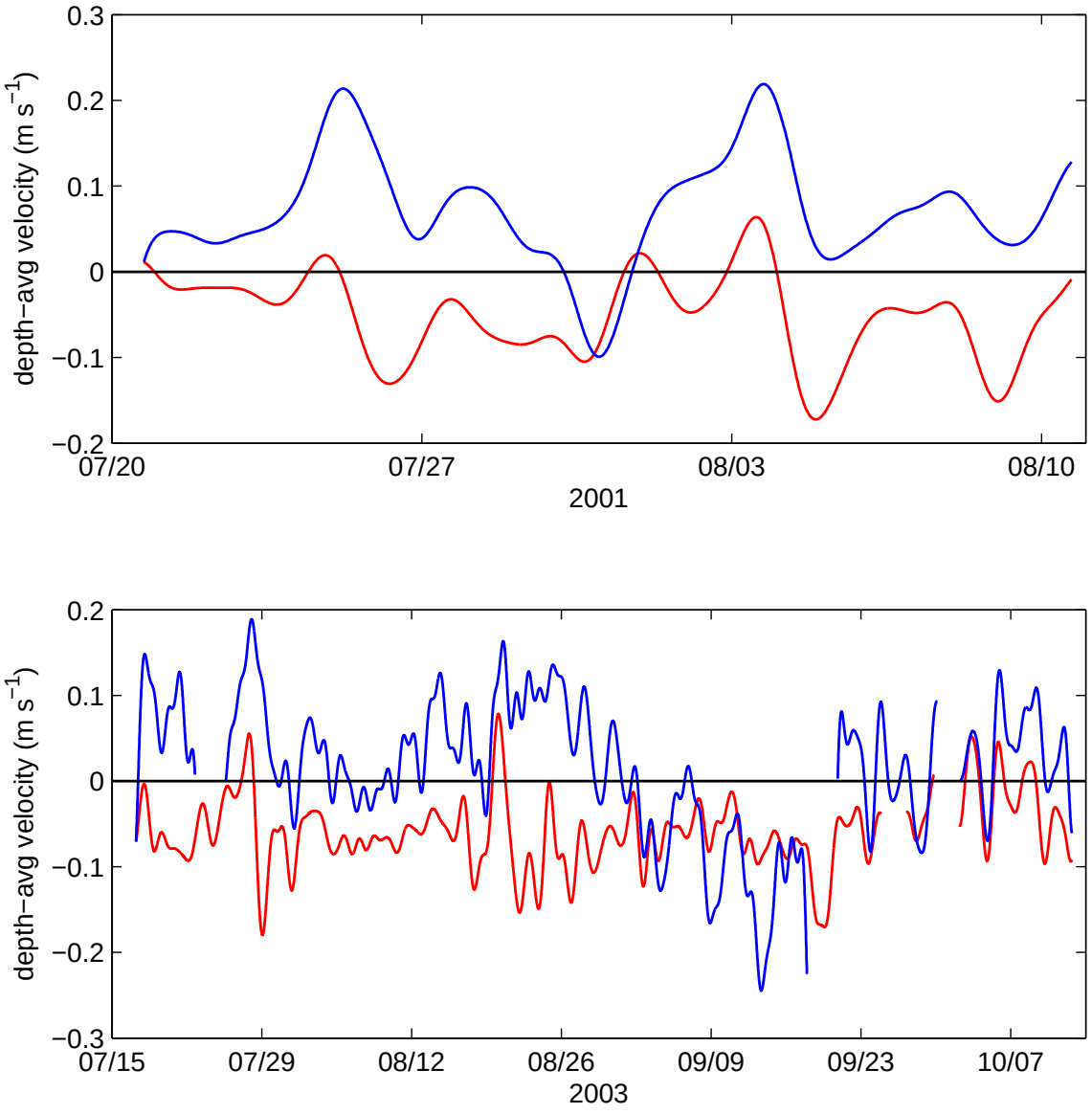

Figure 3-23: 33-hr low-pass filtered depth-average along-shelf flow $\overline{v}$ in (top) 2001 and (bottom) 2003. Red: observed at the 12-m isobath (Node). Blue: predicted from the observed along-shelf wind stress and pressure gradient following Lentz et al. (1999), using the linear bottom drag coefficient r from Figure 3-22 and Eq. (3.45).

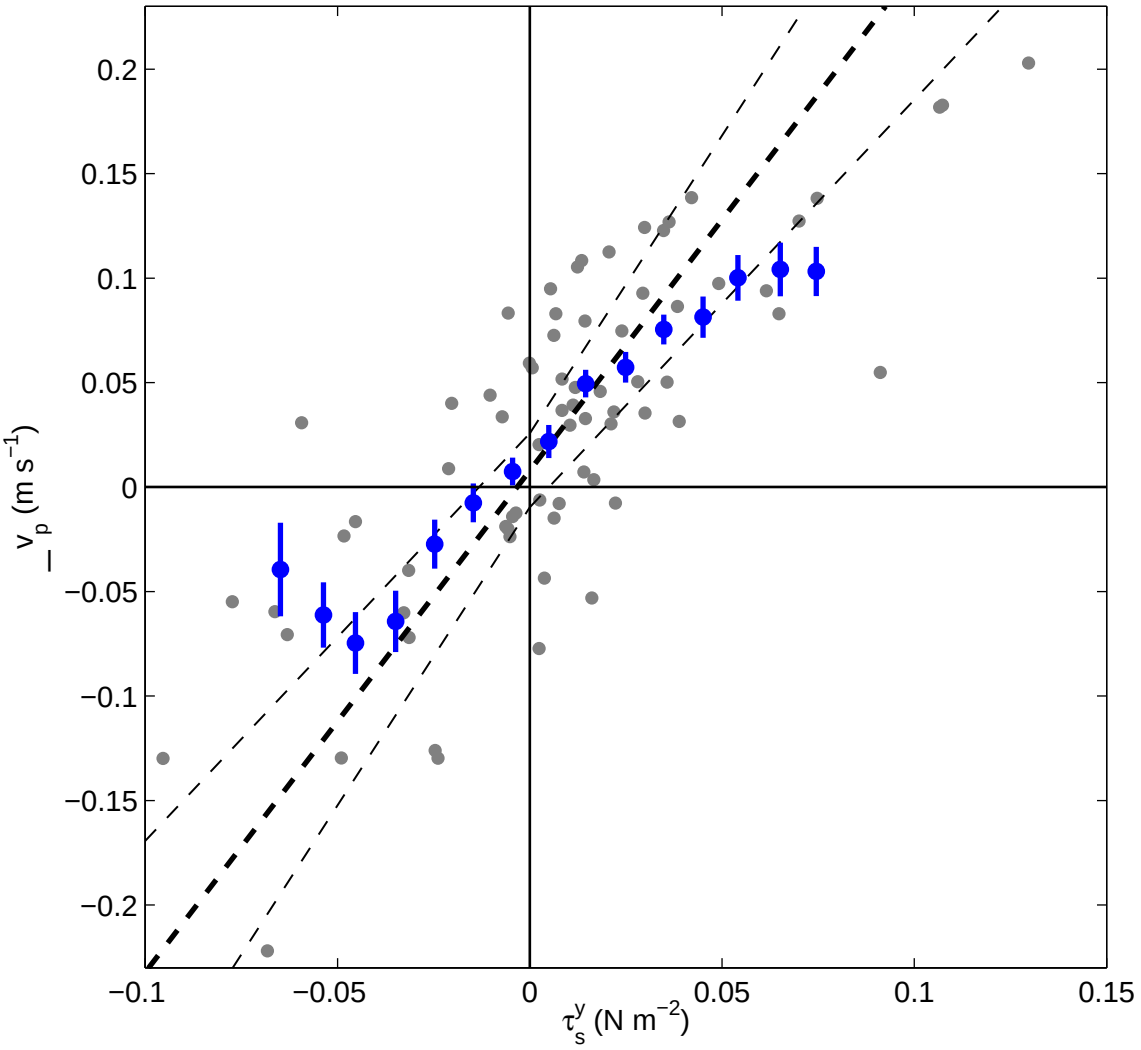

Figure 3-24: Modeled depth-average along-shelf flow $\overline{v}_p$ (Figure 3-23) versus along-shelf wind stress. Blue circles are bin-averaged values. Grey dots are subtidal data plotted every 33 hr, which are the points used to estimate the regression slope and intercept and correlation coefficient, but are a subset of the points that go into the bin averages. Thick dashed line is a best-fit line with 95% confidence limits shown by the thin dashed lines, and has slope 2.4 ± 0.5 m s^{-1} (N m^{-2})$^{-1}$ and intercept (0.01 ± 0.02) m s^{-1}. The two terms are significantly correlated at the 95% confidence level, with $r = 0.78$ ($|r_{95\%}| = 0.23$).

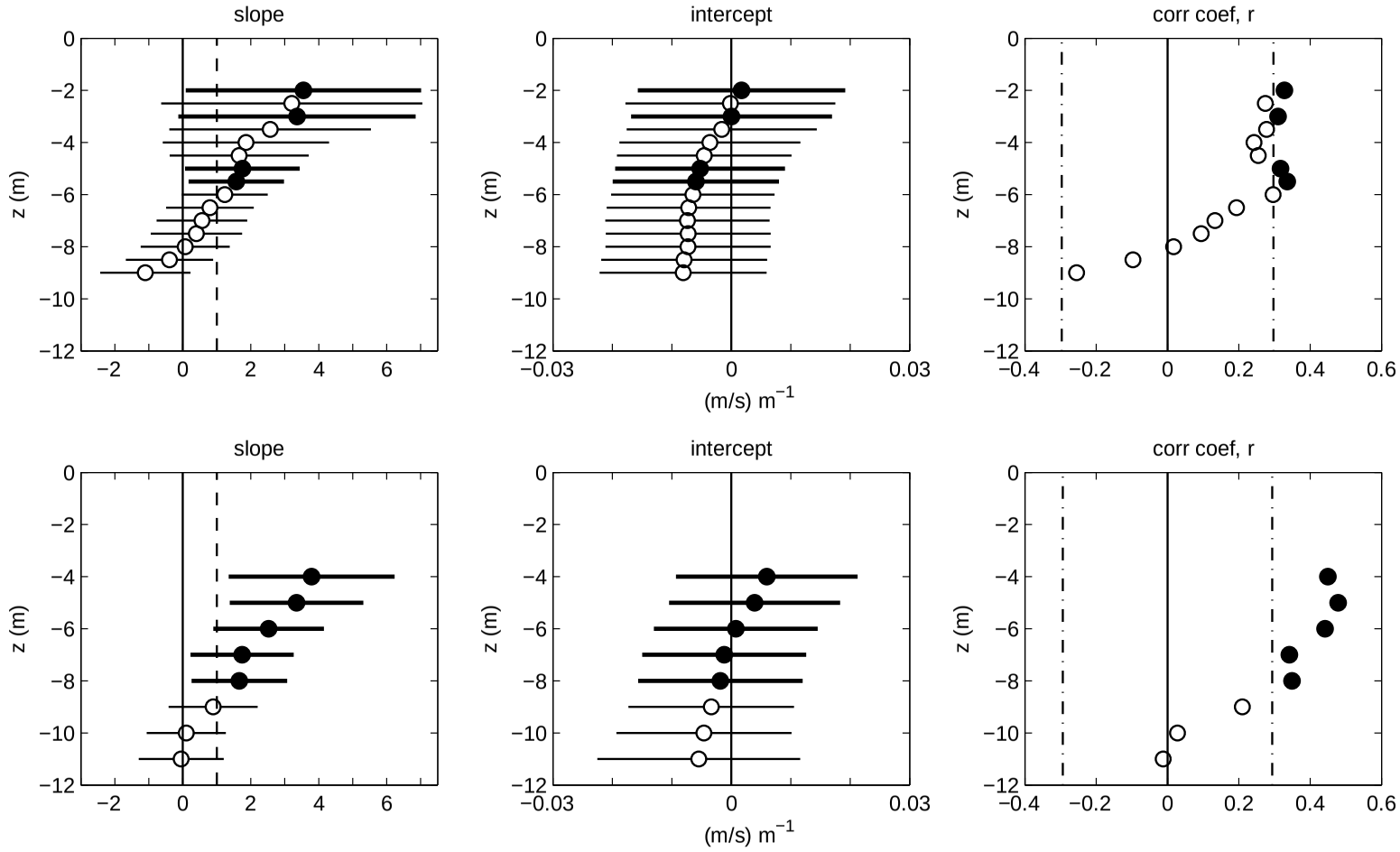

Figure 3-25: Test of thermal wind balance during CBLAST 2003. Comparison of vertical shear in along-shelf velocity with estimated cross-shelf density gradient. Top row: Node. Bottom row: F. The slope and intercept of a regression of $\partial v/\partial z$ against $-g(\partial\rho/\partial x)/\rho_0 f$, and the correlation coefficient of those terms, are shown for each mooring. Solid (open) symbols show depths where the correlation is (is not) significant at the 95% confidence level. Dashed lines in left panels indicate slope = 1. Dash-dot lines in right-hand panels indicate minimum significant correlation coefficient. If the shear were exactly in thermal wind balance, the data in the left-hand panels would lie on the dashed line and in the middle panels would lie on the zero line.

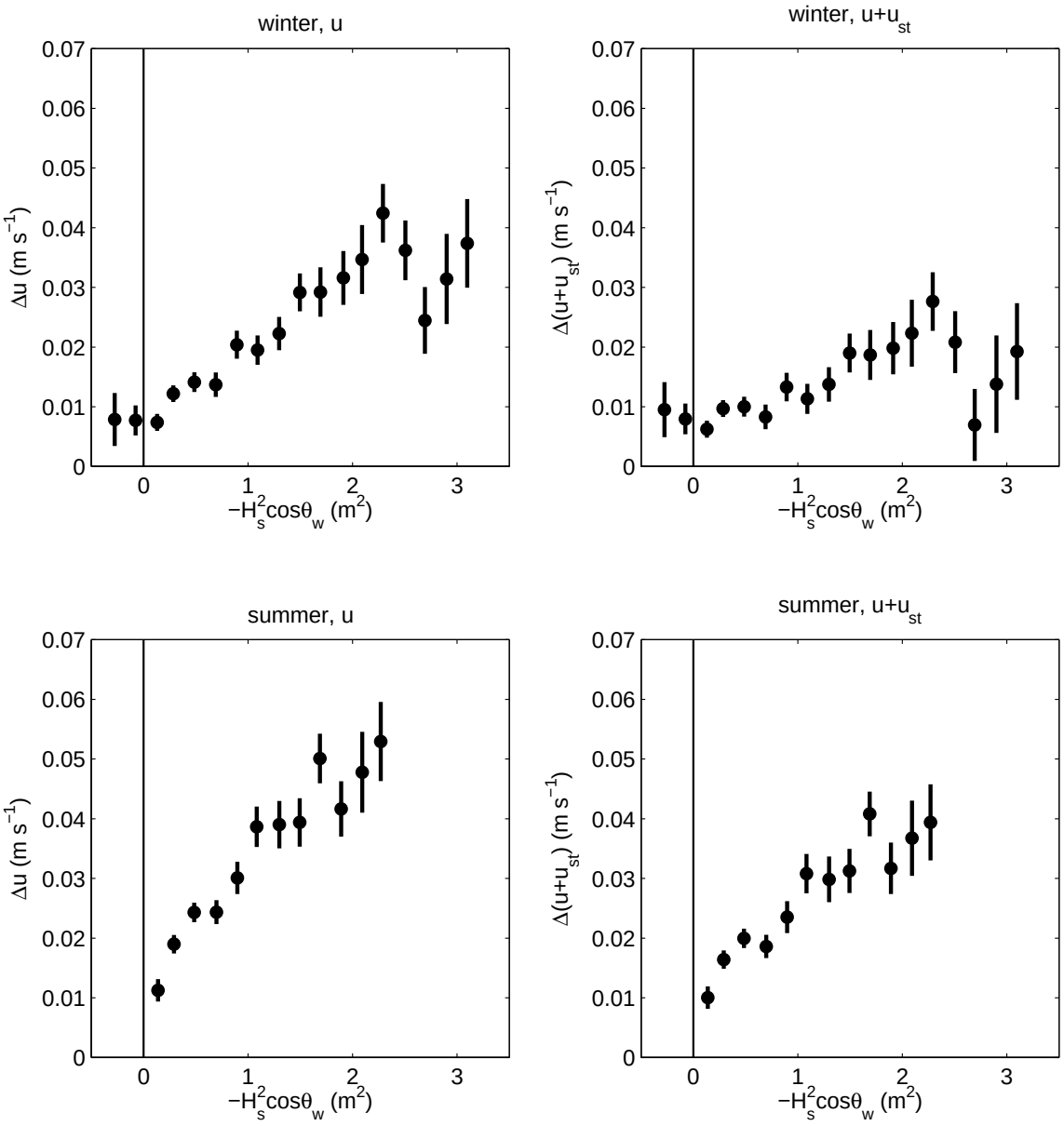

Figure 3-26: (Left) cross-shelf velocity difference Δu between near-surface and near-bottom ADCP bins, and (right) velocity difference including Stokes' drift, $\Delta(u+u_{st})$, at the Node, bin-averaged as a function of wave forcing in (top) winter and (bottom) summer, during times when wind stress was weak. In both winter and summer there is a "background" shear flow during small wave forcing that cannot be accounted for by the balance $u = -u_{st}$ (right panels); the near-surface flow is more offshore than the near-bottom flow. The "extra" shear in the cross-shelf flow is greater in summer than winter and increases with wave forcing (right panels).

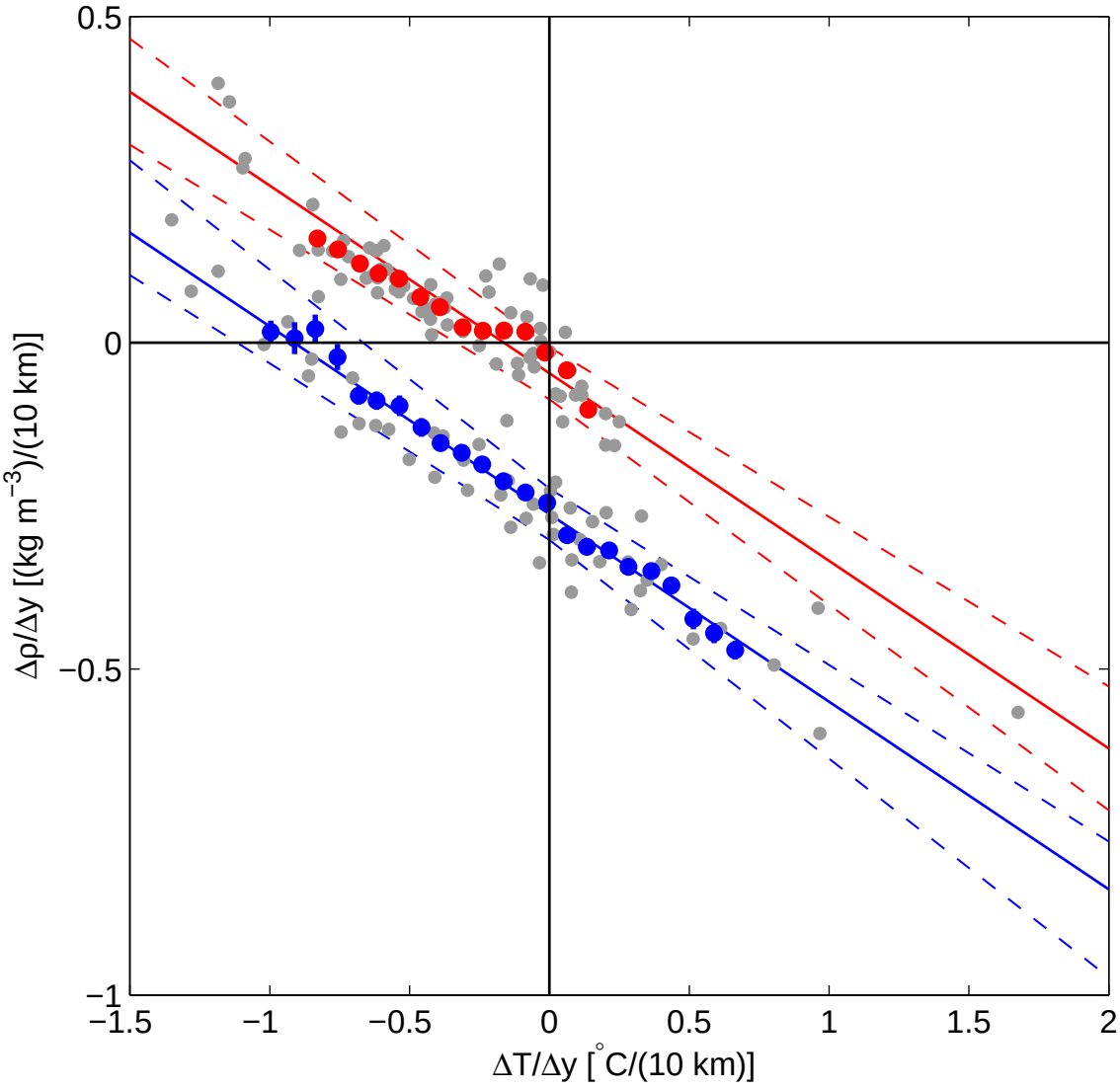

Figure 3-27: Comparison of along-shelf gradients of density and temperature, (blue) near bottom during 2001 and (red) near surface during 2003. Red and blue lines are best least-squares fits with 95% confidence intervals shown by dashed lines. Red and blue dots are bin-averaged values. Grey dots are subtidal data plotted every 33 hr, which are the points used to estimate the regression slopes and intercepts and correlation coefficients, but are a subset of the points that go into the bin averages. The vertical offset in the 2001 (blue) data is due to an uncertain conductivity offset; the 2001 data are only presented to show that the correlation between temperature and density is high near bottom as well as near the surface, and that the slopes are similar. The correlation is $r = -0.94$ ($r_{95\%} = 0.28$) in 2001 and $r = -0.93$ ($r_{95\%} = 0.24$) in 2003. The slope is -0.30 ± 0.03 in 2001 and -0.29 ± 0.03 in 2003. The intercept is $(-0.26 \pm .04)$ kg m^{-3} (10 km)$^{-1}$ in 2001 and (-0.05 ± 0.04) kg m^{-3} (10 km)$^{-1}$ in 2003.

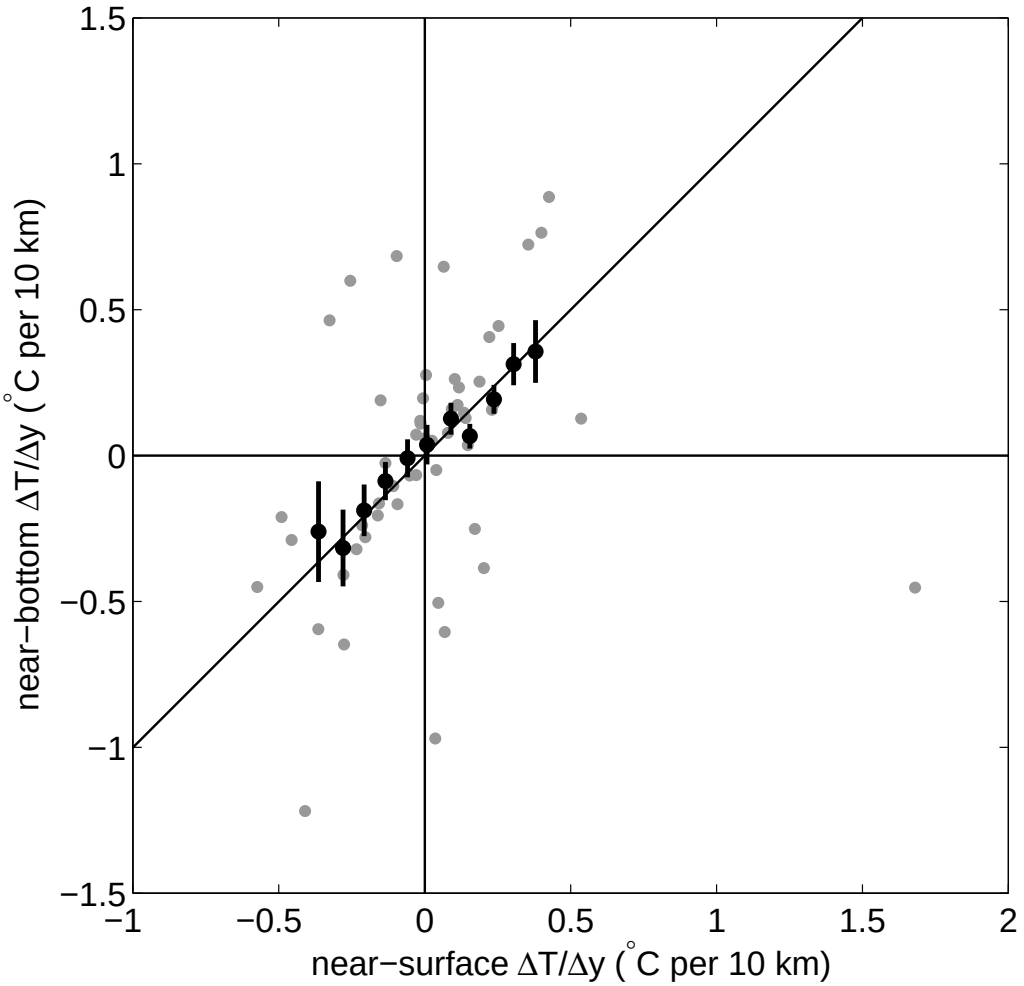

Figure 3-28: Near-surface versus near-bottom along-shelf temperature gradient during CBLAST 2003. Black symbols are bin-averaged values. Grey dots are subtidal data plotted every 33 hr, which are the points used to estimate correlation coefficient, but are a subset of the points that go into the bin averages. Diagonal line has slope 1. The 20-day low-pass filtered time series of near-surface and near-bottom temperature have been subtracted from the data shown, so the variables plotted here are subtidal departures from the (roughly) 20-day mean. The correlation is $r = 0.35$ ($r_{95\%} = 0.27$).

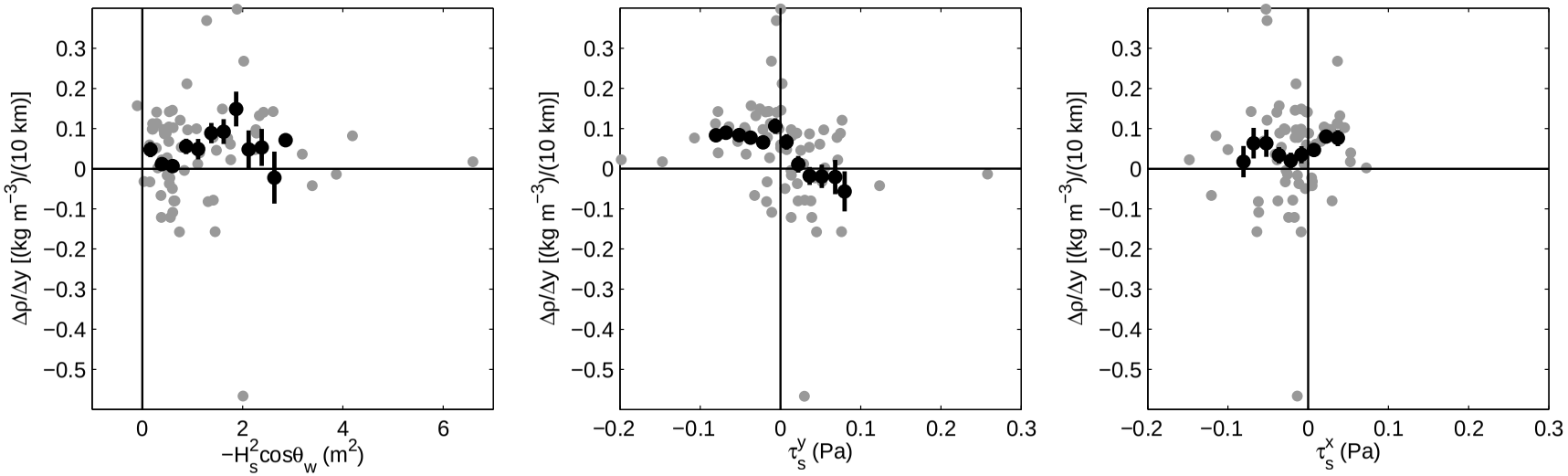

Figure 3-29: Near-surface along-shelf density gradient during CBLAST 2003 versus (left) wave forcing, (middle) along-shelf wind stress, and (right) cross-shelf wind stress. Black symbols are bin-averaged values. Grey dots are subtidal data plotted every 33 hr, which are the points used to estimate the correlation coefficients, but are a subset of the points that go into the bin averages. In the left and right panels, the correlation is not significant at the 95% confidence level, and in the middle panel the correlation is (barely) significant.

Chapter 4

A Heat Budget for the Inner Continental Shelf

This Chapter was prepared as a manuscript for future submission to *Journal of Physical Oceanography* or *Journal of Geophysical Research, Oceans*. The authors are Melanie Fewings and Steven Lentz. Appendices B–D are part of this manuscript.

4.1 Introduction

The continental shelf waters of the Middle Atlantic Bight off the northeastern United States display a strong seasonal variation in temperature (Bigelow, 1933; Fuglister, 1947; Ketchum et al., 1951; Beardsley and Flagg, 1976; Wright and Parker, 1976; Mayer et al., 1979; Beardsley and Boicourt, 1981; Han and Niedrauer, 1981; Beardsley et al., 1985; Linder and Gawarkiewicz, 1998; Lentz et al., 2003b; Mountain, 2003; Shearman and Lentz, 2003, and others). In winter the water temperature is near the freezing point, and in summer the near-surface temperature exceeds 20° C (Figure 4-1). The rise in water temperature in spring and summer over the middle and outer shelf is consistent with a local response to surface heating (*e.g.,* Austin, 1999; Flagg et al., 2002; Lentz et al., 2003a,b). Over the inner shelf (water depth less than $\sim$30 m), however, the water does not warm as much as expected for a balance between surface heating and change in local heat content (Figure 4-2). Apparently, advective transport

of heat cools the inner shelf in summer. The focus of this study is on that advective heat flux, which seems to control the temperature of the inner shelf waters on time scales of months but has previously been difficult to distinguish because it is masked by strong variability on time scales of days (*e.g.,* Austin, 1999).

On the West Coast of North America, cross-shelf advection of heat is an important cooling mechanism for the shelf waters on long time scales in summer, due to the prevailing upwelling-favorable wind stress (Halliwell and Allen, 1987; Strub et al., 1987) and the resulting persistent coastal upwelling circulation (*e.g.,* Lentz, 1987; Lentz and Chapman, 1989; Bryden et al., 1980; Dever and Lentz, 1994). In contrast, the wind stress in the Middle Atlantic Bight does not have a strong mean and the winds are generally weak in summer (Saunders, 1977; Lentz, 2007b), so the upwelling circulation at mid-shelf is weak in the Middle Atlantic Bight compared to on the West Coast.

On time scales of weeks to months, persistent advective cooling in water depths less than $\sim$25 m has never been directly observed in summer over the New England Shelf. Episodic upwelling events do lead to advective cooling of the inner shelf off New Jersey (Kohut et al., 2004) and North Carolina (Austin, 1999) on time scales of days and could produce a mean advective cooling over a time period of weeks. Figure 4-2 implies persistent advective cooling throughout the summer for the northern Middle Atlantic Bight, and the same was inferred off Virginia by comparing the surface heat flux and observed heat content (Bignami and Hopkins, 2003). A numerical modeling study of the summer 2002 heat budget in the northern Middle Atlantic Bight also demonstrated that the increase in water temperature on the inner shelf was smaller than expected from surface heating alone and that an advective heat flux divergence cooled the inner shelf (Wilkin, 2006), in agreement with Figure 4-2.

On shorter time scales (days to weeks), advective transport of heat is important both over the inner shelf and at mid-shelf. Cross-shelf and along-shelf advective heat flux divergences are important in the synoptic heat budget in the Middle Atlantic Bight (Austin, 1999), in the South Atlantic Bight (Atkinson et al., 1989), and off northern California (Lentz, 1987; Lentz and Chapman, 1989; Dever and Lentz, 1994).

In those studies, the cross-shelf advective heat flux was mainly driven by along-shelf wind stress forcing, through coastal upwelling and downwelling circulations. Other mechanisms can also be important for driving a cross-shelf heat flux. In the South Atlantic Bight, when the Gulf Stream interacts with the continental shelf it can drive cross-shelf heat transport across the shelf break (Atkinson et al., 1989); the inner continental shelf is typically spatially far removed from the shelf break, however, so we do not expect cross-shelf heat transport over the Middle Atlantic Bight inner shelf to be strongly influenced by the open ocean circulation.

Recently, a substantial cross-shelf circulation driven by surface gravity waves has been observed over the inner shelf, outside the surf zone (Appendix E). That wave-driven circulation is equal to or greater than the Stokes' drift velocity (Stokes, 1847), but opposite in direction. The strength of the wave-driven circulation suggests that it, and also the heat transport associated with Stokes' drift, may be important contributors to the advective heat flux over the inner shelf. In the heat budgets presented below, we include the effect of Stokes' drift, which has been neglected in previous studies.

We consider the heat balance of a New England inner shelf (water depths 12 m and 27 m) on synoptic and monthly time scales. To determine the relative importance of along-shelf and cross-shelf heat flux divergences when the inner-shelf heat balance departs from a one-dimensional balance, we estimate terms in the three-dimensional heat budget. We observe that the cross-shelf advective heat flux divergence is the dominant cooling mechanism in 12 m and 27 m water on time scales of weeks to months throughout the summer and that Stokes' drift due to surface gravity waves contribute substantially to that heat flux.

4.2 Data

From 2001 through 2007, the near-bottom temperature and the velocity throughout the water column were measured on the 12-m isobath near Martha's Vineyard, on the inner continental shelf of the northeastern United States (Figure 4-3). During

summer/fall 2003 and winter/spring 2004-2005, water temperature and velocity were measured at several depths throughout the water column on the 12-m and 27-m isobaths.

4.2.1 2001-2007: MVCO

At the Martha's Vineyard Coastal Observatory (MVCO) (Figure 4-3), measurements of wind speed and direction, air temperature and pressure, relative humidity, incoming shortwave and longwave radiation, water velocity and temperature, and bottom pressure have been collected since 2001 (Austin et al., 2002). Descriptions of the instruments and data are available at http://www.whoi.edu/mvco. We used the wind velocity measured 12.5 m above sea level on meteorological masts at 41°21.0'N, 70°31.6'W and 41°21.72'N, 70°31.35'W on Martha's Vineyard to calculate wind stress from the Smith (1988) bulk formula. The wind stress and wind velocity values have been linearly adjusted to match the shorter time series of wind measurements at the air-sea interaction tower (ASIT), to better represent the wind stress over the water; the details of the wind stress adjustments are described in Chapter 2. The water velocity and near-bottom temperature and pressure are measured at an underwater node site (Node) on the 12-m isobath, 1.5 km from shore at 41°20.2'N, 70°33.39'W, by a bottom-mounted acoustic Doppler current profiler (ADCP) and temperature and pressure sensors. All the MVCO Node instruments are connected to shore by underwater power and fiber-optic data transmission cables. This capability for continuous data transmission to shore enables the water velocity to be recorded at 2 Hz for long periods of time, so the dominant surface waves are resolved throughout the time series. The 20-min averaged data used here extend from 19 June 2001 to 10 May 2007, although there are several gaps of at least one month in length. The ADCP is a 1200-kHz RDI Workhorse Monitor and records water velocity in 0.5-m bins, from $z = -9.5$ m to $z = -2.0$ m, where $z = 0$ is the mean water level and z is positive upward. The dominant wave characteristics were calculated from the ADCP and bottom pressure data as described at www.whoi.edu/mvco. The water velocity data were de-tided with T_TIDE (Pawlowicz et al., 2002) and low-pass filtered with a half-

amplitude cutoff of 33 hr^{-1} (Flagg et al., 1976; Limeburner et al., 1983). The wind stress, surface heat flux, wave parameters, and water temperature data were low-pass filtered similarly. More details of the data processing for the MVCO time series can be found in Chapter 2.

4.2.2 Summer and Fall 2003: CBLAST

During the 2003 field season of the Coupled Boundary Layers Air-Sea Transfer experiment (CBLAST), Low-Wind Component, numerous surface moorings were deployed in the MVCO area and extending farther offshore (Edson et al., 2007). Here, we use water temperature data from mooring F on the 27-m isobath (Figure 4-3; Table 4.1).

Additional moorings were deployed to measure temperature throughout the water column near the Node and along-shelf east (T1, 41°19.55'N, 70°43.34'W) and west (T2, 41°19.22'N, 70°31.85'W) of the Node on the 15-m isobath (Figure 4-3; Table 4.1). A second deployment at site F was carried out following CBLAST 2003, through 17 October 2003. Instrument depths and deployment dates are given in Table 4.1. A bottom-mounted ADCP was deployed near mooring F and recorded 1-min velocity averages.

All the CBLAST 2003 and supplementary instruments used here had faster than 20-min sample rates. The data have been averaged onto a 20-min interval time base to match the MVCO online data, and then low-pass filtered in the same way as the MVCO data.

4.2.3 Winter and Spring 2004–2005: SWWIM I

To supplement the MVCO water velocity and bottom temperature measurements during winter, the first Stratification, Wind, and Waves on the Inner shelf at MVCO field program (SWWIM I) was carried out from 7 December 2004 to 23 May 2005. Moored temperature sensors were deployed approximately 150 m west of the MVCO Node, at 41°20.22'N, 70°33.50'W. The instruments were Sea-Bird Electronics SBE-37 MicroCATs and Onset Computer Corporation StowAway TidbiT Temperature

Loggers (Table 4.2).

In addition, during SWWIM I a bottom-mounted 600-kHz RDI Workhorse ADCP and moored temperature sensors were deployed on the 27-m isobath at site F (same location as CBLAST 2003 site F; Figure 4-3, Table 4.2). The ADCP was at 41°15.22'N, 70°35.84'W and the temperature mooring was at 41°15.27'N, 70°35.77'W, 130 m southeast of the ADCP. A Sea-Bird Electronics SBE 26*plus* Seagauge Wave and Tide Recorder was mounted on the ADCP tripod to measure temperature and pressure at 27-m depth. The ADCP had 0.5-m bins from $z = -24.5$ m to $z = -3.0$ m.

The MicroCATs sampled temperature every 2.5 min, the TidbiTs recorded temperature every 10 min, and the Seagauge recorded temperature and average pressure every 20 min. The ADCP in 27-m water depth recorded velocity every 20 min by pinging at 2 Hz for 5 minutes (to conserve battery power, avoid aliasing the surface waves, and average over many wave periods). All the SWWIM I data were averaged onto a 20-min interval time base to match the MVCO online data, and then low-pass filtered in the same way as the MVCO data. The TidbiT temperatures have been adjusted based on the MicroCAT temperatures as described in Appendix B.

4.2.4 The Composite Year

We do not have measurements of temperature throughout the water column that extend for a full year. Instead, in some of the following sections we construct a composite year from the SWWIM I and CBLAST 2003 data by first plotting the latter part of the SWWIM I data (January through May), then the CBLAST 2003 data (July through October), followed by the first part of SWWIM I (December to January 1).

The near-bottom water temperature at MVCO and the external forcing conditions (air temperature, relative humidity, wind stress, solar and infrared radiation, and wave height) on time scales of weeks to months during CBLAST 2003 and SWWIM I (black lines) were generally within the envelope of all other observations at MVCO during 2001-2007 (grey shaded areas in Figures 4-1, 4-6, and 4-7). Therefore, we assume the water-column temperatures measured during CBLAST 2003 and SWWIM I are

representative of a typical year at MVCO.

4.3 Methods

4.3.1 Coordinate System

At each mooring location, the water velocity $\boldsymbol{u} = (u, v, w)$ and the wind stress $\boldsymbol{\tau_s} = (\tau_s^x, \tau_s^y, 0)$ are rotated into a local coordinate system, with x positive offshore and y positive along-shelf eastward (Figure 4-3). The along- and cross-shelf directions are defined according to the principal axes of the subtidal depth-averaged flow when waves are small (Appendix E). The resulting along-shelf direction, measured clockwise from due east, is 5.5° at the Node, and 20° and 11° at F during CBLAST 2003 and SWWIM I respectively. The difference in principal axis directions during the two deployments at F is likely due to uncertainty in the compass calibrations during the two ADCP deployments.

4.3.2 Time Scales

We consider variations in water temperature and circulation and surface heat flux on three time scales: high-frequency, synoptic, and low-frequency. Here, high-frequency fluctuations have time scales from 20 min (the sampling period of the data) to $\sim$33 hr and include tidal variability. Synoptic fluctuations have time scales from $\sim$33 hr to a few days and include "weather-band" variability. Low-frequency fluctuations have time scales of a few days to months. We isolate the high-frequency from the synoptic and low-frequency fluctuations with a 33-hr filter (Section 4.2.1), and isolate the synoptic and low-frequency fluctuations from each other with a 7- or 10-day filter of the same form.

4.3.3 1-D Heat Budget: No Advection

The temperature balance equation at a point (x, y, z), neglecting advection and lateral diffusion of heat, is

$$\frac{\partial T(x,y,z,t)}{\partial t} = \frac{1}{\rho_0 c_p}\frac{\partial}{\partial z}K_T\frac{\partial T}{\partial z} \tag{4.1}$$

where T is water temperature, t is time, $\rho_0 = 1025$ kg m^{-3} is a reference density of seawater, c_p is the specific heat capacity of seawater (4010 J kg^{-1} °C^{-1}), and K_T is the turbulent vertical diffusivity. The surface heat flux, including penetrating solar radiation, is incorporated in the term for vertical turbulent mixing of temperature. Vertical integration with the boundary conditions

$$K_T\frac{\partial T}{\partial z}\bigg|_{z=0} = Q_s \tag{4.2}$$

$$K_T\frac{\partial T}{\partial z}\bigg|_{z=-h} = 0 \tag{4.3}$$

where Q_s is the net surface heat flux gives a prediction for the change in depth-average temperature $\langle T\rangle$ with time:

$$\frac{\partial\langle T\rangle}{\partial t} = \frac{Q_s}{\rho_0 c_p h} \tag{4.4}$$

where

$$\langle T\rangle = \frac{1}{h}\int_{-h}^{0} T\,dz \tag{4.5}$$

and h is water depth. See Section 4.3.5 for discussion of the validity of Eq. (4.3).

If the temperature balance is one-dimensional (*i.e.*, no dependence on horizontal position), then from Eq. (4.4), the change in depth-average water temperature over time at a water depth h is determined solely by the surface heat flux:

$$\Delta\langle T\rangle = \frac{1}{\rho_0 c_p h}\int_0^t Q_s(t_1)\,dt_1 \tag{4.6}$$

where $\Delta\langle T\rangle(t) = \langle T\rangle(t) - \langle T\rangle|_{t=0}$. Eq. 4.6 with $Q_s = 140$ W m^{-2} was used to produce the predicted curve in Figure 4-2.

4.3.4 3-D Heat Budget Equation with Advection for a Wedge with Waves

We define the observed area-average temperature of the wedge onshore of a mooring at $x = L$ as

$$\langle\langle T \rangle\rangle \equiv \frac{1}{A} \int_0^L \int_{-h}^0 T \, dz \, dx \tag{4.7}$$

where $h(x)$ is water depth and A is the area of the wedge. The three-dimensional temperature balance equation for the wedge, including wave-driven heat fluxes, is derived in Section D.3 and is

$$\begin{aligned} \frac{\partial}{\partial t} \int_0^L \int_{-h}^0 T \, dz \, dx + \left[\int_{-h}^0 (u + u_{st}) \, \widetilde{T} dz \right] \Big|_{x=L} \\ + \int_0^L \frac{\partial}{\partial y} \left\{ \int_{-h}^0 \left[v \left(T - \langle T \rangle_L \right) - \frac{\omega H_{sig}^2 \sin\theta_w}{16} \frac{\partial T}{\partial z} F(z) G(z) \right] dz \right. \\ \left. + \frac{g H_{sig}^2 \sin\theta_w}{16c} \left(T - \langle T \rangle_L \right) \big|_{z=0} \right\} dx = \int_0^L \frac{Q_s}{\rho_0 c_p} \, dx \end{aligned} \tag{4.8}$$

where u_{st} is the x component of the Stokes' drift velocity [Eq. (D.40)], $\widetilde{T}$ is the depth-varying part of the temperature profile, $\langle T \rangle$ is the depth-average temperature (so that $T = \langle T \rangle + \widetilde{T}$), $\langle T \rangle_L$ is the depth-average temperature at $x = L$, ω is the angular frequency of the dominant waves, H_{sig} is the significant wave height, θ_w is the direction in which the dominant waves are propagating (measured counterclockwise from the positive x direction), $G(z)$ and $F(z)$ are vertical structure functions [Eqs. (D.5) and (D.7)], g is the acceleration due to gravity, and c is the phase speed of the dominant waves. Waves propagating directly onshore have $\theta_w = 180°$.

We can write Eq. (4.8) as an expression for the time rate of change of $\langle\langle T \rangle\rangle$ due to surface, cross-shelf, and along-shelf heat fluxes:

$$\langle\langle T \rangle\rangle_t = \frac{1}{\rho_0 c_p A} \left(H^s + H^{xs} + H^{as} \right) \tag{4.9}$$

where the subscript t represents a partial derivative with respect to time, and the H

variables are heat fluxes into the wedge, per unit along-shelf length (units W m^{-1}):

$$H^s = \int_0^L Q_s \, dx \tag{4.10}$$

is due to surface heating,

$$H^{xs} = -\rho_0 c_p \int_{-h}^{0} (u + u_{st}) \, \widetilde{T} \, dz \Big|_{x=L} \tag{4.11}$$

is due to cross-shelf heat flux divergence, which we decompose into

$$H^{xs}_{circ} = -\rho_0 c_p \int_{-h}^{0} u \widetilde{T} \, dz \Big|_{x=L} \tag{4.12}$$

due to the (depth-varying part of the) cross-shelf circulation observed by the ADCP, and

$$H^{xs}_{waves} = -\rho_0 c_p \int_{-h}^{0} u_{st} \widetilde{T} \, dz \Big|_{x=L} \tag{4.13}$$

due to the Stokes' drift associated with surface gravity waves, so that

$$H^{xs} = H^{xs}_{circ} + H^{xs}_{waves} \tag{4.14}$$

and

$$H^{as} = -\rho_0 c_p \int_0^L \frac{\partial}{\partial y} \left\{ \int_{-h}^{0} \left[v \left(T - \langle T \rangle_L \right) - \frac{\omega H_{sig}^2 \sin\theta_w}{16} \frac{\partial T}{\partial z} F(z) G(z) \right] dz \right. \\ \left. + \frac{g H_{sig}^2 \sin\theta_w}{16 c} \left(T - \langle T \rangle_L \right)|_{z=0} \right\} dx \tag{4.15}$$

is due to divergence of the along-shelf heat flux. The first term in the vertical integral in Eq. (4.15) represents advection of the along-shelf temperature field, and leads to an along-shelf heat flux divergence (via the $\partial/\partial y$ in front of the vertical integral) when there is an along-shelf temperature gradient or a divergence in the along-shelf flow. The two terms involving wave variables are only nonzero if the waves are not propagating directly onshore or offshore, and represent along-shelf heat flux divergence due

to along-shelf variations in wave properties or water temperature.

4.3.5 2-D, 2-Layer Model

We compare the observed temperature variation on time scales of weeks at the Node in summer with a two-dimensional two-layer model in which there is a steady balance between the surface heat flux and the cross-shelf heat flux, and $\partial T/\partial t$ and H^{as} are small. Then T is always in steady state, but the steady state slowly evolves due to the seasonal variations of surface heat flux, cross-shelf heat flux, and vertical mixing.

In the model, there is a flat bottom at depth $z = -h$, a coastline at $x = 0$, and a mooring at $x = L$ (Figure 4-4). The interface between the layers is at a fixed depth $z = -d$. The cross-shelf circulation is constant in x and z within each layer, except for a thin region near the coast ($0 < x < \epsilon$ where $\epsilon \ll L$) where the cross-shelf velocity goes to zero in each layer and upwelling occurs. The circulation is two-dimensional (uniform in the along-shelf direction), so $\partial/\partial y = 0$. Then the temperature balance Eq. (D.15) becomes

$$\frac{\partial (uT)}{\partial x} + \frac{\partial (wT)}{\partial z} = \frac{\partial}{\partial z} K_T \frac{\partial T}{\partial z} \tag{4.16}$$

where $K_T(x, z, t)$ is the turbulent diffusivity of heat. With a coastal boundary condition of no net cross-shelf flow,

$$\int_{-h}^{0} u \, dz = 0 \tag{4.17}$$

the two layers must have equal and opposite volume transports. We define the magnitude of those transports as U_0:

$$u = \frac{U_0}{d} \text{ for } -d < z < 0 \tag{4.18}$$

$$u = -\frac{U_0}{h - d} \text{ for } -h < z < -d \tag{4.19}$$

The water temperature is constant in z within each layer:

$$T = T_1 \text{ for } -d < z < 0 \tag{4.20}$$

$$T = T_2 \text{ for } -h < z < -d \tag{4.21}$$

but can vary with offshore distance. Using a rigid-lid approximation and assuming no heat flux through the bottom, we apply the boundary conditions

$$w|_{z=0} = 0 \tag{4.22}$$

$$w|_{z=-h} = 0 \tag{4.23}$$

$$K_T \frac{\partial T}{\partial z}\bigg|_{z=0} = \frac{Q_s}{\rho_0 c_p} \tag{4.24}$$

$$K_T \frac{\partial T}{\partial z}\bigg|_{z=-h} = 0 \tag{4.25}$$

See the end of this section for discussion of the surface and bottom boundary conditions. We define an interfacial diffusivity K_T^* such that

$$K_T \frac{\partial T}{\partial z}\bigg|_{z=-d} = K_T^* \left(\frac{T_1 - T_2}{h} \right) \tag{4.26}$$

Note that K_T^*/h can also be thought of as an entrainment velocity w_e across the layer interface:

$$K_T \frac{\partial T}{\partial z}\bigg|_{z=-d} = w_e \left(T_1 - T_2 \right) \tag{4.27}$$

For $x > \epsilon$ a vertical integral of Eq. (4.16) over the surface layer gives

$$U_0 \frac{\partial T_1}{\partial x} = \frac{Q_s}{\rho_0 c_p} - w_e \left(T_1 - T_2 \right) \tag{4.28}$$

and over the bottom layer gives

$$-U_0 \frac{\partial T_2}{\partial x} = w_e \left(T_1 - T_2 \right) \tag{4.29}$$

If we define the vertical temperature stratification in the model as

$$\Delta T \equiv T_1 - T_2 \tag{4.30}$$

then adding Eq. (4.28) and Eq. (4.29) yields

$$U_0 \frac{\partial \Delta T}{\partial x} = \frac{Q_s}{\rho_0 c_p} \tag{4.31}$$

Assuming the surface heat flux Q_s is constant in the cross-shelf direction, and setting $T_1 = T_2$ or $\Delta T = 0$ at $x = \epsilon \approx 0$, the temperature stratification as a function of cross-shelf position in the model is

$$\Delta T = \frac{Q_s}{\rho_0 c_p} \frac{x}{U_0} \tag{4.32}$$

The vertical temperature stratification ΔT does not depend on the vertical diffusivity (or entrainment velocity) in this model. In steady state, the net heat flux into the volume onshore of any location x must be zero. Therefore, ΔT adjusts so that the total cross-shelf advective heat flux $\rho_0 c_p U_0 \Delta T / x$ balances the surface heat flux Q_s at every location x independent of the entrainment velocity (as in Eq. (4.32)). The steady-state ΔT is determined by the surface heat flux and the cross-shelf circulation. Only the depth-average temperature $\langle T \rangle$ depends on the entrainment velocity.

The depth-average temperature is

$$\langle T \rangle \equiv \frac{1}{h} \left[T_1 d + T_2 \left(h - d \right) \right] \tag{4.33}$$

Combining Eq. (4.28) and Eq. (4.29), the cross-shelf temperature structure is given by

$$\frac{\partial \langle T \rangle}{\partial x} = \frac{Q_s}{\rho_0 c_p} \frac{1}{U_0} \left(\frac{d}{h} - \frac{w_e}{U_0} x \right) \tag{4.34}$$

The cross-shelf temperature gradient in the model is positive near shore:

$$\frac{\partial \langle T \rangle}{\partial x} > 0 \qquad \text{for} \qquad x < \frac{U_0}{w_e} \frac{d}{h} \tag{4.35}$$

The surface and bottom boundary conditions used in the model (no penetrating radiation, and no heat flux through the bottom) require some justification. The two-layer model assumes all the surface heat flux is absorbed within the top layer. In reality, some of the solar radiation does penetrate into the lower half of the water column. To estimate the fraction of solar radiation remaining in the water column I/I_0 as a function of depth at MVCO, we use the Paulson and Simpson (1977) double exponential formula $I/I_0 = Re^{z/\zeta_1} + (1-R)e^{z/\zeta_2}$ with the coefficients for Jerlov (1968) coastal water Type III: $R = 0.78$, $\zeta_1 = 1.4$ m, and $\zeta_2 = 7.9$ m. Predictions from this formula compared well to observations at ~ 4 m depth on the 15-m isobath near MVCO in summer 2003 (*personal communication, G. Gerbi*). Based on the observed mean values of net surface heat flux Q_s and net solar radiation at the surface from August 2003, and with $I/I_0 = 0.125$ for a layer interface depth of $z = -5.5$ m, about 17% of the surface heat flux penetrates into the lower layer. We neglect this when comparing the two-layer model with observations.

The two-layer model, and the calculations of terms in the observed heat budget, assume all of the shortwave radiation is absorbed within the water column and no solar energy reaches the bottom [Eq. (D.23)]. Using the Paulson and Simpson (1977) formula and August observed heat fluxes, only 7% of the net surface heat flux penetrates to the bottom at the Node, so this is a reasonable assumption. We also neglect conductive heat transfer into the bottom.

4.4 Results

4.4.1 Observed Annual Cycle of Temperature

Water temperature in the MVCO area shows a pronounced annual cycle, with a maximum near-surface temperature of 23.6°C at F during CBLAST 2003, and a minimum temperature of −1.2°C at the Node during SWWIM I (Figure 4-1). During the six years 2001-2007, the near-bottom water temperature at the MVCO Node ranged from −1.8°C to 21.6°C. Synoptic variations (variations on time scales of a few days) about

the seasonal cycle are an order of magnitude smaller than the seasonal cycle itself: the standard deviation of synoptic variations in near-bottom water temperature at MVCO (time scales $>$ 33 hr) relative to the 10-day low-pass filtered temperature is only 0.3°C, and the variations have a maximum of 1.2°C and a minimum of -2.2°C, whereas the seasonal variation in depth-average temperature is 15–20°C at both sites.

The vertical temperature stratification also has a strong seasonal cycle (Figure 4-5, top). The thermal stratification reached a maximum of 0.3°C m^{-1} in August 2003 at both Node and F, although the thermal stratification was generally stronger at F than at the Node in late summer (August and early September). In winter, the temperature stratification at the Node is often negative (coldest water near the surface) on synoptic time scales: during December 2004 through February 2005 the thermal stratification reached a minimum of -0.03°C m^{-1}. The (negative) temperature stratification at F was weaker than at the Node in winter. In both summer and winter, the synoptic variations in temperature stratification are substantial at the Node and F; the inner shelf can go from unstratified to relatively strongly stratified ($>$ 2°C difference over the water column) within a couple of days, for example during September 2003 (Figure 4-5, top).

The cross-shelf temperature difference between the 12-m and 27-m isobaths (separated by $\sim$10 km) also varies between summer and winter, although not as consistently as the stratification or the absolute temperature. Generally, the depth-average temperature at the Node is warmer than the depth-average temperature in the top 12 m at F in summer, and colder in winter (Figure 4-5, bottom), so that the cross-shelf temperature gradient in the upper water column is positive in winter and negative in summer. The cross-shelf temperature difference displays substantial synoptic variability, however, and occasionally changes sign in both summer (August) and late winter (January-March).

4.4.2 Surface Heat Flux

At MVCO, the net surface heat flux is on average positive (ocean warming) on synoptic and longer time scales from mid-March through the end of September, and

negative (ocean cooling) from October through mid-March (Figure 4-6a). The pronounced seasonal cycle in net surface heat flux, with maximum heating in June and July, is partly due to the seasonal cycle in solar radiation (Figure 4-6b). The longwave, evaporative, and sensible components of the surface heat flux are an order of magnitude smaller than the shortwave heat flux in summer, and comparable in size to the shortwave heat flux in winter, but are almost always negative (ocean cooling; Figure 4-6c,d). Evaporative cooling is strongest in late fall when the water is still relatively warm but there are large wind stress events that bring cold dry air off the continent, and weakest in summer when the wind stress is small and atmospheric relative humidity is high (Figures 4-6d and 4-7). The sensible heat loss is largest in winter because the water is warm compared to the cold air that blows off the continent during the passage of synoptic weather systems (Figure 4-6e). In late summer when the water is colder than the air on average, the sensible heat flux warms the ocean but its magnitude is much smaller than in winter. These results are consistent with previous studies of surface heat flux in the Middle Atlantic Bight (Bunker, 1976; Joyce, 1987; Austin and Lentz, 1999), over nearby Georges Bank (Beardsley et al., 2003), and in the Gulf of Maine (Mountain et al., 1996).

4.4.3 Heat Budget on Synoptic Time Scales

In this section, we consider variations in water temperature on time scales of a few days, the time scales associated with synoptic weather systems. Seasonal variations in temperature (with time scales of weeks to months) are considered in Section 4.4.4. To determine whether the variations in water temperature on time scales of days described in Section 4.4.1 can be explained by the observed surface heating and advective heat flux divergences, we compare the terms in Eq. (4.9) (Figure 4-8). We also compared the local temperature change and surface heating terms in Eq. (4.4); the results for the relation between water temperature and surface heating for that 1-D analysis are similar to the results presented here for the wedge-shaped volume.

Onshore of the Node in summer, the surface (red) and cross-shelf (green) heat fluxes and the changes in local heat content (blue) are all of similar size (Figure 4-8,

upper left). The part of the along-shelf heat flux divergence we can estimate (black line) is smaller than the other terms but not negligible. Onshore of the Node in winter, the surface heat flux and change in local heat content have a tendency to balance and the cross-shelf heat flux is relatively small on synoptic time scales (Figure 4-8, upper right). On longer time scales onshore of the Node, there is a tendency for the surface and cross-shelf heat fluxes to balance in summer; that balance is discussed in Section 4.4.4.

Onshore of F in summer, the surface heat flux is less important than the cross-shelf heat flux and changes in heat content, which are both large terms but do not balance (Figure 4-8, lower left). Onshore of F in winter, the cross-shelf heat flux is negligible and changes in local heat content are large compared to the surface heat flux term (Figure 4-8, lower right). The residual in the synoptic heat budget (not shown) is large in both seasons at both mooring locations and probably indicates that divergence of the along-shelf heat flux is important.

The surface heat flux variations are more substantial compared to the variations in local heat content onshore of the Node than onshore of F, because the water is twice as shallow at the Node so the influence of the surface heating is larger. There is a significant correlation between local temperature changes and surface heating at both sites, however (Table 4.3). The correlation is stronger at the Node than at F and during stratified than unstratified times. Still, the local heat content at both Node and F varies far more (twice as much at the Node, and four times as much at F) on synoptic time scales than can be accounted for by the surface heat flux alone, as measured by the standard deviations of those terms on subtidal time scales (Table 4.3).

When the temperature stratification is small, the synoptic heat budget at the Node is closer to a 1-D balance (between surface heating and local temperature change) than when the temperature stratification is strong. When the temperature difference between the near-surface and near-bottom instruments at the Node is less than 0.2°C, about 70% of the synoptic variation in water temperature at the Node can be explained by the surface heat flux ($r^2 = 0.68$ in Table 4.3). In contrast, during

stratified times at the Node and all times at F, the surface heating fluctuations are only large enough to explain 35–60% of the synoptic variation in water temperature.

To determine whether the part of the synoptic variance in water temperature that is not explained by surface heating [$\sim 30\%$ (40%) at the Node (F) in winter, and $\sim 50\%$ (65%) at the Node (F) in summer] can be explained by cross-shelf advection of heat, we compare the left-hand side of Eq. (4.9) with the first two terms on the right-hand side of Eq. (4.9).

During unstratified conditions (when the cross-shelf heat flux is expected to be small because the temperature is vertically uniform), synoptic variations in surface heat flux together with cross-shelf heat flux explain no more of the variance in water volume heating than is explained by the surface heat flux alone, at either site (see r^2 columns in Table 4.3). During stratified conditions, however, the surface and cross-shelf heat fluxes together explain 20-25% more of the variance than does the surface heat flux alone (Table 4.3).

About 30% of the variance in water temperature on time scales of days at the Node, and 40-45% at F, remains unexplained by our surface and cross-shelf heat flux estimates. Although some of that variance is probably due to errors in our estimates of the heat budget terms, the unexplained variance in the synoptic heat balance likely indicates that the along-shelf heat flux divergence is an important contribution to the heat budget on time scales of days in both summer and winter (Figure 4-8). We can estimate part of the along-shelf heat flux divergence at the Node in summer (H_{adv}^{as}), and that term is nearly as large as the surface heat flux.

In a heat budget on the North Carolina inner shelf, the net surface heat flux and the along-shelf wind stress were strongly positively correlated, due to the northwest-southeast orientation of the coastline, and the usually northeastward passage of synoptic weather systems (Austin, 1999). Also, the along-shelf heat flux was driven by the along-shelf wind stress through coastal upwelling and downwelling on time scales of days. As a result, there was a correlation between the surface heat flux and the along-shelf heat flux on synoptic time scales. In contrast, at MVCO where the coastline runs east-west, the net surface heat flux and along-shelf wind stress are only

weakly correlated, with a positive correlation in summer and negative in winter (Table 4.4). The cross-shelf wind stress and surface heat flux are negatively correlated in both summer and winter.

During winter, the unstable temperature stratification on the inner shelf (Section 4.4.1) leads to advective warming of the inner shelf when the cross-shelf circulation is upwelling. For example, in February 2005, with the exception of two synoptic events the subtidal cross-shelf velocity $u+u_{st}$ in the upper half of the water column at the Node was always positive (upwelling) (Figure 4-9, top). During the same period, the temperature stratification was nearly always inverted (coldest water near the surface; Figure 4-9, middle). As a result, the cross-shelf heat flux was warming the inner shelf during the upwelling circulation (Figure 4-9, bottom). The temperature difference between near-surface and bottom and the cross-shelf heat flux at the Node were significantly correlated, with $r^2 = 0.37$ ($r^2 > 0.20$ is significant at the 95% confidence level), and the cross-shelf heat flux was of the same order as the other terms in the heat budget during February (see green line in upper left panel of Figure 4-8, and compare to surface heat flux in bottom panel of Figure 4-9).

The observed temperature inversion in winter (Figure 4-5, top) is consistent with previous observations of inverted temperature stratification in winter over large areas of the Middle Atlantic Bight continental shelf, including southwest of Martha's Vineyard (*e.g.* Bigelow, 1933). The observed temperature inversion cannot be sustained by pressure effects; the potential temperature is also inverted. The inverted temperature stratification was confirmed by the surface and bottom MicroCAT instruments (Table 4.2) so it is not an artifact of the adjustments made to the TidBiT temperatures (Appendix B). The inverted temperature stratification is consistent with the presence of fresh water near the surface that stabilizes the density stratification in winter. We do not have measurements of the salinity stratification at the Node in winter, but we can calculate an upper bound on the vertical mixing in order for the inverted temperature stratification to be sustained without a compensating salinity stratification, as follows. Since the actual estimated vertical mixing is large compared to that upper bound, the temperature inversion is too large to be simply the result

of strong surface cooling.

If the surface heat loss is turbulently transferred to depth so there is a 1-D temperature balance

$$\frac{\partial}{\partial z}\left(K_T \frac{\partial T}{\partial z}\right) = \frac{\partial T}{\partial t} \tag{4.36}$$

then integrating vertically with the surface boundary condition $K_T \partial T/\partial z|_{z=0} = Q_s/\rho_0 c_p$ gives

$$K_T \frac{\partial T}{\partial z} = \frac{Q_s}{\rho_0 c_p} - \int_z^0 \frac{\partial T}{\partial t}\, dz' \tag{4.37}$$

If we assume the temperature stratification is constant horizontally and in time, the temperature profile is

$$T(z,t) = T_s(t) + Sz \tag{4.38}$$

where T_s is the sea-surface temperature and $S = \partial T/\partial z$ is a constant. The time rate of change of temperature is then independent of z:

$$\frac{\partial T}{\partial t} = \frac{\partial T_s}{\partial t} \tag{4.39}$$

so Eq. (4.37) becomes

$$K_T \frac{\partial T}{\partial z} = \frac{Q_s}{\rho_0 c_p} - \frac{\partial T_s}{\partial t} \int_z^0 dz' \tag{4.40}$$

$$K_T \frac{\partial T}{\partial z} = \frac{Q_s}{\rho_0 c_p} + \frac{\partial T_s}{\partial t} z \tag{4.41}$$

Evaluating the above equation at $z = -h$ by assuming no heat flux into the bottom $\left(K_T \partial T/\partial z|_{z=-h} = 0\right)$ gives

$$\frac{\partial T_s}{\partial t} = \frac{Q_s}{\rho_0 c_p h} \tag{4.42}$$

which, combined with Eq. (4.41), yields

$$K_T \frac{\partial T}{\partial z} = \frac{Q_s}{\rho_0 c_p}\left(1 + \frac{z}{h}\right) \tag{4.43}$$

Integrating vertically gives

$$\frac{\partial T}{\partial z}\langle K_T \rangle = \frac{Q_s}{2\rho_0 c_p} \tag{4.44}$$

where $\langle K_T \rangle$ is the vertically averaged turbulent diffusivity. Then for typical February 2005 values of $\partial T/\partial z \sim (-0.1°\text{C})/(11\text{ m})$ and $Q_s \sim -100$ W m^{-2}, the turbulent vertical diffusivity should be no larger than $\langle K_T \rangle \sim \text{O}\,(10^{-3})$ m^2 s^{-1} if the observed temperature gradient is sustained by surface cooling. The K profile parameterization (Large et al., 1994) predicts $K_T \sim \text{O}\,(10^{-1})$ m^2 s^{-1} for the observed forcing, however, and direct covariance estimates in the MVCO area in October 2003 indicated K_T was approximately twice as large on average as the K profile parameterization estimates (Gerbi et al., under revision). Another indication that the temperature inversions in February are not due to surface cooling but likely due to freshwater near the surface stabilizing the density stratification is that the net surface heat flux was positive during the first half of February 2005, while the temperature was colder near the surface than the bottom (Figure 4-9, middle and bottom panels).

4.4.4 Heat Budget on Seasonal Time Scales

Seasonal 1-D Heat Budget: No Advection

The time-integrated heat budgets at the Node and F both indicate that the heat balance is far from 1-D during summer on this inner shelf (Figure 4-10). The observed temperature in summer at each mooring (blue lines) does not rise as rapidly as would be expected from the accumulated surface heating (red lines): the temperature increases only 1/3 to 2/3 as much from spring (March) to summer as expected due to the surface heat flux. This suggests advective cooling of the inner shelf is important during spring and summer. The imbalance between accumulated surface heating and observed temperature (indicated by a difference in slope between the red and blue curves) develops earlier at the Node, where it begins in April, than at F where it does not clearly begin until August.

The nearly constant observed water temperature during August and September (when the accumulated surface heating reaches its maximum) at both the Node (12-m

water depth) and F (27-m water depth) is not due to the near-surface water approaching radiative equilibrium with the atmosphere. The observed net surface heat flux remained positive throughout August and September, rather than approaching zero as if the ocean and atmosphere were in thermal equilibrium. Also, a calculation of the net surface heat flux as a function of sea-surface temperature using the mean observed air temperature and pressure, relative humidity, incoming shortwave and longwave radiation, and wind speed during August with the Fairall et al. (2003) bulk algorithms indicates the sea-surface temperature must reach 27°C before the net surface heat flux becomes zero. The observed near-surface temperature does not exceed 22°C.

In winter at the Node the water does not cool quite as much as expected from the accumulated surface heat loss (if the red and blue lines were aligned at the beginning of the December deployment, the red line would reach a lower value than the blue during February-March), apparently indicating some advective warming of the inner shelf in winter. At F during winter, the accumulated surface cooling and local temperature change roughly balance, indicating an approximately one-dimensional heat balance as in Eq. (4.6) (Figure 4-10) except in February and March, when the water cools and then heats more rapidly than can be explained by the surface heat flux. Advective transport of heat seems to be important at F during those mid-winter events.

Seasonal Heat Budget with Advection

The 1-D heat budget in Section 4.4.4 indicates advective heat flux divergence is important for cooling the inner shelf on time scales of weeks to months in summer. To determine whether the advective heat flux terms we can estimate from observations account for the observed cooling, we consider the time integral of Eq. (4.9) (Figure 4-11). Because we do not have measurements of the terms in Eq. (4.9) for the entire year, the correct vertical locations of the time-integrated surface (red) and cross-shelf (green) heat flux curves in Figure 4-11 are unknown; only the slopes have meaning because the integration constants for the time integrals of H^s and H^{xs} are unknown for each mooring deployment. The red and green curves have been positioned vertically

to best illustrate whether or not the observed slope of the accumulated cross-shelf or surface heat input to the volume agrees with the slope necessary to close the heat budget. We aligned the red and green curves with the blue observed temperature at the beginning of the deployment for CBLAST 2003, and on March 11 for SWWIM I, when the transition to consistent surface heating (spring/summer conditions, with $H^s > 0$ on time scales of days and longer) happened for 2005.

In summer, the observed change in water temperature is very small compared to the surface heat input; at the Node, the water actually cools slightly in August and September, and at F the temperature is nearly constant, while the surface heating continues to accumulate (compare slope of red curve with slope of blue curve in summer, Figure 4-11, left panels; if the heat budgets were 1-D the slopes would be equal). The observed cross-shelf heat input (green) at both the Node and F in summer is strikingly similar to the heat input needed to close the heat balance, so that the sum of the surface and cross-shelf heat fluxes is close to the observed temperature change and the residual heat input needed to close the budget (black) after accounting for surface and cross-shelf heat fluxes is relatively small. This indicates the summer heat budgets at the Node and F are nearly two-dimensional, with surface heating H^s and cross-shelf advection of heat H^{xs} roughly balancing each other (Figure 4-12, top). The accumulated heat due to H^s and the heat loss due to H^{xs} are 5–7 times as large as the equivalent change in local water temperature from the beginning of CBLAST 2003 to the beginning of October, when the seasonal breakdown in temperature stratification occurs (Figure 4-11, left). The thick green and red curves are almost mirror images of each other during August through October: the cross-shelf heat flux seems to adjust to oppose the surface heat flux on time scales of weeks and longer.

The approximate balance between surface heating and cross-shelf advective cooling suggests that the along-shelf heat flux divergence H^{as} (Eq. (4.15)) is a relatively small term on time scales of weeks to months in summer at the Node and at F. Supporting that idea, the part of the along-shelf heat flux that we can calculate from the observations, H^{as}_{adv} (Eq. (C.2)) which is due to advection of the along-shelf temperature gradient, is small compared to the cross-shelf heat flux on long time scales at the

Node (light blue line in upper left of Figure 4-11). H_{adv}^{as} is a relatively crude estimate of the advective part of the along-shelf heat flux divergence, so we do not include it directly in the budget but simply plot it for the Node in summer (the only case in which we can estimate it) to show its approximate size.

From December through mid-March at the Node, the water cooled less than expected from the surface cooling, and from mid-March through May, the water warmed less than expected from the surface heating (Figure 4-11, upper right). The cross-shelf heat flux divergence (green) has the right sign to help close the heat budget in both cases (it warms the inner shelf in December through February, and cools the inner shelf in mid-March through the end of the deployment, as in mid-summer during CBLAST 2003) although its magnitude is too small. The accumulated residual (black) is comparable to the cross-shelf heat flux, and small compared to the surface heat flux. Throughout the SWWIM I deployment, the time-integrated heat budget for the volume onshore of F is to first order a one-dimensional balance between the accumulated surface heat flux and the change in water temperature, consistent with the 1-D budgets in Section 4.4.4 (Figure 4-11, lower right, and Figure 4-12, bottom). The cross-shelf heat fluxes at the Node and F in winter are small compared to the surface heat flux in spite of strong wind stress and wave forcing, because the vertical temperature stratification over the inner shelf is small. In agreement with the 1-D budget and the CBLAST 2003 summer budget (Figure 4-11, upper left), beginning in April soon after the surface heat flux becomes positive on time scales of days to weeks, there is a growing discrepancy between the accumulated surface heating (red) in summer and the change in volume-average water temperature $\langle\langle T\rangle\rangle$ (blue) at the Node.

Decomposition of Seasonal Cross-Shelf Heat Transport

To determine what time scales of evolution of the cross-shelf circulation and the temperature stratification contribute to the cross-shelf heat flux (on time scales of ~ 1 week and longer), we decompose the cross-shelf heat flux into the parts due to the time-mean circulation and temperature profile over each deployment, the synoptic

(time scale $>$ 33 hrs) fluctuations in the circulation and temperature profiles, and the "high-frequency" (time scale $<$ 33 hrs) fluctuations in the circulation and temperature (each of which, if the fluctuations are correlated, could lead to a time-mean cross-shelf heat flux).

The time-mean cross-shelf velocity profiles u and $u+u_{st}$ at the Node and F during CBLAST 2003 and the Node during SWWIM I were offshore near the surface and onshore lower in the water column. During CBLAST 2003 at F, the velocity was more strongly offshore near the surface than the bottom (Figure 4-13). The mean temperature profile was positively stratified at both Node and F, more strongly in summer than winter. As a result, warmer surface water was carried offshore and replaced with cooler near-bottom water. Therefore, the mean circulation at the Node resulted in an offshore heat flux H^{xs} [Eq. (4.11)] (Figure 4-14 upper panels, dark blue), even taking into account H^{xs}_{waves}, which is onshore because $u_{st} < 0$ [Eq. (4.13)]. At F, the cross-shelf heat flux due to the mean circulation was offshore during SWWIM I and likely also offshore during CBLAST 2003 (Figure 4-14 lower panels, dark blue) although the cross-shelf flow at mid-depths is sensitive to uncertainty in the coordinate system during the summer deployment, due to the strongly vertically sheared along-shelf flow during summer (not shown).

At the Node, the cross-shelf heat flux due to the time-mean flow accounts for about 2/3 of the total cross-shelf heat flux during CBLAST 2003 (Figure 4-14, top left; compare dark blue and green lines). The remainder of the heat flux is mostly due to "high-frequency" motions with time scales shorter than 33 hrs (red), which includes some contribution from tides (light blue); correlated fluctuations of $u + u_{st}$ and T on subtidal time scales (longer than 33 hrs, black) are a small contribution. The time-mean flow at the Node in summer does not seem to be wind-driven, unless the response to cross-shelf wind forcing is not symmetric in the direction of the wind stress. The mean cross-shelf wind stress was weakly onshore during CBLAST 2003 (Table 4.5), opposite from the direction that would cause the observed mean circulation; the mean along-shelf wind stress was weakly upwelling-favorable, consistent with the form of the observed circulation, but the circulation at the Node is not driven by the along-

shelf wind (Chapter 2). The parts of the cross-shelf heat fluxes H^{xs} and H^{xs}_{circ} that are due to correlated velocity and temperature fluctuations with time scales between 6 hr and 33 hr (*i.e.*, "high-frequency" fluctuations) are significantly correlated with the cross-shelf wind stress when the temperature difference between the near-surface and near-bottom instruments at the Node is greater than 1.8 °C, but are not correlated with the along-shelf wind stress or the surface gravity wave forcing. The correlation of H^{xs} with cross-shelf wind stress is negative and reaches $r = -0.80$ ($|r_{95\%}| = 0.55$) or stronger. This is consistent with the cross-shelf circulation that contributes to H^{xs}_{circ} being mainly driven by the cross-shelf wind stress (Chapter 2), and with a short set-up time for wind-driven cross-shelf circulation on the inner shelf (so that wind-driven motions contribute to the "high-frequency" heat flux). The negative sign of the correlation indicates cooling of the inner shelf when the wind blows from land to sea, moving warm surface water offshore to be replaced by colder near-bottom water. Although the tidal contribution to H^{xs} estimated by T_TIDE (light blue in Figure 4-14, top left) may be an underestimate if substantial baroclinic tidal motions are present but not exactly in phase with the barotropic tides, the tide appears to contribute only half the "high-frequency" cross-shelf heat flux divergence, with the remainder driven by the cross-shelf wind stress.

In contrast to the Node, although there is a large uncertainty in the cross-shelf heat flux due to the mean circulation at F, the total cross-shelf heat flux H^{xs} at F during CBLAST is between half and entirely due to the correlated subtidal fluctuations of $u + u_{st}$ and T (Figure 4-14, bottom left, compare black and green lines). The "high-frequency" (red) motions at F are a small contribution to H^{xs}. When the temperature difference between the near-surface and near-bottom instruments at F is at least 1.2° C (including both CBLAST 2003 and SWWIM I), the subtidal cross-shelf heat flux at F is significantly negatively correlated with the along-shelf wind stress at the 95% confidence level. The correlation reaches $r = -0.66$ ($|r_{95\%}| = 0.34$), indicating that upwelling-favorable wind stress at F is associated with an offshore heat flux. This is consistent with a coastal upwelling circulation at mid-shelf, in which warm near-surface water moves offshore and colder near-bottom water moves

onshore. The subtidal cross-shelf heat flux H^{xs} at F is not significantly correlated with the cross-shelf wind stress or the surface gravity wave forcing.

Surface gravity wave forcing contributes to the cross-shelf heat transport H^{xs} in two ways, and the two parts can cancel each other (probably explaining the lack of correlation of H^{xs} with waves even when H^{xs}_{waves} is not negligible). The first is through H^{xs}_{circ}, which is the heat flux due to u, the Eulerian cross-shelf circulation detected by the ADCP. That circulation is partly driven by waves at the Node (Appendix E). The second is through H^{xs}_{waves}, which is the heat flux due to u_{st}. At both the Node and F, H^{xs}_{waves} is onshore and warms the inner shelf, in opposition to H^{xs}_{circ} (Figure 4-15). H^{xs}_{waves} is significantly positively correlated with onshore surface gravity wave forcing at F, even though the total cross-shelf heat flux H^{xs} is not (see previous paragraph). Note that H^{xs}_{waves} at the Node and F cannot be directly compared because the reference temperature T_L is different at the two sites (see Section D.3).

Comparison with 2-D, 2-Layer Model

The cross-shelf circulation $\widetilde{u} + \widetilde{u}_{st}$ at the Node does not vary much on time scales of several days to weeks in summer (Figure 4-16a). The upper-layer velocity is persistently offshore, and the lower-layer velocity is onshore. The adjustment of the cross-shelf heat flux to oppose the surface heat flux in summer (Section 4.4.4) apparently takes place through adjustment of the temperature profile, not the cross-shelf circulation profile. To explore how the net cross-shelf heat flux H^{xs} can be equal and opposite to the surface heat flux at the Node in summer when the cross-shelf circulation is roughly constant, we compare the observed heat flux with the simple 2-layer model described in Section 4.3.5 (Figure 4-4).

In the model, the temperature is always in steady state, similar to the observed summertime heat budget at the Node, in which the change in local heat content is small compared to the accumulated surface heat flux and cross-shelf heat flux (Figure 4-11, left). The time for the volume onshore of the Node to be flushed by the mean circulation $u+u_{st}$ in summer is 2.4 days, so it is reasonable to use a steady-state model for the heat balance on time scales longer than a few days. The cross-shelf

heat flux and the surface heat flux balance by design in the two-layer model, but the model predictions for the strength of the vertical temperature stratification, the sign of the cross-shelf temperature gradient, and the effective distance that a water parcel travels when being flushed through the volume onshore of the Node are consistent with observations, as follows.

The model predicts the vertical temperature stratification will be determined solely by the surface heat flux, the strength of the (constant) two-layer circulation, and the distance from shore, through Eq. (4.32). We use a layer interface of $z = -5.5$ m to estimate the vertically-averaged, time-varying (7-day low-pass filtered) temperatures T_1 and T_2 for the upper and lower layers, and the observed time-mean $U_0 = 0.06$ m^2 s^{-1} from the depth-varying part of $u+u_{st}$ at the Node during CBLAST 2003 (using $u+u_{st}$ rather than just u based on the form of H^{xs} in Eq. (4.11)). The observed quantities $U_0\Delta T$ and $Q_s L$ are in reasonable agreement (Figure 4-16b,c), consistent with the model capturing the main features of the circulation, and suggesting the distance that water parcels travel toward shore before leaving the volume onshore of the Node in summer is close to the actual distance to shore L.

The model predicts a negative cross-shelf temperature gradient $\partial\langle T\rangle/\partial x$ (colder water farther from shore) only if the vertical mixing exceeds a critical value: $K_T^* > U_0 d/L$ (Eqs. (4.26), (4.27), and (4.35)). The observed summertime $\partial\langle T\rangle/\partial x$ between F and the Node is negative, so the model suggests that the effective mixing is $K_T^* > 2\times10^{-4}$ m^2 s^{-1} based on the observed $U_0 = 0.06$ m^2 s^{-1}, $d = 5.5$ m, and $L = 1.5$ km. This is reasonable, given that the K profile parameterization (Large et al., 1994) suggests K_T is often as large as O $(10^{-2} - 10^{-1})$ m^2 s^{-1} at 2 m depth for the observed surface heat flux and wind stress during August 2003. Therefore, the observations at the Node are consistent with the mechanism for balancing H^s and H^{xs} in summer that is captured by the two-layer model, *i.e.*, an upwelling circulation that is nearly constant in time, and a temperature stratification that adjusts depending on the surface heat flux.

4.5 Discussion

We observe strong seasonal cycles in temperature and vertical thermal stratification at both the Node and F. The warmest water and strongest thermal stratification occurred in August, and the coldest water and a thermal stratification near zero or inverted occurred in January or February. The water at the shallower site was generally warmer than the water offshore in summer, and colder in winter. These results are all consistent with previous observations of the seasonal cycle of temperature of Middle Atlantic Bight shelf waters (Bigelow, 1933; Linder and Gawarkiewicz, 1998; Lentz et al., 2003b; Lentz, 2007b, and others). In addition, we observe reversals of the cross-shelf temperature gradient between the 12- and 27-m isobaths in the upper 12 m of the water column on time scales of days in all seasons (Figure 4-5).

The substantial cooling of the inner shelf during summer observed here is similar to the summertime coastal upwelling on the West Coast of the United States in that the dominant terms in the heat balance on time scales of months are the surface heat flux Q_s and the cross-shelf advective heat flux (*e.g.,* Lentz, 1987). Nevertheless, there are important differences between the persistent upwelling observed here at the Node, and the summertime upwelling on the West Coast that is driven by the along-shelf wind stress. First, although the mean along-shelf wind stress was upwelling-favorable during the part of August 2003 for which there are temperature data, that mean wind stress was very weak (< 0.01 N m^{-2}, Table 4.5) in contrast to the strong upwelling-favorable wind stress that drives West Coast summer upwelling. Second, the cross-shelf circulation over the shallow inner shelf near MVCO is not driven by the along-shelf wind stress, but by the cross-shelf wind stress (Chapter 2) and surface gravity wave forcing (Appendix E). The details of the summertime (stratified) cross-shelf circulation at the Node are not well understood.

Previous observations of advective heat transport over the North Carolina continental shelf, onshore of the 23-m isobath, demonstrated that on time scales of days the cross-shelf heat flux is a dominant term in August, and the along-shelf heat flux in October (Austin, 1999). The synoptic cross-shelf heat flux was explained by coastal

upwelling and downwelling circulations driven by the along-shelf wind stress. We find a similar synoptic upwelling and downwelling driven by the along-shelf wind stress near the 27-m isobath near MVCO. In addition, we find synoptic and higher-frequency upwelling and downwelling driven by the cross-shelf wind stress onshore of the 12-m isobath. In fall, the cross-shelf heat flux in the North Carolina study became negligible as the vertical temperature stratification broke down, and the surface heat flux became the dominant source of changes in water temperature. At MVCO, the cross-shelf heat flux also becomes small when the vertical temperature stratification breaks down, and surface heating and cooling is an important term in the synoptic heat budget, particularly at the shallower 12-m site. The North Carolina study was based on data from the months of August and October, so could not address the complete seasonal cycle. Neither the cross-shelf nor the along-shelf heat flux was a dominant term in the mean heat balance in August or October, in contrast to MVCO where the cross-shelf heat flux is a strong cooling influence on time scales of months in summer. The North Carolina August data covered less than one month, however, so the actual mean cross-shelf heat flux may have been masked by the strong synoptic variability.

A numerical modeling study (Wilkin, 2006) of the summertime 2002 heat budget near MVCO also found the change in depth-average water temperature in summer was smaller than expected from surface heating alone, in agreement with these and previous (Hutto et al., 2003; Pritchard et al., 2002) observations. The Wilkin model was not designed specifically to look at the shallow inner-shelf circulation near the MVCO Node; the model grid spacing was 1 km and the distance between the Node and shore is only 1.4 km, so the circulation near the Node in the model may not be adequately resolved for comparison to our study. In the Wilkin model, the water temperature at the Node and F increased throughout July but not as fast as the surface heat flux would suggest, and became constant or decreasing in August, similarly to the August 2003 observations (Figure 4-10). The summertime surface heat flux was substantially canceled in the Wilkin model by a divergence in the horizontal advective heat flux near the coast of Martha's Vineyard (Wilkin, 2006, his Figures 10 and 11),

consistent with the cooling cross-shelf heat flux divergence we observe. Near mooring F (which was also deployed in summer 2002), the Wilkin model indicates less cooling due to advective heat flux divergence than near the south coast of Martha's Vineyard, in agreement with the smaller discrepancy between accumulated temperature change and surface heating we observe at F than at the Node.

The advective heat flux divergence in the Wilkin model is partly a cooling due to the mean (tidally averaged) circulation, in agreement with our observations at the Node and F (black and dark blue curves in Figure 4-14, left). Near and east of the MVCO Node, a divergence in the modeled advective heat flux due to high-frequency motions attributed to tides warmed the inner shelf. That model heat flux was due to the combined along-shelf and cross-shelf divergence. The observed cross-shelf heat flux divergence due to high-frequency motions at the Node during August 2003 resulted in a net advective cooling, not warming. We do not have observations of the along-shelf heat flux divergence on tidal time scales (moorings T1 and T2 are too far apart to resolve the relevant temperature gradients). The along-shelf velocity and the near-bottom water temperature at the Node are not in quadrature in the long (2001–2007) MVCO time series or during CBLAST, however, suggesting that there is an along-shelf heat flux due to tides near bottom at the Node, but the sign of the divergence of that heat flux is not known from observations. The tidal eddy heat flux that brings warm water from the northeast to the area near and east of the Node in the numerical model may also be an overestimate. The tidally generated warm water bulge in the modeled mean surface temperature east of the Node for July and August 2002 is not present in the mean temperature field of satellite observations from the same period ((Wilkin, 2006), his Figure 2). Nevertheless, the observations presented here and Wilkin's model both show that advective heat flux divergence is an important cooling mechanism in the MVCO area in summer both on long time scales (weeks to months) and during synoptic events.

Previous heat budget studies, including those of Austin (1999) and Wilkin (2006), have not considered the contribution of Stokes' drift (Stokes, 1847), although part of the contribution of surface waves to the heat budget has been included through the

(unrecognized) influence of waves on the circulation u recently demonstrated by Lentz (Appendix E). There is a tendency for the wave-driven contribution to u to oppose u_{st} (Appendix E). As a result, there is a tendency for H^{xs}_{waves} to oppose H^{xs}_{circ} when wave forcing is important, because u and u_{st} both act on the same temperature profile $\widetilde{T}(z)$ to produce a cross-shelf heat flux. Previous studies have likely overestimated the cross-shelf heat flux, since inclusion of u_{st} in this study led to a substantial reduction of the magnitude of H_{xs}, even at the deeper site (Figure 4-15). These results suggest the need to incorporate wave forcing in numerical models of the inner shelf circulation and heat budget.

4.6 Summary and Conclusions

On the shallow inner shelf at MVCO, in 12- to 27-m water depth, surface heating and cross-shelf advective cooling are the dominant terms in the heat budget on time scales of weeks to months in summer. In mid-summer (August), the local water temperature over the inner shelf is nearly constant in spite of strong surface heating, due to an offshore flux of heat which is partly driven by surface gravity waves, partly the cross-shelf wind, and partly the along-shelf wind (at the deeper site) (Figure 4-12, top). This is in contrast to previously observed mid-shelf sites in the Middle Atlantic Bight where the cross-shelf heat flux is less important, the surface heat flux and change in local water temperature are dominant, and surface gravity waves and cross-shelf wind have not been considered. The along-shelf heat flux, although not directly observed here, seems to be negligible on seasonal time scales in the summer temperature balance onshore of the 12- and 27-m isobaths. In winter, the heat balance is closer to one-dimensional at both sites, with surface cooling and change in local heat content balancing (Figure 4-12, bottom).

The temperature difference between the near-surface and near-bottom water is always small compared to the temperature difference between summer and winter (Figure 4-1). It is that relatively small vertical temperature stratification, however, that enables the large cross-shelf advective heat flux out of the inner shelf in summer.

The net cross-shelf heat flux H^{xs} at the Node in summer is mostly due to the mean circulation (including Stokes' drift) acting on the mean temperature profile, with some contribution ($\sim 1/3$) from correlated fluctuations with time scales shorter than 33 hrs driven partly by tides and partly by cross-shelf winds. In contrast, the net cross-shelf heat flux at F may be entirely due to correlated fluctuations with time scales longer than 33 hrs, which are driven by the along-shelf wind through coastal upwelling and downwelling similar to mid-shelf.

We compare the summertime heat budget onshore of the 12-m isobath with a simple two-layer model in which the temperature stratification is assumed to have evolved to reach a steady state so that the net surface heat flux into the volume $Q_s L$ equals the net advective heat loss from the volume due to the mean circulation, $-\rho_0 c_p U_0 \Delta T$. There is good agreement between this model and the part of the Node summertime cross-shelf heat flux that is due to the time-mean circulation (Figure 4-16). The remaining $\sim 1/3$ of the cross-shelf heat flux at the Node in summer, which is due to high-frequency motions, is caused partly by tides but has the opposite sign (here, it cools the volume) from a numerical model tidal eddy heat flux found for the MVCO area (Wilkin, 2006). Nevertheless, that model tidal heat flux could be due to along-shelf heat flux divergence not resolved here.

On synoptic time scales, the residual in the heat budget is large at both locations at all times of year, likely indicating that along-shelf heat flux divergence is important on synoptic time scales. During stratified conditions in 12-m water depth, the surface heat flux, change in local heat content, and cross-shelf heat flux are all important. This is the first continental shelf heat budget in which the surface heat flux has played an important role on synoptic time scales in summer; in the North Carolina inner shelf heat budget (Austin, 1999) the surface heat flux was a dominant term in the synoptic heat budget only after the stratification broke down in fall. The importance of the surface heat flux for synoptic fluctuations in summer water temperature at MVCO is due to the shallow water depth compared to previous studies. The surface heat flux should become an even more important term in synoptic heat budgets progressively closer to shore. During stratified conditions in 27-m water depth, the surface heat

flux is less important than in 12-m water depth but the other three terms (change in local temperature and cross-shelf advection) are large, in agreement with previous inner and mid-shelf studies. During unstratified conditions, the cross-shelf heat flux is a minor term in the heat budget at both sites; at the 12-m site, surface heat flux, change in local heat content, and along-shelf advection are all important, and at the 27-m site the surface heat flux is again less important and the dominant balance is between change in local heat content and (presumably) along-shelf advection.

We document a warming of the inner shelf on synoptic time scales during winter by the cross-shelf heat flux in 12-m water depth, due to the combination of an upwelling circulation with an inverted temperature stratification (coldest water near the surface) that is a common feature of this area, since freshwater runoff trapped near the coast during winter can stabilize an inverted temperature profile caused by surface cooling. The inverted temperature stratification in winter 2004–2005 was a feature of the shallowest part of the inner shelf (the temperature is inverted at the 12-m but not the 27-m site).

The contribution of wave-driven fluctuations in velocity and temperature to the heat budget through the Stokes' drift u_{st} is substantial and has not been included in previous studies. The entirely separate contribution of waves to the heat budget due to the wave-driven Eulerian circulation documented in Appendix E has automatically been included in previous studies as part of the observed circulation u, but was not recognized as being due to waves. Because the wave-driven circulation in u tends to oppose the Stokes' drift u_{st}, the net effect of waves on the heat budget may actually be small. The cross-shelf heat flux may have been overestimated in previous studies because the canceling effect of the Stokes' drift was neglected.

The cross-shelf heat flux is an important cooling mechanism for the shallow inner shelf on time scales of months during summer. The observed cross-shelf heat flux in 12 m and 27 m water is approximately the right size to produce the observed summer water temperature, which is much cooler than would be expected from surface heating alone. The cross-shelf heat flux alone provides a mechanism for the departure of the inner shelf heat balance from one-dimensional, shown in Figure 4-2. A substantial

along-shelf heat flux divergence is not required.

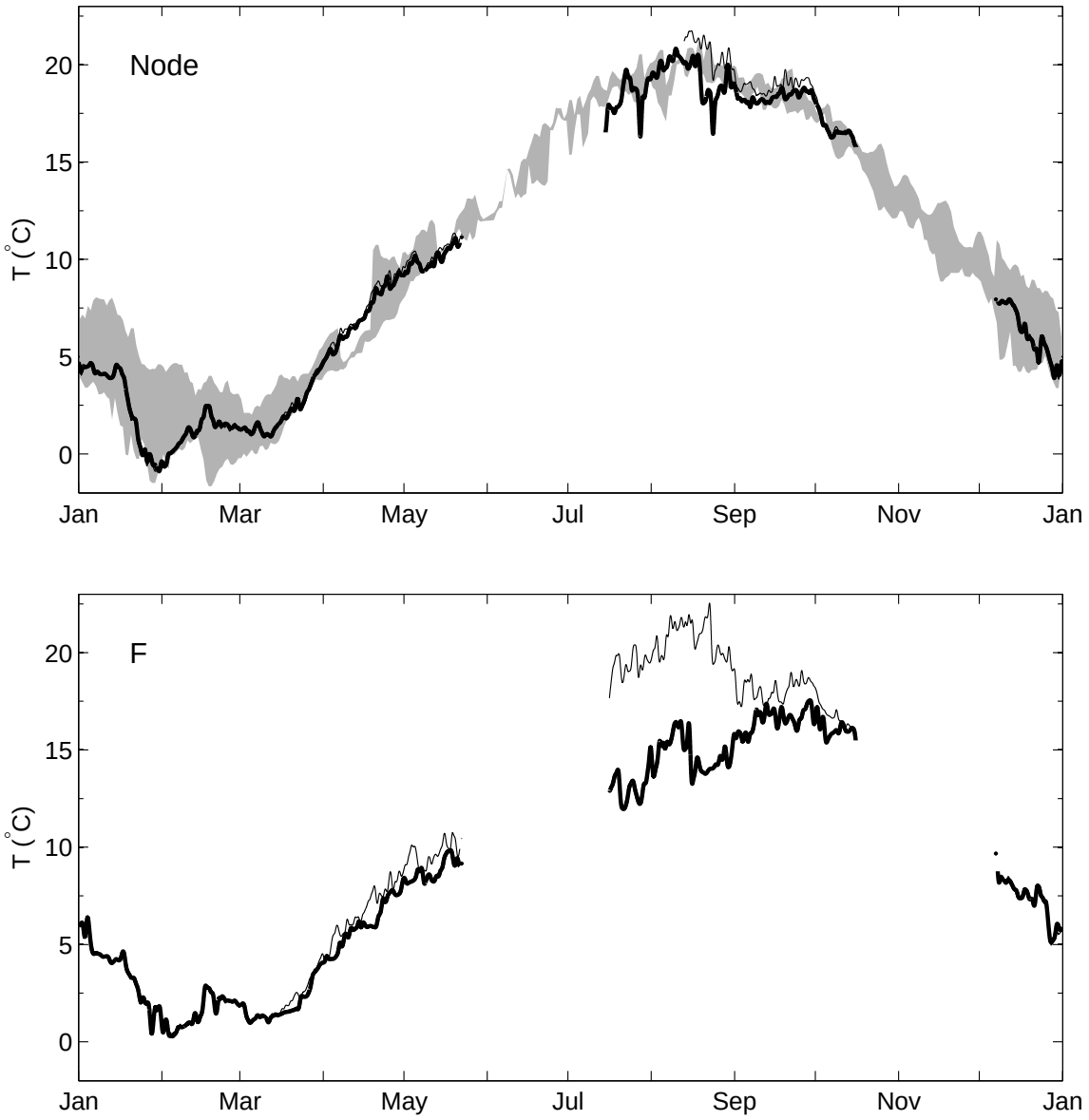

Figure 4-1: Top panel: 33-hr low-pass filtered temperature in 12-m water depth at the Martha's Vineyard Coastal Observatory in Massachusetts. Thick line: near-bottom temperature, and thin line: near-surface temperature, from summer 2003 and winter 2004–5. Grey shading: envelope of near-bottom temperature from 2001–2007, during all times other than the experiments represented by the thick black lines; data are sparse in early summer. Bottom panel: similar but in 27-m water depth (at mooring F), and without the envelope of 2001–2007 values.

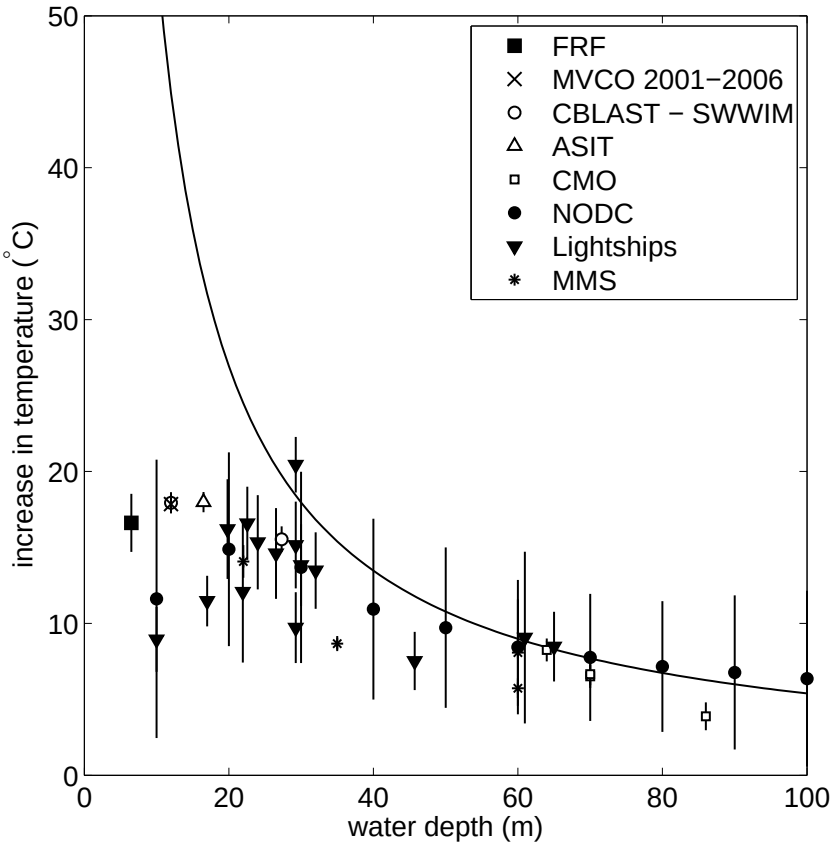

Figure 4-2: Solid line: predicted depth-average temperature increase due to the mean net surface heat flux 140 W m^{-2} observed at MVCO over a period of six months (March 1 through August 31), as a function of water depth, assuming no advection of heat (Section 4.3.3). Symbols: observed change in 10-day average temperature from March 1 to August 31. Vertical bars show ± one standard deviation. US Army Corps of Engineers Field Research Facility (FRF) daily CTD data are described at http://www.frf.usace.army.mil; for Coastal Mixing and Optics (CMO) data, see Lentz et al. (2003b); National Ocean Data Center (NODC) archived shipboard data are described in Lentz et al. (2003b); lightship temperature measurements are described at http://dlaweb.whoi.edu/DIG_RES/lightship_data.html; for the Minerals Management Service (MMS) Hatteras Study, see Berger et al. (1994).

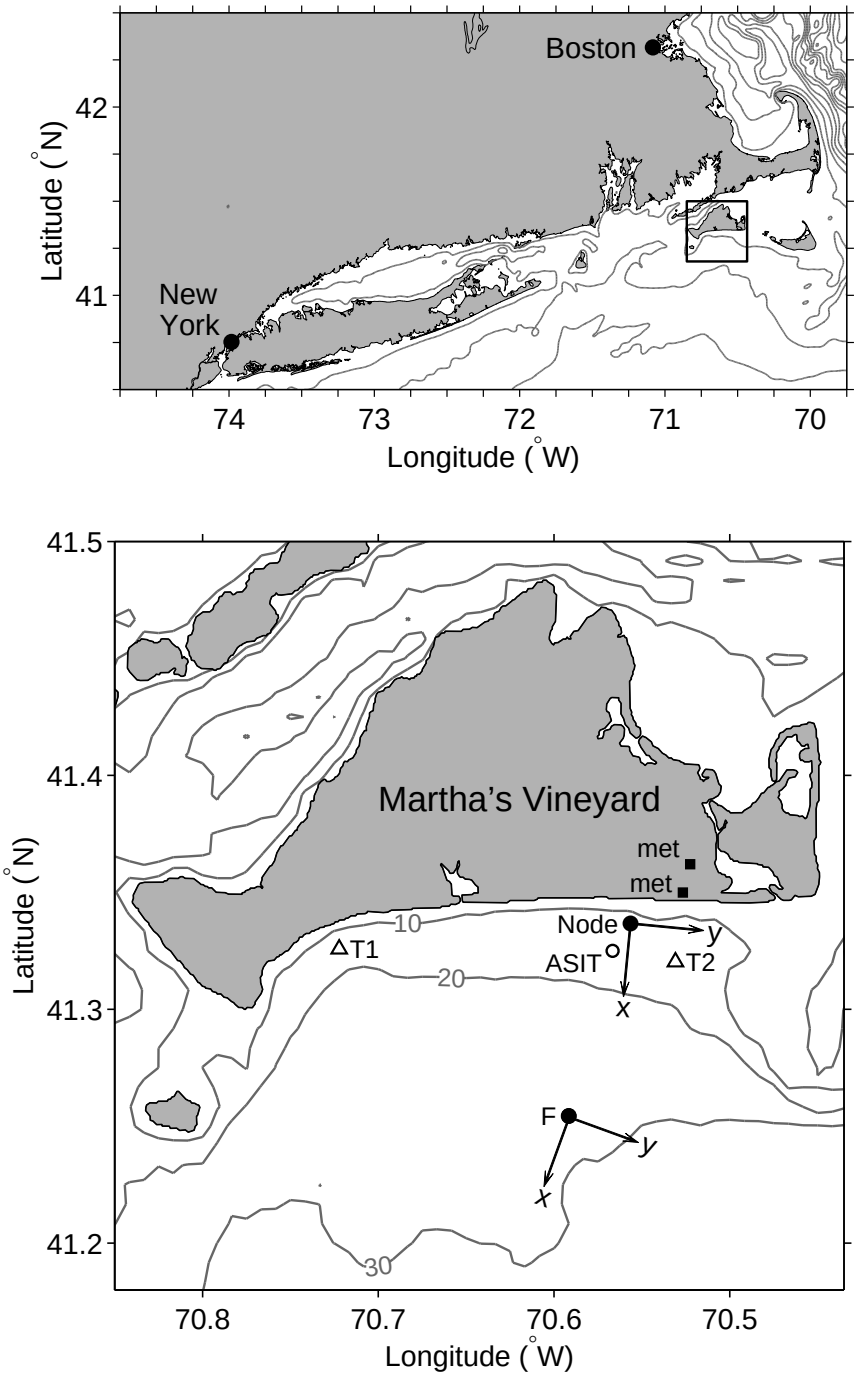

Figure 4-3: Top panel: location of detailed map of study area (square outline). Isobaths are shown in increments of 20 m (*i.e.*, the 20-m, 40-m, 60-m... isobaths). Bottom panel: detailed map of study area, with Node and F principal axis coordinate systems from CBLAST 2003 (Appendix E). Isobaths are labeled in meters. Solid dots: moorings Node and F, deployed during CBLAST 2003 and SWWIM I. Triangles: moorings T1 and T2, deployed during CBLAST 2003 only. Circle: MVCO air-sea interaction tower (ASIT). Squares: MVCO meteorological masts.

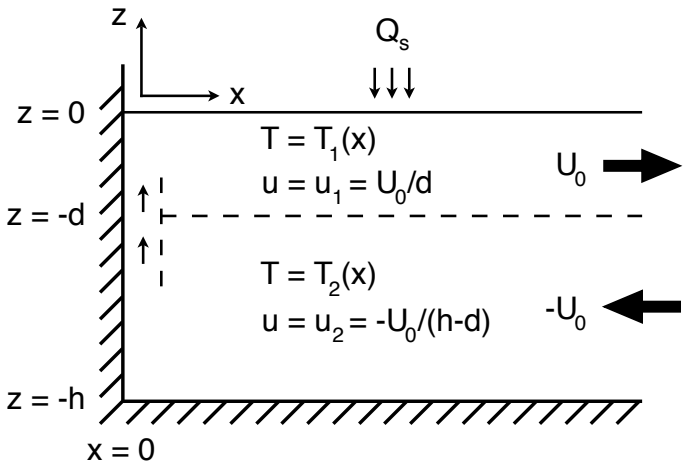

Figure 4-4: Cartoon of 2-D, 2-layer model described in Section 4.3.5. The cross-shelf velocity is constant in x except very near the coast, where upwelling occurs. The temperature varies with x in each layer.

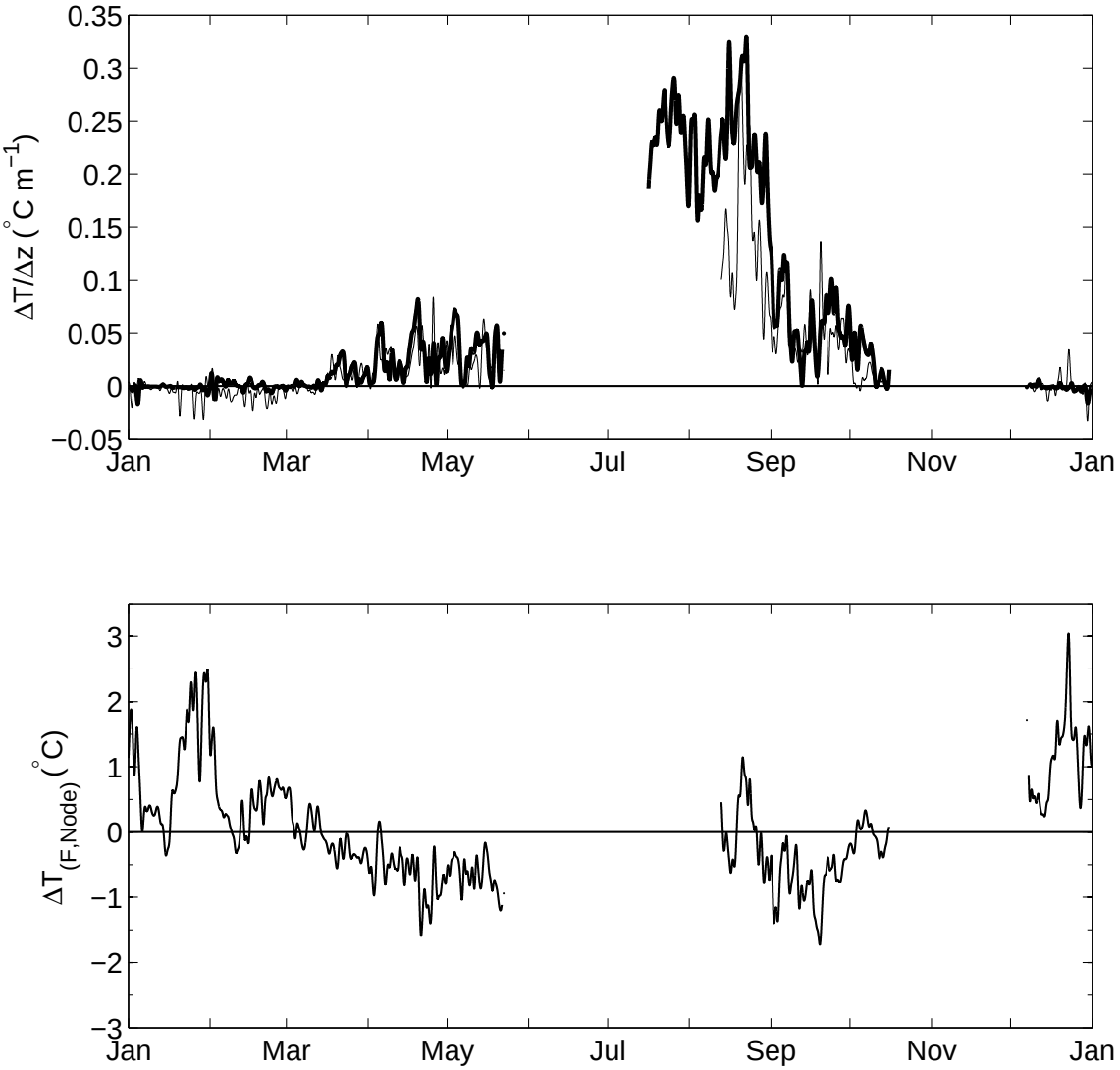

Figure 4-5: Top panel: 33-hr low-pass filtered bulk vertical temperature stratification $\Delta T/\Delta z$ between the near-surface and near-bottom instruments in 12-m (Node, thin line) and 27-m (F, thick line) water depth at MVCO. Bottom panel: 33-hr low-pass filtered cross-shelf difference in the average temperature of the upper 12 m of the water column between mooring F and the MVCO Node, $\Delta T_{(\mathrm{F,Node})}$, as a function of time. Positive indicates the water at F is warmer than at the Node. The two sites are separated by $\sim$10 km.

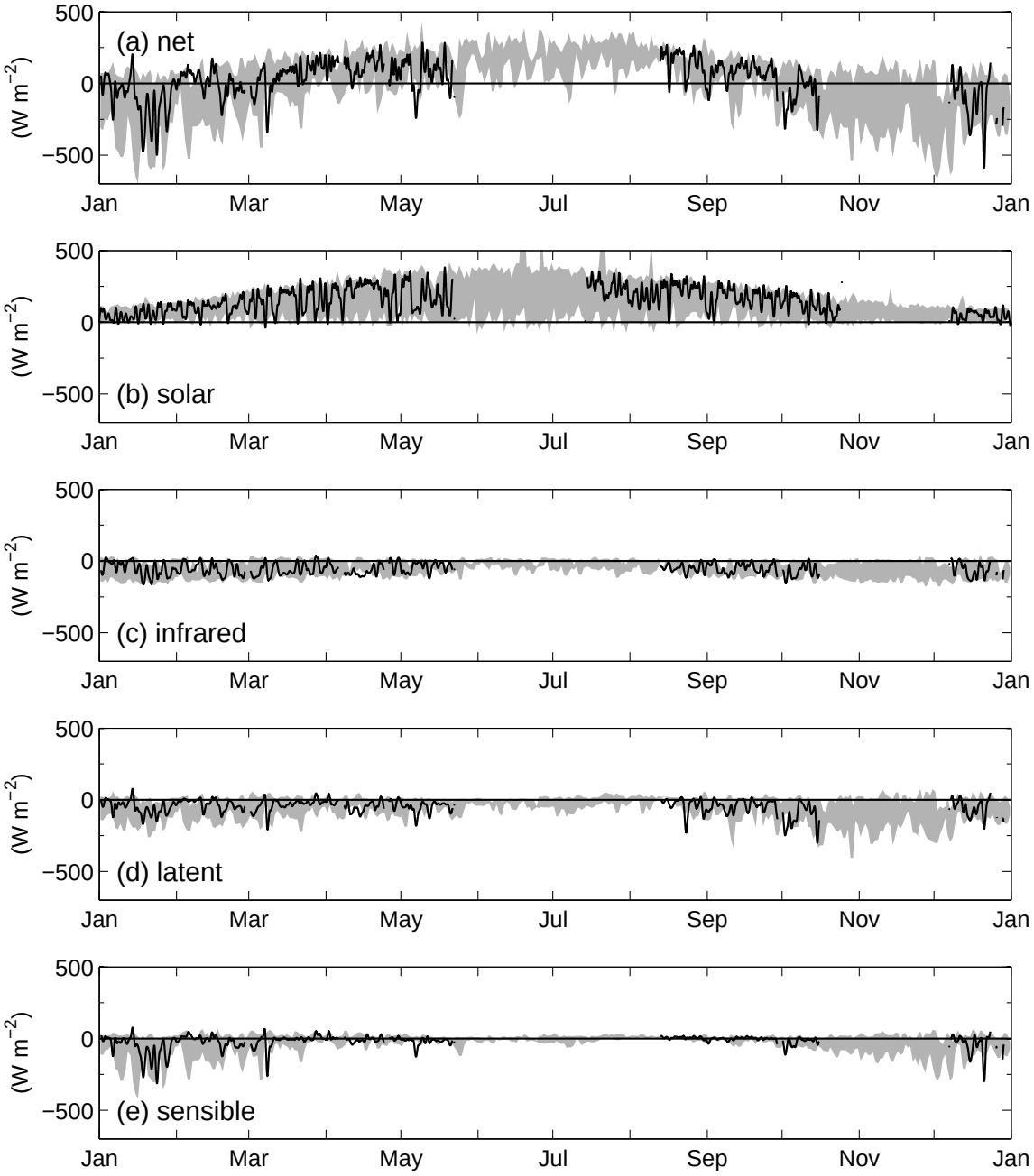

Figure 4-6: 33-hr low-pass filtered net surface heat flux Q_s and its components at the Node. Positive heat flux indicates ocean is warming. Black line: CBLAST 2003 (summer) and SWWIM I (winter/spring). Grey shading: envelope of other measurements at MVCO (2001-2007).

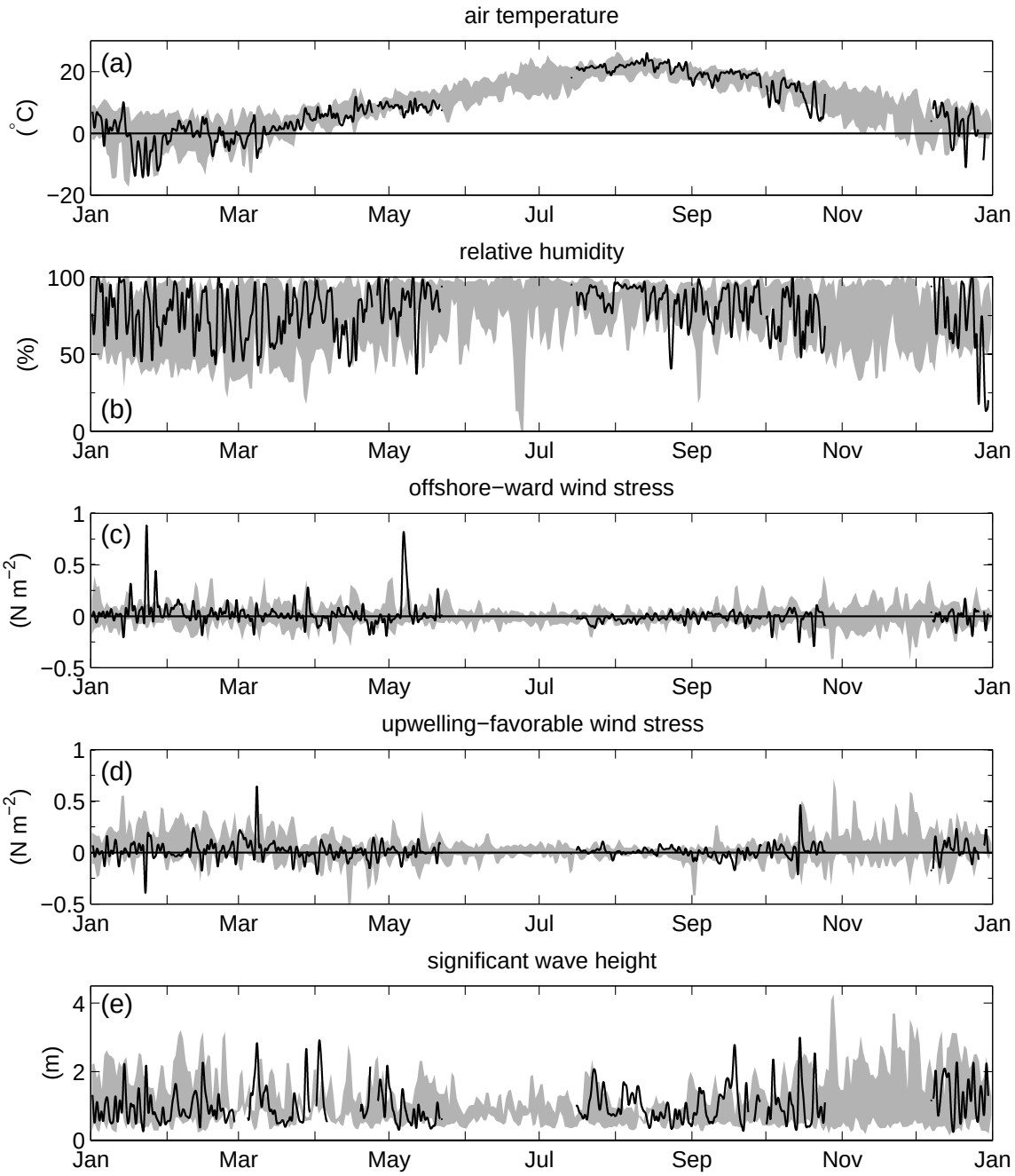

Figure 4-7: 33-hr low-pass filtered MVCO air temperature, relative humidity, wind stress in Node coordinate system, and significant wave height at the Node. Black line: CBLAST 2003 (summer) and SWWIM I (winter/spring). Grey shading: envelope of other measurements at MVCO (2001-2007).

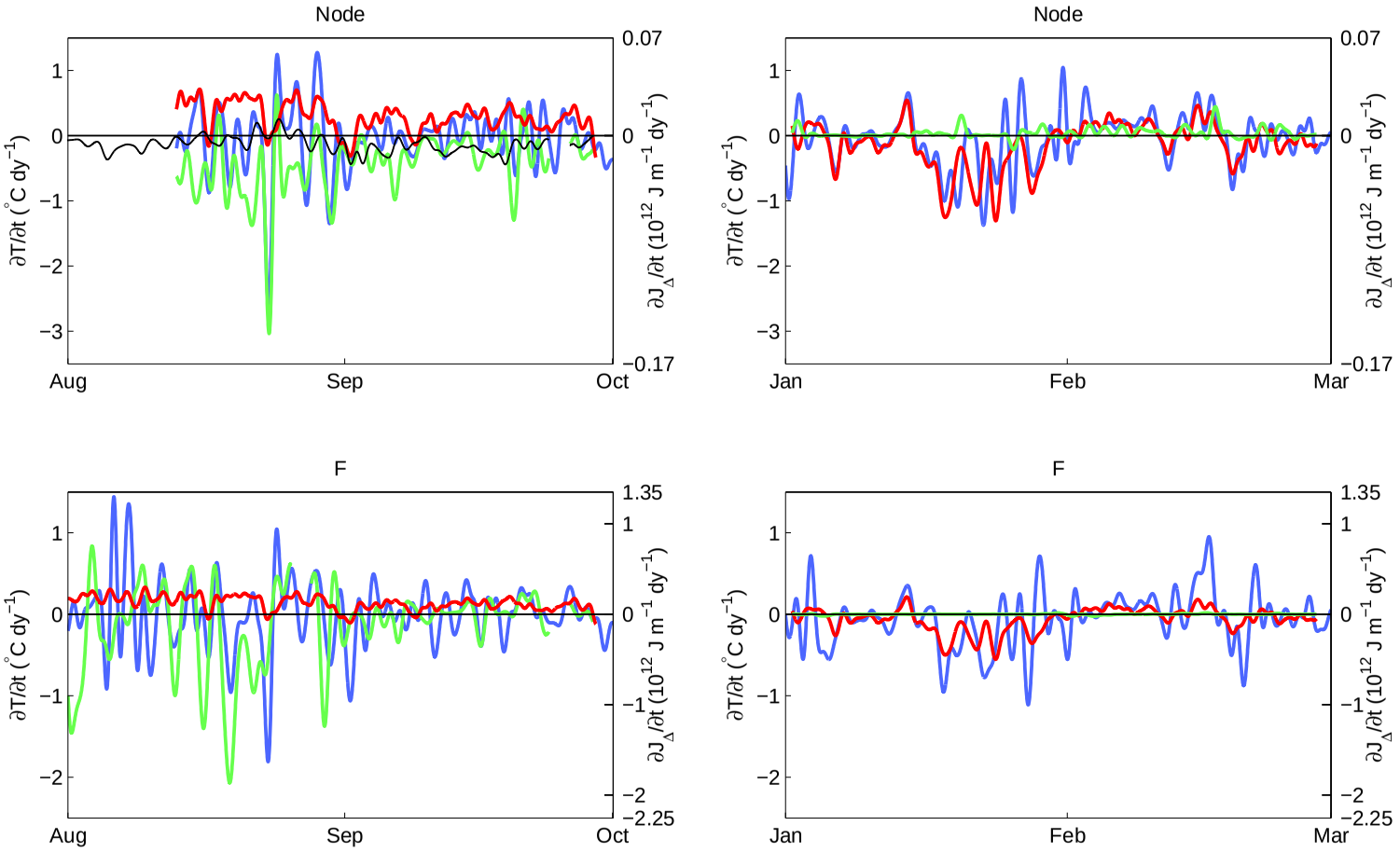

Figure 4-8: Synoptic changes in water volume average temperature, low-pass filtered with a 33-hr cutoff. Top panels: onshore of the 12-m isobath, for summer (left) and winter (right). Bottom panels: onshore of the 27-m isobath. Blue: observed $\partial\langle\langle T\rangle\rangle/\partial t$ (time derivative of Eq. (4.7)). Red: predicted from surface heat flux, using Eqs. (4.9) and (4.10). Green: predicted due to cross-shelf advective heat flux, using Eq. (4.11). Black, in upper left: predicted due to advection of along-shelf temperature gradient, using Eq. (C.2). Equivalent change in heat content per unit along-shelf length, J_Δ, is shown on the right axis, where $J_\Delta = \rho_0 c_p A\langle\langle T\rangle\rangle$ and A is the area of the wedge onshore of the mooring.

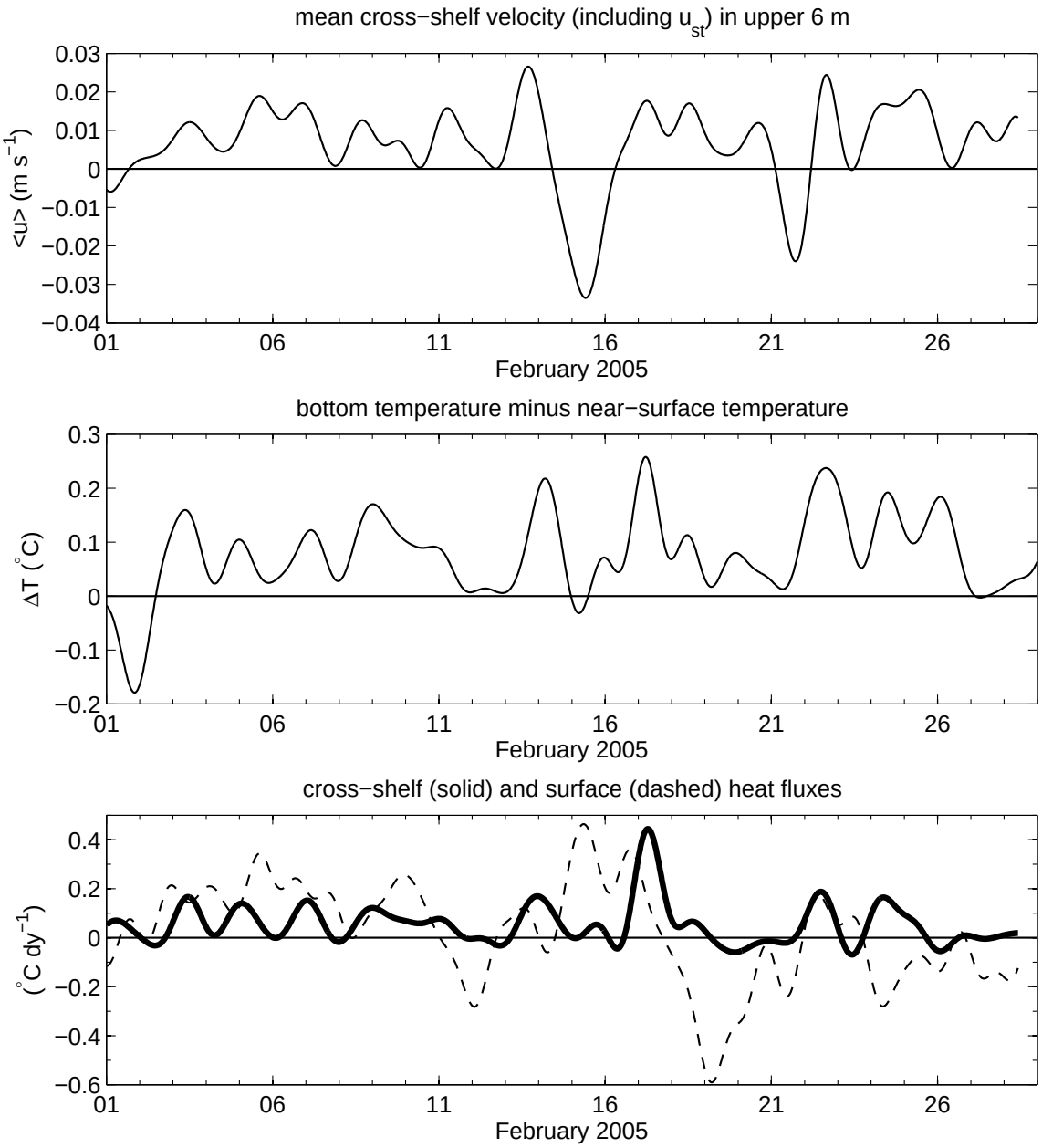

Figure 4-9: Advective heating of the inner shelf in winter, due to upwelling when the temperature stratification is inverted at the Node. Top: mean cross-shelf velocity $u + u_{st}$ in the upper half of the water column; positive indicates upwelling. Middle: temperature difference between near-surface and near-bottom instruments; positive indicates unstable temperature stratification. Bottom: (solid) total cross-shelf heat flux from Eq. (4.11) including the effects of waves and (dashed) surface heat flux, plotted as expected change in area-average temperature; positive indicates the inner shelf is warming. All four time series have been low-pass filtered with a 33-hr cutoff.

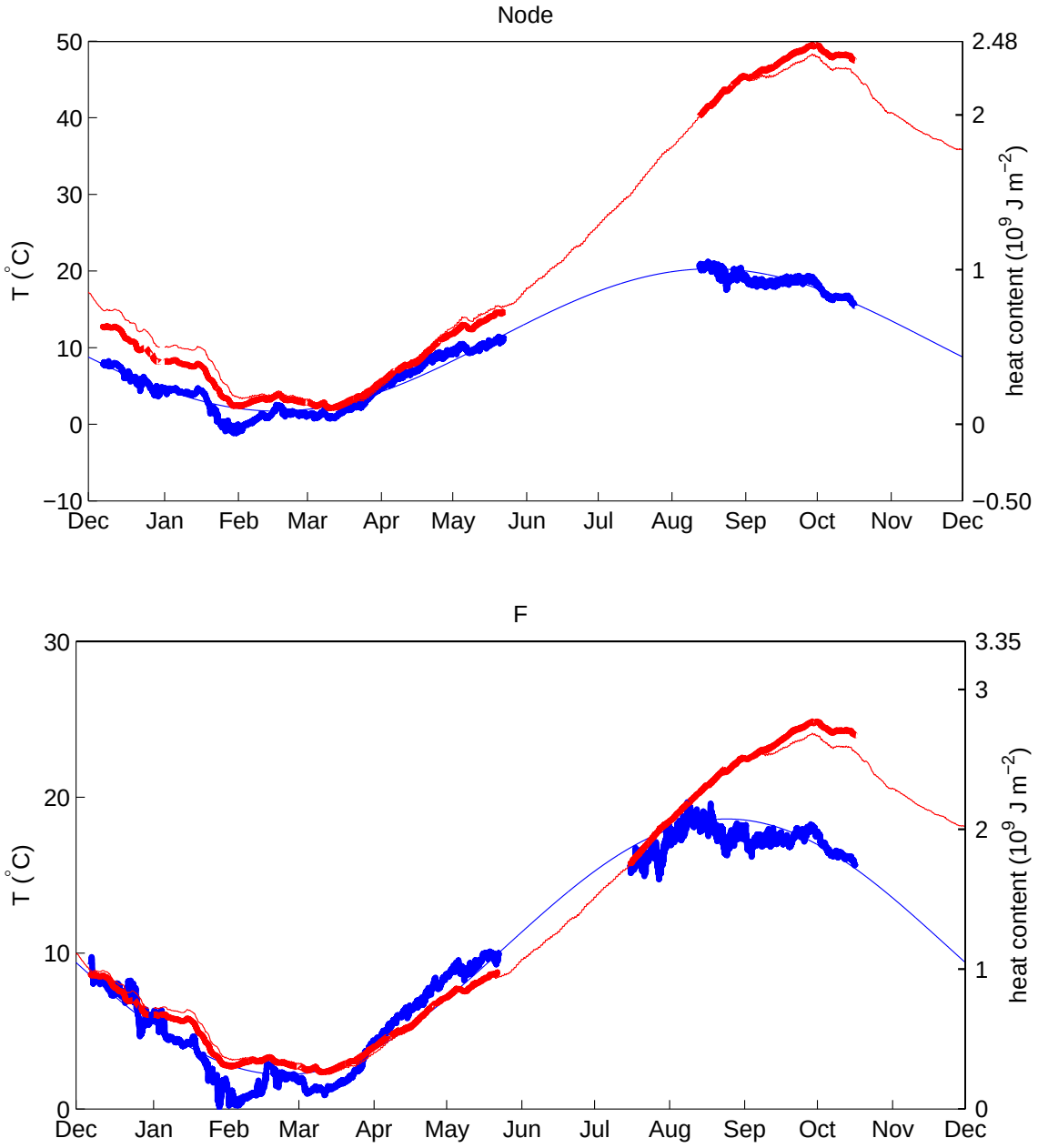

Figure 4-10: Annual cycle of depth-average temperature on the 12-m (top panel) and 27-m (bottom panel) isobaths. Thick blue: observed $\langle T \rangle$ from Eq. (4.5). Thick red: predicted from surface heat flux, assuming the one-dimensional heat balance in Eq. (4.6). Thin blue: best fit sinusoidal annual cycle of $\langle T \rangle$. Thin red: predicted annual cycle from observed meteorological variables and best fit sinusoidal annual cycle of near-surface temperature (not shown). Equivalent water column heat content per unit horizontal area is shown on the right axis, relative to heat content of a water column at 0°C. The vertical positions of the red curves are arbitrary; the red curves have been aligned as described in Section C.1 to show times when the slopes of the red and blue curves agree, indicating a one-dimensional heat budget.

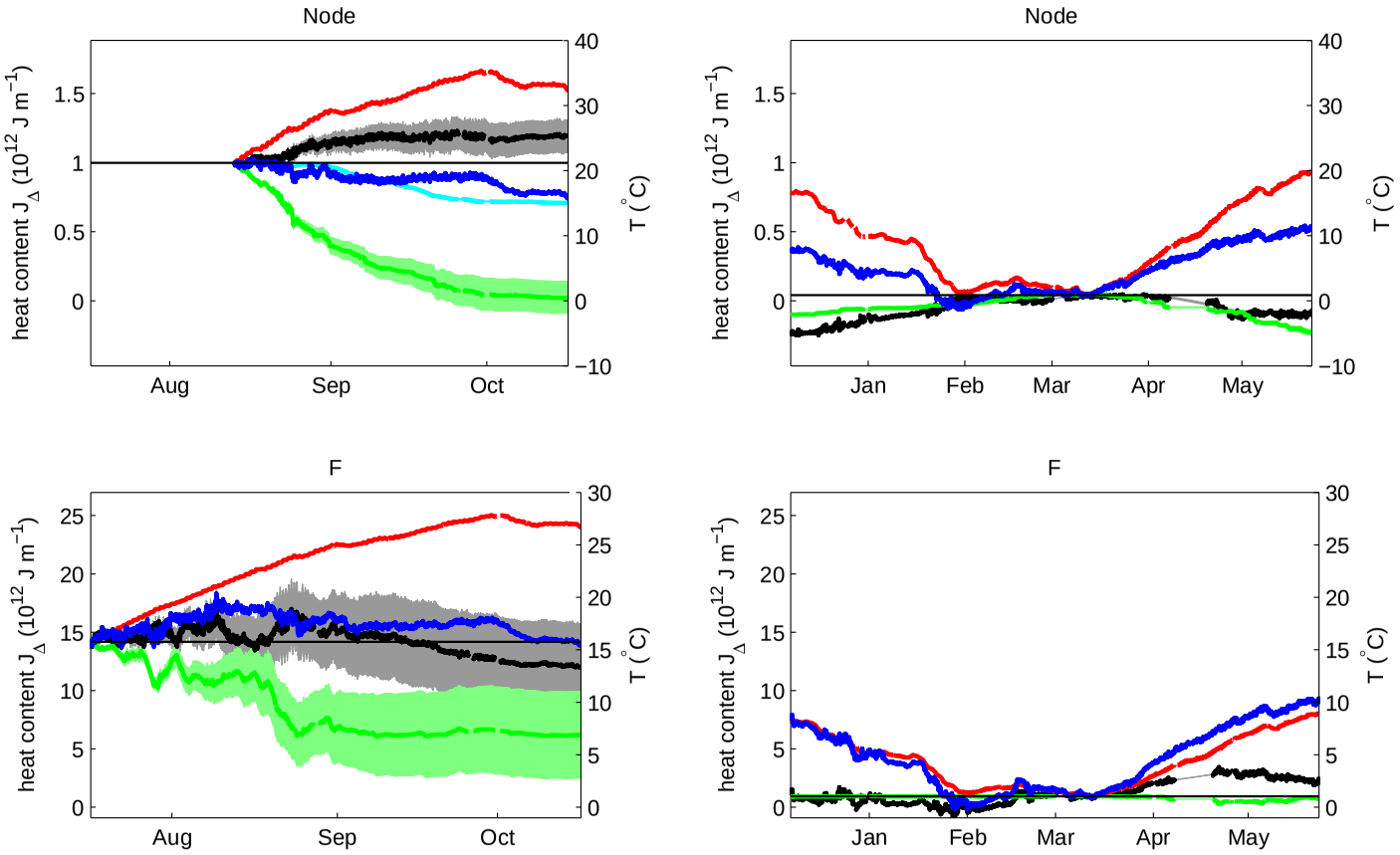

Figure 4-11: Time-integrated heat budget for a triangular volume onshore of the (top panels) 12-m or (bottom panels) 27-m isobath, expressed as accumulated change in heat content per unit along-shelf length, in summer (left) and winter (right). Note different vertical axis scales for Node and F. Blue: observed area-average heat content, J_Δ (reference "zero" on heat content axis is arbitrary). Red: predicted change in heat content J^s due to observed surface heat flux H^s (J^s is the time integral of H^s). Green: predicted change J^{xs} due to cross-shelf heat flux H^{xs} (including waves). Black: residual $J_\Delta - J^{xs} - J^s$. The shaded areas around the curves show the range produced by rotating the coordinate system $\pm 5°$. For the Node in summer (top left), the estimated part of the along-shelf heat flux H^{as}_{adv} is shown in light blue. The equivalent volume-average temperature $\langle\langle T \rangle\rangle$ is shown on the right axis, where $\langle\langle T \rangle\rangle = J_\Delta / \rho_0 c_p A$.

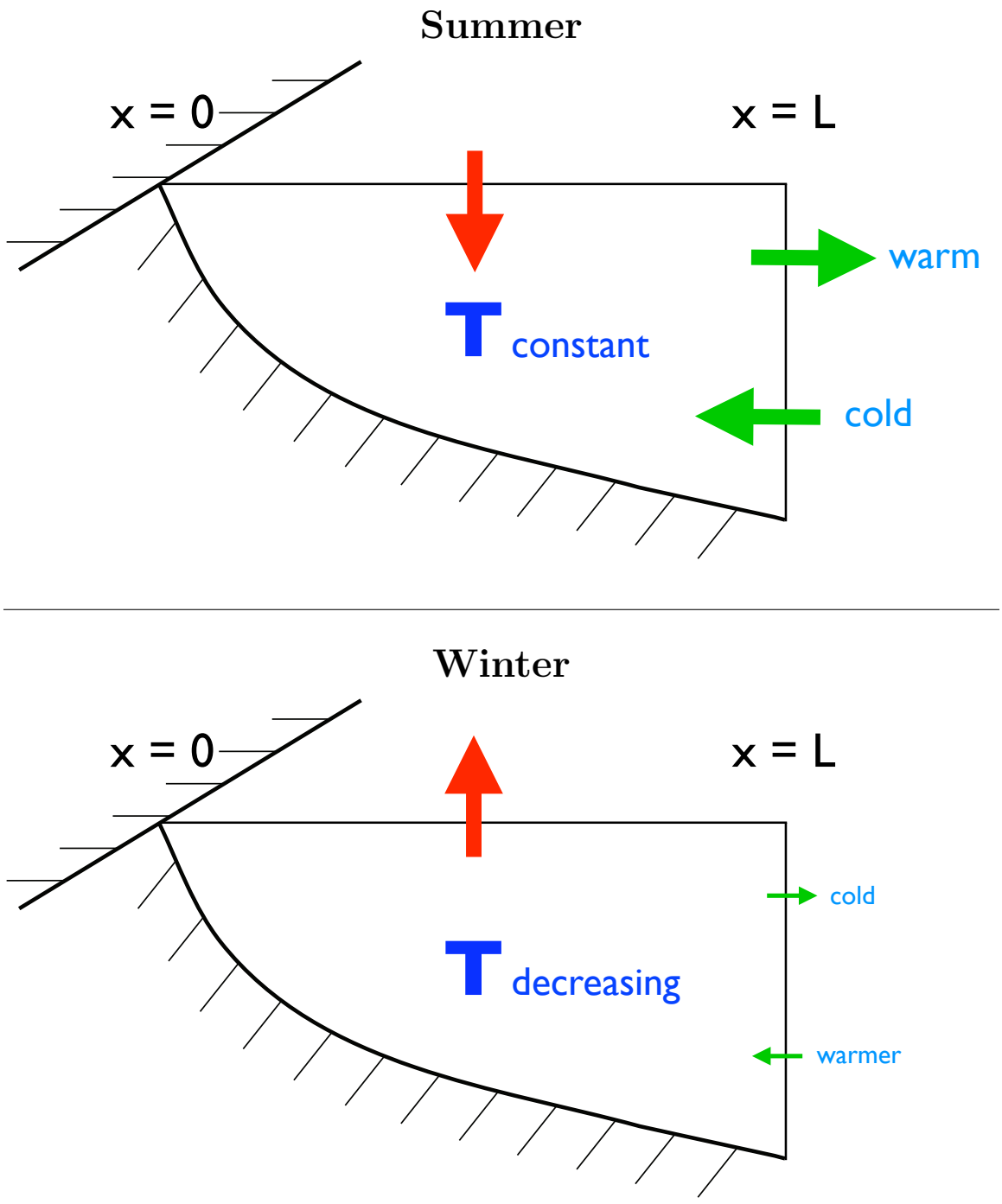

Figure 4-12: Top panel: cartoon of heat balance in summer on time scales of weeks to months. The net surface heat flux (red arrow) heats the inner shelf water. The cross-shelf heat flux (green arrows) cools the inner shelf and approximately cancels the surface heating, so the water temperature (blue T) remains nearly constant. Bottom panel: cartoon of heat balance in winter on time scales of days to months. The net surface heat flux (red arrow) cools the inner shelf water. The cross-shelf heat flux (green arrows) warms the inner shelf but is small in comparison to the surface heat flux, so the water temperature (blue T) decreases.

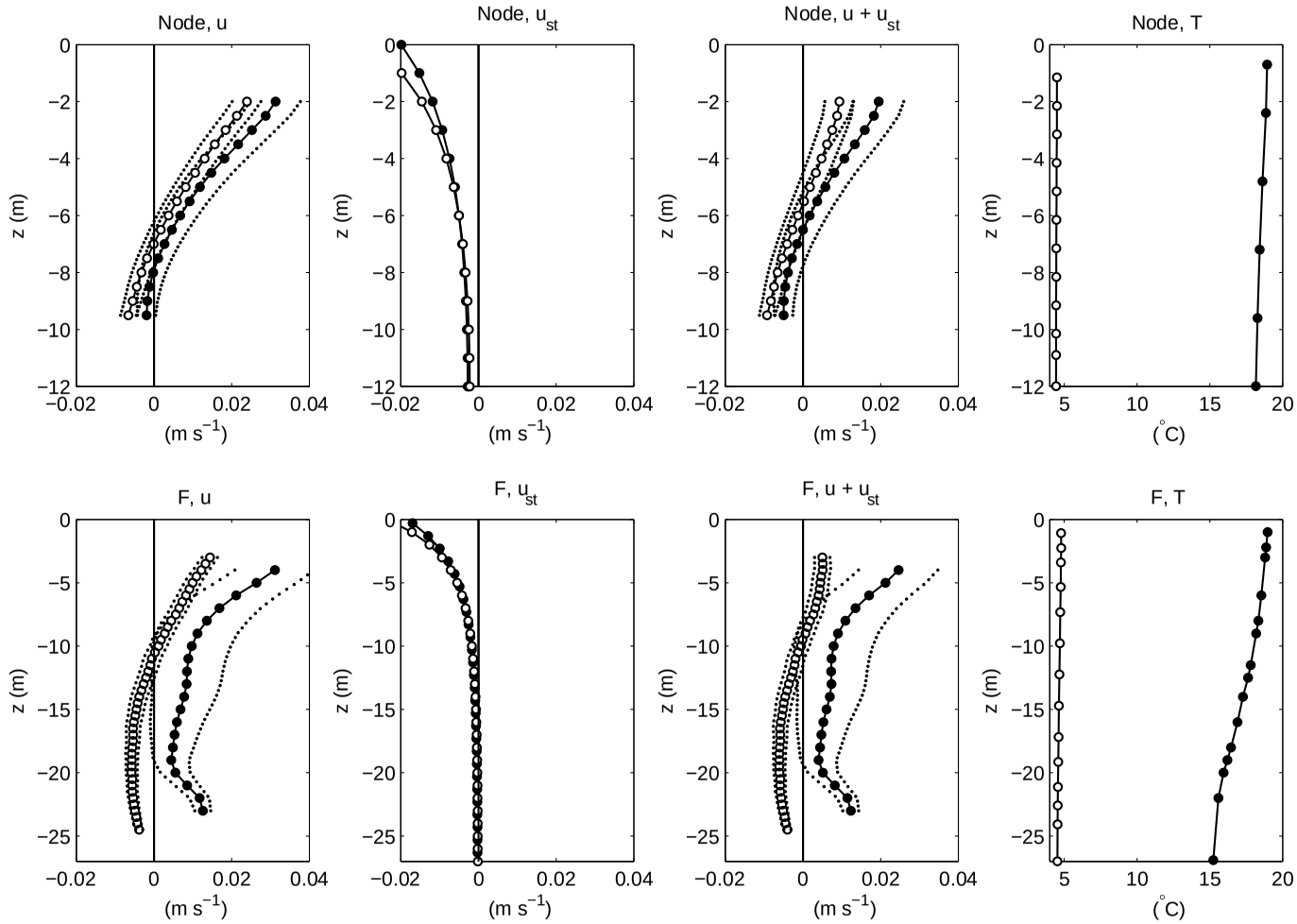

Figure 4-13: Top row: Node, and bottom row: F. Left to right: time-mean profiles of the of the cross-shelf velocities u, u_{st}, $u + u_{st}$, and temperature T during CBLAST 2003 (solid symbols) and SWWIM I (open symbols), over all times when velocity, wave, and temperature data were concurrently available. Dotted lines show range produced by rotating the coordinate system $\pm 5°$.

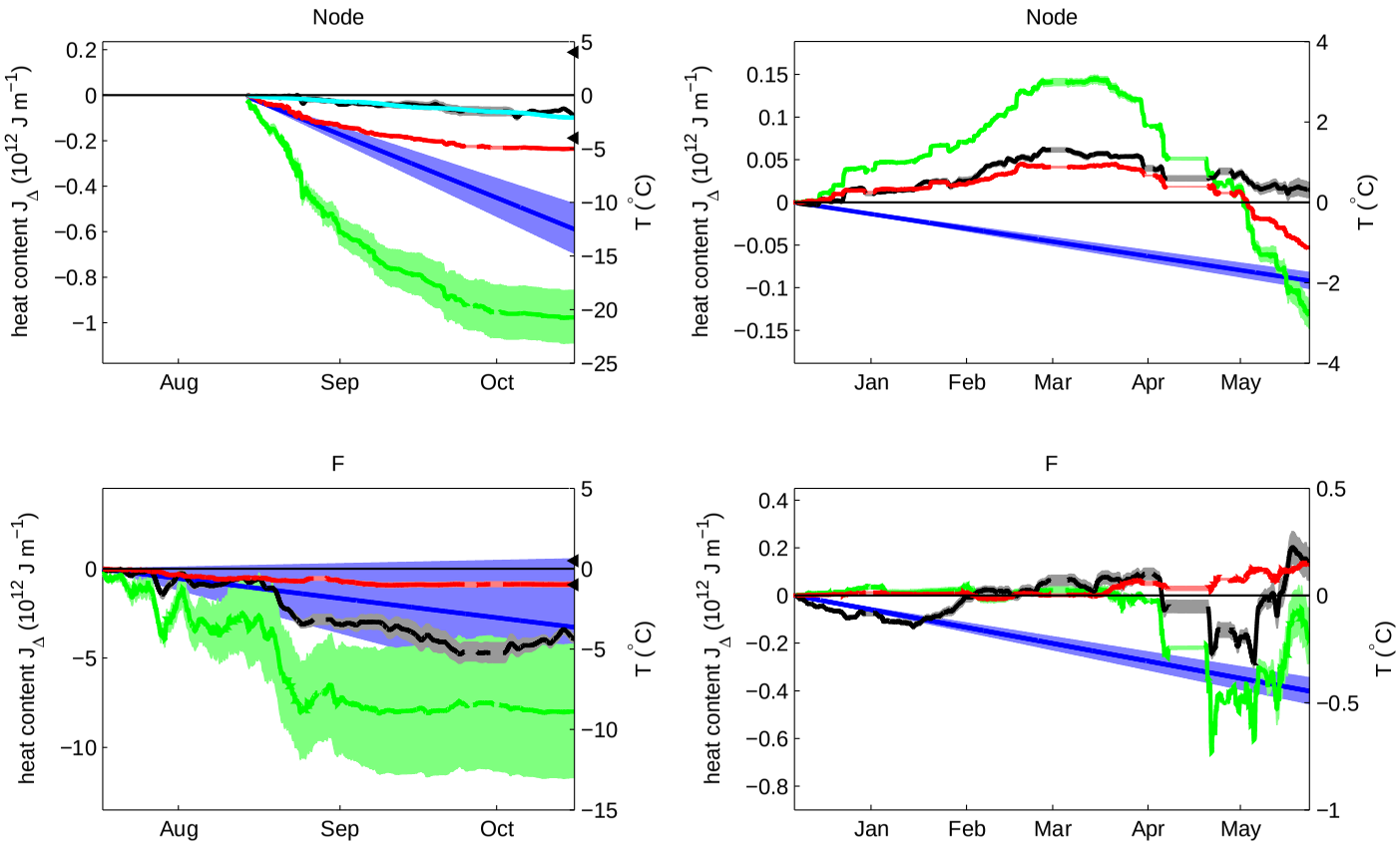

Figure 4-14: Decomposition of the cross-shelf heat flux from the 3-D time-integrated heat budget (Figure 4-11) based on the time scale of the velocity and temperature fluctuations. Top panels: onshore of 12-m isobath, and bottom panels: onshore of 27-m isobath, for summer (left) and winter (right). Note different axis scales; triangles in panels at left indicate axis limits of panels at right. Green: total change in heat content due to cross-shelf heat flux, J^{xs}, as in Figure 4-11. Blue: the part due to the time-mean (depth-varying part of the) profiles of velocity (including u_{st}) and temperature during that deployment (CBLAST 2003 or SWWIM I). Black: due to velocity and temperature fluctuations with time scales longer than $\sim$33 hrs. Red: due to velocity and temperature fluctuations with time scales shorter than $\sim$33 hrs, including tides. Light blue: due to the tidal velocity and temperature fluctuations predicted by T_TIDE (Pawlowicz et al., 2002) for the Node during CBLAST 2003.

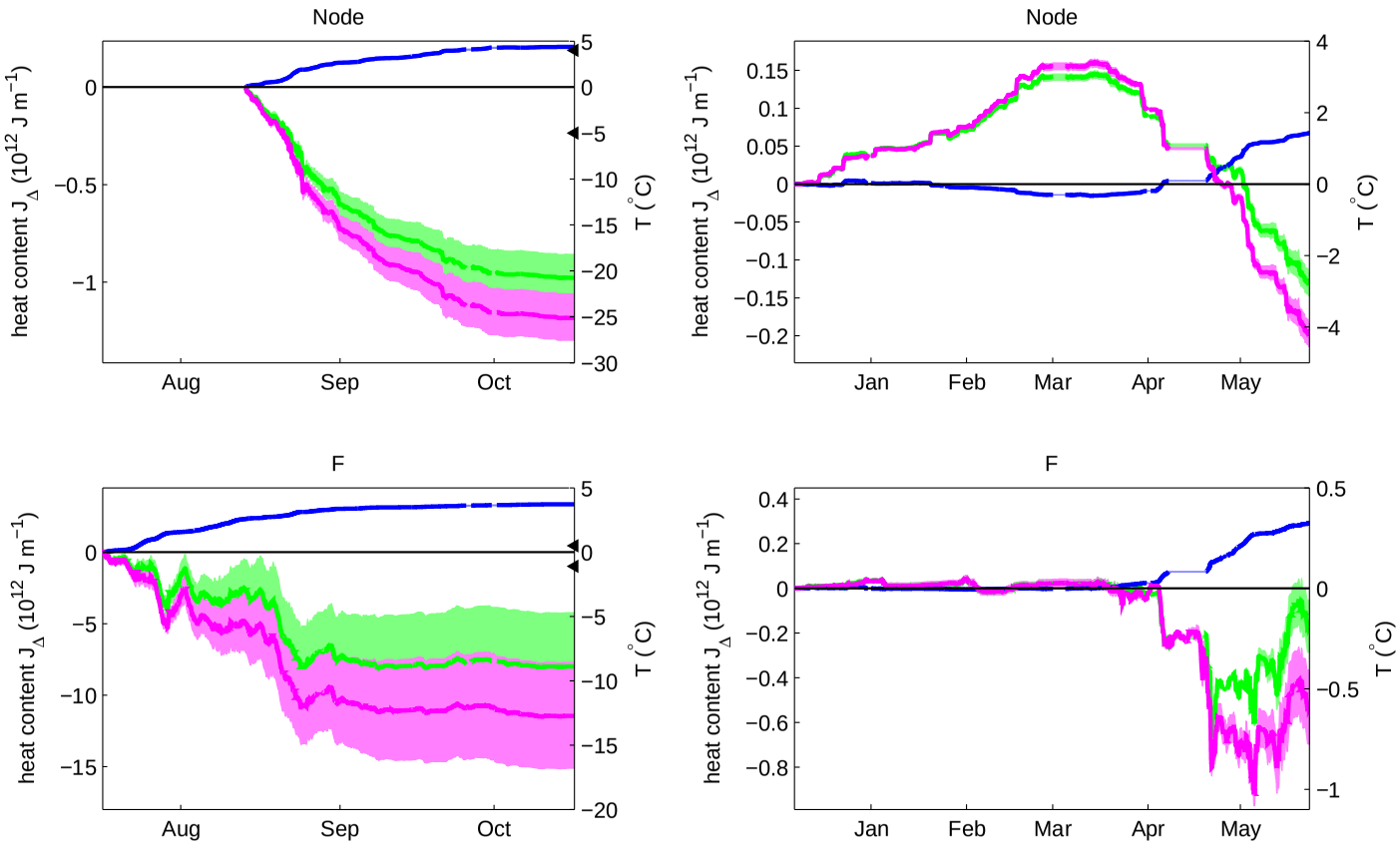

Figure 4-15: Decomposition of the cross-shelf heat flux (on all time scales) for the 3-D time-integrated heat budget (Figure 4-11) into the parts due to the Eulerian wave-averaged circulation and due to the wave-induced fluctuations in velocity and temperature. Top panels: onshore of 12-m isobath, and bottom panels: onshore of 27-m isobath, for summer (left) and winter (right). Note different axis scales; triangles in panels at left indicate axis limits of panels at right. Green: total change in heat content due to cross-shelf heat flux, $J^{xs} = J^{xs}_{circ} + J^{xs}_{waves}$, as in Figure 4-11. Magenta: due to cross-shelf circulation u observed by the ADCP, J^{xs}_{circ}. Blue: due to waves, J^{xs}_{waves}.

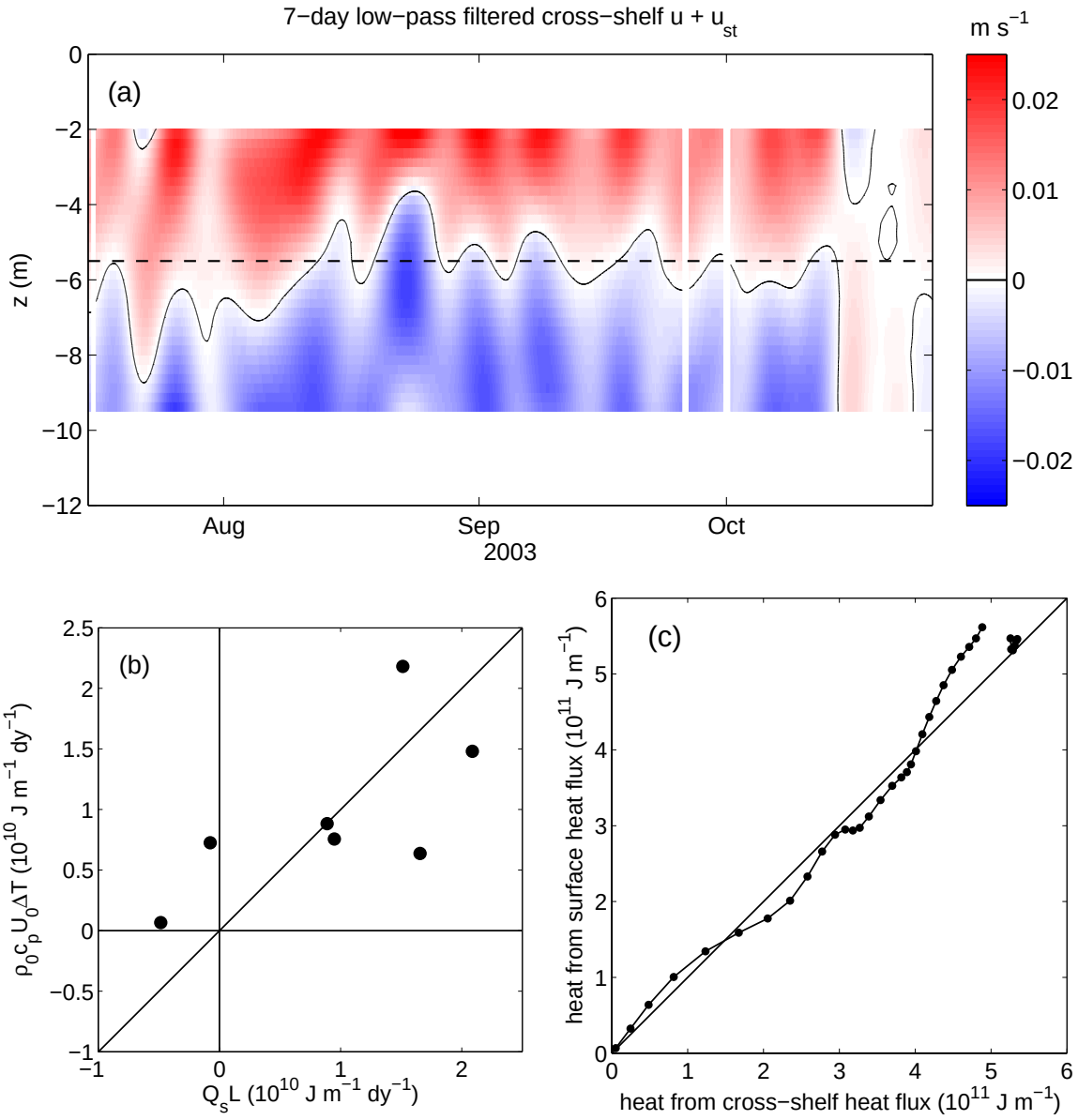

Figure 4-16: (a) Cross-shelf velocity $\widetilde{u} + \widetilde{u}_{st}$ at Node during summer 2003, with consistent offshore flow (red) in the upper layer. The layer interface at $z = -5.5$ m used for comparison with the two-layer model is indicated by the dashed line. (b) Modeled cross-shelf advective heat flux vs. observed surface heat flux from Section 4.3.5, calculated with time-mean U_0 and 7-day low-pass filtered Q_s and ΔT from summer 2003, plotted every 7 days. Diagonal line has slope 1. The two quantities are significantly correlated at the 95% confidence level. (c) Comparison of accumulated heat due to surface heat flux (on horizontal axis) and heat loss due to cross-shelf heat flux (on vertical axis) at Node during summer 2003 (CBLAST). Line with dots: from two-layer model (Section 4.3.5), $\rho_0 c_p \int U_0 \Delta T \, dt$ vs. $\int Q_s L \, dt$, with observed time-mean U_0 and 7-day low-pass filtered Q_s and ΔT. Time integrals are over the CBLAST 2003 deployment for times when $u + u_{st}$, Q_s, and T are all available. Diagonal line has slope 1.

Table 4.1: CBLAST 2003 Temperature Measurements.

	Node	T1	T2	F (CBLAST)	F (supplement)
Start (2003)	13 Aug	15 Jul	15 Jul	16 Jul	28 Aug
End (2003)	17 Oct	17 Oct	17 Oct	27 Aug	17 Oct
Instrument	0.7	1.0	1.0	1.0	1.0
depths	2.4	7.5	7.5	2.2	3.0
(m)	4.8	16.3	14.9	2.9	6.0
	7.2			6.0	9.0
	9.6			8.0	12.5
	11.99 (MVCO)			11.5	16.0
				12.5	19.0
				14.0	22.0
				16.0	26.9 (ADCP tripod)
				18.0	
				20.0	
				22.0	
Water depth (m)	12	16.5	15	27.3	27.3

Table 4.2: SWWIM I Temperature Measurements, 7 Dec 2004 - 23 May 2005.

	Node		F	
	Depth (m)	Type	Depth (m)	Type
Instruments	1.15	MicroCAT	1.1	MicroCAT
	2.15	TidbiT	2.3	TidbiT
	3.15	TidbiT	3.4	MicroCAT
	4.15	TidbiT	5.3	TidbiT
	5.15	TidbiT	7.3	MicroCAT
	6.15	TidbiT	9.8	TidbiT
	7.15	TidbiT	12.2	MicroCAT
	8.15	TidbiT	14.7	TidbiT
	9.15	TidbiT	17.2	MicroCAT
	10.15	TidbiT	19.2	TidbiT
	10.9	TidbiT	21.1	MicroCAT
	12 (MVCO)	MicroCAT	22.6	TidbiT
			24.1	MicroCAT
			27 (ADCP tripod)	Seagauge
Water depth (m)	12		27	

Table 4.3: Synoptic Variations in Temperature, Surface Heat Flux, and Cross-Shelf Heat Flux. The standard deviations (std) of $\partial\langle\langle T\rangle\rangle/\partial t$ and of the surface heat flux and the cross-shelf heat flux (converted to temperature change, $H^s/\rho_0 c_p A$ or $H^{xs}/\rho_0 c_p A$) and their squared correlations are shown for synoptic time scales, using 33-hr low-pass filtered data. The best-fit sinusoidal seasonal cycle has been removed from each time series. "Strat" ("unstrat") indicates times when the absolute value of the temperature difference between the near-surface and near-bottom measurements was greater (less) than 0.2°C. Units of the standard deviations are $\left(^\circ\mathrm{C\ dy}^{-1}\right)$. The minimum r^2 that is significant at the 95% confidence level is shown in parentheses.

Node	$std\left(\frac{\partial\langle\langle T\rangle\rangle}{\partial t}\right)$	$std\left(\frac{H^s}{\rho_0 c_p A}\right)$	$std\left(\frac{H^{xs}}{\rho_0 c_p A}\right)$	$r^2\left(\frac{\partial\langle\langle T\rangle\rangle}{\partial t}, \frac{H^s}{\rho_0 c_p A}\right)$	$r^2\left(\frac{\partial\langle\langle T\rangle\rangle}{\partial t}, \frac{H^s+H^{xs}}{\rho_0 c_p A}\right)$	fraction of variance remaining
Strat	0.44	0.20	0.37	0.48 (0.07)	0.70 (0.07)	0.30
Unstrat	0.36	0.34	0.16	0.68 (0.04)	0.70 (0.04)	0.30

F	$std\left(\frac{\partial\langle\langle T\rangle\rangle}{\partial t}\right)$	$std\left(\frac{H^s}{\rho_0 c_p A}\right)$	$std\left(\frac{H^{xs}}{\rho_0 c_p A}\right)$	$r^2\left(\frac{\partial\langle\langle T\rangle\rangle}{\partial t}, \frac{H^s}{\rho_0 c_p A}\right)$	$r^2\left(\frac{\partial\langle\langle T\rangle\rangle}{\partial t}, \frac{H^s+H^{xs}}{\rho_0 c_p A}\right)$	fraction of variance remaining
Strat	0.35	0.09	0.42	0.35 (0.04)	0.62 (0.04)	0.38
Unstrat	0.31	0.14	0.02	0.58 (0.06)	0.56 (0.06)	0.44

Table 4.4: Correlation of Surface Heat Flux with Wind Stress at MVCO, 2001–2007. Correlation coefficient r of low-pass filtered net surface heat flux Q_s with low-pass filtered along-shelf wind stress or cross-shelf wind stress. Minimum r for significance with 95% confidence is in parentheses.

	Along-Shelf Wind Stress r (r_s)	Cross-Shelf Wind Stress r (r_s)
summer	0.23 (0.09)	-0.46 (0.09)
winter	-0.42 (0.08)	-0.40 (0.08)

Table 4.5: Mean Wind Stress (units Pa). Positive indicates upwelling-favorable and offshore-ward.

	Along-Shelf Wind Stress		Cross-Shelf Wind Stress	
	CBLAST 2003	SWWIM I	CBLAST 2003	SWWIM I
Node	0.004	0.02	-0.008	0.03
F	0.002	0.02	-0.009	0.03

Chapter 5

Conclusions

In this thesis, the water circulation and the evolution of water temperature over the inner continental shelf south of Martha's Vineyard, Massachusetts, are investigated with time series of water velocity, temperature, density, and bottom pressure; surface gravity wave characteristics; wind stress; and heat flux between the ocean and atmosphere calculated from observations during 2001–2007, along with simple models. The key questions addressed are

1. What are the dominant processes that drive cross-shelf circulation on time scales of days to months over the inner continental shelf off New England?

2. Which dynamical balances are dominant over this inner shelf?

3. What are the mechanisms that control water temperature over the inner shelf?

Six-year-long time series of wind stress, dominant wave height and period, and water velocity profiles from an underwater cabled coastal observatory in 12 m water depth south of Martha's Vineyard are used to determine the separate dependence of the cross-shelf velocity profile on cross-shelf winds and along-shelf winds. During small waves, cross-shelf wind stresses are the dominant mechanism driving the cross-shelf circulation and exchange on this inner shelf, as in Figure 2-14, bottom. The along-shelf wind stress does not drive a substantial cross-shelf circulation, in contrast to mid-shelf (Figure 2-14, top). This is likely true in a wide variety of inner shelf locations.

The observed cross-shelf velocity profiles and cross-shelf transport in the surface layer during winter roughly agree with a simple two-dimensional, unstratified model of cross-shelf wind stress forcing. The cross-shelf velocity profile is more vertically sheared, and the surface layer transport stronger, in summer than in winter for a given offshore wind stress.

When waves are large, the Eulerian cross-shelf circulation is no longer roughly symmetric in the wind direction. During large waves and onshore winds the cross-shelf velocity profile is nearly vertically uniform, because the wind- and wave-driven shears cancel. In contrast, during large waves and offshore winds the profile is strongly vertically sheared, because the wind- and wave-driven shears have the same sign. Waves also lead to a large difference between the Eulerian circulation and the estimated Lagrangian transport of nutrients, plankton, heat, salt, and pollutants during combined wind and wave forcing. The estimated Lagrangian velocity profile in winter is similar to the wind-driven part of the Eulerian circulation alone, as if the waves were not present, because the contribution of wave-driven Stokes' drift to the Lagrangian profile approximately cancels the contribution of waves to the Eulerian circulation. The relative importance of wave, cross-shelf wind, and along-shelf wind forcing depends on water depth, wave height, and wind strength. The answer to Question 1 above is that cross-shelf wind and surface gravity waves are the dominant forcing mechanisms for cross-shelf circulation over this inner shelf.

The subtidal, depth-average cross-shelf momentum budget at MVCO is not geostrophic, as would be expected at mid-shelf. Instead, the inner shelf is a region where multiple dynamical balances are (sometimes simultaneously) important: geostrophy and coastal setup and set-down due to the cross-shelf wind. In winter, the Coriolis term and cross-shelf pressure gradient at the 12-m isobath are substantial and significantly correlated, as in a pure geostrophic balance at mid-shelf. At other times, particularly in summer, the cross-shelf wind stress and cross-shelf pressure gradient are positively correlated, consistent with coastal set-up and set-down driven by the cross-shelf wind stress. The estimated momentum flux divergence due to shoaling surface gravity waves is also a leading-order term in the budget, but is not correlated

with the cross-shelf pressure gradient, in contrast to what is expected for set-down due to shoaling waves outside the surf zone. It is likely that the pressure gradient due to wave-driven set-down occurs over a spatial scale too small to resolve with these observations. The wave radiation stress gradient and cross-shelf wind stress are important at the same time for onshore winds, and both contribute to making the cross-shelf momentum balance ageostrophic. The other estimated terms in the cross-shelf momentum budget are at least an order of magnitude weaker than the dominant terms.

The along-shelf momentum budget is more complex than the cross-shelf. No estimated term is negligible. The main balance is between the wind stress and pressure gradient. The bottom stress, acceleration, Coriolis, Hasselmann wave stress, and nonlinear advection terms, although of secondary importance, are about half as large as the pressure gradient. This is in contrast to the cross-shelf budget, in which the secondary terms are an order of magnitude smaller than the three or four dominant terms. The along-shelf pressure gradient is consistent with a local sea level response to wind forcing, rather than being dominated by a remotely generated pressure gradient. There is a strong relation between the along-shelf depth-average flow and the along-shelf wind stress. This may be due to along-shelf accelerations caused by the time-varying imbalance between wind stress and along-shelf pressure gradient, combined with a bottom stress that is approximately linearly related to the along-shelf subtidal flow. The answer to Question 2 above is that in the cross-shelf direction, dynamical balances usually associated with the surfzone (wave-driven coastal set-down) and with the mid-shelf (geostrophy), as well as a balance unique to the inner shelf (coastal set-up and set-down by the cross-shelf wind) are all important over this inner shelf; in the along-shelf direction, the main balance is between the wind stress and pressure gradient, similar to mid-shelf sites in this region.

The measurements of along-shelf density gradient available for this study were mainly collected during summer, when the wind forcing and wave forcing are relatively weak. Measurements of the along-shelf density gradient during strong winter forcing would likely help to resolve which secondary terms in the along-shelf momen-

tum budget are the most important. Sea-level displacements over horizontal scales too small to resolve with these observations seem to be leading to dynamically important pressure gradients in both the along-shelf and cross-shelf directions. The wave radiation stress gradient and the amount of wave dissipation over the inner shelf are also very uncertain. It will be important in future studies to measure pressure gradients and spatial variations in wave characteristics on smaller scales.

On time scales of weeks to months in summer, the water over this inner shelf is persistently cooled due to a mean upwelling circulation combined with vertical temperature stratification. The cross-shelf heat flux nearly balances the surface heat flux throughout mid-summer, so the water temperature is almost constant in spite of strong surface heating (Figure 4-12, top). The along-shelf heat flux divergence, though not estimated directly, is apparently small. In winter, the heat balance is more one-dimensional at both sites, with the surface heat loss and the change in water column heat content closer to equal and the cross-shelf heat flux small (Figure 4-12, bottom). In spring, the transition from a one-dimensional to a more complex heat balance occurs earlier at the shallower site. The heat transport due to surface gravity waves (Stokes' drift) is included in the heat budget, to our knowledge for the first time, and is substantial in both 12- and 27-m water depth.

On time scales of a few days, during stratified conditions all the heat balance terms are important at the shallow site: cross-shelf heat flux, change in local water column heat content, and also the surface heat flux, due to the small water depth. At the deeper site, surface heat flux is less important on synoptic time scales but the cross-shelf heat flux and local change in temperature are substantial during stratified conditions. The fluctuating part of the cross-shelf heat flux is correlated with the along-shelf wind stress at the deeper site, but with the cross-shelf wind stress at the shallower site. During unstratified conditions, cross-shelf heat flux is negligible in the synoptic heat balances, while the surface heat flux is an important term, particularly at the shallower site. The residual in the synoptic heat budget is large in all cases and probably indicates that along-shelf heat flux divergence is important on time scales of days in all seasons, even though its influence on time scales of weeks to months in

summer is small.

The cross-shelf heat flux on time scales of weeks to months at the shallow site in summer agrees well with a simple two-layer model in which the cross-shelf velocity (including the Stokes' drift) is constant in time, with offshore flow near the surface and onshore flow near the bottom. The temperature profile adjusts so that the inner shelf heat content is in a quasi-steady state, with the slowly-evolving surface heating and cross-shelf advection balancing on time scales longer than the flushing time for the volume, a few days. This is very different from previous continental shelf heat budgets off the East Coast of the United States, in which the surface heating and change in water temperature tend to balance on long time scales in summer. The answer to Question 3 above is that the dominant mechanisms controlling the water temperature over this inner shelf on seasonal time scales are surface heat flux (in both summer and winter) and cross-shelf heat transport (in summer), though along-shelf heat transport seems to be important on shorter time scales; also, heat transport due to surface gravity waves is not negligible.

The results of this study are applicable to the inner shelf regions of broad, shallow, highly productive shelves, where wind-, wave-, and buoyancy-driven circulation can all be important. Although several previous authors have noted cross-shelf circulations driven by the cross-shelf wind, this is the first comprehensive study of the form of the response of the circulation as a function of the strength of the cross-shelf wind stress. This is also the first observational study to demonstrate that surface gravity waves have a substantial influence on the heat budget of the inner continental shelf.

Recent theoretical and numerical modeling studies have considered the effects of surface gravity waves on the transport of heat, momentum, and other tracers within the Generalized Lagrangian Mean framework (*e.g.*, Ardhuin et al., 2007). Because observations of coastal circulation and tracer transport are usually made in an Eulerian framework, however, in future it will be important to consider how the new theoretical and numerical model predictions can be accurately tested by observational studies.

The main message of this thesis is that future observational and model studies of inner continental shelves should consider the effects of cross-shelf wind stress and surface gravity wave forcing, even well outside the surfzone. An understanding of the roles of cross-shelf winds and waves in driving the circulation over the continental shelves is a prerequisite for understanding the function of continental shelf ecosystems and the transport of pollutants, heat, salt, and other tracers of local and global importance, such as dissolved carbon, on the continental shelf.

Appendix A

Adjustment of Wind Stress

Because the MVCO meteorological masts Met A and Met B are on land (Figure 2-2), the wind velocity measured at the masts is not a good representation of the wind velocity over the water, particularly when the wind is blowing from the north (from land toward the ocean). A shorter time series of wind velocity is available from the MVCO Air-Sea Interaction Tower (ASIT), which is located on the 15-m isobath (Figure 2-2). The ASIT wind stress time series covers 2 August 2004 through 10 May 2007, with gaps (53% data coverage).

To form a longer time series representative of wind stress over the water, we linearly adjusted the wind stresses from Met A and Met B based on linear regressions against the ASIT wind stress for each 10° interval of wind stress direction (Figures A-1–A-4). We adjusted the true eastward and northward components of wind stress separately to allow for variations in both wind stress angle and magnitude between the ASIT and land-based time series. For example, the adjusted eastward wind stress component at Met A, $\tau^e_{A_a}$, was calculated as

$$\tau^e_{A_a} = a\tau^e_A + b \tag{A.1}$$

where τ^e_A is the eastward wind stress component calculated from observations at Met A, and a and b are the best-fit slope and intercept from the linear regression of

the ASIT wind stress against Met A, for a given wind stress direction at Met A:

$$\tau^e_{ASIT} = a\tau^e_A + b \tag{A.2}$$

The regression slopes are between 1 and 3 (1 and 10), and the intercepts between -0.01 and 0.03 Pa (-0.02 and 0.04 Pa) for Met A (B), with the largest slopes for angles at which the wind is blowing from land to sea (Figures A-1–A-4, open circles). We estimated slopes and intercepts for angles with correlation coefficient at least 0.5 between the two time series, and linearly interpolated those slopes and intercepts to cover all wind stress directions. The adjusted Met A and Met B time series, when regressed against the ASIT wind stress, have slopes near 1 and intercepts near zero (Figures A-1–A-4, black squares).

We then combined the adjusted Met A and Met B time series, using Met A when available because it is closer to the water, and Met B otherwise. The final combined wind stress time series has a regression slope near 1, intercept less than 0.01 Pa, and correlation coefficient greater than 0.8 (mostly > 0.9) compared to ASIT for all wind stress directions (Figure A-5).

We constructed a long wind velocity time series at 12.5 m above sea level by using the Smith (1988) bulk formula for wind stress with the default air density (1.22 kg m^{-3}) and air temperature (10°C) to infer wind velocity from the adjusted wind stress time series. We used that wind velocity to calculate the bulk surface heat flux.

The results for cross-shore volume transport as a function of cross-shore and along-shore wind stress are not significantly different at the 95% confidence level when calculated with the ASIT or the combined, adjusted wind stress time series, for the periods when both wind stress time series are available (Figures A-6 and A-7). Therefore, we do not think the results presented in this manuscript are artifacts of the adjusted wind stress time series.

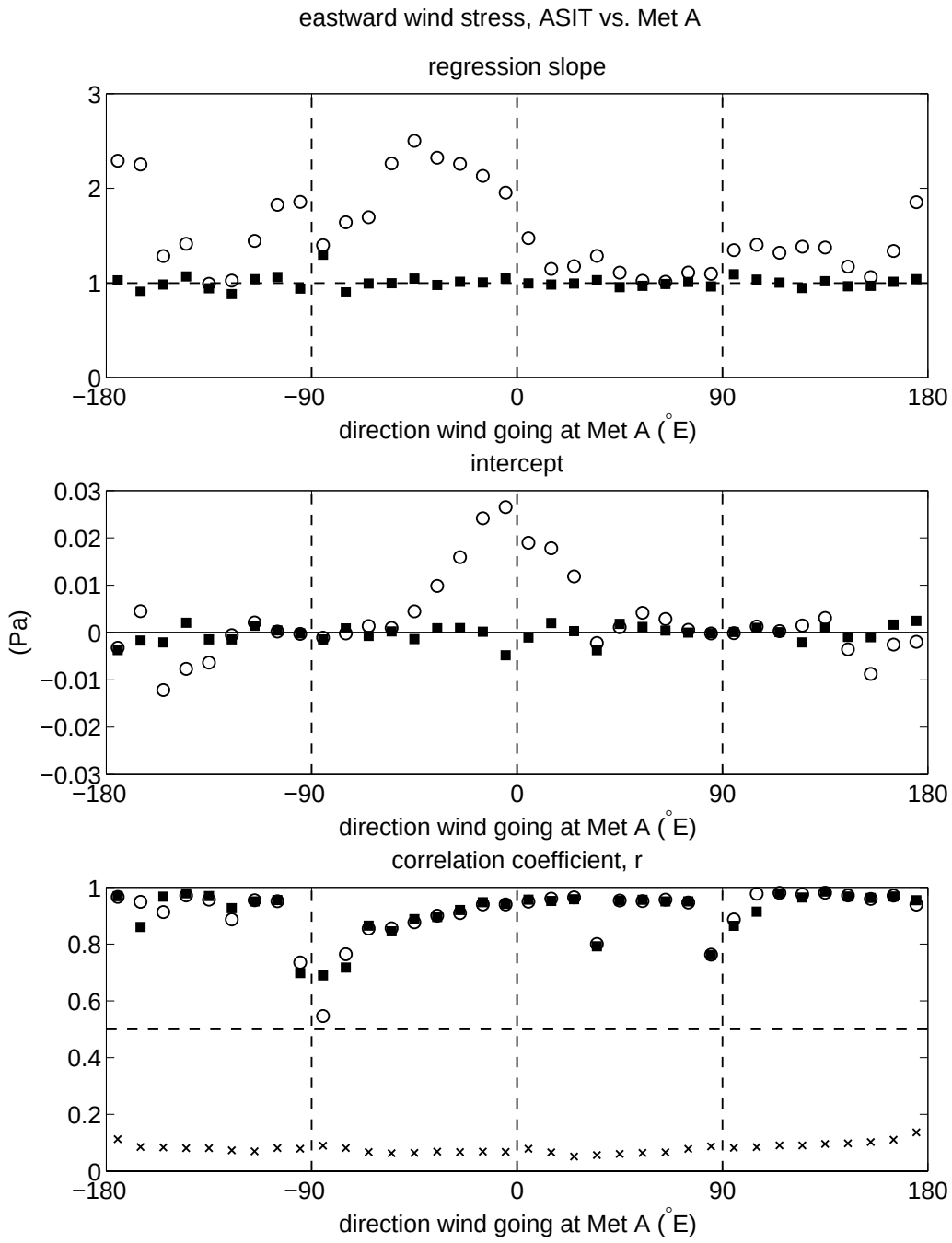

Figure A-1: Linear regression slope and intercept and correlation coefficient for the eastward wind stress component at ASIT regressed against the eastward wind stress component at Met A (see Figure 2-2 for wind measurement locations). Open circles: with original 20-min data. Black squares: after linearly adjusting Met A to match ASIT as described in Appendix A. "x" symbols in lower panel indicate minimum correlation that is significant at the 95% confidence level.

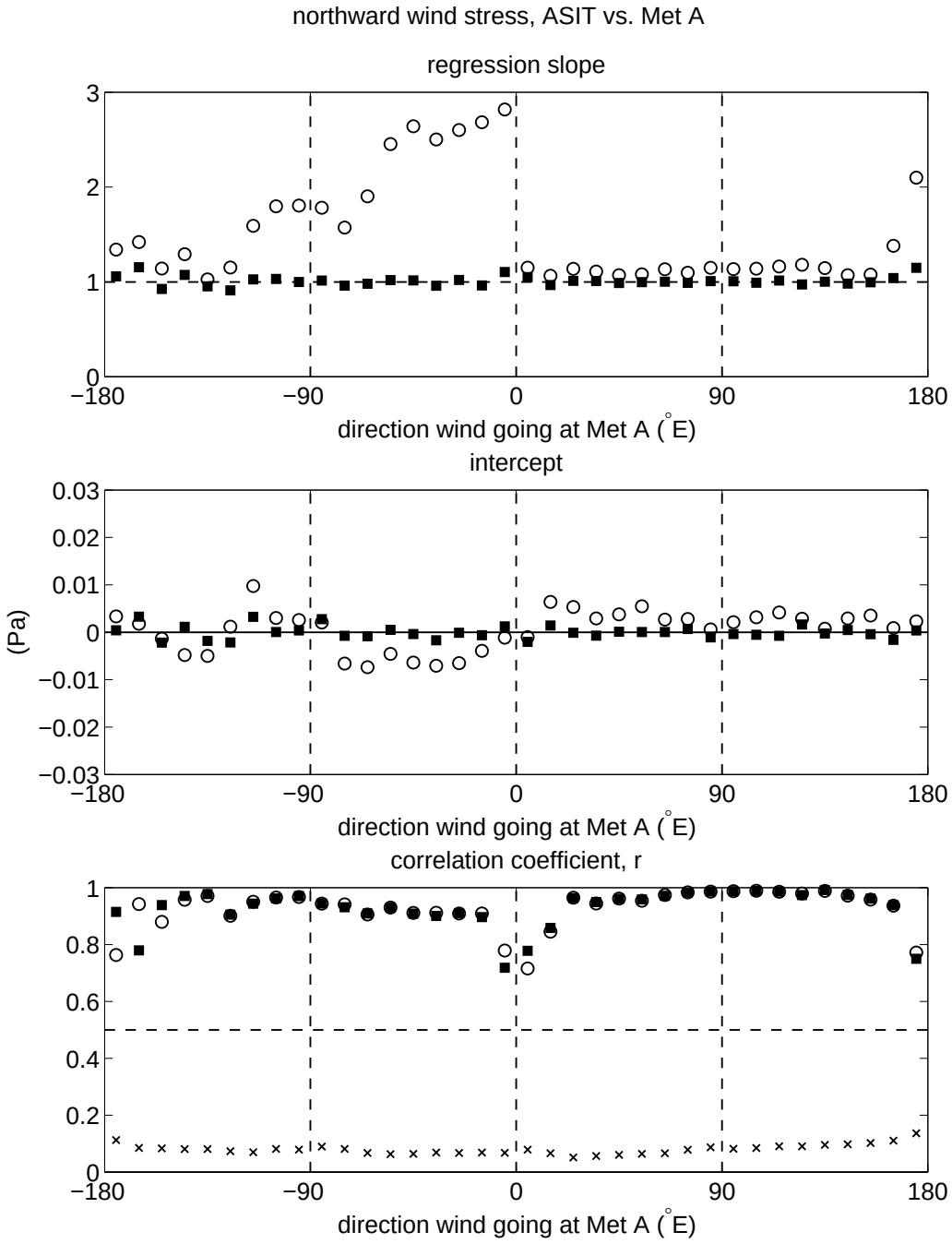

Figure A-2: Same as Figure A-1, but for northward wind stress component at Met A.

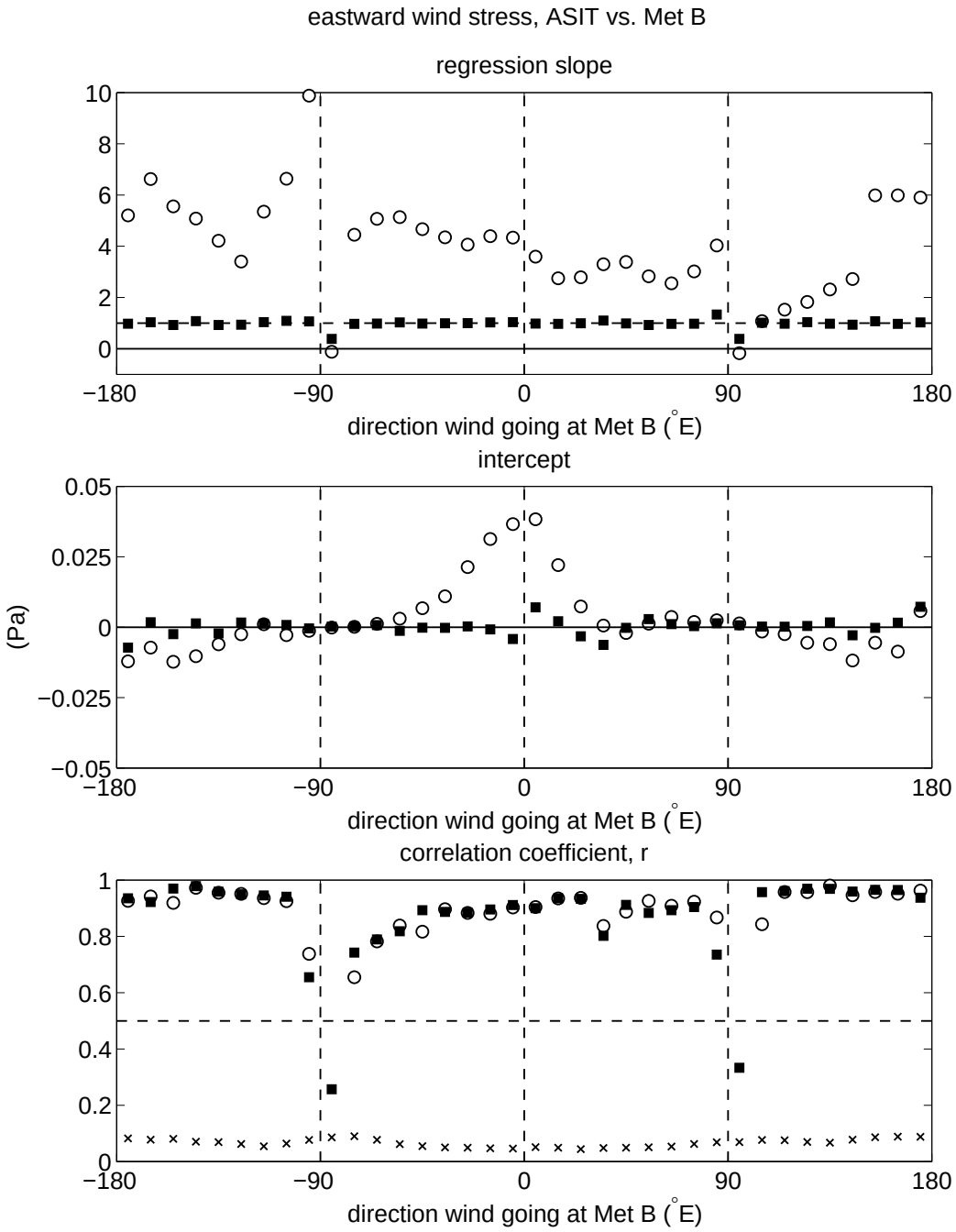

Figure A-3: Same as Figure A-1, but for eastward wind stress component at Met B.

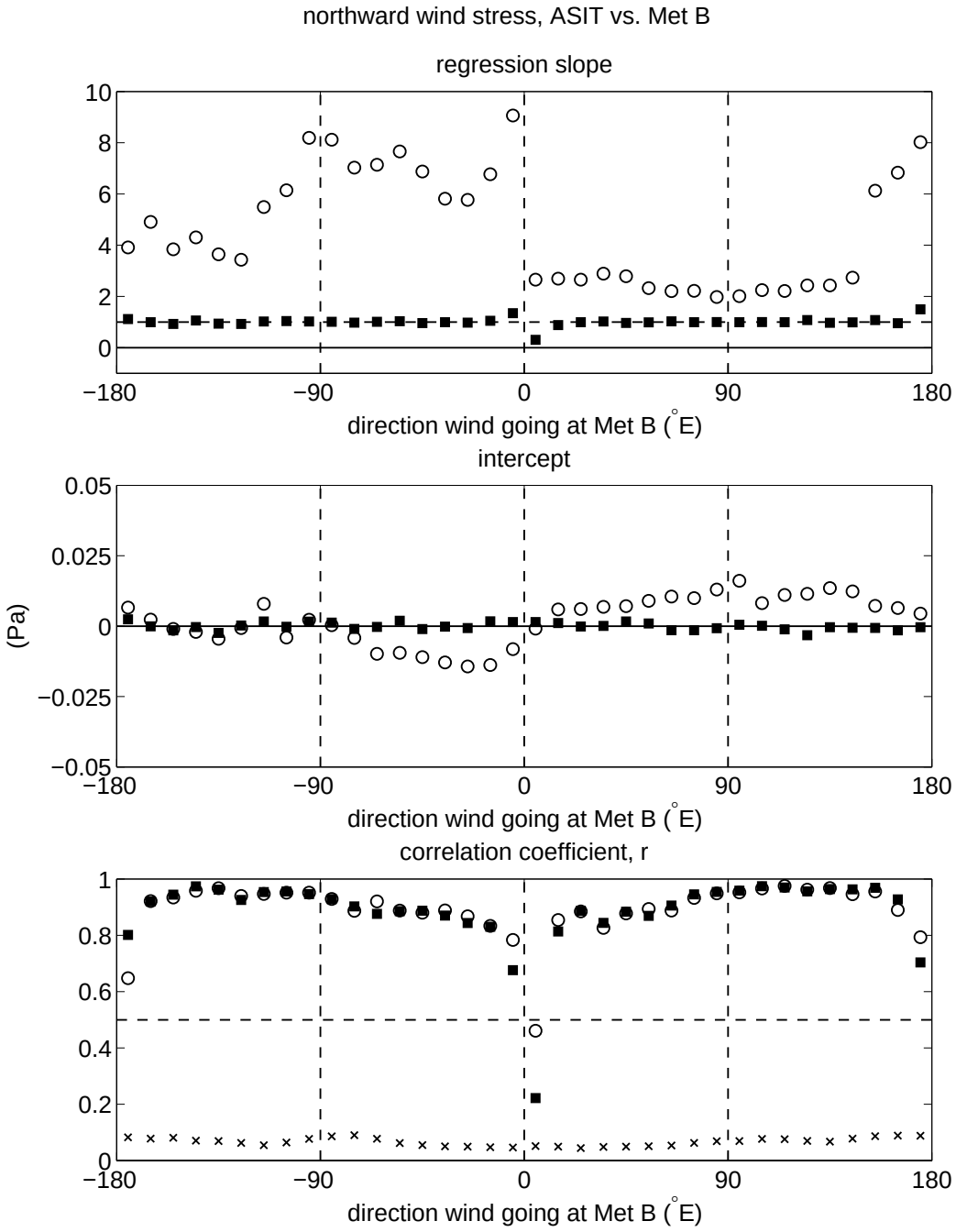

Figure A-4: Same as Figure A-1, but for northward wind stress component at Met B.

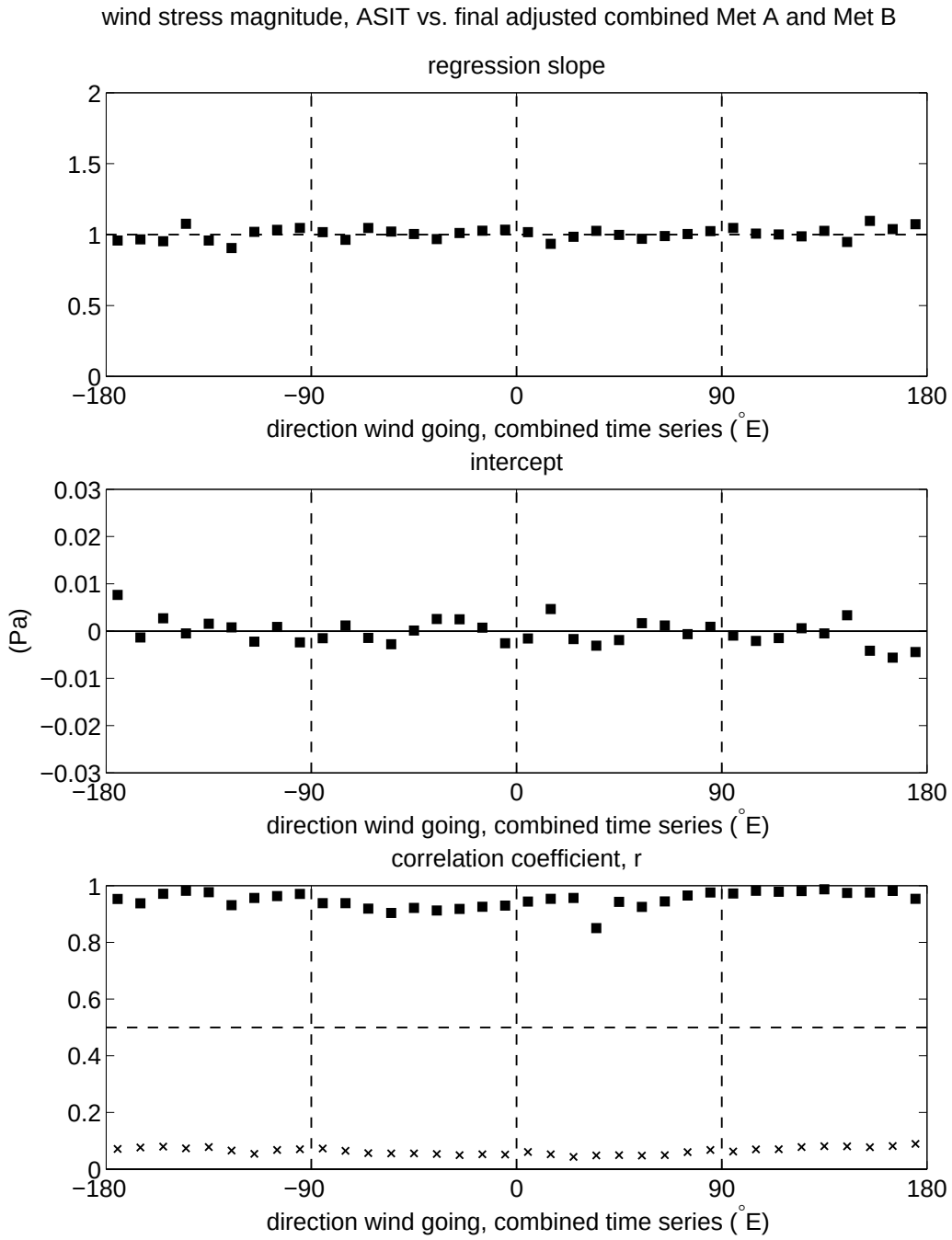

Figure A-5: Same as Figure A-1, but for wind stress magnitude of the final combined time series of wind stress from adjusted Met A and Met B.

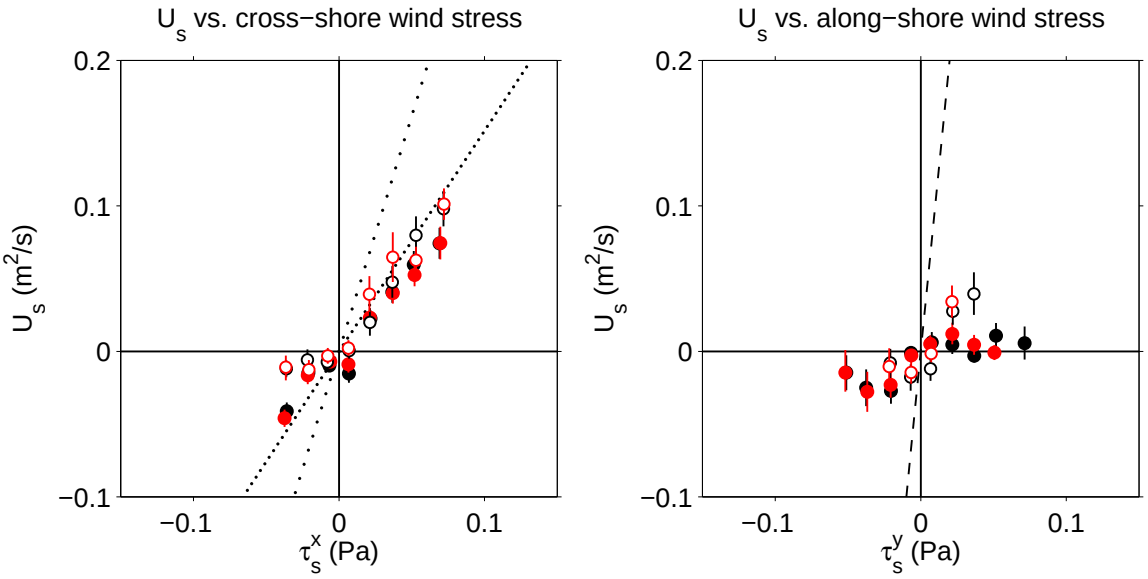

Figure A-6: Same as Figure 2-9, but with ASIT wind stress (red) and adjusted wind stress from shore masts (black), using only times when both wind stress time series are available.

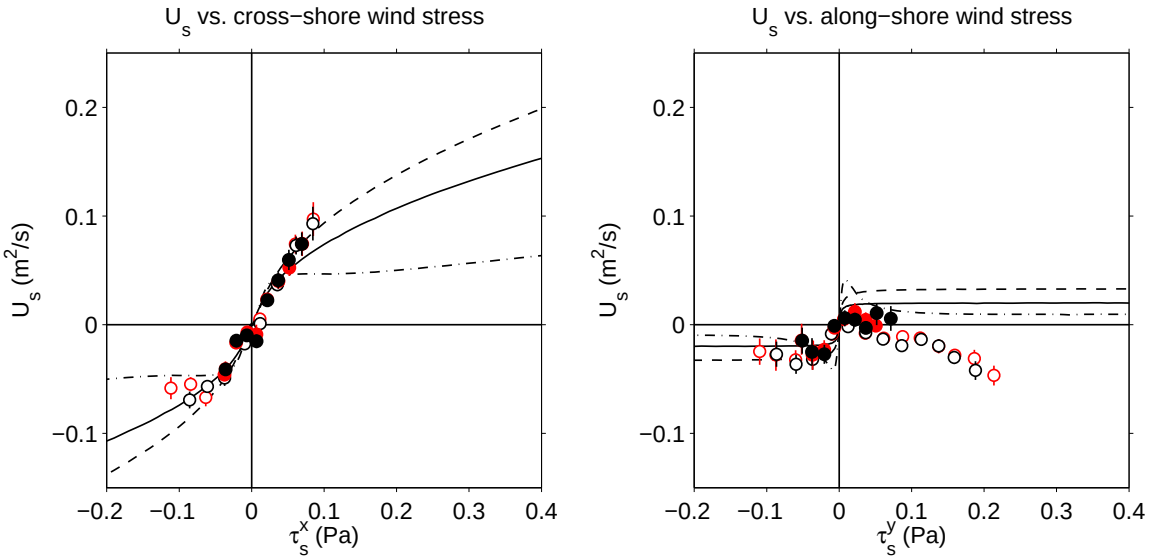

Figure A-7: Same as Figure 2-10, but with ASIT wind stress (red) and adjusted wind stress from shore masts (black), using only times when both wind stress time series are available.

Appendix B

Correction of TidbiT Temperatures

During SWWIM I, at times when the MicroCATs at Node and F indicated the water column was well-mixed in temperature, the TidbiT sensor readings deviated from the MicroCAT readings. The deviation was approximately a linear function of ambient temperature for each TidbiT. TidbiTs are less accurate and have coarser temperature resolution than MicroCATs, according to the manufacturers' specifications. Consequently, we applied a linear correction to the temperature output from each TidbiT, determined by regressing the TidbiT temperature against MicroCAT temperatures linearly interpolated to the TidbiT position. To calculate the regression coefficients, we used only times when the water column was well-mixed within 0.05°C according to the MicroCATs. The resulting linear corrections are given in Table B.1; the slopes are between 0.992 and 0.998, and the intercepts are between -0.04 °C and 0.23 °C. The results presented here do not change substantially if we instead use only the MicroCATs and not the TidbiTs to calculate the heat budget terms.

Table B.1: SWWIM I TidbiT Corrections

Mooring	Instrument Depth (m)	Corrected Temperature
Node	2.15	$0.996\,T_{measured} + 0.067\,^{\circ}\mathrm{C}$
Node	3.15	$0.995\,T_{measured} + 0.070\,^{\circ}\mathrm{C}$
Node	4.15	$0.996\,T_{measured} + 0.026\,^{\circ}\mathrm{C}$
Node	5.15	$0.997\,T_{measured} + 0.035\,^{\circ}\mathrm{C}$
Node	6.15	$0.995\,T_{measured} + 0.215\,^{\circ}\mathrm{C}$
Node	7.15	$0.996\,T_{measured} - 0.041\,^{\circ}\mathrm{C}$
Node	8.15	$0.995\,T_{measured} + 0.058\,^{\circ}\mathrm{C}$
Node	9.15	$0.996\,T_{measured} - 0.014\,^{\circ}\mathrm{C}$
Node	10.15	$0.997\,T_{measured} - 0.015\,^{\circ}\mathrm{C}$
Node	10.90	$0.997\,T_{measured} - 0.029\,^{\circ}\mathrm{C}$
F	2.3	$0.992\,T_{measured} + 0.162\,^{\circ}\mathrm{C}$
F	5.3	$0.995\,T_{measured} + 0.232\,^{\circ}\mathrm{C}$
F	9.8	$0.993\,T_{measured} + 0.059\,^{\circ}\mathrm{C}$
F	14.7	$0.993\,T_{measured} + 0.165\,^{\circ}\mathrm{C}$
F	19.2	$0.993\,T_{measured} + 0.159\,^{\circ}\mathrm{C}$
F	22.6	$0.992\,T_{measured} + 0.105\,^{\circ}\mathrm{C}$

Appendix C

Calculation of Heat Budget Terms from Observations

We use the 20-min average data to represent all wave-averaged quantities. The dominant wave period is on the order of 5 sec, so a 20-min average is an average over approximately 250 wave periods. For vertical integrals (including Eq. (4.5)), we used a trapezoidal estimate except in Section C.3, and we extrapolated the observations to the surface and bottom by assuming the temperature and velocity were constant vertically between the near-bottom instrument and the sea floor, and between the near-surface instrument and the water surface. There is no substantial change in the results if a linear extrapolation to the surface and/or bottom is used instead. To estimate $h(x)$, we used the National Geophysical Data Center (http://www.ngdc.noaa.gov) high-resolution bathymetry linearly interpolated onto a grid with 50-m spacing in the x direction. Note that local curvature of the isobaths (Figure 4-3) and resulting variations in the true along-shelf and cross-shelf coordinate directions may cause inaccuracy in the calculation of the temperature gradients by mapping part of the cross-shelf temperature gradient onto the along-shelf gradient estimated here, and vice versa.

C.1 Surface Heat Flux

The surface heat flux Q_s was calculated at each mooring location with the Fairall et al. (2003) bulk algorithms. The wind speed, air temperature, relative humidity, air pressure, and downward shortwave and longwave radiation were obtained from the MVCO shore masts. The sea-surface temperature was approximated by the near-surface water temperature measured at the mooring site. When the near-surface water temperature was not available at the Node, the near-bottom water temperature was used instead (to construct the long time series of net surface heat flux for 2001-2006 in Figure 4-6). We estimate the uncertainty in the low-pass filtered net surface heat flux to be ± 8 W m^{-2} based on the daily average heat flux error values found by Colbo and Weller (2007). This does not include errors in the surface heat flux due to uncertainties in the coefficients in the bulk formulae.

When the surface heat flux is integrated in time to yield a prediction for the water column temperature according to Eq. 4.4, there is an unknown constant of integration (the predicted initial water temperature). To plot the predicted temperature during CBLAST 2003, we calculated a best-fit sinusoidal annual cycle of near-surface temperature at each mooring based on the near-surface temperature measurements from CBLAST 2003 and SWWIM I, then used that year-long sine curve of SST to calculate a net surface heat flux using the MVCO meteorological data, then aligned that yearly cycle to the sinusoidal temperature cycle on March 11 when the observed surface heat flux changes sign for the year (thin red lines in Figure 4-10), then plotted the CBLAST 2003 (SWWIM I) prediction (thick red line in Figure 4-10) starting from the yearly cycle value at the beginning (end) of the deployment, matching mean values over 10 days.

C.2 Surface Heating for 3-D Budget

H^s was estimated from Eq. (4.10) for the 3-D temperature balance by assuming the surface heat flux Q_s varies linearly in the x direction, and then estimating $Q_s(x,t)$

from the values calculated for the Node and F. The distance L between each mooring and the coast was estimated using the latitude and the longitude of the mooring, the latitude of the coast, and the principal axis direction for that mooring.

C.3 Observed Temperature for 3-D Budget

The observed average temperature of the wedge-shaped volume is defined in Eq. (4.7) and was estimated by using

$$A = \int_0^L h(x)\, dx \tag{C.1}$$

for the area of the wedge. During times when temperature data were available at both Node and F (during the SWWIM I deployment and latter part of CBLAST 2003) the temperature of the wedge onshore of each mooring was calculated by linearly extrapolating the temperature data from Node and F into the region onshore of the Node, and linearly interpolating temperature along the bottom between Node and F. During times when temperature data were only available at F (beginning of CBLAST 2003), the temperature onshore of F was estimated by assuming horizontal isotherms and then adding a positive temperature offset equal to the offset between the two methods at the time when Node temperature data first became available.

C.4 Cross-Shelf Advective Heat Flux Divergence

The observed cross-shelf heat flux divergence was calculated in two parts: H^{xs}_{circ} and H^{xs}_{waves}, as in Eq. (4.14). H^{xs}_{circ}, the rate of change of heat content in the wedge due to onshore heat transport by the depth-varying part of the cross-shelf circulation observed by the ADCP, was calculated from Eq. (4.12). Only the depth-varying part of u affects H^{xs}_{circ} because the depth-average part of u integrates to zero by definition when multiplied by the depth-varying part of the temperature profile, which is the $\widetilde{T}$ that appears in Eq. 4.12 due to the introduction of the reference temperature $\langle T \rangle_L$ (see Appendix D). The introduction of the reference temperature avoids two problems described by Montgomery (1974): the arbitrary zero of the temperature scale and our

inability to resolve changes in heat content due to changes in the water volume in the wedge [now included in H^{as}, Eq. (4.15), and not considered here] as opposed to changes in heat content due to the depth-varying part of the circulation (which does not change the volume of the wedge).

H^{xs}_{waves}, the rate of increase of heat content in the wedge due to onshore heat transport by the correlated fluctuations of temperature and velocity induced by the waves, was calculated from Eq. (4.13) by using Eq. (D.40) to estimate u_{st} from the observed dominant wave period and significant wave height.

C.5 Along-Shelf Advective Heat Flux Divergence

We can estimate the part of the along-shelf advective heat flux divergence H^{as} [Eq. (4.15)] onshore of the Node due to advection of the along-shelf temperature gradient $\partial T/\partial y$,

$$H^{as}_{adv} = \int_0^L \int_{-h}^0 v \frac{\partial}{\partial y} \left(T - \langle T \rangle_L\right) \, dz \, dx \tag{C.2}$$

where L is the cross-shelf position of the Node mooring, by using moorings T1 and T2 to estimate the along-shelf temperature gradient. Those moorings were deployed on approximately the 15-m isobath (Figure 4-3). If we assume the along-shelf velocity as a function of σ decreases linearly from its value at the Node to $v = 0$ at $x = 0$, then

$$v\left(x, \sigma, t\right) = v(L, \sigma, t) \frac{x}{L} \tag{C.3}$$

and if we assume the along-shelf temperature gradient (as a function of $\sigma \equiv z/h$) is constant in x, then

$$\frac{\partial T}{\partial y}\left(x, \sigma, t\right) = \frac{\partial T}{\partial y}\left(x|_{h=15 \text{ m}}, \sigma, t\right) \tag{C.4}$$

Using the fact that $\langle T \rangle_L$ is a function only of t, and changing coordinates from z to σ in the vertical integral,

$$H^{as}_{adv} = \int_0^L \frac{x}{L} h(x) \int_{-1}^0 v(L, \sigma, t) \frac{\partial T}{\partial y}\left(x|_{h=15 \text{ m}}, \sigma, t\right) \, d\sigma \, dx \tag{C.5}$$

The vertical integral was estimated by interpolating v and T onto a common σ grid, using the longitudes of T1 and T2 to calculate the distance Δy between those two moorings, and then estimating $\partial T/\partial y$ as

$$\frac{\partial T}{\partial y} = \frac{T|_{T2} - T|_{T1}}{\Delta y} \tag{C.6}$$

The remainder of the along-shelf heat flux divergence, the contribution from divergence in the along-shelf velocity, cannot be estimated observationally. Measurements of the along-shelf velocity gradient were not made during CBLAST 2003 or SWWIM I.

Appendix D

Derivation of 3-D Temperature Balance with Waves

We derive a temperature balance equation for a wedge-shaped volume that extends from the shore at $x = 0$ to a mooring at $x = L$, from the mean water surface at $z = 0$ to the bottom at $z = -h(x)$, and 1 m in the along-shelf direction. The derivation closely follows those of Lentz (1987), Lentz and Chapman (1989), Dever and Lentz (1994), and Austin (1999), but is extended to include the effects of surface gravity waves. The additional temperature balance terms due to the waves are equivalent to those in the tracer transport equation found by McWilliams et al. (2004).

We separate the full water velocity $\mathbf{u}$ into a contribution due to the surface gravity waves, $\mathbf{u}'$, and a contribution due to the "wave-averaged" flow, $\overline{\mathbf{u}}$:

$$\mathbf{u} \equiv \overline{\mathbf{u}} + \mathbf{u}' \tag{D.1}$$

where the overbar indicates a time mean over a wave period T_w, using the notation

$$\overline{b}(x, y, z, t) \equiv \frac{1}{T_w} \int_{t-T_w/2}^{t+T_w/2} b(x, y, z, t)\, dt \tag{D.2}$$

for any variable b. We define the wave-fluctuating component of any quantity b as $b' \equiv b - \overline{b}$. Then $\overline{\mathbf{u}}$ varies only on time scales that are long compared to a wave period.

D.1 Velocity due to Surface Gravity Waves

In order to calculate the water velocity induced by the surface gravity waves, we use the results of linear wave theory (*e.g.,* LeBlond and Mysak, 1978). The surface displacement due to the waves is

$$\eta(x, y, t) = a(x) \cos\left(\mathbf{k} \cdot \mathbf{x} - \omega t + \phi\right) \tag{D.3}$$

where $a(x)$ is the wave amplitude, $\mathbf{k}$ is the wave vector, ω is the angular wave frequency, t is time, and ϕ is an arbitrary phase. The horizontal component of the water velocity due to wave fluctuations is

$$\mathbf{u'_H}(x, y, z, t) = \hat{\mathbf{k}}_\mathbf{w} \eta(x, y, t) \omega G(z) \tag{D.4}$$

where $\hat{\mathbf{k}}_\mathbf{w}$ is a unit wave vector and

$$G(z) = \frac{\cosh\left[k\left(z + h\right)\right]}{\sinh kh} \tag{D.5}$$

where k is the wavenumber. The vertical component of the water velocity due to wave fluctuations is

$$w'(x, y, z, t) = \frac{\partial \eta(x, y, t)}{\partial t} F(z) \tag{D.6}$$

where

$$F(z) = \frac{\sinh\left[k\left(z + h\right)\right]}{\sinh kh} \tag{D.7}$$

so that

$$w'|_{z=0} = \frac{\partial \eta}{\partial t} \tag{D.8}$$

We assume the wave amplitude a varies slowly in the x direction due to shoaling, but is constant over spatial scales of the order of one wavelength $\lambda = 2\pi/k$ so that the above equations hold at any one point in space. To determine how the wave amplitude changes as the waves shoal, we assume no dissipation of wave energy so

the wave energy flux is constant:

$$c_g E = \text{constant} \tag{D.9}$$

where c_g is the wave group velocity and $E = \rho_0 g a^2/2$ is the wave energy per unit volume. For a monochromatic wave, the wave amplitude and significant wave height H_{sig} are related by

$$a^2 = \frac{{H_{sig}}^2}{8} \tag{D.10}$$

Then by combining Eq. (D.9) and Eq. (D.10) we can estimate H_{sig} at any x location using $H_{sig}|_{12}$ measured on the 12-m isobath at MVCO and $c_g(x)$ calculated from linear wave theory:

$$H_{sig}(x) = \sqrt{\frac{\left(H_{sig}^2 c_g\right)\big|_{12}}{c_g(x)}} \tag{D.11}$$

D.2 Temperature Fluctuations from Surface Gravity Waves

We separate the temperature field $T(x, y, z, t)$ into a contribution from the surface gravity waves, T', and a "wave-averaged" background temperature field $\overline{T}$. We assume that T' is mainly due to advection of the background vertical temperature gradient $\frac{\partial \overline{T}}{\partial z}$ by the vertical velocity due to the waves, w':

$$\frac{\partial T'}{\partial t} + w' \frac{\partial \overline{T}}{\partial z} = 0 \tag{D.12}$$

By using Eq. (D.6), integrating in time over a wave period and neglecting variations of $\frac{\partial \overline{T}}{\partial z}$ on wave time scales, we can solve for the temperature fluctuations due to waves:

$$T'(x, y, z, t) = -\eta F(z) \frac{\partial \overline{T}}{\partial z} \tag{D.13}$$

D.3 Temperature Balance Derivation

The temperature balance equation including advection is

$$\left(\frac{\partial T}{\partial t} + \mathbf{u}\cdot\nabla T\right) = \frac{1}{\rho_0 c_p}\frac{\partial q}{\partial z} \tag{D.14}$$

where $q(x,y,z,t)$ represents sources of heat. Using the continuity equation $\nabla\cdot\mathbf{u}=0$, Eq. (D.14) becomes

$$\left[\frac{\partial T}{\partial t} + \nabla\cdot(\mathbf{u}T)\right] = \frac{1}{\rho_0 c_p}\frac{\partial q}{\partial z}. \tag{D.15}$$

Introducing a reference temperature $\langle\overline{T}\rangle_L$, defined as the depth-average temperature at the mooring site $x=L$ averaged over a wave period T_w,

$$\langle\overline{T}\rangle_L \equiv \left(\frac{1}{h}\int_{-h}^{0}\overline{T}(z)\,dz\right)\Big|_{x=L} = \langle\overline{T}\rangle\big|_{x=L} \tag{D.16}$$

(where $\langle b\rangle$ denotes the depth average of any variable b) gives, since $\nabla\cdot\left(\mathbf{u}\langle\overline{T}\rangle_L\right)=0$ because $\langle\overline{T}\rangle_L$ is a function of time only,

$$\left\{\frac{\partial T}{\partial t} + \nabla\cdot\left[\mathbf{u}\left(T-\langle\overline{T}\rangle_L\right)\right]\right\} = \frac{1}{\rho_0 c_p}\frac{\partial q}{\partial z}. \tag{D.17}$$

Integrating vertically from the bottom $z=-h(x)$ to the surface $z=\eta(x,y,t)$ gives

$$\int_{-h}^{\eta}\left\{\frac{\partial T}{\partial t} + \nabla\cdot\left[\mathbf{u}\left(T-\langle\overline{T}\rangle_L\right)\right]\right\}dz = \frac{1}{\rho_0 c_p}\int_{-h}^{\eta}\frac{\partial q}{\partial z}\,dz. \tag{D.18}$$

Using $\nabla = \nabla_{\mathbf{H}} + \hat{\mathbf{z}}\frac{\partial}{\partial z}$, where $\nabla_{\mathbf{H}} \equiv \hat{\mathbf{x}}\frac{\partial}{\partial x} + \hat{\mathbf{y}}\frac{\partial}{\partial y}$, and using the Leibniz rule to move the $\frac{\partial}{\partial t}$ and $\nabla_{\mathbf{H}}$ operators outside the integral, Eq. (D.18) becomes

$$\begin{aligned}
&\frac{\partial}{\partial t}\int_{-h}^{\eta} T\,dz - \frac{\partial\eta}{\partial t}\,T|_{z=\eta} + \nabla_{\mathbf{H}}\cdot\int_{-h}^{\eta}\mathbf{u}_{\mathbf{H}}\left(T-\langle\overline{T}\rangle_L\right)\,dz \\
&\qquad - (\nabla_{\mathbf{H}}\eta)\cdot\mathbf{u}_{\mathbf{H}}\left(T-\langle\overline{T}\rangle_L\right)\big|_{z=\eta} + \left[\nabla_{\mathbf{H}}(-h)\right]\cdot\mathbf{u}_{\mathbf{H}}\left(T-\langle\overline{T}\rangle_L\right)\big|_{z=-h} \\
&\qquad\qquad + w\left(T-\langle\overline{T}\rangle_L\right)\big|_{z=\eta} - w\left(T-\langle\overline{T}\rangle_L\right)\big|_{z=-h} \\
&\qquad\qquad\qquad = \frac{q|_{z=\eta} - q|_{z=-h}}{\rho_0 c_p}
\end{aligned} \tag{D.19}$$

We apply the surface boundary conditions

$$\frac{\partial \eta}{\partial t} + \mathbf{u_H} \cdot \nabla_{\mathbf{H}} \eta = w|_{z=\eta} \tag{D.20}$$

$$q|_{z=\eta} = Q_s \tag{D.21}$$

where Q_s is the net surface heat flux, and bottom boundary conditions

$$w|_{z=-h} = -\mathbf{u_H} \cdot \nabla_{\mathbf{H}} h \tag{D.22}$$

$$q|_{z=-h} = 0 \tag{D.23}$$

(see Section 4.5 for discussion of the validity of Eq. (D.23)). Then Eq. (D.19) becomes

$$\frac{\partial}{\partial t} \int_{-h}^{\eta} T \, dz - \frac{\partial \eta}{\partial t} \langle \overline{T} \rangle_L + \nabla_{\mathbf{H}} \cdot \int_{-h}^{\eta} \mathbf{u_H} \left(T - \langle \overline{T} \rangle_L \right) \, dz = \frac{Q_s}{\rho_0 c_p} \tag{D.24}$$

Taking the time mean over a wave period of each term in Eq. (D.24) and using the approximation

$$\overline{\int_{-h}^{\eta} b \, dz} \approx \int_{-h}^{0} \overline{b} \, dz + \overline{\eta \, b'|_{z=0}} \tag{D.25}$$

for any variable b, we have

$$\underbrace{\overline{\frac{\partial}{\partial t} \int_{-h}^{\eta} T \, dz}}_{A} - \underbrace{\overline{\frac{\partial \eta}{\partial t} \langle \overline{T} \rangle_L}}_{B} + \nabla_{\mathbf{H}} \cdot \underbrace{\overline{\int_{-h}^{\eta} \mathbf{u_H} \left(T - \langle \overline{T} \rangle_L \right) \, dz}}_{C} = \frac{\overline{Q}_s}{\rho_0 c_p} \tag{D.26}$$

Considering each term of Eq. (D.26) separately, noting that $\overline{b'} = 0$ for any variable b,

$$A = \frac{\partial}{\partial t} \int_{-h}^{0} \overline{T} \, dz \tag{D.27}$$

$$B = 0 \tag{D.28}$$

$$C = \int_{-h}^{0} \underbrace{\overline{\mathbf{u_H} \left(T - \langle \overline{T} \rangle_L \right)}}_{C1} \, dz + \underbrace{\overline{\eta \mathbf{u_H} \left(T - \langle \overline{T} \rangle_L \right)}\Big|_{z=0}}_{C2} \tag{D.29}$$

$$C1 = \overline{\left(\overline{\mathbf{u}}_\mathbf{H} + \mathbf{u}'_\mathbf{H}\right)\left(\overline{T} - \langle\overline{T}\rangle_L + T'\right)} \tag{D.30}$$

$$= \overline{\overline{\mathbf{u}}_\mathbf{H}\left(\overline{T} - \langle\overline{T}\rangle_L\right)} + \overline{\overline{\mathbf{u}}_\mathbf{H} T'} + \overline{\mathbf{u}'_\mathbf{H}\left(\overline{T} - \langle\overline{T}\rangle_L\right)} + \overline{\mathbf{u}'_\mathbf{H} T'} \tag{D.31}$$

$$= \overline{\mathbf{u}}_\mathbf{H}\left(\overline{T} - \langle\overline{T}\rangle_L\right) + \overline{\mathbf{u}'_\mathbf{H} T'} \tag{D.32}$$

and using $\overline{\eta} = 0$, Eq. (D.4), Eq. (D.13), and $\overline{\eta^3} = 0$,

$$C2 = \overline{\eta\left(\overline{\mathbf{u}}_\mathbf{H} + \mathbf{u}'_\mathbf{H}\right)\left(\overline{T} - \langle\overline{T}\rangle_L + T'\right)}\Big|_{z=0} \tag{D.33}$$

$$= \overline{\eta\overline{\mathbf{u}}_\mathbf{H}\left(\overline{T} - \langle\overline{T}\rangle_L\right)}\Big|_{z=0} + \overline{\eta\overline{\mathbf{u}}_\mathbf{H} T'}\Big|_{z=0} + \overline{\eta\mathbf{u}'_\mathbf{H}\left(\overline{T} - \langle\overline{T}\rangle_L\right)}\Big|_{z=0} + \overline{\eta\mathbf{u}'_\mathbf{H} T'}\Big|_{z=0} \tag{D.34}$$

$$= \overline{\eta T'}\overline{\mathbf{u}}_\mathbf{H}\big|_{z=0} + \overline{\eta\mathbf{u}'_\mathbf{H}}\left(\overline{T} - \langle\overline{T}\rangle_L\right)\big|_{z=0} \tag{D.35}$$

Using Eq. (D.4) and Eq. (D.13), it is possible to show that the ratio of the first to the second term in Eq. (D.35) is $O\left(|\mathbf{u}_\mathbf{H}|/c\right)$, where c is the wave phase speed. For typical values $|\mathbf{u}_\mathbf{H}| < 0.3$ m s^{-1} and $c > 6$ m s^{-1}, $|\mathbf{u}_\mathbf{H}|/c < 5 \times 10^{-2}$ so we neglect the first term in Eq. (D.35). Then Eq. (D.26) becomes

$$\frac{\partial}{\partial t}\int_{-h}^{0}\overline{T}\,dz + \nabla_\mathbf{H}\cdot\left\{\int_{-h}^{0}\left[\overline{\mathbf{u}}_\mathbf{H}\left(\overline{T} - \langle\overline{T}\rangle_L\right) + \underbrace{\overline{\mathbf{u}'_\mathbf{H} T'}}_{D}\right]dz + \underbrace{\overline{\eta\mathbf{u}'_\mathbf{H}}\left(\overline{T} - \langle\overline{T}\rangle_L\right)\big|_{z=0}}_{E}\right\} = \frac{\overline{Q}_s}{\rho_0 c_p} \tag{D.36}$$

Terms D and E are present in Eq. (D.36) solely due to wave forcing. D is a horizontal temperature flux present at all depths due to correlated fluctuations in cross-shelf velocity and temperature generated by waves. E is a horizontal temperature flux at the surface due to the volume transport that takes place above the wave troughs in an Eulerian reference frame. Using Eq. (D.4), Eq. (D.13), and Eq. (D.11) to write Eq. (D.36) in terms of wave-averaged variables only,

$$\frac{\partial}{\partial t}\int_{-h}^{0}\overline{T}\,dz + \nabla_\mathbf{H}\cdot\left\{\int_{-h}^{0}\left[\overline{\mathbf{u}}_\mathbf{H}\left(\overline{T} - \langle\overline{T}\rangle_L\right) - \hat{\mathbf{k}}_\mathbf{w}\frac{\omega H_{sig}^2}{16}\frac{\partial\overline{T}}{\partial z}F(z)G(z)\right]dz + \hat{\mathbf{k}}_\mathbf{w}\frac{gH_{sig}^2}{16c}\left(\overline{T} - \langle\overline{T}\rangle_L\right)\big|_{z=0}\right\} = \frac{\overline{Q}_s}{\rho_0 c_p} \tag{D.37}$$

Integrating in the cross-shelf direction from the coast at $x = 0$ to a mooring at $x = L$, using $\overline{u} = 0$ and $H_{sig} = 0$ at $x = 0$ and Eq. (D.16), and defining $\widetilde{b} \equiv b - \langle b \rangle$ for any variable b, so that $\widetilde{T}$ is the depth-varying part of the temperature profile and $\overline{T}\big|_{x=L} - \langle \overline{T} \rangle\big|_{x=L} = \widetilde{\overline{T}}\Big|_{x=L}$, the temperature balance equation is

$$\begin{aligned}
&\frac{\partial}{\partial t}\int_0^L \int_{-h}^0 \overline{T}\, dz\, dx \\
&\quad + \left\{ \int_{-h}^0 \left[\widetilde{\overline{u}}\widetilde{\overline{T}} - \frac{\omega H_{sig}^2 \cos\theta_w}{16} \frac{\partial \overline{T}}{\partial z} F(z) G(z) \right] dz + \frac{g H_{sig}^2 \cos\theta_w}{16c}\, \widetilde{\overline{T}}\Big|_{z=0} \right\}\Bigg|_{x=L} \\
&\qquad + \int_0^L \frac{\partial}{\partial y} \left\{ \int_{-h}^0 \left[\overline{v} \left(\overline{T} - \langle \overline{T} \rangle_L \right) - \frac{\omega H_{sig}^2 \sin\theta_w}{16} \frac{\partial \overline{T}}{\partial z} F(z) G(z) \right] dz \right. \\
&\qquad\qquad \left. + \frac{g H_{sig}^2 \sin\theta_w}{16c} \left(\overline{T} - \langle \overline{T} \rangle_L \right)\Big|_{z=0} \right\} dx = \int_0^L \frac{\overline{Q}_s}{\rho_0 c_p}\, dx
\end{aligned} \tag{D.38}$$

where θ_w is the direction in which the waves are propagating, measured counterclockwise from the positive x direction. It is possible to show that

$$-\int_{-h}^0 \frac{\omega H_{sig}^2 \cos\theta_w}{16} \frac{\partial \overline{T}}{\partial z} F(z) G(z)\, dz + \frac{g H_{sig}^2 \cos\theta_w}{16c}\, \widetilde{\overline{T}}\Big|_{z=0} = \int_{-h}^0 \overline{u}_{st} \widetilde{\overline{T}}\, dz \tag{D.39}$$

where $\overline{u}_{st}$ is the x component of the Stokes' drift velocity (Stokes, 1847),

$$\overline{u}_{st}(z,t) = -\frac{g k H_{sig}^2 \cos\theta_w}{8c} \frac{\cosh\left[2k\left(z+h\right)\right]}{\sinh\left(2kh\right)} \tag{D.40}$$

so Eq. (D.38) becomes

$$\begin{aligned}
&\frac{\partial}{\partial t}\int_0^L \int_{-h}^0 \overline{T}\, dz\, dx + \left[\int_{-h}^0 \left(\overline{u} + \overline{u}_{st} \right) \widetilde{\overline{T}}\, dz \right]\Bigg|_{x=L} \\
&\qquad + \int_0^L \frac{\partial}{\partial y} \left\{ \int_{-h}^0 \left[\overline{v} \left(\overline{T} - \langle \overline{T} \rangle_L \right) - \frac{\omega H_{sig}^2 \sin\theta_w}{16} \frac{\partial \overline{T}}{\partial z} F(z) G(z) \right] dz \right. \\
&\qquad\qquad \left. + \frac{g H_{sig}^2 \sin\theta_w}{16c} \left(\overline{T} - \langle \overline{T} \rangle_L \right)\Big|_{z=0} \right\} dx = \int_0^L \frac{\overline{Q}_s}{\rho_0 c_p}\, dx
\end{aligned} \tag{D.41}$$

No wave-fluctuating quantities were observed directly, so the primed notation is not needed except in the derivation of Eq. (D.41). Therefore, outside of this Appendix, we drop the overbar notation and all variables are considered wave-averaged.

Appendix E

Observations of Undertow over the Inner Continental Shelf

This Appendix is a manuscript that was submitted to *Journal of Physical Oceanography*. This manuscript and the manuscript in Chapter 2 were submitted as companion papers. Both manuscripts were reviewed and are currently under revision for resubmission. Because this manuscript is primarily the work of Steven Lentz, this manuscript is not part of Melanie Fewings' thesis work but is included here for completeness and reference.

Observations of Undertow over the Inner Continental Shelf

Steven J. Lentz

Woods Hole Oceanographic Institution, Woods Hole, MA

Melanie Fewings

Woods Hole Oceanographic Institution, Woods Hole, MA

Peter Howd

USGS, St. Petersburg, FL

Janet Fredericks

Woods Hole Oceanographic Institution, Woods Hole, MA

Kent Hathaway

USACE CHL Field Research Facility, Kitty Hawk, NC

August 16, 2007;

to be submitted to JPO

Corresponding author:

Steven J. Lentz

Woods Hole Oceanographic Institution, MS 21

Woods Hole, MA 02543

slentz@whoi.edu

Abstract

Surface gravity waves propagating toward the beach force a shoreward "mean" flow (Stokes drift) above the wave troughs and a compensating seaward flow below the wave troughs commonly referred to as undertow. Observation of velocity profiles and wave characteristics from two inner-shelf sites well seaward of the surfzone (off Martha's Vineyard, Massachusetts and North Carolina) indicate that observed offshore transports are primarily wave-driven undertow. Theoretical estimates of the wave-driven offshore transport from linear wave theory and observed wave characteristics account for 50% or more of the observed offshore transport variability and reproduce the dependence on wave height and water depth.

Average cross-shelf velocity profiles, during weak wind stresses, are curved with maximum offshore flow (1 - 6 cm s^{-1}) and vertical shear near the surface, and weak flow and shear in the lower half of the water column. These observed inner-shelf profiles do not resemble the parabolic profiles observed within the surfzone. Instead, the inner-shelf profiles are consistent with a dynamical balance between the Coriolis force associated with the offshore flow and an alongshore "Hasselmann wave stress" due to the influence of the earth's rotation on surface gravity waves. The close agreement between the predicted profiles forced by the Hasselmann wave stress and observed winter profiles provides compelling evidence for the importance of the Hasselmann wave stress in forcing oceanic flows. Summer profiles are more vertically sheared than either winter profiles or model profiles, presumably due to stronger stratification. It is unclear how stratification modifies the summer profiles.

E.1 Introduction

There is an onshore volume transport associated with surface gravity waves propagating toward the coast. If there are no along-shelf variations in the flow field, such as rip currents, there must be a compensating offshore flow, which is commonly referred to as undertow. For linear surface gravity waves, the onshore (Stokes) transport is

$$Q_w \approx \frac{gH_{sig}^2}{16c} cos(\theta_w), \tag{E.1}$$

where g is gravitational acceleration, H_{sig} is the significant wave height (defined as four times the standard deviation of the sea level variations due to the surface waves), c is the phase speed of the waves, and θ_w is the wave direction relative to onshore (*e.g.*, Stokes, 1847; LeBlond and Mysak, 1978; Mei, 1983). This onshore transport is concentrated above the wave troughs in an Eulerian frame or is the vertically distributed Stokes drift in a Lagrangian frame. The compensating depth-averaged offshore flow is

$$u_w = \frac{-Q_w}{h} = \frac{gh}{16c} \left(\frac{H_{sig}}{h} \right)^2 cos(\theta_w), \tag{E.2}$$

where h is the water depth and u_w is positive offshore. For shallow water waves ($kh << 1$, where k is the wave number), $c \approx \sqrt{gh}$ and (E.2) reduces to

$$u_w \approx \frac{\sqrt{gh}}{16} \left(\frac{H_{sig}}{h} \right)^2 cos(\theta_w). \tag{E.3}$$

In the subsequent analysis the waves are not assumed to be shallow-water waves.

E.1.1 Undertow Transport

There have been numerous theoretical and laboratory studies of undertow in the vicinity of the surfzone (*e.g.*, Nadaoka and Kondoh, 1982; Svendsen, 1984; Stive and Wind, 1986; Putrevu and Svendsen, 1993; Ting and Kirby, 1994; Govender et al., 2002). In the ocean, "mean" (average over many wave periods) offshore flows have often been observed at single depths in the surfzone (*e.g.*, Wright et al., 1982; Mas-

selink and Black, 1995). There are also a few observations of velocity profiles that provide accurate estimates of the offshore transport to test (E.2) and to characterize the vertical structure of undertow (Haines and Sallenger, 1994; Garcez Faria et al., 2000; Reniers et al., 2004). The observational studies of Haines and Sallenger (1994); Garcez Faria et al. (2000); Reniers et al. (2004), conducted in 1982, 1994, and 1997 respectively, all examined current profiles measured from sled systems that sampled different locations within and just seaward of the surfzone (water depths 1 - 4 m) at the Army Corps Field Research Facility (FRF), near Duck, North Carolina. Haines and Sallenger (1994) did not compare below trough transport estimates to $-Q_w$. Garcez Faria et al. (2000) found reasonable agreement between $-Q_w$ and the observed offshore transport except on the shoreward side of a shore-parallel sandbar. Inclusion of an estimate of the onshore transport due to wave rollers improved the agreement. Reniers et al. (2004) found poorer agreement between $-Q_w$ plus the wave-roller transport and the observed offshore transport, which they attributed to alongshore variability.

Seaward of the surfzone ($H_{sig}/h < 0.5$), over the inner shelf, little is known about undertow and its relative contribution to the cross-shelf transport. (The offshore edge of the surfzone will be crudely defined as where $\gamma = H_{sig}/h \approx 0.5$.) For shore-normal waves ($\theta_w = 0$) with $H_{sig} = 2$ m, the depth-averaged offshore flow estimated from (E.3) is 2.5 cm s^{-1} in 10 m of water. This is comparable to observed depth-averaged cross-shelf flows below the wave troughs over inner shelves (*e.g.*, Lentz and Winant, 1986; Lee et al., 1989; Lentz and Raubenheimer, 1999; Kirincich et al., 2005), suggesting wave forcing is important over the inner shelf.

E.1.2 Undertow Profiles

Estimates of the offshore transport using (E.2) are based only on (E.1), volume conservation, and the assumption of no along-shelf variations in the flow. Consequently, while (E.2) may be used to infer whether observed offshore transports are forced by surface waves, it does not provide much insight into the underlying dynamics. However, the vertical structure of undertow does provide insight into the dynamics.

Undertow in the surfzone is typically assumed to be the result of a dynamical balance between the surface wave forcing F^x (wave-radiation stress divergence, Longuet-Higgins and Stewart (1962)), a resulting cross-shelf pressure gradient (wave setup), and the vertical gradient of the turbulent stress:

$$0 = F^x - g\eta_x + (Au_z)_z. \tag{E.4}$$

where η_x is the cross-shelf sea surface slope, A is a turbulent eddy viscosity, and u is the offshore flow (*e.g.*, Svendsen, 1984; Stive and Wind, 1986; Putrevu and Svendsen, 1993; Haines and Sallenger, 1994; Garcez Faria et al., 2000; Reniers et al., 2004). The dominant balance is between the wave forcing and the cross-shelf pressure gradient (*e.g.*, Longuet-Higgins and Stewart, 1964; Bowen et al., 1968; Guza and Thornton, 1981; Holman and Sallenger, 1985; Nielsen, 1988; Lentz and Raubenheimer, 1999; Raubenheimer et al., 2001). Assuming no net cross-shelf transport (E.2), a constant eddy viscosity, vertically uniform wave forcing, an onshore surface stress due to the waves, and either no flow at the bottom or an onshore wave streaming in the wave bottom boundary layer (*e.g.*, Longuet-Higgins, 1953; Stive and Wind, 1986), (E.4) yields parabolic velocity profiles with maximum offshore flow in the interior, decreasing toward both the surface and bottom (Fig. E-1a; *e.g.* Haines and Sallenger, 1994). Models with explicit wave boundary layers or more "realistic" eddy viscosity profiles yield similar parabolic profiles (*e.g.*, Putrevu and Svendsen, 1993; Garcez Faria et al., 2000). The vertical structure of undertow within the surfzone in laboratory studies is consistent with these models (*e.g.*, Nadaoka and Kondoh, 1982; Putrevu and Svendsen, 1993; Ting and Kirby, 1994; Govender et al., 2002).

In the few oceanographic field studies of undertow in the vicinity of the surfzone, offshore flows of order 1 - 10 cm s^{-1} were observed throughout the water column, except very near the surface where there is often onshore flow (Haines and Sallenger, 1994; Garcez Faria et al., 2000; Reniers et al., 2004). Although these three studies were all conducted at the same site in different years, the observed vertical structure of the undertow varied. Haines and Sallenger (1994) observed maximum offshore flows

at mid depth at all sites. Garcez Faria et al. (2000) found maximum offshore flows near the bottom over a shore-parallel bar where the waves were breaking, with weaker, more vertically uniform offshore flows onshore and offshore of the bar. Reniers et al. (2004) found maximum offshore flow near the bottom within the surfzone and near the surface seaward of the surfzone.

Laboratory studies (*e.g.*, Nadaoka and Kondoh, 1982; Putrevu and Svendsen, 1993; Ting and Kirby, 1994; Govender et al., 2002) and the observational studies cited above suggest that undertow profiles may be quite different within and seaward of the surfzone. In the laboratory studies, seaward of the surfzone the offshore flow increases linearly with height above the bottom. Putrevu and Svendsen (1993) showed that a model which included steady streaming in the wave bottom boundary layer and a weak eddy viscosity outside the surfzone resulted in a velocity increase with height above the bottom similar to the laboratory results.

The laboratory studies cited above were not conducted in a rotating tank. A completely different dynamical balance is possible if the Earth's rotation is important. In particular, Hasselmann (1970) showed that the Coriolis force acting on the surface wave velocities would induce a small (order f/ω, where ω is the wave frequency ~ 1 s^{-1}, and f is the Coriolis frequency $\sim 10^{-4}$ s^{-1}) along-crest wave velocity $\tilde{v}$ that is in phase with the vertical wave velocity $\tilde{w}$. Though $\tilde{v}$ is small, the resulting wave stress $\tilde{\tau}^w = -\rho_\circ < \tilde{v}\tilde{w} >$ (subsequently referred to as the Hasselmann wave stress) can be substantial relative to the wind stress. It has been suggested that this is a potentially important forcing mechanism for both shelf flows (*e.g.*, Xu and Bowen, 1994; Newberger and Allen, 2006) and the open ocean circulation (*e.g.*, Hasselmann, 1970; McWilliams and Restrepo, 1999; Ardhuin et al., 2004; Polton et al., 2005). If the vertical divergence in this along-crest wave stress

$$\frac{\partial \tilde{\tau}^w}{\partial z} = -\rho_\circ \frac{H_{sig}^2 f \omega k}{16} \frac{cosh(2k[z+h])}{sinh^2(kh)} = -\rho_\circ f u_{st} \tag{E.5}$$

is balanced by the Coriolis force in the alongshore momentum balance

$$\rho_\circ f u = \frac{\partial \tilde{\tau}^w}{\partial z} = -\rho_\circ f u_{st}, \tag{E.6}$$

the resulting mean flow profile $u(z)$ is equal and opposite to the Stokes drift u_{st} (Fig. E-1b), so there is no net particle displacement (Ursell, 1950). Consequently, this mean flow satisfies the transport constraint given by (E.2).

The constant eddy viscosity, no rotation ($f = 0$) profiles that satisfy (E.4), and the inviscid wave-stress with rotation ($f \neq 0$) velocity profiles that satisfy (E.6) have opposite curvature (Fig. E-1). As discussed in Section E.4.1, the no rotation velocity profiles are parabolic, with weaker flow near the surface and bottom. The inviscid velocity profiles with rotation have small vertical shear in the lower water column and larger shear near the surface, with maximum offshore flow near the surface. Consequently the vertical structure of the observed profiles may indicate the dominant dynamical balance.

Observations are presented here of wave-driven offshore flows (undertow) consistent with (E.2) extending well seaward of the surfzone into water depths of 5 - 13 m, over the inner shelves of Martha's Vineyard, Massachusetts and North Carolina. In both cases, undertow is the dominant component of the depth-averaged subtidal cross-shelf circulation. When wind stresses are weak, mean cross-shelf velocity profiles over the inner shelf (seaward of the surfzone) resemble the negative Stokes drift profile (Fig. E-1b) associated with a dynamical balance between the Coriolis force and the Hasselmann wave stress (E.6) more than the parabolic profiles typically associated with the surfzone (Fig. E-1a). The observed cross-shelf flow profiles depend on wind stress, as well as the wave forcing. This manuscript focuses on only the wave-driven cross-shelf flow. The response of the cross-shelf flow at the Martha's Vineyard site to wind forcing and combined wind and wave forcing is presented in Chapter 2.

E.2 Data Sets and Processing

Current and wave observations from two locations are analyzed: $\sim$3.5 years of data from the Martha's Vineyard Coastal Observatory (MVCO), located on the south coast of Martha's Vineyard, south of Cape Cod, Massachusetts, and two months of data from the 1997 SandyDuck field program conducted near the Army Corps of Engineers Field Research Facility (FRF) on the North Carolina inner shelf.

MVCO current observations are from a bottom-mounted RDI 1200-kHz Broad-Band Acoustic Doppler Current Profiler (ADCP) deployed 1.5 km offshore in 12 m of water. Twenty-minute averages of current profiles and surface-wave characteristics, including wave spectra and average wave direction as a function of frequency, for the period 1 June 2001 to 26 May 2006 were obtained from the MVCO website at http://www.whoi.edu/mvco. The ADCP has a sample rate of 2 Hz and 0.5-m vertical bins between 2.5 m and 10 m above the bottom. There are several gaps in the time series lasting 1 - 4 months. Additionally, four periods of data when both the ADCP signal strength and the signal correlation are small were discarded (6 February - 17 April 2002, 22 February - 4 April 2004, 8 - 19 April 2005, and 20 February - 7 March 2006) because bin-to-bin velocity differences and wave characteristics are anomalous during these periods. Significant wave height H_{sig}, average wave period and wave direction θ_w were estimated from wave spectra of the ADCP current observations as described at the MVCO website. Wind observations are from a 10-m shore mast (12.5 m above mean sea level).

SandyDuck current profiles are from 6 upward-looking SonTek/YSI Acoustic Doppler Profilers (ADPs) (5.2–12.0 m depth) and one upward-looking RDI BroadBand 1200-kHz ADCP (12.7 m depth), deployed from 17 September to 10 November 1997. Six of the profilers were deployed on a cross-shelf transect in water depths of 5.2 m, 6.5 m, 7.7 m, 8.7 m, 12.0 m, and 12.7 m (0.3, 0.5, 0.6, 0.8, 1.2, and 1.5 km offshore). The seventh profiler was deployed in 6.5 m water (0.5 km offshore) about 100 m to the south. The ADP at 5.2 m depth was a 3000-kHz unit with 0.25-m bins, and the other ADPs were 1500-kHz units with 0.5-m bins. The ADPs recorded 3.5-minute

mean velocities every 5 min. The ADCP at 12.7 m recorded 1-min mean velocities and had 0.5-m bins. The velocities from the ADCP were low-pass filtered using a filter with a half-power period of 4 minutes to approximate the 3.5-min averaging of the ADPs. Wave characteristics were not available at the current-profiler sites, so H_{sig} was estimated at each site by interpolating H_{sig} observations in 4 m, 6 m, 8 m and 13 m of water to the water depths of the current profilers. The SandyDuck current profiler sites were generally seaward of the surfzone. Consequently, results are similar if H_{sig} is assumed to not vary between the 13-m and 5-m isobaths and the 8-m array estimate is used for all 7 current profiler sites. Wind observations are from an anemometer at the end of the FRF pier at a height of 19 m.

Wave-driven onshore transport Q_w and hence the predicted depth-averaged offshore flow u_w at MVCO and the SandyDuck sites were estimated using (E.2) and the observed significant wave height, average wave period, and wave direction. Estimates of u_w assuming shallow water waves (E.3) and $\theta_w = 0$ are similar (not presented), though $kh \approx 1 - 3$ so these are not shallow-water waves. For MVCO, the Stokes velocity profile $u_{st}(z,t)$ was estimated by integrating (E.5) over the frequency band 0.047 - 0.5 Hz using the observed wave spectra. The wave transport Q_w, estimated by integrating u_{st} from the surface to the bottom, is well correlated with Q_w estimated from (E.1) (correlation 0.98), but is 15% smaller.

Observed depth-averaged offshore flows below the wave troughs u_{da} were estimated from the velocity profiles using a trapezoidal rule and assuming velocities were uniform between the shallowest (deepest) observation and the surface (bottom). Linear extrapolations of the current profiles to the surface and bottom gave similar results (not shown). Wind stress was estimated using the drag coefficient proposed by Fairall et al. (2003). To focus on subtidal variability, tidal and other high-frequency motions were removed using a low-pass filter with a 24-hour half-power point (diurnal flows are weak at this site).

The cross-shelf flow is sensitive to the choice of coordinate systems because the flow is strongly polarized alongshore. The cross-shelf direction is defined here as aligned with the minor principal axis of the depth-averaged subtidal flow at each site when

waves are small. The resulting offshore direction is roughly perpendicular to the local isobaths and the mean depth-averaged flow during small waves is alongshore. The subsequent analysis includes all wave conditions. Only times of small waves ($H_{sig} <$ 0.5 m) were included in estimating the principal axes to determine the coordinate frame orientation because this study shows that surface waves drive a substantial subtidal offshore flow below the wave troughs (Section E.3.1).

E.3 Results

E.3.1 Depth-Averaged Flow

Mean significant wave heights, H_{sig}, are 1.0 m at MVCO and 0.9 m at the SandyDuck sites. Standard deviations of H_{sig} are $\sim$0.5 m at both sites, and wave events typically have time scales of order a day (see u_w in Fig. E-2). The largest significant wave heights are 4.5 m during the MVCO deployment and 3.5 m during the Sandy Duck deployment. Average wave periods typically ranged from 4 - 7 s during the MVCO deployment and 4 - 16 s during SandyDuck. At MVCO, the maximum $H_{sig}/h = 0.38$ and H_{sig}/h is greater than 0.2 less than 3% of the time, suggesting this site was always well outside the surfzone. During the SandyDuck study H_{sig}/h was less than 0.5 at all sites, with the exception of one event when the outer edge of the surfzone was at about the 7-m isobath (see Section E.3.2).

Mean depth-average cross-shelf flows u_{da} are offshore at both MVCO (0.8 cm s^{-1}) and SandyDuck (0.6-2.1 cm s^{-1}). Standard deviations of the subtidal cross-shelf flows are 1-2 cm s^{-1} at both sites. Subtidal depth-averaged offshore flows exceed 2 cm s^{-1} 12% of the time at MVCO. In contrast, onshore flows exceed 2 cm s^{-1} less than 0.1% of the time (Fig. E-2, lower time series). There is a clear correspondence between the observed depth-averaged offshore flows u_{da} and estimates of the wave-driven offshore flow, u_w (upper time series, Fig. E-2). Correlations between subtidal u_{da} and u_w from the SandyDuck and MVCO observations range from 0.97 in 5.2 m water depth to $\sim$0.7 in 12 m water depth (Fig. E-3a) indicating that wave forcing accounts for

$\sim 50\%$ or more of the variance in u_{da}. Linear regression slopes for u_{da} versus u_w are approximately 1.0 with no obvious dependence on water depth (Fig. E-3b) and intercepts are less than 1 cm s^{-1}. The depth-averaged offshore flow decreases with increasing water depth h in a manner consistent with (E.2) (Fig. E-4). Bin averages of the depth-averaged offshore flow as a function of H_{sig}/h exhibit no significant deviation from the wave-driven offshore flow predicted by (E.2) for the range of water depths and wave heights observed (Fig. E-5).

The bin averages in Fig. E-5 are all seaward of the surfzone ($H_{sig}/h < 0.5$). The agreement between u_{da} and u_w implies that the circulation is two-dimensional (uniform along-shelf) and indicates that wave rollers do not make a significant contribution to the onshore volume flux seaward of the surfzone, in contrast to results from the vicinity of the surfzone (Garcez Faria et al., 2000). The residual subtidal depth-averaged cross-shelf flow $u_{da} - u_w$ has a mean of less than 0.1 cm s^{-1}, a standard deviation of 0.8 cm s^{-1}, and a maximum magnitude of 3.3 cm s^{-1}. Thus, the residual depth-averaged cross-shelf flow is generally small relative to the accuracy of the ADCP observations and the uncertainty in the depth-averaged flow estimates. It is striking that there are no large depth-averaged offshore flow events on time scales of days that are inconsistent with undertow in either the MVCO or SandyDuck observations. In summary, the observed, subtidal, depth-averaged offshore flows at MVCO and the SandyDuck sites are consistent with wave-driven undertow given by (E.2).

E.3.2 Vertical Structure

The vertical structure of the offshore flow varies across the inner shelf for the SandyDuck event shown in Fig. E-6. Based on the observed onshore decrease in H_{sig}, or on $H_{sig}/h \approx 0.5$, the offshore edge of the surfzone during this event is between the 6-m and 8-m isobaths. At the two shallow sites within the surfzone (water depths 5.2 m and 6.5 m), the maximum offshore flow is near the bottom. Between 600 m and 1200 m offshore the offshore flow is vertically uniform, while at the site farthest offshore the maximum offshore flow is in the upper half of the water column. This cross-shelf variation in the vertical structure is qualitatively consistent with previous

theory, laboratory results, and ocean observations (Nadaoka and Kondoh, 1982; Putrevu and Svendsen, 1993; Reniers et al., 2004). However, an onshore and southward wind stress during this event ($\tau_s^x \approx -0.09$ N m^{-2}and $\tau_s^y \approx -0.44$ N m^{-2}) undoubtedly influenced the vertical structure of the offshore flow.

The longer time series from MVCO indicate that wind stress has a substantial impact on the vertical structure of the cross-shelf flow (Chapter 2). During weak wind stresses (defined as $|\tau_s| < 0.03$ N m^{-2}), the mean cross-shelf flow profile is curved with small shear near the bottom, large shear near the surface, and maximum flow near the surface (Fig. E-7, $H_{sig} > 0.5$ m). During onshore wind stresses, the average cross-shelf flow profile is less sheared because the wind-driven shear opposes the wave-driven shear (not shown). During offshore wind stresses, the average cross-shelf profile is more sheared because the wind-driven shear enhances the wave-driven shear. The response of the cross-shelf circulation to wind stress and to combined wind stress and wave forcing is examined in Chapter 2 using the MVCO observations. When the wind stress is weak and the wave heights are small ($H_{sig} < 0.5$ m), the depth-averaged flow is approximately zero (Section E.3.2) but there is still a vertically sheared cross-shelf flow with offshore flow in the upper half of the water column and onshore flow in the lower half of the water column (Fig. E-7, $H_{sig} < 0.5$ m). The cause of this mean cross-shelf circulation during weak wind and wave forcing is not known, but is assumed here to not be wave forcing.

To focus on the wave-driven flow, the mean cross-shelf flow profile during weak winds and weak waves is subtracted from the observed profiles and only periods of weak wind stress magnitudes at MVCO are considered in the remainder of the analysis here and in Section E.4. For the range of H_{sig} that has a sufficient number of events (10 or more) to estimate reliable average profiles, 0.3 m $< H_{sig} <$ 3 m, the bin-averaged near-surface offshore flow (relative to the mean profile for weak forcing) increases from 0 cm s^{-1} to 6 cm s^{-1} at an approximately linear rate with increasing H_{sig} up to 2.3 m (Fig.E-8). There is the suggestion that the near-surface offshore flow stops increasing for $H_{sig} > 2.3$ m. The mid-depth flow also increases as H_{sig} increases, but the rate is slower and the dependence is more quadratic (see Section E.4.1). The near-

bottom flow is approximately zero for $H_{sig} < 1.0$ m, then increases to over 2 cm s^{-1} at $H_{sig} = 3$ m. While the MVCO observations do not include density profiles, the average offshore flow profiles for summer (typically stronger stratification) are more sheared than the average winter profiles (typically weaker stratification), suggesting a dependence on stratification (Fig. E-9). In summer, the flow is weakly onshore in the lower half of the water column, in contrast to weak offshore flow in winter. However, as discussed in Section E.4.1, it is unclear how stratification impacts the velocity structure.

E.4 Discussion

E.4.1 Dynamics

While the agreement between the theoretical Stokes transport and the observed cross-shelf transport (Fig. E-3-E-5) supports the assumption that the depth-average offshore flow is wave-driven, it sheds little light on the dynamics. To investigate the dynamics of undertow outside the surfzone, the observed velocity profiles are compared to a simple model that builds on a previous model proposed by Xu and Bowen (1994). Assuming steady, linear dynamics with no alongshore variations and constant density, continuity and the momentum balances are

$$\int_{-h}^{0} u\, dz = -Q_w, \tag{E.7}$$

$$-fv = -g\eta_x + F^x + (Au_z)_z, \tag{E.8}$$

$$fu = -fu_{st} + (Av_z)_z. \tag{E.9}$$

The wave forcing consists of the onshore Stokes transport Q_w, the cross-shelf radiation stress divergence F^x, assumed to be independent of depth, and the Hasselmann wave stress associated with the Earth's rotation fu_{st}, given by (E.5). The surface and

bottom boundary conditions used are a surface tangential stress and wave streaming at the bottom, both due to the thin viscous wave boundary layers (Longuet-Higgins, 1953; Xu and Bowen, 1994). We assume wave breaking is not occurring seaward of the surfzone. Given the wave forcing and a turbulent eddy viscosity A, equations (E.7 - E.9) are solved numerically for u, v, and η_x by iteratively determining the η_x that satisfies (E.7) (for details see Lentz, 1995). For simplicity, the model was run assuming a constant eddy viscosity. Model runs with a more "realistic" eddy-viscosity profile for an unstratified flow (Lentz, 1995) yield similar results.

For a wide range of eddy viscosities the model cross-shelf flow profiles fall into two distinct groups (Fig. E-9) corresponding to the two extremes in Fig. E-1. For large eddy viscosities ($A \geq 10^{-3}$ m^2 s^{-1}), the profiles are parabolic with a maximum offshore flow at mid depth. For small eddy viscosities ($A \leq 10^{-4}$m^2 s^{-1}), the profiles have the opposite curvature with maximum offshore flow near the surface. Except in the transition between these two regimes and near the boundaries, the profiles are not very sensitive to the magnitude of the eddy viscosity. The relevant non-dimensional parameter is δ_E/h, where $\delta_E = (A/f)^{1/2}$ is the Ekman scale. Parabolic profiles correspond to $\delta_E/h > 1$ (large A or small f) and the dominant momentum balance is (E.8) with $f \approx 0$. This is the balance typically assumed for the surfzone (*e.g.*, Svendsen, 1984; Stive and Wind, 1986; Putrevu and Svendsen, 1993; Haines and Sallenger, 1994; Garcez Faria et al., 2000; Reniers et al., 2004). The profiles with maximum offshore flow near the surface correspond to $\delta_E/h < 1$ (small A and large f). The dominant balance determining the cross-shelf velocity profile in this case is (E.9) with $A \approx 0$ so that $u \approx -u_{st}$.

The model profiles with $\delta_E/h < 1$ (small A) accurately reproduce the observed average winter profile from MVCO (Fig. E-9). The model profiles with $\delta_E/h < 1$ (large A) do not resemble the observed average profiles. The model profile with $\delta_E/h = 0$ ($u = -u_{st}$) also reproduces the observed dependence of u on H_{sig} (averaged over all seasons) at mid-depth and near the bottom (lower two dashed lines in Fig. E-8). However, the observed near-surface flow increases more rapidly with increasing H_{sig} than predicted. The agreement is closer for winter averages, but the observed flow

still increases slightly more rapidly with increasing H_{sig} than the predicted flow. The agreement between the observed winter profile and the model profiles with relatively small eddy-viscosities is somewhat surprising given that vertical mixing may be large at this site in winter. Semidiurnal tidal currents are strong (25 cm s^{-1}) in the along-shelf direction suggesting tidal mixing may be significant. However, the vertical structure of the wave-driven cross-shelf flow did not exhibit a significant dependence on the strength of the tidal flow. There is also often strong surface cooling in winter that should drive convection. The vertical shear in the average cross-shelf flow does decrease for increased surface cooling, as expected.

The average summer profile is more vertically sheared than either the winter or the model profiles (Fig. E-9). Since the relevant model response is essentially inviscid ($A \approx 0$), suppression of turbulent mixing by the stratification does not seem to explain the discrepancy; the observed profiles have more shear than the inviscid response. However, the over-simplified model does not include two- or three-dimensional effects, buoyancy forcing, or other potentially important elements of the dynamics such as the relative vorticity of the mean flow. For example, vertical mixing and the cross-shelf circulation acting on the stratification may influence the dynamics by creating buoyancy forcing similar to the stratified inner-shelf response to wind forcing (Austin and Lentz, 2002). The influence of stratification and vertical mixing processes in both winter and summer is the subject of ongoing research that includes obtaining moored observations of the stratification throughout the year and numerical modeling.

E.4.2 Cross-Shelf Exchange

It is worth considering how the wave-driven cross-shelf transports compare to wind-driven cross-shelf transports. Previous studies have shown that at mid shelf the cross-shelf transport in the surface boundary layer driven by an along-shelf wind stress (τ_s^y), Q_τ, is roughly equal to the Ekman transport $U_E = \tau_s^y/\rho_\circ f$ (*e.g.*, Smith, 1981; Lentz, 1992; Shearman and Lentz, 2003). To estimate the relative importance

of wave and wind-driven cross-shelf transport, consider

$$\frac{Q_w}{U_E} = \frac{\rho_\circ g f}{16c} \frac{H_{sig}^2}{\tau_s^y}. \tag{E.10}$$

For both SandyDuck and MVCO, H_{sig}^2 and τ_s^y are correlated with a typical regression slope of 20–30 m^4 N^{-1}. Assuming $H_{sig}^2/\tau_s^y = 25$ m^4 N^{-1}, Q_w is 10–20% of U_E, depending on the wave period, over the middle to outer shelf (water depths > 10 m in Fig. E-10). Two recent observational studies found that Q_τ decreases from roughly U_E at the 30–50 m isobath toward zero in shallow water (Lentz et al., 2001; Kirincich et al., 2005). Note these studies may have overestimated the cross-shelf transport driven by the along-shelf wind stress because they did not account for either the surface gravity wave forcing or cross-shelf wind stresses, both of which are correlated with the along-shelf wind stress (Chapter 2). The decrease in Q_τ as the depth decreases combined with the increase in Q_w as the depth decreases suggests that shallower than some critical water depth the wave-driven transport will be larger than the wind-driven transport. For a simple model case (Fig. E-10; $\tau_s^y = 0.1$ N m^{-2} and an unstratified turbulent eddy-viscosity profile), Q_w is greater than Q_τ for water depths less than 20 m. In general, this critical depth will depend on the width of the inner shelf (i.e., the region over which the wind-driven transport is reduced) and hence on the strength of the wind forcing and the stratification (Lentz, 1995; Austin and Lentz, 2002).

Though the observed Eulerian wave-driven cross-shelf transports can be substantial over the inner shelf, they may not be effective at driving cross-shelf exchange. Net particle transports are due to the sum of the Eulerian flow and the Lagrangian Stokes drift. Since the mean Eulerian and Stokes drift profiles are nearly equal, but with opposite directions in winter ($u \approx -u_{st}$), the net cross-shelf exchange due to waves is probably small. The larger discrepancy between u and u_{st} in the summer mean profiles (Fig. E-9) suggests a larger cross-shelf exchange.

E.5 Summary

Observations from two sites along the East Coast of the United States provide compelling evidence that the depth-averaged offshore flow (below the wave troughs) seaward of the surfzone, in water depths of 5 - 13 m, is primarily undertow driven by surface gravity waves, independent of the wind forcing. The evidence for this is the significant correlation between the predicted (from equation E.2) and observed depth-averaged cross-shelf flows (Fig. E-3) and the consistency with theory of the dependence of the observed depth-averaged offshore flow on both water depth and wave height (Fig. E-4 and E-5).

The observed average cross-shelf velocity profile seaward of the surfzone forced by waves (during weak wind stresses) is curved with maximum shear and offshore flow near the surface (below the wave troughs), and weak shear and flow in the lower half of the water column (Fig. E-7). This vertical structure of the cross-shelf flow seaward of the surfzone is different from the parabolic profiles with maximum offshore flow at mid-depth or near the bottom observed in the surfzone (Fig. E-1a; Haines and Sallenger, 1994; Garcez Faria et al., 2000; Reniers et al., 2004). The parabolic surfzone profiles are consistent with a dynamical balance between onshore wave-radiation stress divergence, a cross-shelf pressure gradient (wave setup), and turbulent stress divergence. The observed average cross-shelf velocity profiles seaward of the surfzone during winter are consistent with an inviscid balance between the Coriolis force associated with the offshore flow and the Hasselmann wave stress associated with the influence of the Earth's rotation on surface waves (Fig. E-1b and E-9). The agreement provides some of the first direct observational evidence for the importance of the Hasselmann wave stress in forcing oceanic flows. The average summer cross-shelf velocity profile is more sheared than either the average winter profile or the model profiles (Fig. E-9). This is presumably due to the stronger stratification in summer, but the influence of stratification on the dynamics is unclear. Suppression of turbulent stresses by the stratification does not appear to be the explanation, since the assumed momentum balance is essentially inviscid. Observations and model studies

of undertow during stratified conditions over the inner shelf are needed to understand the dynamics of the summer profiles.

Given the fundamental nature of the wave-driven transport, it seems likely that undertow will be present on most inner shelves exposed to waves. Wave-driven undertow is likely to be significant relative to wind-driven cross-shelf flows in water depths less than about 20 m. The observed cross-shelf velocities of a few centimeters per second associated with wave forcing over the inner shelf suggest flushing times of a day or less. However, since the Lagrangian Stokes drift associated with the surface gravity waves opposes the observed Eulerian flow, the wave-driven flow may be a less effective mechanism for particle exchange than suggested by the observed Eulerian flows. The connection between undertow within and offshore of the surfzone and the resulting particle transport between the surfzone and the inner shelf is an important unresolved problem.

Acknowledgments. This research was funded by the Ocean Sciences Division of the National Science Foundation under grants OCE-0241292 and OCE-0548961. The long time series available from the Martha's Vineyard Coastal Observatory were essential to this study. Operations at the MVCO are partially funded by the Woods Hole Oceanographic Institution. The deployment of the cross-shelf transect of ADP's during SandyDuck was funded by the USGS Center for Coastal Geology. The wind and some of the processed wave data used were acquired, processed and archived by the staff at the Field Research Facility of the U.S. Army Engineer Waterways Experiment Station's Coastal Engineering Research Center.

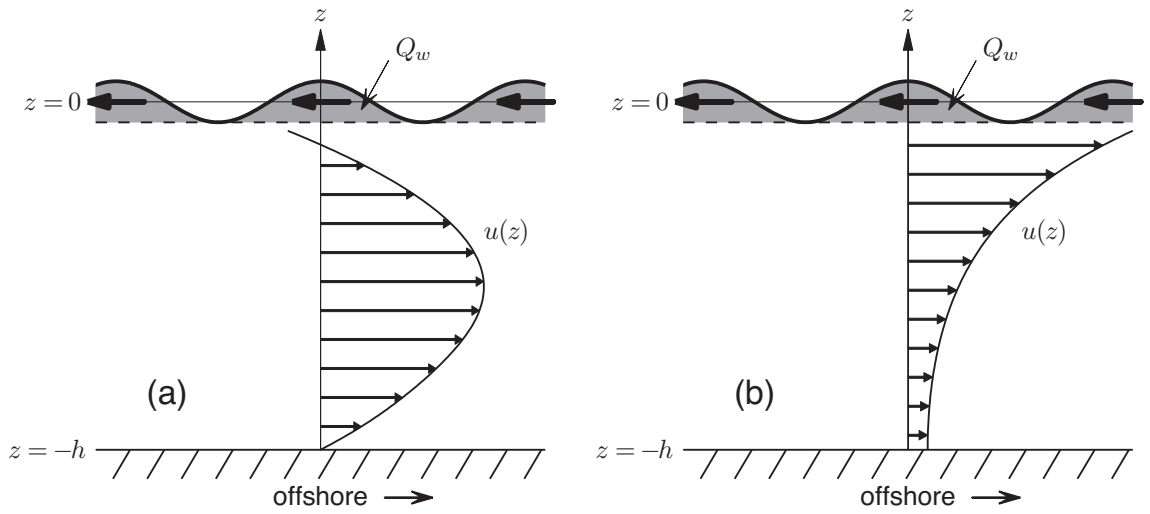

Figure E-1: Schematics of (a) a parabolic offshore flow profile consistent with (E.4) and (b) an offshore flow profile driven by the Hasselmann wave stress given by (E.6). The parabolic profile (a) is often observed in the surfzone and is associated with relatively strong vertical mixing when the Earth's rotation is not dynamically important. The Hasselmann profile (b) is associated with relatively weak vertical mixing and the Earth's rotation is dynamically important through both the Coriolis force and the wave forcing.

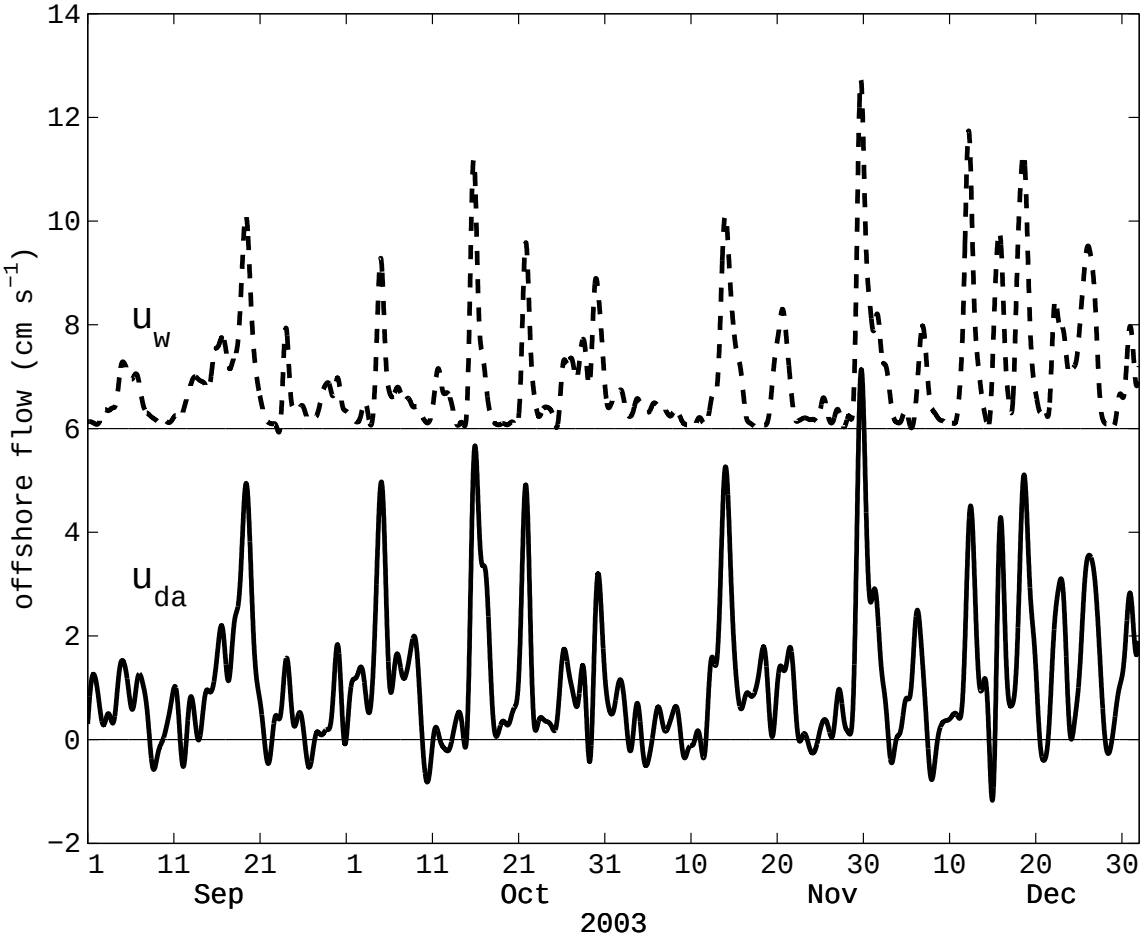

Figure E-2: Observed depth-averaged cross-shelf flow u_{da} over a four month period from the Martha's Vineyard Coastal Observatory and the depth-averaged wave-driven offshore flow u_w estimated using (E.2) and the observed wave characteristics. Time series of u_w has been offset +6 cm s^{-1} for clarity.

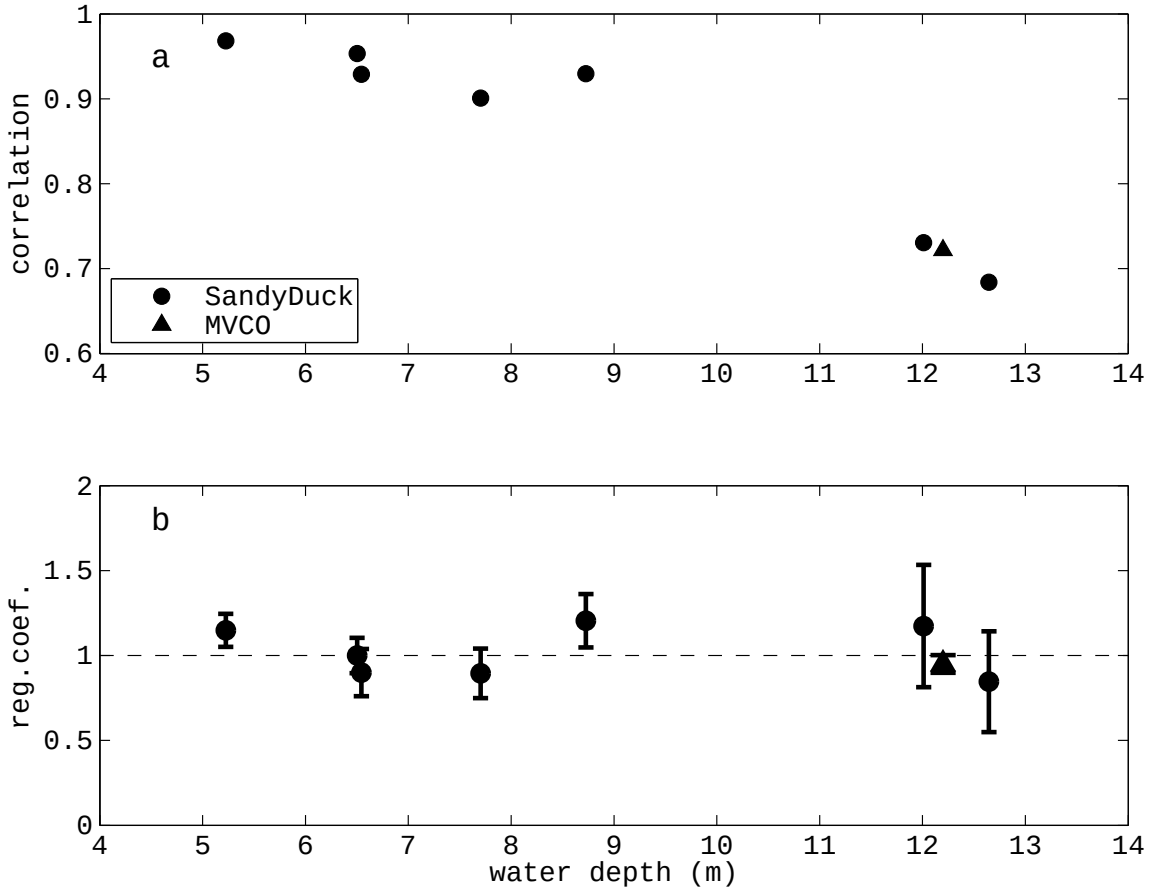

Figure E-3: The (a) correlation and (b) regression coefficient a from linear regressions of the form $u_{da} = au_w + b$ for the seven SandyDuck sites and MVCO. The error bars in (b) correspond to the 95% confidence intervals on the regression slope estimates. Intercepts are all less than 1 cm s^{-1}.

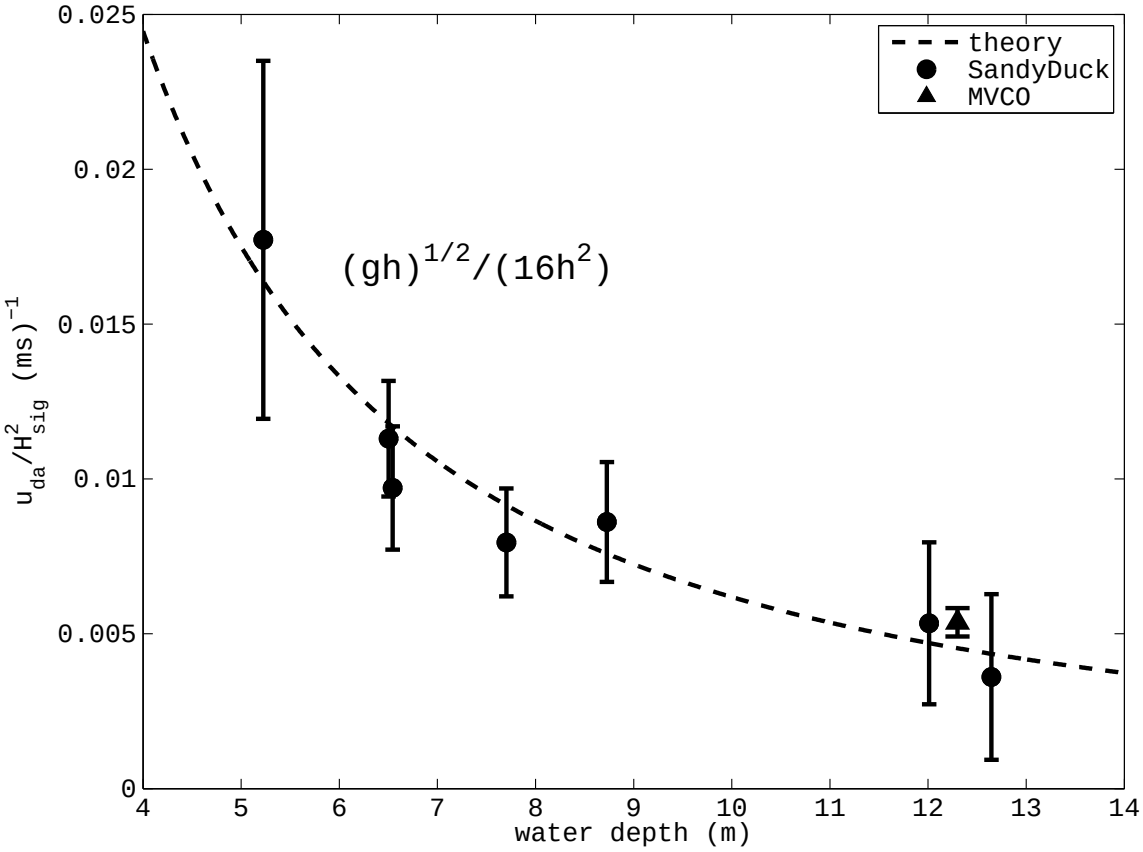

Figure E-4: Linear regression slope of u_{da} versus H_{sig}^2 as a function of water depth for the seven SandyDuck sites and MVCO. Dashed line is theoretical dependence of u_w/H_{sig}^2 on water depth based on (E.3). The error bars indicate the 95% confidence intervals on the regression slope estimates.

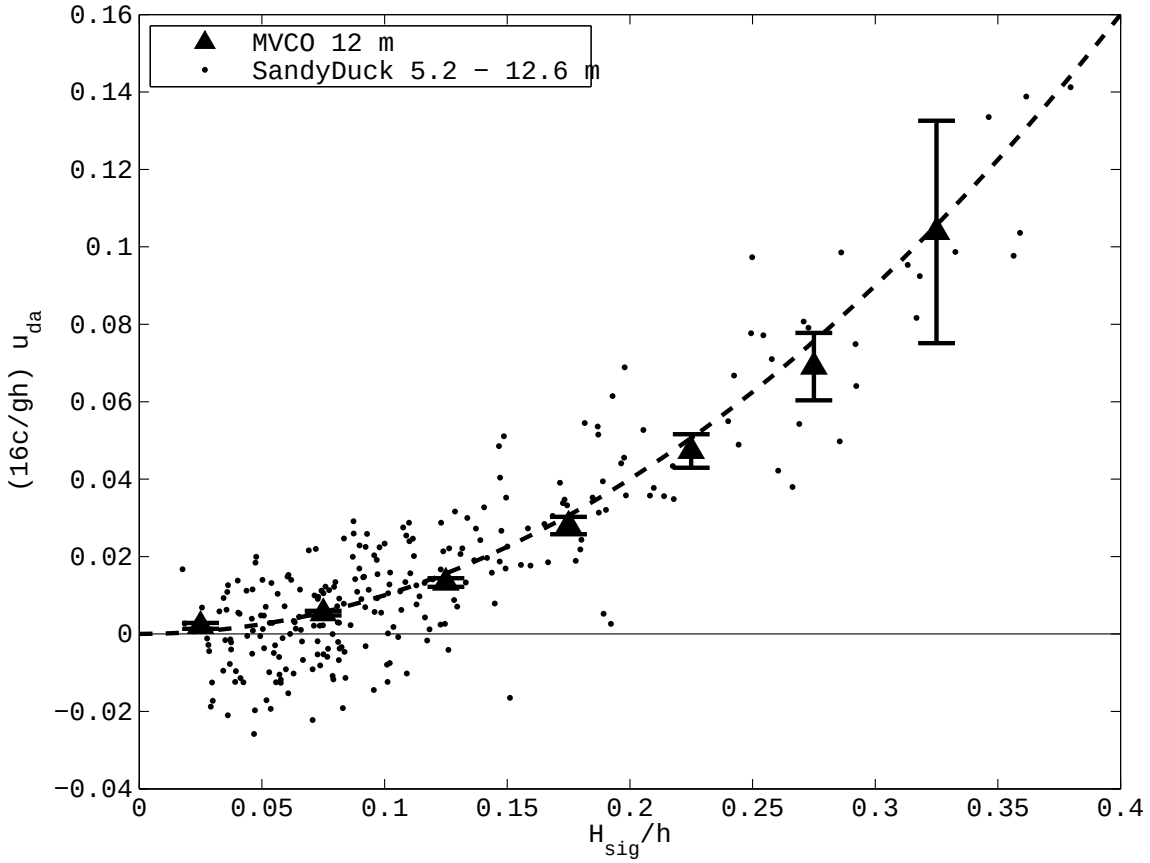

Figure E-5: Bin averages of normalized depth-averaged offshore flow as a function of H_{sig}/h for the MVCO current observations and individual daily averages for all the SandyDuck sites. The dashed line is the theoretical prediction from (E.2). The current observations are from sites seaward of the offshore edge of the surfzone, which is roughly at $H_{sig}/h \approx 0.5$. The error bars indicate the standard errors of the bin averages for the MVCO observations.

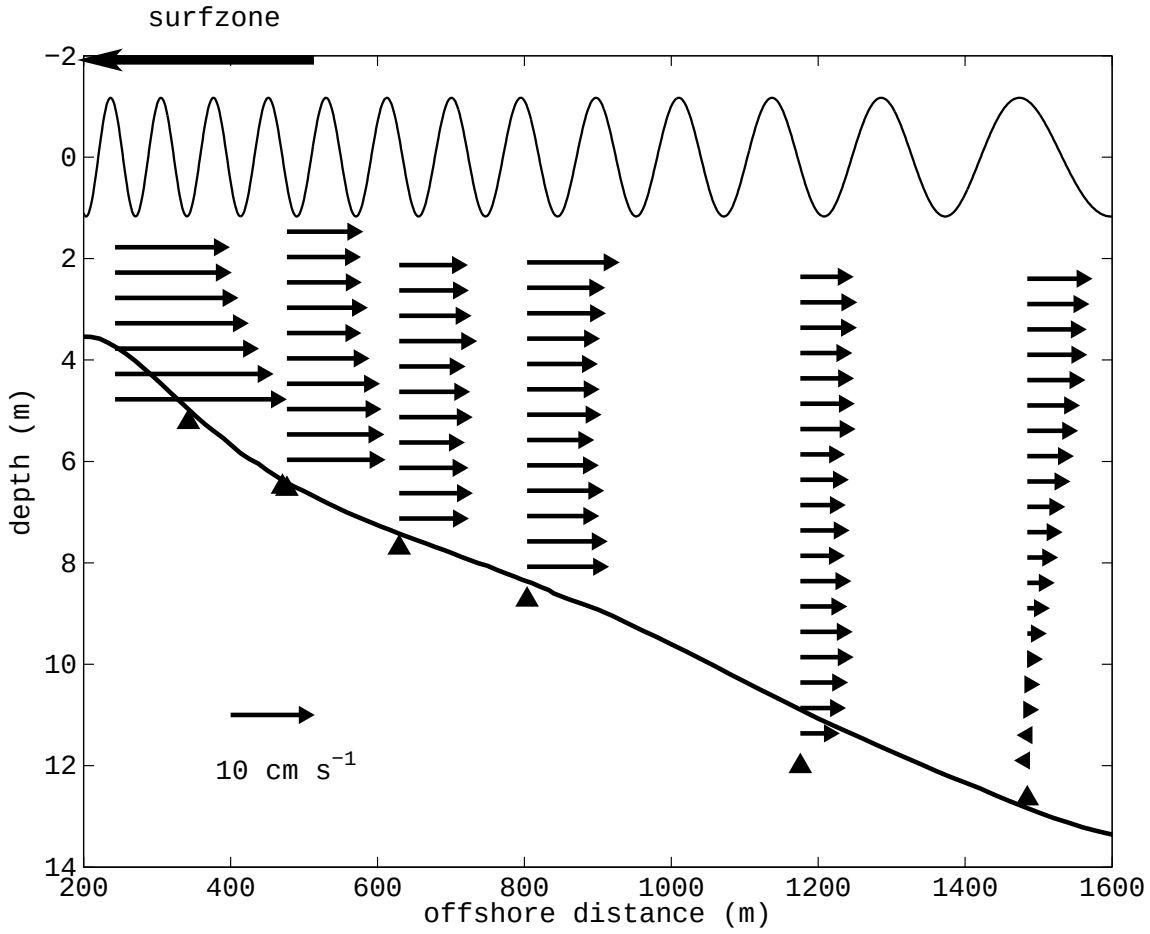

Figure E-6: Offshore section showing the bathymetry, locations of the ADCPs deployed during SandyDuck, and an example of the wave-driven offshore flow averaged over the time period 17:00-23:00 19 October 1997, when the average significant wave height was 3.3 m. The offshore edge of the surfzone is at about the 7-m isobath. A schematic of the corresponding linear, monochromatic wave (10 s period) is also shown. Bathymetry within 1000 m of the coast is from a survey taken August 13, 1997. The bathymetry farther offshore is from a ship survey conducted in the fall of 1994.

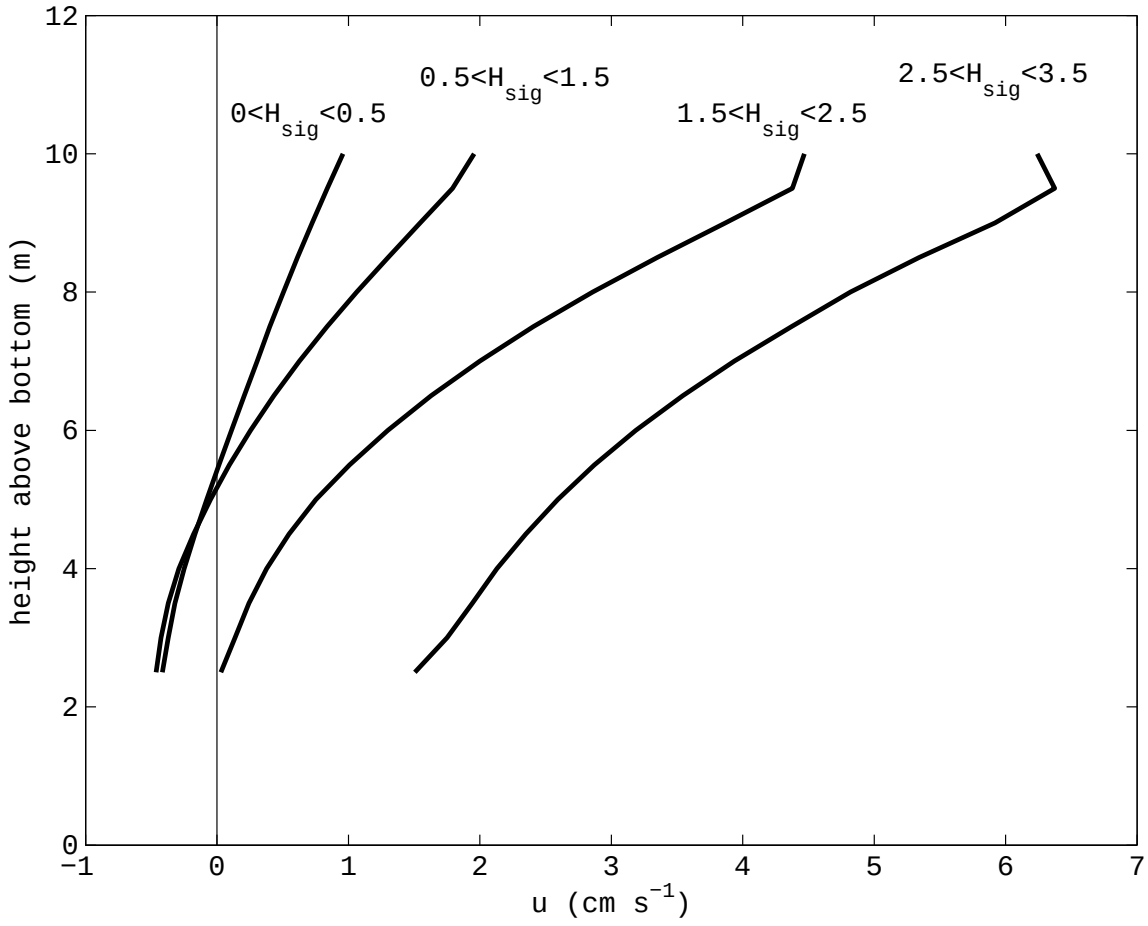

Figure E-7: Average offshore flow profiles from MVCO for different ranges of H_{sig} during periods when the wind stress magnitude was small ($|\tau^s| < 0.03$ N m^{-2}). Standard errors of the means are 0.1 cm s^{-1} for $0 < H_{sig} < 0.5$ and $0.5 < H_{sig} < 1.5$, 0.4 cm s^{-1} for $1.5 < H_{sig} < 2.5$, and 1.6 cm s^{-1} for $2.5 < H_{sig} < 3.5$. The current observations in the top bin ($h = 10$ m) may be contaminated by surface reflections from the side-lobes of the ADCP acoustic pulses during large waves because of the reduced water depth under the wave troughs.

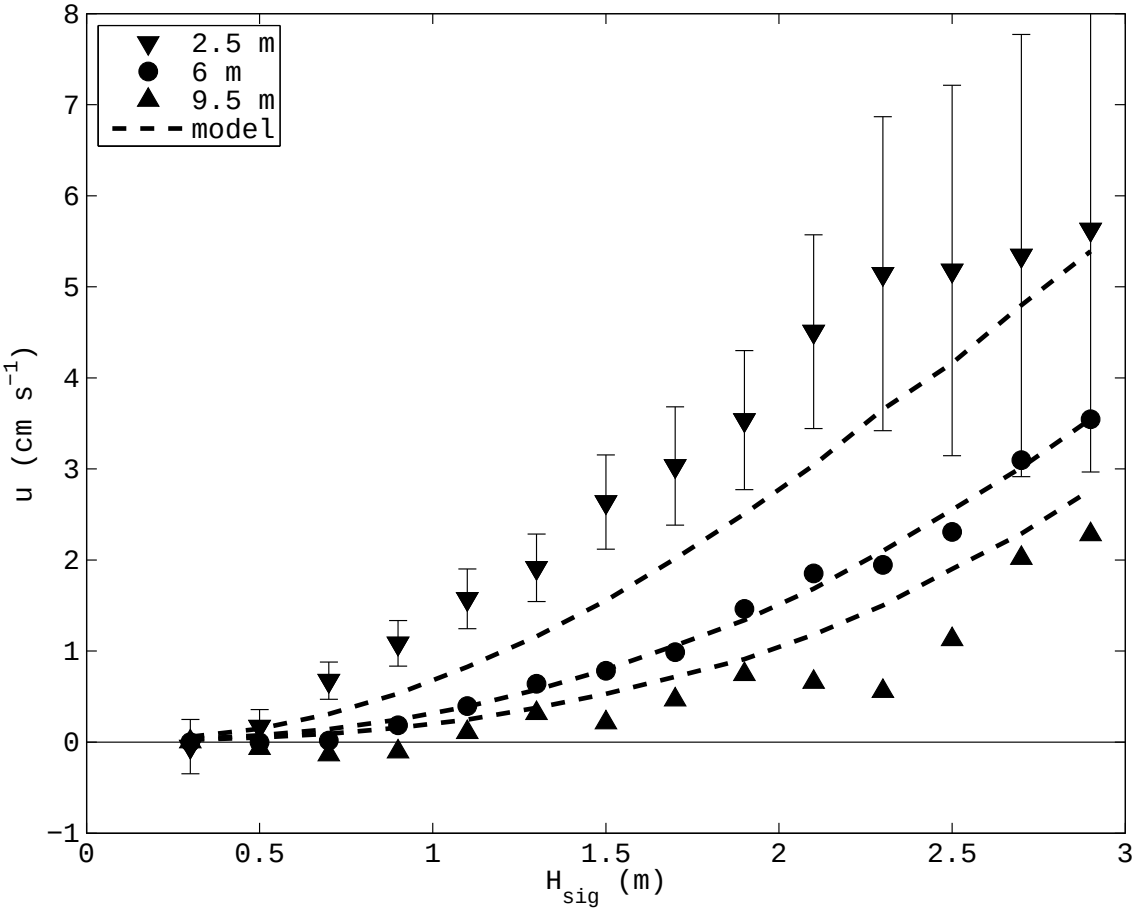

Figure E-8: Bin-averaged cross-shelf velocities at 2.5 m, 6 m, and 9.5 m below the surface as a function of significant wave height H_{sig} (symbols) at MVCO, water depth 12 m. Bin-average Stokes velocities at the same depths are also shown (dashed lines). Averages are over 0.2 m increments of H_{sig} and the mean cross-shelf velocity profile during weak wind stresses and waves has been subtracted from the observations. Standard errors of the means for the 6 m and 9.5 m cross-shelf velocities are similar to those shown for the 2.5 m cross-shelf velocities. The second "good" current bin at 2.5 m below the surface is used to reduce possible inaccuracies associated with side-lobe reflections during large waves (see Fig. E-7).

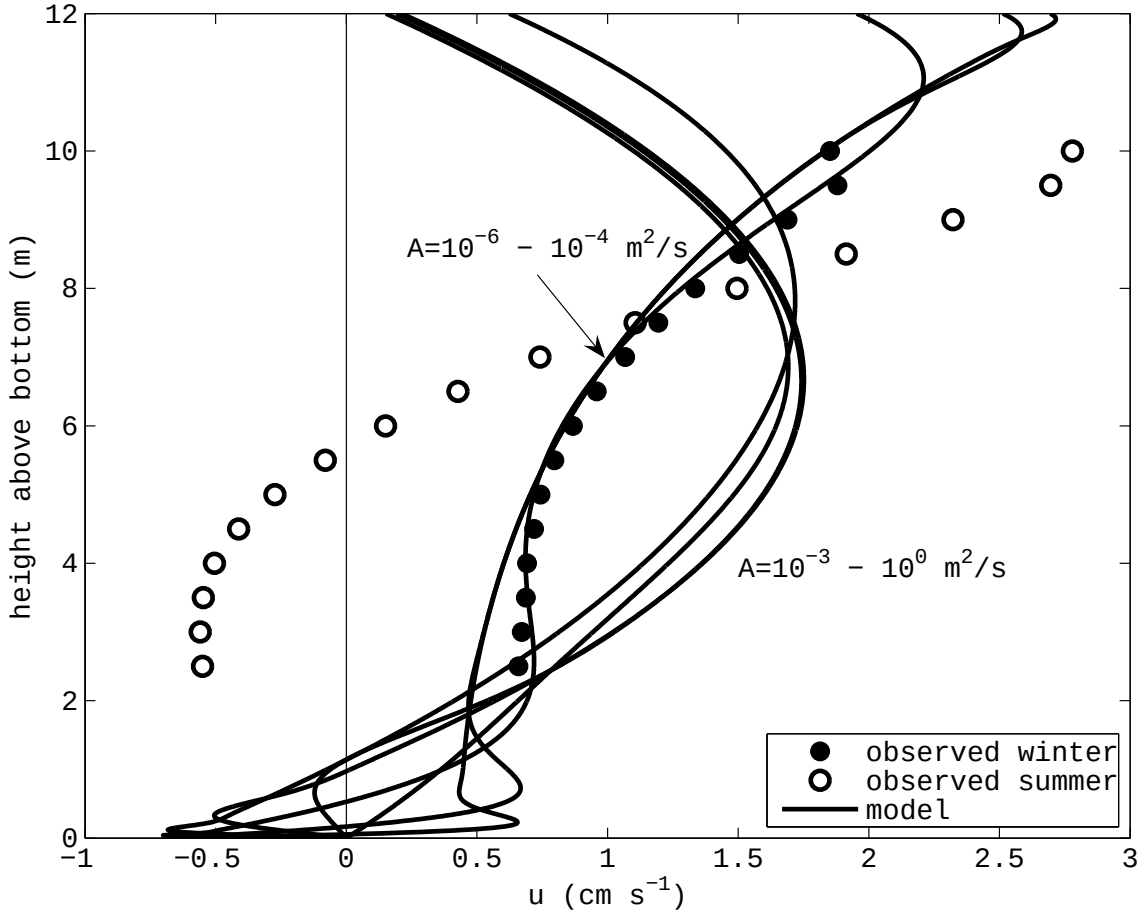

Figure E-9: Average cross-shelf velocity profiles from the model described in Section E.4.1 for various constant eddy viscosities A (lines) and observed average profiles from MVCO during winter (October - March) and summer(April - September) for $1 < H_{sig} < 2$ and $|\tau^s| < 0.03$ N m^{-2}. Model profiles were computed using the average significant wave height (1.3 m) and wave period (6.4 s) of the observed winter profiles (summer values are essentially the same). Standard errors of the means are 0.3 cm s^{-1} for the winter profile and 0.5 cm s^{-1} for the summer profile.

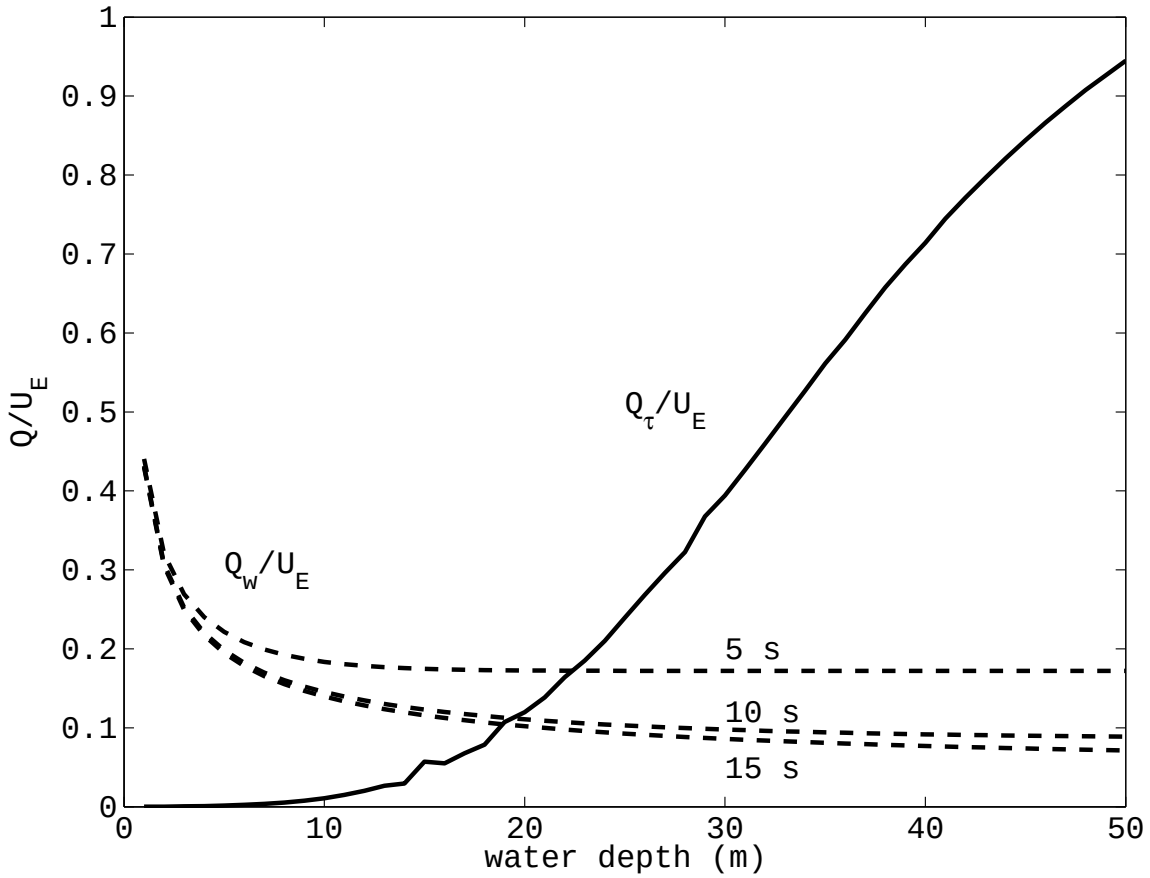

Figure E-10: The wave-driven transport (Q_w) normalized by the Ekman transport (U_E) as a function of water depth for wave periods of 5, 10, and 15 s estimated from (E.10) assuming $H_{sig}^2/\tau_s^y = 25$ m^4 N^{-1} (dashed lines). The solid line shows the normalized cross-shelf transport (Q_τ) driven by an along-shelf wind stress ($\tau_s^y = 0.1$ N m^{-2}) as a function of water depth from a two-dimensional model (no along-shelf variation) with an unstratified turbulent eddy viscosity that increases linearly from zero at each boundary over 10% of the boundary layer thickness and is constant in the interior (see Lentz, 1995).

Bibliography

J. S. Allen. Models of wind-driven currents on the continental shelf. *Annual Review of Fluid Mechanics*, 12:389–433, 1980.

J. S. Allen and R. L. Smith. On the Dynamics of Wind-Driven Shelf Currents. *Philosophical Transactions of the Royal Society of London. Series A, Mathematical and Physical Sciences*, 302(1472):617–634, 1981.

D. G. Andrews and M. E. McIntyre. Planetary Waves in Horizontal and Vertical Shear: The Generalized Eliassen-Palm Relation and the Mean Zonal Acceleration. *Journal of the Atmospheric Sciences*, 33(11):2031–2048, 1976.

F. Ardhuin, B. Chapron, and T. Elfouhaily. Waves and the air-sea momentum budget: Implications for ocean circulation modeling. *J. Phys. Oceanogr.*, 34:1741–1755, 2004.

F. Ardhuin, N. Rascle, and K. Belibassakis. Explicit wave-averaged primitive equations using a Generalized Lagrangian Mean. *Ocean Modelling*, accepted, 2007.

L. P. Atkinson, E. Oka, S. Y. Wu, T. J. Berger, J. O. Blanton, and T. N. Lee. Hydrographic variability of southeastern United States shelf and slope waters during the Genesis of Atlantic Lows Experiment: Winter 1986. *Journal of Geophysical Research*, 94(C8):10699–10713, August 1989.

J.A. Austin. The role of the alongshore wind stress in the heat budget of the North Carolina inner shelf. *Journal of Geophysical Research*, 104(C8):18,187–18,204, 1999.

Jay A. Austin and Steven J. Lentz. The relationship between synoptic weather systems and meteorological forcing on the North Carolina inner shelf. *Journal of Geophysical Research*, 104(C8):18,159–18,185, August 1999.

Jay A. Austin and Steven J. Lentz. The inner shelf response to wind-driven upwelling and downwelling. *J. Phys. Oceanogr.*, 32:2171–2193, July 2002.

T. C. Austin, J. B. Edson, W. R. McGillis, M. Purcell, R. A. Petitt Jr., M. K. McElroy, C. W. Grant, J. Ware, and S. K. Hurst. A network-based telemetry architecture developed for the Martha's Vineyard Coastal Observatory. *IEEE Journal of Oceanic Engineering*, 27(2):228–234, 2002.

R. C. Beardsley and W. C. Boicourt. On estuarine and continental-shelf circulation in the Middle Atlantic Bight. In B. A. Warren and C. Wunsch, editors, *Evolution of Physical Oceanography: Scientific Surveys in Honor of Henry Stommel*, chapter 7, pages 198–233. Cambridge, Mass: MIT Press, 1981.

R. C. Beardsley and C. N. Flagg. The water structure, mean currents, and shelf-water/slope-water front on the New England continental shelf. *Memoires Societé Royale des Sciences de Liège*, 10(6):209–255, 1976.

Robert C. Beardsley, David C. Chapman, Kenneth H. Brink, Steven R. Ramp, and Ronald Schlitz. The Nantucket Shoals Flux Experiment (NSFE79). Part I: A basic description of the current and temperature variability. *J. Phys. Oceanogr.*, 15: 713–748, June 1985.

Robert C. Beardsley, Steven J. Lentz, Robert A. Weller, Richard Limeburner, James D. Irish, and James B. Edson. Surface forcing on the southern flank of Georges Bank, February–August 1995. *J. Geophys. Res.*, 108(C11), 2003. doi: 10.1029/2002JC001359.

T. J. Berger, W. C. Boicourt, J. H. Churchill, P. Hamilton, R. J. Wayland, and D. R. Watts. A physical oceanographic field program offshore of North Carolina. Tech. Rep. MMS 94, Science Applications International Corporation, 463 pp., 1994.

H. B. Bigelow. Plankton of the offshore waters of the Gulf of Maine. *Bulletin of the U. S. Bureau of Fisheries*, 40:1–509, 1926.

H. B. Bigelow. Studies of the waters on the continental shelf, Cape Cod to Chesapeake Bay. I. The cycle of temperature. *Papers in Physical Oceanography and Meteorology*, 2(4):1–135; http://hdl.handle.net/1912/1144, 1933.

F. Bignami and T. S. Hopkins. Salt and heat trends in the shelf waters of the southern Middle-Atlantic Bight. *Continental Shelf Research*, 23(6):647–667, 2003.

Pierre E. Biscaye, Charles N. Flagg, and Paul G. Falkowski. The Shelf Edge Exchange Processes experiments, SEEP-II: An introduction to hypotheses, results and conclusions. *Deep Sea Research II*, 41(23):231–252, 1994.

Jackson O. Blanton. Ocean currents along a nearshore frontal zone on the continental shelf of the Southeastern United States. *Journal of Physical Oceanography*, 11: 1627–1637, December 1981.

A. J. Bowen, D. L. Inman, and V. P. Simmons. Wave "set-down" and set-up. *Journal of Geophysical Research*, 73(8):2569–2577, 1968.

Kenneth H. Brink. Wind-driven currents over the continental shelf. In Kenneth H. Brink and Allan R. Robinson, editors, *The Global Coastal Ocean: Processes and Methods*, volume 10 of *The Sea: Ideas and Observations on Progress in the Study of the Seas*, chapter 1, pages 3–20. John Wiley & Sons, Inc., New York, 1998.

Wendell S. Brown, Neal R. Pettigrew, and James D. Irish. The Nantucket Shoals Flux Experiment (NSFE79). Part II: The structure and variability of across-shelf pressure gradients. *J. Phys. Oceanogr.*, 15:749–771, June 1985.

Wendell S. Brown, James D. Irish, and Clinton D. Winant. A description of subtidal pressure field observations on the northern California continental shelf during the Coastal Ocean Dynamics Experiment. *Journal of Geophysical Research*, 92(C2): 1605–1636, 1987.

H.L. Bryden, D. Halpern, and R.D. Pillsbury. Importance of eddy heat flux in a heat budget for Oregon coastal waters. *Journal of Geophysical Research*, 85(C11): 6649–6653, 1980.

A. F. Bunker. Computations of surface energy flux and annual air–sea interaction cycles of the North Atlantic Ocean. *Monthly Weather Review*, 104(9):1122–1140, 1976.

K. Colbo and R. A. Weller. The accuracy of the IMET sensor package. *Journal of Atmospheric and Oceanic Technology*, under review, 2007.

G. T. Csanady. The arrested topographic wave. *Journal of Physical Oceanography*, 8:47–62, January 1978.

C. N. Cudaback, L. Washburn, and E. Dever. Subtidal inner-shelf circulation near Point Conception, California. *Journal of Geophysical Research*, 110(C10007): doi:10.1029/2004JC002608, 2005.

E. P. Dever and S[teven] J. Lentz. Heat and salt balances over the northern California shelf in winter and spring. *J. Geophys. Res.*, 99(C8):16,001–16,017, August 1994.

James B. Edson, Timothy Crawford, Jerry Crescenti, Tom Farrar, Nelson Frew, Greg Gerbi, Costas Helmis, Tihomir Hristov, Djamal Khelif, Andrew Jessup, Haf Jonsson, Ming Li, Larry Mahrt, Wade McGillis, Albert Plueddemann, Lian Shen, Eric Skyllingstad, Tim Stanton, Peter Sullivan, Jielun Sun, John Trowbridge, Dean Vickers, Shouping Wang, Quing Wang, Robert Weller, John Wilkin, Dick Yu, and Chris Zappa. The Coupled Boundary Layers and Air-Sea Transfer experiment in low winds (CBLAST-Low). *Bulletin of the American Meteorological Society*, page in press, 2007.

Vagn Walfrid Ekman. On the influence of the Earth's rotation on ocean-currents. *Arkiv för Matematik, Astronomi och Fysik*, 2(11):1–53, 1905.

C. W. Fairall, E. F. Bradley, J. E. Hare, A. A. Grachev, and J. B. Edson. Bulk parameterization of air-sea fluxes: Updates and verification for the COARE algorithm. *Journal of Climate*, 16:571–591, February 2003.

Paul G. Falkowski, Richard T. Barber, and Victor Smetacek. Biogeochemical controls and feedbacks on ocean primary production. *Science*, 281:200–206, July 1998.

F. Feddersen, R. T. Guza, S. Elgar, and T. H. C. Herbers. Alongshore momentum balances in the nearshore. *J. Geophys. Res.*, 103:15,667–15,676, 1998.

C. N. Flagg, J. A. Vermersch, and R. C. Beardsley. 1974 MIT New England Shelf Dynamics Experiment (March, 1974) Data Report, Part II: The moored array. Report 76-1, Massachusetts Institute of Technology, 1976.

C. N. Flagg, L. J. Pietrafesa, and G. L. Weatherly. Springtime hydrography of the southern Middle Atlantic Bight and the onset of seasonal stratification. *Deep Sea Research Part II: Topical Studies in Oceanography*, 49(20):4297–4329, 2002.

P. S. Fratantoni and R. S. Pickart. Variability of the shelf break jet in the Middle Atlantic Bight: Internally or externally forced? *Journal of Geophysical Research*, 108(C5):3166, 2003. doi: 10.1029/2002JC001326.

Frederick C. Fuglister. Average monthly sea surface temperatures of the western North Atlantic Ocean. *Papers in Physical Oceanography and Meteorology*, 10(2): 1–25; http://hdl.handle.net/1912/1057, 1947.

A. F. Garcez Faria, E. B. Thornton, T. C. Lippman, and T. P. Stanton. Undertow over a barred beach. *J. Geophys. Res.*, 105:16999–17010, 2000.

R. W. Garvine. A simple model of coastal upwelling dynamics. *J. Phys. Oceanogr.*, 1:169–179, 1971.

Gregory P. Gerbi, John H. Trowbridge, James B. Edson, Albert J. Plueddemann, Eugene A. Terray, and Janet J. Fredericks. Measurements of momentum and heat transfer across the air-sea interface. *Journal of Physical Oceanography*, under revision.

P. M. Glibert. Inorganic carbon uptake by phytoplankton in Vineyard Sound, Massachusetts. II. comparative primary productivity and nutritional status of winter and summer assemblages. *Journal of Experimental Marine Biology and Ecology*, 86(2):101–118, 1985.

K. Govender, G. P. Mocke, and M. J. Alport. Video-imaged surf zone wave and roller structures and flow fields. *J. Geophys. Res.*, 107(C7): 3072,doi10.1029/2000JC000755, 2002.

H. H. Gran and T. Braruud. A quantitative study of the phytoplankton in the Bay of Fundy and the Gulf of Maine. *Journal of the Biological Board of Canada*, 1: 279–467, 1935.

R. T. Guza and E. B. Thornton. Wave set-up on a natural beach. *J. Geophys. Res.*, 86(C5):4133–4137, 1981.

J. W. Haines and A. H. Sallenger, Jr. Vertical structure of mean cross-shore currents across a barred surf zone. *J. Geophys. Res.*, 99(C7):14223–14242, 1994.

G. R. Halliwell and J. S. Allen. The large-scale coastal wind field along the west coast of North America, 1981-1982. *Journal of Geophysical Research*, 92(C2):1861–1884, 1987.

G. Han and T. Niedrauer. Hydrographic Observations and Mixing Processes in the New York Bight, 1975-1977. *Limnology and Oceanography*, 26(6):1126–1141, 1981.

K. Hasselmann. Wave-driven inertial oscillations. *Geophys. Fluid Dyn.*, 1:463–502, 1970.

T. H. C. Herbers, E. J. Hendrickson, and W. C. O'Reilly. Propagation of swell across a wide continental shelf. *Journal of Geophysical Research*, 105(C8):19729–19737, 2000.

R. A. Holman and A. H. Sallenger, Jr. Setup and swash on a natural beach. *J. Geophys. Res.*, 90(C1):945–953, 1985.

Lara Hutto, Jeff Lord, Paul Bouchard, Robert A. Weller, and Mark Pritchard. SecNav/CBLAST 2002 Field Experiment: Deployment/Recovery Cruises and Data Report. Technical Report WHOI-2003-07, Woods Hole Oceanographic Institution, 2003.

Lara Hutto, Tom Farrar, and Robert A. Weller. CBLAST 2003 Field Work Report. Technical Report WHOI-2005-04, Woods Hole Oceanographic Institution, 2005.

Adriana Huyer. Coastal upwelling in the California Current system. *Progress in Oceanography*, 12:259–284, 1983.

N. G. Jerlov. *Optical Oceanography*. Elsevier, 1968.

T. M. Joyce. Meteorology and air-sea interactions. In J. D. Milliman and W. R. Wright, editors, *The marine environment of the U. S. Atlantic Continental Slope and Rise*, pages 5–26. Boston: Jones and Bartlett, 1987.

Bostwick H. Ketchum, Alfred C. Redfield, and John C. Ayers. The oceanography of the New York Bight. *Papers in Physical Oceanography and Meteorology*, 12(1): 1–46; http://hdl.handle.net/1912/1060, 1951.

Anthony R. Kirincich, John A. Barth, Brian A. Grantham, Bruce A. Menge, and Jane Lubchenco. Wind-driven inner-shelf circulation off central Oregon during summer. *Journal of Geophysical Research*, 110(C11), 2005. doi: 10.1029/2004JC002611.

J. T. Kohut, S. M. Glenn, and R. J. Chant. Seasonal current variability on the New Jersey inner shelf. *Journal of Geophysical Research*, 109(C07S07): doi:10.1029/2003JC001963, 2004.

P. K. Kundu and I. M. Cohen. *Fluid mechanics*. Academic Press: San Diego, 2nd edition, 2002.

W. G. Large, J. C. McWilliams, and S. C. Doney. Oceanic vertical mixing: a review and a model with a nonlocal boundary layer parameterization. *Reviews of Geophysics*, 32(4):363–404, 1994.

P. H. LeBlond and L. A. Mysak. *Waves in the Ocean*. New York: Elsevier, 1978.

T. N. Lee, E. Williams, R. E. J. Wang, and L. Atkinson. Response of South Carolina continental shelf waters to wind and Gulf Stream forcing during winter of 1986. *Journal of Geophysical Research*, 94:10715–10754, 1989.

Thomas N. Lee, Wen Jei Ho, Vassiliki Kourafalou, and John D. Wang. Circulation on the continental shelf of the southeastern United States. part I: Subtidal response to wind and Gulf Stream forcing during winter. *Journal of Physical Oceanography*, 14:1001–1012, June 1984.

S. J. Lentz. A heat budget for the northern California shelf during CODE 2. *Journal of Geophysical Research*, 92(C13):14491–14509, 1987.

S. J. Lentz. The surface boundary layer in coastal upwelling regions. *J. Phys. Oceanogr.*, 22(12):1517–1539, 1992.

S. J. Lentz and D. C. Chapman. Seasonal differences in the current and temperature variability over the northern California shelf during the Coastal Ocean Dynamics Experiment. *Journal of Geophysical Research*, 94(C9):12571–12592, 1989.

S. J. Lentz, M. Carr, and T. H. C. Herbers. Barotropic tides on the north carolina shelf. *J. Phys. Oceanogr.*, 31:1843–1859, 2001.

Steven J. Lentz. Current dynamics over the northern California inner shelf. *J. Phys. Oceanogr.*, 24:2461–2478, December 1994.

Steven J. Lentz. Sensitivity of the inner-shelf circulation to the form of the eddy viscosity profile. *J. Phys. Oceanogr.*, 25:19–28, January 1995.

Steven J. Lentz. The influence of stratification on the wind-driven cross-shelf circulation over the North Carolina shelf. *J. Phys. Oceanogr.*, 31:2749–2760, September 2001.

Steven J. Lentz. Observations of the mean circulation over the Middle Atlantic Bight continental shelf. *Journal of Physical Oceanography*, under revision, 2007a.

Steven J. Lentz. Seasonal variations in the circulation of the Middle Atlantic Bight continental shelf. *Journal of Physical Oceanography*, under revision, 2007b.

Steve[n] [J.] Lentz and Britt Raubenheimer. Field observations of wave setup. *J. Geophys. Res.*, 104(C11):25867–25,875, November 1999.

S[teven] J. Lentz and C. D. Winant. Subinertial currents on the southern California shelf. *J. Phys. Oceanogr.*, 16:1737–1750, November 1986.

Steve[n] [J.] Lentz, R. T. Guza, Steve Elgar, Falk Feddersen, and T. H. C. Herbers. Momentum balances on the North Carolina inner shelf. *J. Geophys. Res.*, 104(C8): 18,205–18,226, August 1999.

Steven J. Lentz, Robert C. Beardsley, James D. Irish, J. Manning, and Robert A. Weller. Temperature and salt balances on Georges Bank February–August 1995. *J. Geophys. Res.*, 108(C11), 2003a. doi: 10.1029/2001JC001220.

Steve[n] [J.] Lentz, Kipp Shearman, Steve[n] [P.] Anderson, Al Plueddemann, and Jim Edson. Evolution of stratification over the New England shelf during the Coastal Mixing and Optics study, August 1996–June 1997. *J. Geophys. Res.*, 108(C1), 2003b. doi: 10.1029/2001JC001121.

Zhenjiang Li and Robert H. Weisberg. West Florida shelf response to upwelling favorable wind forcing: Kinematics. *Journal of Geophysical Research*, 104(C6): 13,507–13,527, June 1999a.

Zhenjiang Li and Robert H. Weisberg. West Florida continental shelf response to upwelling favorable wind forcing 2. Dynamics. *Journal of Geophysical Research*, 104(C10):23,427–23,442, October 1999b.

L. C. Lillick. Seasonal Studies of the Phytoplankton off Woods Hole, Massachusetts. *Biological Bulletin of the Marine Biological Laboratory*, 73(3):488–503, 1937.

Richard Limeburner, Carol A. Alessi, Robert C. Beardsley, Leslie K. Rosenfeld, Steven J. Lentz, Uwe Send, Clinton D. Winant, John S. Allen, George R. Halliwell, Jr., Wendell S. Brown, and James D. Irish. CODE-2: Moored Array and Large-Scale Data Report. Technical Report 85-35, WHOI, 1983.

Christopher A. Linder and Glen Gawarkiewicz. A climatology of the shelfbreak front in the Middle Atlantic Bight. *Journal of Geophysical Research*, 103(C9):18,405–18,423, August 1998. doi: 10.1029/98JC01438.

Yonggang Liu and Robert H. Weisberg. Momentum balance diagnoses for the West Florida Shelf. *Continental Shelf Research*, 25:2054–2074, 2005.

M. S. Longuet-Higgins. Mass transport in water waves. *Phil. Trans. Roy. Soc. London A*, 245:535–581, 1953.

M. S. Longuet-Higgins and R. W. Stewart. Changes in the form of short gravity waves on long waves and tidal currents. *Journal of Fluid Mechanics Digital Archive*, 8 (4):565–583, 1960.

M. S. Longuet-Higgins and R. W. Stewart. Radiation stresses in water waves; a physical discussion, with applications. *Deep-Sea Research*, 11(4):529–562, 1964.

M. S. Longuet-Higgins and R. W. Stewart. Radiation stress and mass transport in gravity waves, with application to "surf-beats". *J. Fluid Mech.*, 13:481–504, 1962.

C. Marrase, E. Lin Lim, and D. A. Caron. Seasonal and daily changes in bacterivory in a coastal plankton community. *Mar. Ecol. Prog. Ser.*, 82:281–289, 1992.

A.K. Masse. *Estuary-shelf interaction: Delaware Bay and the inner shelf*. PhD thesis, University of Delaware, Newark, 216 pp. 1988.

G. Masselink and K. P. Black. Magnitude and cross-shore distribution of bed return flow measured on natural beaches. *Coastal Eng.*, 25:165–190, 1995.

D. A. Mayer, D. V. Hansen, and D. A. Ortman. Long-term current and temperature observations on the Middle Atlantic shelf. *Journal of Geophysical Research*, 84(C4): 1776–1792, 1979.

Jr. McCreary, J. P., H. S. Lee, and D. B. Enfield. The response of the coastal ocean to strong offshore winds: with application to circulations in the Gulfs of Tehuantepec and Papagayo. *Journal of Marine Research*, 47:81–109, 1989.

J. C. McWilliams and J. M. Restrepo. The wave-driven ocean circulation. *J. Phys. Oceanogr.*, 29:2523–2540, 1999.

J. C. McWilliams, J. M. Restrepo, and E. M. Lane. An asymptotic theory for the interaction of waves and currents in coastal waters. *Journal of Fluid Mechanics*, 511:135–178, 2004.

C. C. Mei. *The applied dynamics of ocean surface waves*. John Wiley & Sons, Inc., New York, NY USA, 1983. 740 pp.

R. B. Montgomery. Comments on 'Seasonal variability of the Florida current,' by Niiler and Richardson. *Journal of Marine Research*, 32(3):533–534, 1974.

D. G. Mountain. Variability in the properties of Shelf Water in the Middle Atlantic Bight, 1977-1999. *Journal of Geophysical Research*, 108(C1):1029–1044, 2003.

D. G. Mountain, G. A. Strout, and R. C. Beardsley. Surface heat flux in the Gulf of Maine. *Deep Sea Research Part II: Topical Studies in Oceanography*, 43(7): 1533–1546, 1996.

K. Nadaoka and T. Kondoh. Laboratory measurements of velocity field structures in the surfzone by LDV. *Coastal Eng. Jpn.*, 25:125–145, 1982.

P. A. Newberger and J. S. Allen. Forcing a three-dimensional, hydrostatic primitive-equation model for application in the surf zone, Part 2: Application to DUCK94. *J. Geophys. Res.*, submitted, 2006.

P. Nielsen. Wave setup: A field study. *J. Geophys. Res.*, 93(C12):15,643–15,652, 1988.

Marlene Noble and Bradford Butman. On the longshelf structure and dynamics of subtidal currents on the Eastern United States Continental Shelf. *Journal of Physical Oceanography*, 13:2125–2146, December 1983.

J. E. O'Reilly and C. Zetlin. Seasonal, horizontal, and vertical distribution of phytoplankton chlorophyll a in the northeast U.S. continental shelf ecosystem. Technical Report NOAA NMFS 139, US Department of Commerce, 1998.

C. A. Paulson and J. J. Simpson. Irradiance Measurements in the Upper Ocean. *Journal of Physical Oceanography*, 7(6):952–956, 1977.

Rich Pawlowicz, Robert C. Beardsley, and Steven J. Lentz. Harmonic analysis including error estimates in MATLAB using T_TIDE. *Computers and Geosciences*, 2002.

N. R. Pettigrew. *The dynamics and kinematics of the coastal boundary layer off Long Island*. PhD thesis, Woods Hole Oceanographic Institution, Woods Hole, Massachusetts, 1981.

J. A. Polton, D. M. Lewis, and S. E. Belcher. The role of wave-induced Coriolis-Stokes forcing on the wind-driven mixed layer. *J. Phys. Oceanogr.*, 35:444–457, 2005.

Mark Pritchard, Jason Gobat, William M. Ostrom, Jeffrey Lord, Paul Bouchard, and Robert A. Weller. CBLAST-Low 2001 Pilot Study: Mooring Deployment Cruise and Data Report. Technical Report WHOI-2002-03, Woods Hole Oceanographic Institution, 2002.

U. Putrevu and I. A. Svendsen. Vertical structure of the undertow outside the surf zone. *J. Geophys. Res.*, 98(C12):22707–22716, 1993.

R. Raubenheimer, R. T. Guza, and S. Elgar. Field observations of wave-driven setdown and setup. *J. Geophys. Res.*, 106(C3):4629–4638, 2001.

B. Cameron Reed. Linear least-squares fits with errors in both coordinates. II: Comments on parameter variances. *American Journal of Physics*, 60(1):59–62, 1992.

A. J. H. M. Reniers, E. B. Thornton, T. P. Stanton, and J. A. Roelvink. Vertical flow structure during Sandy Duck: observations and modeling. *Coastal Eng.*, 51: 237–260, 2004.

G. A. Riley. Seasonal fluctuations of the phytoplankton population in New England Coastal Waters. *Journal of Marine Research*, 6:114–125, 1947.

J. Roughgarden, S. Gaines, and H. Possingham. Recruitment dynamics in complex life cycles. *Science*, 241(4872):1460–1466, 1988.

P. M. Saunders. Wind stress on the ocean over the eastern continental shelf of North America. *Journal of Physical Oceanography*, 7(4):555–566, 1977.

Oscar Schofield, Trisha Bergmann, Paul Bissett, J. Frederick Grassle, Dale B. Haidvogel, Josh Kohut, Mark Moline, and Scott M. Glenn. The Long-Term Ecosystem Observatory: An integrated coastal observatory. *IEEE Journal of Oceanic Engineering*, 27(2):146–154, April 2002.

J. T. Scott and G. T. Csanady. Nearshore currents off Long Island. *Journal of Geophysical Research*, 81(C30):5401–5402, 1976.

Kipp Shearman and Steven J. Lentz. Dynamics of mean and subtidal flow on the New England shelf. *J. Geophys. Res.*, 108(C8), 2003. doi: 10.1029/2002JC001417.

R. K. Shearman and S. J. Lentz. Observations of tidal variability on the New England shelf. *Journal of Geophysical Research*, 109(C06010):doi:10.1029/2003JC001972, 2004.

R. L. Smith. A comparison of the structure and variability of the flow field in three coastal upwelling regions: Oregon, Northwest Africa, and Peru. In F. A. Richards, editor, *Coastal Upwelling*, pages 107–118. American Geophysical Union, 1981.

Stuart D. Smith. Coefficients for sea surface wind stress, heat flux, and wind profiles as a function of wind speed and temperature. *J. Geophys. Res.*, 93:15,467–15,472, 1988.

M. Stive and H. Wind. Cross-shore mean flow in the surfzone. *Coastal Eng.*, 10: 325–340, 1986.

G. G. Stokes. On the theory of oscillatory waves. *Trans. Camb. Phil. Soc.*, 8:441–455, 1847.

P. T. Strub, J. S. Allen, A. Huyer, and R. L. Smith. Seasonal cycles of currents, temperatures, winds, and sea level over the northeast Pacific continental shelf: 35°N to 48°N. *Journal of Geophysical Research*, 92(C2):1507–1526, 1987.

I. A. Svendsen. Mass flux and undertow in a surf zone. *Coastal Engineering*, 8: 347–365, 1984.

I. A. Svendsen and U. Putrevu. Nearshore Mixing and Dispersion. *Proceedings of the Royal Society of London, Series A*, 445:561–576, 1994.

H. U. Sverdrup. On the process of upwelling. *J. Mar. Res.*, 1:155–164, 1938.

H. U. Sverdrup. On conditions for the vernal blooming of phytoplankton. *Journal du Conseil International pour l'Exploration de la Mer*, 18:287–295, 1953.

K. R. Thompson and D. T. Pugh. The subtidal behavior of the Celtic Sea–II. Currents. *Continental Shelf Research*, 5(3):321–346, 1986.

E. B. Thornton and R. T. Guza. Transformation of Wave Height Distribution. *Journal of Geophysical Research*, 88(C10):5925–5938, 1983.

E. B. Thornton and R. T. Guza. Surf zone longshore currents and random waves: Field data and models. *Journal of Physical Oceanography*, 16(7):1165–1178, 1986.

Charles E. Tilburg. Across-shelf transport on a continental shelf: Do across-shelf winds matter? *J. Phys. Oceanogr.*, 33:2675–2688, 2003.

F. C. K. Ting and J. T. Kirby. Observations of undertow and turbulence in a laboratory surf zone. *Coastal Eng.*, 24:51–80, 1994.

F. Ursell. On the theoretical form of ocean swell on a rotating earth. *Mon. Not. Roy. Astron. Soc., Geophys. Suppl.*, 6:1–8, 1950.

John J. Walsh, Pierre E. Biscaye, and Gabriel T. Csanady. The 1983–1984 Shelf Edge Exchange Processes (SEEP)-I experiment: Hypotheses and highlights. *Continental Shelf Research*, 8(5–7):345–456, 1988.

Georges L. Weatherly and Paul J. Martin. On the Structure and Dynamics of the Oceanic Bottom Boundary Layer. *Journal of Physical Oceanography*, 8:557–570, July 1978.

John L. Wilkin. The summertime heat budget and circulation of southeast New England shelf waters. *Journal of Physical Oceanography*, 36:1997–2011, November 2006.

L. D. Wright, R. T. Guza, and A. D. Short. Dynamics of a high-energy dissipative surf zone. *Mar. Geology*, 45:41–62, 1982.

W. R. Wright and C. E. Parker. A volumetric temperature/salinity census for the Middle Atlantic Bight. *Limnology and Oceanography*, 21(4):563–571, July 1976.

Z. Xu and A. J. Bowen. Wave- and Wind-Driven Flow in Water of Finite Depth. *Journal of Physical Oceanography*, 24(9):1850–1866, 1994.